The development of magnetic materials on flexible substrates for spintronic applications

BAHAALDIN, ALA,SAFAALDIN

The development of magnetic materials on flexible substrates for spintronic applications

Ala Safaaldin Bahaaldin

Department of Physics
University of Durham

This dissertation is submitted for the degree of
Doctor of Philosophy

July 2019

I would like to dedicate this thesis to Allah for giving me this opportunity, the strength and the patience to complete my dissertation and to my loving parents: to my mother, who sacrificed her whole life for her children and to my father, who gave me great advice and who is always encouraging me and protecting me ...

Acknowledgement

And Finally. A thesis that experienced excitement and frustration, hard work, controversies and complements, etc. ends here. In general, the life of a Ph.D. student seems difficult. However, I have to confess that I had comparatively good time during my thesis. And here, I would like to write my heart felt gratitude to all people who provided this great experience for me. I was always busy in doing different experiments during that period. This experiment gave me an insight that: if you wish to think up something new, all you have to do is to go and attempt some different things and the innovation will follow automatically. I gratefully acknowledge the scholarship that is granted to me from the Republic of Iraq, the Higher Committee for Education Development in Iraq (HCED). Also, for all this guidance, ideas and encouragement, I am grateful to my supervisor, Prof. Del Atkinson, without his suggestion of this thesis it would never have come into being. Thank you for your understanding and willingness to be there whenever a discussion is needed. I would also like to thanks to my co supervisor Dr. Aidan Hindmarch for giving me some notes in the lab and for having a high morals that I have never seen before. I would like to thank my parents [my father and my mother] who have been supporting me in all my life. I am blessed to have parents who never said any objections to any of my desires. I always enjoyed the freedom they gave me, and which absolutely helped me in becoming a highly independent person. I would like to thank Dr. Sinan Azzawi for his help, especially the understanding of experimental technique of the beginning of my Ph.D. Also, I would like to say thanks to Dr. Shaimaa Bahaaldin [my sister] for her supporting and given me some notes during my Phd studies. Next, I thank all colleagues from Durham University [Dr. Oto Obong, Mr. Ben and Mr. Charles] in whom spent with them one of the best times of my life. Coming from Iraq and living in a western country like United Kingdom was a completely challenging and it would not have been possible without having some good friends. At last, I would like to thank to my government that grants me this opportunity to have a new knowledge and experiences. Also, thanks for all the people who directly and indirectly assisted me to be who I am.

Declaration

I, Ala Safaaldin Bahaaldin, declare that this thesis titled, "The development of magnetic materials on flexible substrates for spintronic applications", the work presented in it are my own and has not been submitted at any univeristy as examination for any other degree. The samples investigated in chapter 6, 7 and 8 were made by the author. The samples investigated in chapter 8 was undertaken by Prof. D. Atkinson to carry microscopic images with support from Mr. S. Mallick in the Laboratory of Prof. S. Bedanta at NISER, Bhubaneswar, India. All the preparations, analysis and calculations of samples were done by the author. AutoCAD, Gwyddion and imagej programs were used by the author. XRR (X Ray Reflectivity), MR (Magnetometry) Hall and MOKE (Magneto optic Kerr Effect) presented in this thesis were made by the author. XRD measurements were done in Lancaster university. All of the samples deposition, structure and fabrication were done in Durham university.

Ala Safaaldin Bahaaldin
July 2019

Abstract

Flexible electronic is a field of technology for assembling electronic circuits and devices on flexible substrates; which are characterized by their low cost, conformable and light weight properties compared to conventional silicon-based electronic devices. The addition of ferromagnetic materials to flexible substrates will allow the introduction of additional functionalities including memory and sensors. Here, I present a detailed study of the development of perpendicular magnetic anisotropy (PMA) in Pt/Co/Pt multi-layered systems and demonstrate the conditions for controlling the anisotropy. Two typical kinds of substrates have been introduced for preparing trilayer thin-film structure by deposition of magnetic films (Pt/Co/Pt) on them. Magnetron sputtering was used to deposit a series of Pt/Co/Pt trilayers where magnetic anisotropy was studied using Atomic Force Microscope, x-ray diffraction, x-ray reflectivity, Magneto-Optical Kerr effect magnetometry and Hall–effect measurements. The effect of Co thickness on the anisotropy, coercivity and switching behaviour were examined and compared between polymeric and silicon substrates. The substrate was found to have a significant effect. A clear PMA was observed for Co thicknesses that range from 0.3 to 0.7 nm. Additional increments in the Co thickness makes the magnetization return to the in-plane direction, with a rapid drop in both the coercivity and the remanence. Further improvements in the PMA were obtained through the thickness of the Pt buffer layer, with higher coercive fields for both flexible plastic and silicon dioxide substrates. However, the thickness of the Pt capping layer did not have any systematic effect on the anisotropy. The results of a study of the interplay between microstructure and the magnetic properties of ultrathin Ru/Co/Ru and Pt/Co/Pt trilayer thin films with PMA is also presented. The maximum values of PMA are observed for the Co thickness by using Pt in comparison with Ru. The effective magnetic anisotropy and coercive field are very sensitive to Ru buffer layer thickness. The values of coercive field increase approximately from 10 of using Ru in comparison with about 1000 Oe for the Pt case. This is associated to the larger grains growth of Pt while Ru has a smaller grains growth. The surface roughness have an impact on the Hall resistivity on the ferromagnetic/non-magnetic thin films. Observation of the magnetic domain structure by means of polar kerr microscopy reveals that out-of-plane magnetization reversal occurs through then nucleation of bubbles on silicon dioxide.

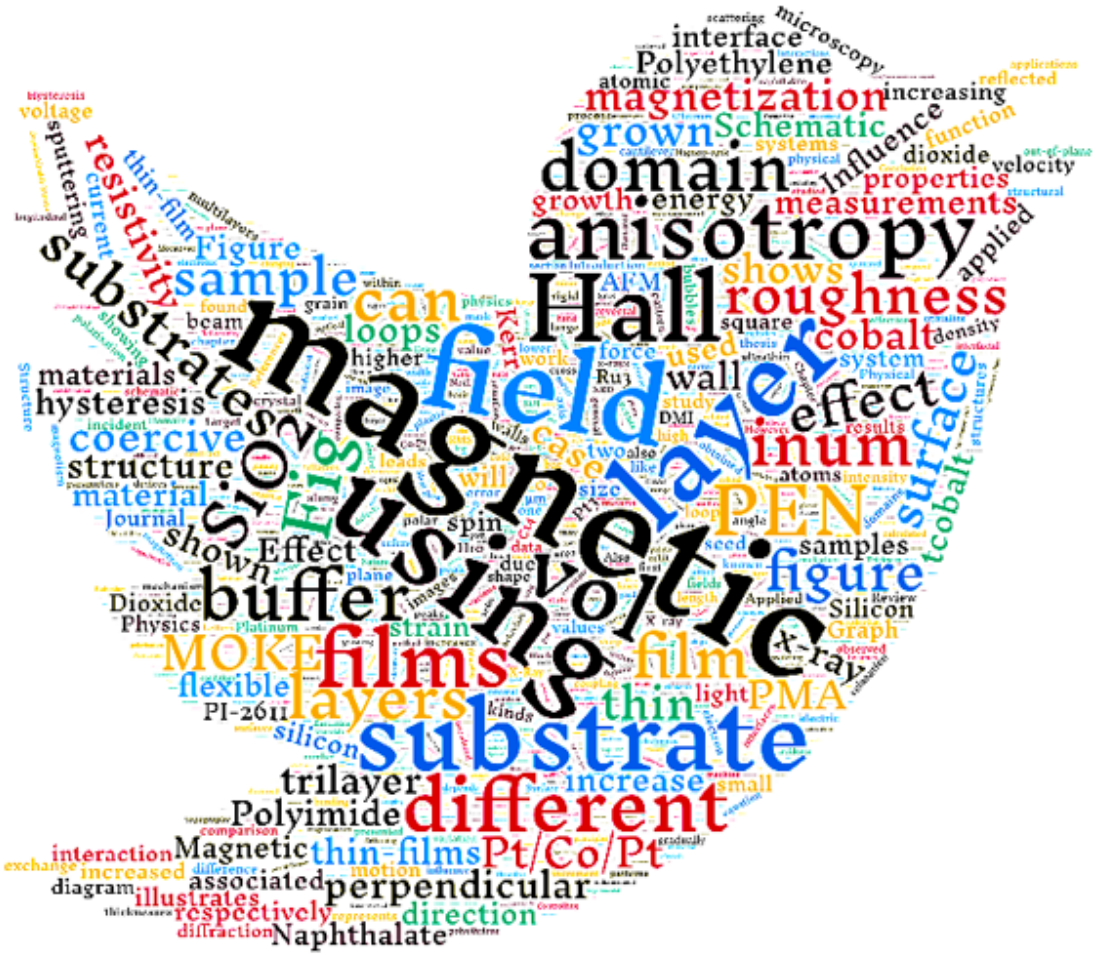
magnetic
field
layer
substrate
films
buffer
Hall
anisotropy
domain
magnetization
roughness
PEN
figure
different
thin
layers
film
MOKE
sample
Figure
resistivity
thin-film
sputtering
voltage
hysteresis
coercive
structure
material
Journal
shown
Effect
Dioxide
Physics
Platinum
strain
flexible
PI-2611
silicon
trilayer
Polyimide
Magnetic
interaction
exchange
increased
diagram
associated
illustrates
respectively
diffraction
Naphthalate
perpendicular
direction
thin-films
Pt/Co/Pt
PMA
X-ray
Graph
Silicon
samples
seed
Applied
Review
Physical
system
surface
effect
cobalt
platinum
interface
Polyethylene
atomic
microscopy
scattering
reflected
applications
increasing
function
Influence
Schematic
grown
systems
physical
dioxide
velocity
properties
measurements
growth
energy
applied
shows
AFM
square
density
used
force
wall
Ru3
DMI
study
results
atoms
intensity
domains
structures
structural
out-of-plane
can
loops
higher
grain
beam
found
physics
Kerr
work
lower
two
also
like
will
heads
size
spin
loop
angle
data
shape
plane
image
values
kinds
light
small
increase
motion
difference
comparison
presented
gradually
Controllers
Current
multilayers
polarization
showing
chapter
thesis
within
bubbles
reversal
Ru
Alloy
Fields
length
known
observed
electric
Substrate
Structure
schematic
incident
target
crystal
Co
Pt
Ru
Si
Al
O
H
N
C
x-ray
Hysteresis

Table of contents

List of figures

Nomenclature

Acronyms / Abbreviations

QCM	Quartz Crystal Microbalance
AFM	Atomic Force Microscope
PMA	Perpendicular Magnetic Anisotropy
DMI	Dzyaloshinskii-Moriya Interaction
SiO_2	Silicon Dioxide
FCC	Face Centered Cubic
HCP	Hexagonal Close Packed
PEN	Polyethylene Naphthalate
PI-2611	Polyimide
RMS	Root Mean Square
OHE	Ordinary Hall Effect
MOKE	Magneto-Optical Kerr Effect Magnetometry
FvdM	Frank-van-der-Merwe
DW	Domain Wall
VM	Volume-Weber
SK	Stranski-Krastanov
AHE	Anomalous Hall Effect

XRR X-Ray Reflectivity

XRD X-Ray Diffraction

Chapter 1

Introduction and structure of thesis

1.1 Introduction

Recently, the flexible electronics play an effective role in developing technology. In fact, there is a high interest to focus on the advantages of flexible electronics that offers flexible, low-cost electronic circuits leaving expensive rigid silicon-based systems [1]. In all modern electronic systems [2], memory plays an important role in the data storage, processing and communication [3–6] using both rigid and flexible substrates. For the manufacture of magnetic film on the flexible substrates, an appropriate insulating layer was often a necessity to reduce the roughness of the flexible substrate for ensuring a continuous and functional layer of magnetic materials [7–9]. Several studies have indicated that the use of plastic bases in the electronics industry is somehow challenging.

Where, the plastic bases possess some unique features and that is why they exist in many applications. Many materials and architectures used in flexible memories including flash-type memories, ferroelectric memory [6] and resistive switching memories [10] ; which have been studied by several research groups. Also, the properties of flexible device should not change after or while being strained; this point represents an essential requirement. From another point of view, however, it would be interesting if their properties can be greatly modulated frequently.

1.2 Aim of this work

The purpose of this thesis is to highlight and understand the effect of perpendicular magnetic anisotropy (PMA) using different types of substrate such as silicon dioxide (rigid), polyethylene naphthalate (PEN) and polyimide (flexible/rigid) substrates that is also affected by the Hall resistivity due to Lorentz effect. Also, the usage of non-magnetic materials (like: Pt and Ru) that grow on those substrates represents a key role for technological applications in the data storage devices.

Taking a thorough understanding of the mechanisms of magnetic domain walls in trilayer thin films through the sputtering deposition has been accomplished in this study. The main goal was to focus on the out of plane anisotropy magnetic materials, in particular the Pt/Co/Pt and Ru/Co/Ru trilayer system. Where, a detailed structural analysis was presented; which shows the reduction in the roughness using different thicknesses of buffer layer. The study also investigated the relationship between domain wall structure and improving the magnetisation behaviour; in order to establish a new knowledge about the relationship between a domain wall and enhancing PMA using rigid/flexible substrates. Where, having further knowledge about the behaviour and mechanisms of controlling the domain walls in thin-films plays a key role in the design of future spintronics devices.

1.3 Thesis Outline

This thesis begins with a general introduction of the background and physical theories describing magnetism, how it can be controlled at the nanoscale and the used technique for investigating the magnetic properties; which in turn opens the discussions about these properties as well as the structural behaviour of sputtered magnetic material.

Chapter 2 provides a general background of magnetism that is relevant to the main subject of this thesis; which is primarily focuses on the basic theories used for discussing and

analysing the obtained results. In order to set this study in the coming chapters within the context of the magnetism in nonmagnetism/ferromagnetism, a brief review on some of the most relevant theories is introduced at the first part of this chapter. The second part focuses on the Anomalous Hall Effect (AHE), where there are two contribution of the AHE, one is coming from the Lorentz force and the other is coming from spin-dependent scattering. Therefore, the experiments and analysis that are undertaken in this thesis were focused on the impact of Hall resistivity based on the Lorentz force effect.

Chapter 2 takes into consideration the spin orbit interaction (SOI) or spin orbit coupling (SOC), which represents an important physical concept for the behaviour of ferromagnetic systems. The magnetic interactions in multi-atom systems help in demonstrating the most complex magnetic behaviour in crystalline systems. The electronic arrangement of a system, leads to some interactions such as those of crystalline field exchange. These interactions can work together to provide the final magnetic state of the material that can include Dzyaloshinskii-Moriya interaction (DMI); where these effects can be combined to determine the domain-wall structure and magnetocrystalline anisotropy, which depend on the exchange and the crystalline field interactions.

Chapter 3 presents the background theory and practical implementation of all processes of sample fabrication. The cutting and cleaning of the sample in substrates is first introduced before discussing the thin film deposition. The next section is the background of the material deposition with focusing on the main deposition system, its main features and the growth conditions of thin-film. The vapour phase growth modes are explained; in order to have clear understanding and linking the magnetic results with any structural changes such as in the platinum or ruthenium and/or the influence of defects /imperfections that may arise when using the different kinds of rigid and flexible substrates.

In chapter 4, we discuss the utilized experimental techniques with including a detail demonstration of the sample holder and new masks. This chapter introduces the experimental

techniques and the obtained results from each technique. Also, it deals with the Hall voltage magneto geometry and magneto optical Kerr effect magneto geometry and imaging measurement capabilities.

Chapter 5 gives a detailed discussion that covers the experimental implementation of x-ray reflectivity and atomic force microscopy. The x-ray reflectivity technique is an important matter as it gives information about the thickness density of thin-film, density and interface width. The AFM (atomic force microscope) technique was used on both silicon dioxide and flexible/rigid plastic substrates; which is discussed in detail in this chapter to understand the structure of substrates.

Chapter 6, demonstrates the advantage and disadvantage of using flexible/rigid substrates depending on the surfaces roughness, stronger-weaker perpendicular magnetic anisotropy (PMA) and Hall resistivity. Moreover, this chapter discusses the impact of bending for decreasing the coercive field associated with the important role of interfacial PMA.

Chapter 7, illustrates the Hall resistivity of both Ru and Pt non-magnetic materials. Also, it includes the pattern data of x-ray diffraction and structure morphology using atomic force microscope. The correlation between perpendicular magnetic anisotropy and grain size of trilayer thin film is demonstrated in this chapter using different kinds of substrates.

Chapter 8 describes the manufacturing of magnetic thin-films on flexible substrates. The data analysis of domain-wall can give us a clear understanding of the implementation of magnetic behaviour that is compared between SiO_2 and PEN substrates. The manufacturing of magnetic thin-films on SiO_2 and PEN substrate has been studied with the analysis of image magnetization. Presenting the magnetization of domain-wall structure using the polar Kerr microscopy is also introduced in this chapter, using the analysis of Kerr microscopy images on the bubbles of trilayer thin-films.

Chapter 9 summarizes the key results obtained from this work with the main conclusion. Also, it introduces the possible future work based on the findings of this thesis.

Chapter 2

The physical basis of magnetic properties in films and the Hall effect

2.1 Introduction

In this chapter, a general interaction of magnetism is first discussed with focusing primarily on those basic theories that assist on analysing the results presented later in this thesis. In order to set the study in the context of the whole discussion about magnetism in magnetic/nonmagnetic multilayers in the coming chapters, a brief review of the most relevant theories is presented. This chapter takes into consideration the study of the spin orbit interaction (SOI) or spin orbit coupling (SOC), which represents an important material concept for the behaviour of FM (abbreviation of Ferromagnetism). Magnetic interactions in multi-atomic systems can help in explaining the most complex magnetic behaviour of crystalline systems. The electronic arrangement of a system is demonstrated using this theory, which produces some interactions such as the crystalline field exchange. These reactions can work together to provide the final magnetic state of the material. This can be noticed in the interaction of Dzyaloshinskii-Moriya (DMI), domain-walls and magnetocrystalline anisotropy, which depend on DMI exchange and interactions.

The final section of this chapter focuses on the Anomalous Hall Effect (AHE), that is directly proportional with the magnetisation. In addition, the following discussion of the resistivity characteristics and the impact of Hall voltage will be limited to what is directly applicable in the experiments mentioned here.

2.2 Magnetic energy theory

The magnetic domain structure depends on several factors including the exchange interaction, magnetic anisotropy, magnetostatic energy, zeeman energy and reorientation of spins through intermediaries (in some thin-film systems), such as in the Dzyaloshinskii-Moriya interaction. The high interface to volume ratio means that interactions in the interface have a great importance.

2.2.1 Ferromagnetism

Ferromagnetism forms the basis of this research work, as it is helpful in reviewing some of the key physics. The effect of attraction or repulsion between materials is called the Magnetism phenomenon [11]. A magnetic moment results from the electrons within a material. The spin is intrinsic to the electron, which is quantized into two states called spin-up and spin-down. Magnetic moments are associated with both the orbital and spin angular momenta.

In ferromagnetic materials, the orbital angular momentum is largely quenched, and the magnetic moment comes from the imbalance in the electrons' spins will result in magnetizing quenching and spin alignment; which in turn results in the 'bulk' magnetism [12]. That means the angular momentum of the orbital will be high in the free metal ion; which will be decreased when ligands are attached to it. The contribution of the orbital to the magnetic moment is called quenched when it equals to zero.

2.2.2 Exchange interaction

The exchange interactions in ferromagnets is the mechanism by which the spins have a direct effect on each other. The simple explanation is that the parallel-spin electrons will have separate wave functions because of the Pauli exclusion principle, leading to reduced Coulomb interaction between electrons and thus a lower total energy [13]. Here, "a" and "b" refer to the adjacent spins, J_{ex} refers to the exchange interaction, Coulomb integral, C, and the overlapping integration, B, as follows:

$$J_{ab} = (J_{ex} - CB^2)/(1 - B^4)\,, \tag{2.1}$$

the exchange constant J_{ab}, in turn, the energy associated with two electron spins that is determined by the Heisenberg-Hamilton exchange:

$$J_{Heis} = -2\,J_{ab} < s_a . s_b > , \tag{2.2}$$

where the spin momenta are given as s_a and s_b. If J_{ab} is positive, the exchange energy prefers electrons with parallel spins; which is an essential cause of ferromagnetism in materials. While, if J_{ab} is negative, the interaction prefers electrons with antiparallel spins, potentially leading antiferromagnetism [14].

2.2.3 Spin-Orbit Interaction (SOI)

The spin orbit Interaction (SOI) is known as the interaction of the electron spins with the electric field through the associated magnetic field in the electrons rest frame and therefore the electrons movement are within a crystal [15]. The principle of the SOI can be understood by considering an electron orbiting a nucleus. The spin-orbit interaction (SOI) gives rise to magnetocrystalline anisotropy and supplies a mechanism for energy dissipation to the lattice. As illustrated in Fig. 2.1, in the frame of reference of the electron, the nucleus orbits the electron forming a closed loop.

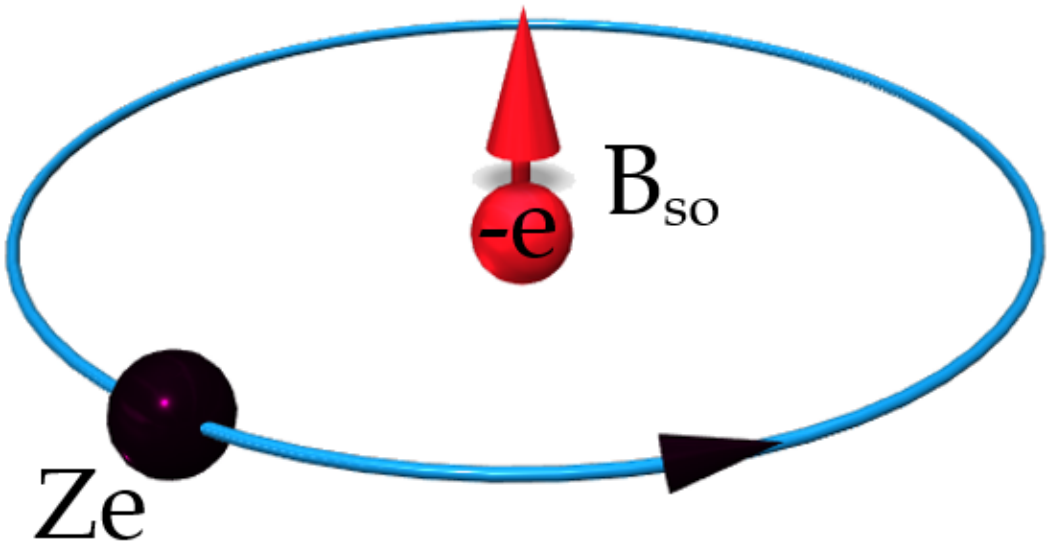

Fig. 2.1 A schematic diagram illustrating the electron that is moving in the field created by a proton. The spin-orbit interaction is due to this magnetic field B_{so}, affecting on the intrinsic magnetic moment of the electron.

This orbiting positive charge makes a magnetic field that interacts with the spin of electron. As a result, the spin moment of the electron is coupled to the orbital. For a single electron orbiting a positively charge nucleus, the SOI Hamiltonian is given by [16];

$$H_{SOI} = \frac{Ze^2}{2m_e^2c^2r^3}\, L\,.\,S\,, \tag{2.3}$$

where m_e is the electron's mass, c is the revolving speed of the nucleus around the electrons, Z is the atomic number of the nuclei and r is the radius of the electron orbital. The expectation value r^{-3} is proportional to Z^3 , hence the SOI scales with Z^4; which demonstrates the reason why the SOI is strong in heavy elements like Pt, Ta and Ir. Therefore, it is significant to note that orbital hybridisation as well plays an important role when considering complete crystals rather than single atoms. When calculating the response of a system to the SOI, it is mostly introduced as it shown here;

$$H_{SOI} = \lambda L\,.\,S\,, \tag{2.4}$$

where λ is a fixed value that is proportional to the force of the SOI. The magnetic moment on an atom is related with its whole angular momentum J ; which is a totality of the orbital angular momentum L and the spin angular momentum S [17]. Also, the SOI represents a small influence that can be applied after a strong contributions from the field. This is recognized as the L-S coupling regime, by which the total angular moment J is calculated and the SOI is applied [16].

2.2.4 Anisotropy

The magnetization orientation depends on the material system that is defined by the term magnetic anisotropy, K. There are different types of magnetic anisotropy such as the crystal, shape, exchange and stress anisotropy or anisotropy induced by magnetic annealing, plastic deformation and irradiation [18].

Magnetocrystalline Anisotropy

A strong interaction between the orbit and lattice is defined by the spin-orbit interaction that acts against the attempts to rotate the spin away from the preferred lattice axes. The anisotropy energy is the energy needed to rotate the magnetization away from an easy direction into a hard axis direction [18–21]. This type occurs from the spin-orbit coupling; which in other words defines the interaction between the spin and orbital motion of each electron (in this case the linkage between 3d spin and orbital angular momentum). There is a positive correlation between the external field and orbit; where the spin of electron reorients by an external field, as well as its orbit. In the presence of an external magnetic field, a magnetic dipole will test a torque. The impact of the torque will lead to align the magnetic dipole (i,e. the magnetic field generated by the orbiting electron) in the direction of the applied magnetic field [22].

Shape Anisotropy

The shape anisotropy is mediated by the dipolar interaction. This interaction is dependent on the sample shape, hence the shape anisotropy becomes a significant matter in thin films. More details about this topic will be discussed in the following section [23].

Out-of-plane 'Perpendicular' Magnetic Anisotropy (PMA) in X/Co/X thin-films

In order to develop a PMA in a multilayered system with interface induced (PMA), there is a need to identify the best setup for growing the X/FM or FM/X , where FM and X are pointing to ferromagnetic , and the capping FM/X or based layer X/FM respectively. Generally, when the magnetic anisotropy constant (K) is > 0 then the magnetic anisotropy is perpendicular (PMA); i.e., out of the plane and when K is < 0, then the magnetic anisotropy is in the plane (IMA), as illustrated in Fig. 2.2.

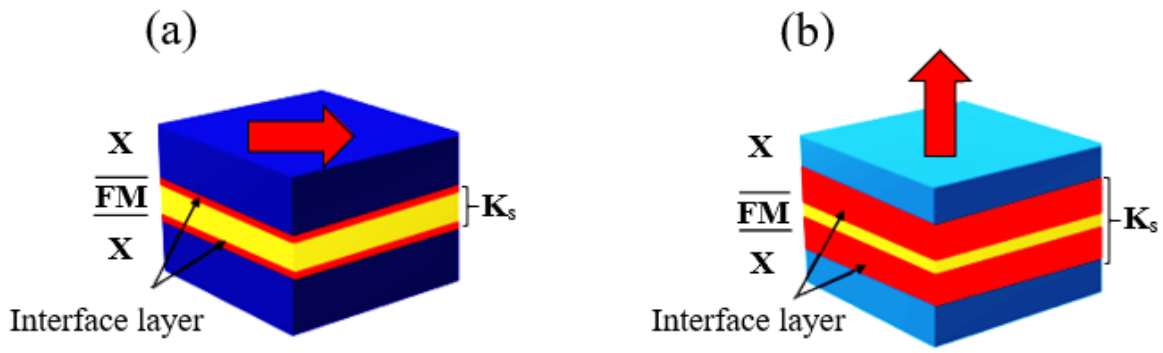

Fig. 2.2 A schematic diagram showing the effect of the ferromagnetic layer thickness on the magnetic anisotropy energy (a) a thick FM layer, (b) a very thin magnetic film.

K defines the magnetic anisotropy (MA) axes of material. However, the MA depends on other parameters, such as the volume, interface layer, temperature, pressure,etc [24]. K is known here as an effective magnetic anisotropy energy (K_{eff}) [23], where equation 2.5 shows that it has a volume term K_v and an interface of surface term. K_s represents the influence that depends on the magnetic layer thickness, t_{films}.

$$K = K_{eff} = K_v + 2\frac{K_s}{t_{film}} \cdot \tag{2.5}$$

In bulk systems, the anisotropy of a system is dominated by the volume term when the thickness of ferromagnetic layer becomes large. While, in thin-film systems, the influence of surfaces or interfaces can be large enough to change the preferential direction of the magnetization from in-plane to out-of plane. Fig. 2.3 illustrate the differences between hard axis and easy axis.

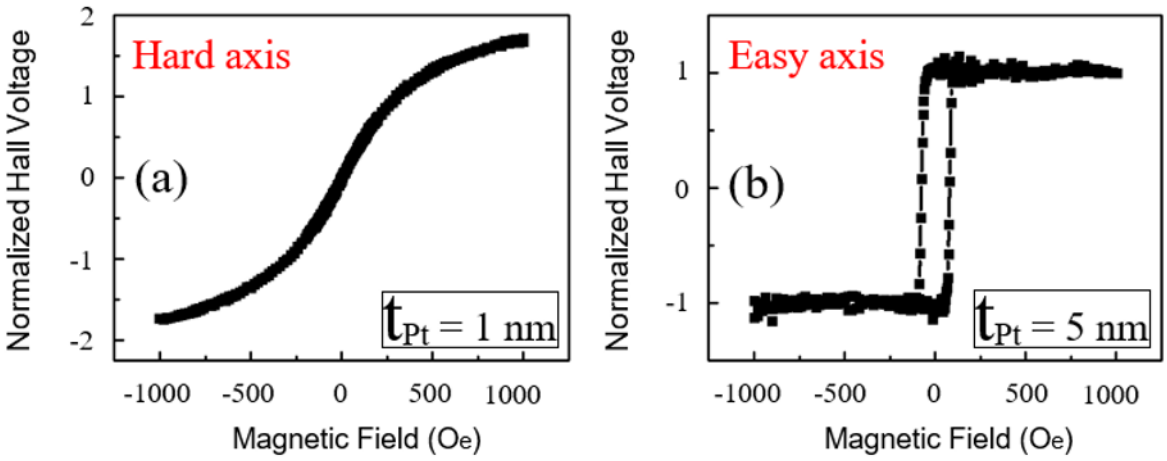

Fig. 2.3 A typical hysteresis loop for (a) t_{Pt}/Co 0.4/t_{Pt} nm [in-plane] and (b) t_{Pt}/Co 0.4/t_{Pt} nm [out-of-plane] using silicon dioxide.

2.3 The influence of roughness, interdiffusion, and strain on anisotropy

The influence of roughness, interdiffusion and strain on magnetic anisotropy are discussed in this section. So far, the individual layers, multi-layered systems have been represented as they have perfect flat layers and sharp interfaces between the layers at the atomic level. In practice, films cannot usually be grown in such an ideal way [19]. In contrast, the "real" surface/interface areas show finite width, i.e. the vertical area of the surface/interface area

has roughness, chemical intermixing or both. At the interface between two layers of different kinds of materials, there is often a region of interdiffusion, i.e. a gradual transition from one material to the other in the vertical direction. Each of these components can have a strong impact on the anisotropy [23]. In the case of roughness, for symmetry reasons, the atoms presented in the following steps reduce the general interface of crystalline origin and decrease the PMA for Co/Pt (111) [25]. The effect of interdiffusion, on the one hand, may reduce the magnetocrystalline interface anisotropy because it leads to some randomisation of the bonds between ferromagnetic and non-ferromagnetic layers [26, 27].

Strain changes the overlap of the atomic wave functions and therefore the spin orbit interaction; which in turn change the magnetocrystalline anisotropy, this effect is known as magneto-elastic anisotropy [28–30]. The effect of the strain, roughness and degree of interdiffusion can be dependent on the layer thickness as well, due to variations between 2D and 3D growth modes with thickness. When reducing the thickness of a layer to a few atomic layers, the magnetic layer can become discontinuous, so that it is divided into islands. Then, lower K_s can occur compared to the effect in a continuous layer due to the discontinuous layer having a lower interface area [31, 32, 23].

2.4 Magnetization curves and hysteresis loops

The hysteresis loop defines a non-linear, irreversible relationship between the magnetisation, M, or the magnetic flux density, B, and the applied magnetic field H_{ext}. Figure 2.4 shows a typical hysteresis loop of a ferromagnetic material that demonstrates the following aspects: Point O (origin) shows the demagnetized state. From this initial state of the material, with an increment in the applied field (H_{ext}) in a positive direction, the magnetisation of the material increases in the direction of H_{ext}, as shown in Fig. 2.4, from O to a [33].

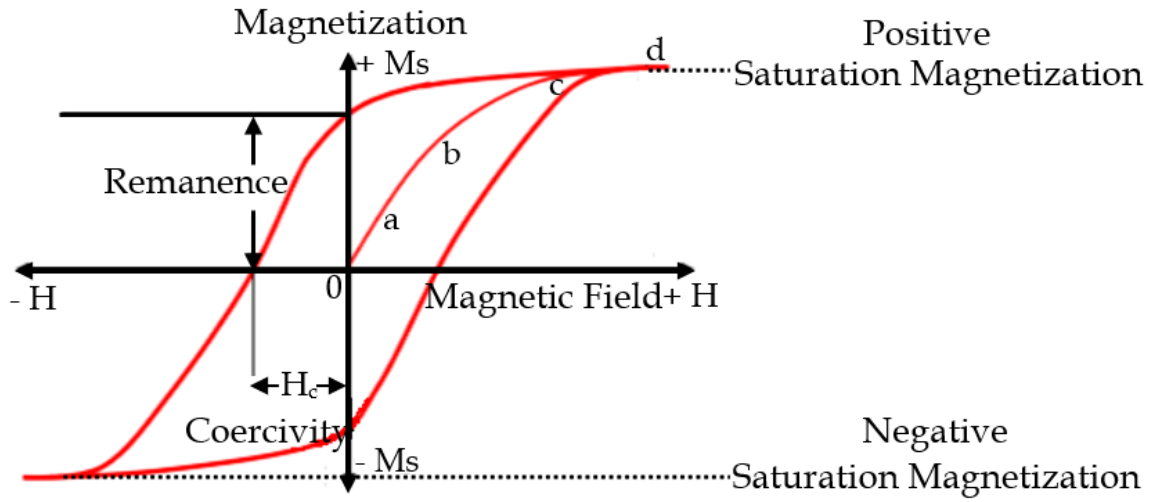

Fig. 2.4 A typical hysteresis loop with key parameters indicated.

The material's magnetisation (M) becomes saturated ($+M_s$) when the external field H_{ext} is sufficiently high, by aligning all the magnetic moments in the H_{ext} direction of the material. Additional increases in the external field gives no further change in the magnetisation. The term "virgin curve" refers to a region between the demagnetized state "O" and saturation. Reducing the field to zero leads to a positive remanent magnetisation state. The term remanence ($+M_r$) indicates that M does not reduce to zero but holds a net magnetisation. Demagnetizing the material with a reverse field means reducing M_r to zero by applying an external field H_{ext} in the negative direction; which is called by a coercive field or coercivity, H_c. The material can be saturated in the opposited direction by an additional increase of the field in the negative direction to obtain the opposite saturated flux direction ($-M_s$). Where the material reaches again to a remanent magnetisation ($-M_r$) when H_{ext} field is again reduced to zero. The term "major hysteresis loop" means that the hysteresis loop is traced out from $+M_s$ to $-M_s$, while the "minor loop" occurs when the field H_{ext} is not enough for saturating the sample [33].

2.5 Magnetic Domain Walls

The domain wall (DW) is a small area between two various magnetic domains. Inside the DW, the magnetization rotates from one domain magnetization direction to another. The width of the domain wall depends on the competition between the energy of the exchange (A) and the anisotropy (K) [34, 35].

$$\Delta \alpha \sqrt{\frac{A}{K}} . \tag{2.6}$$

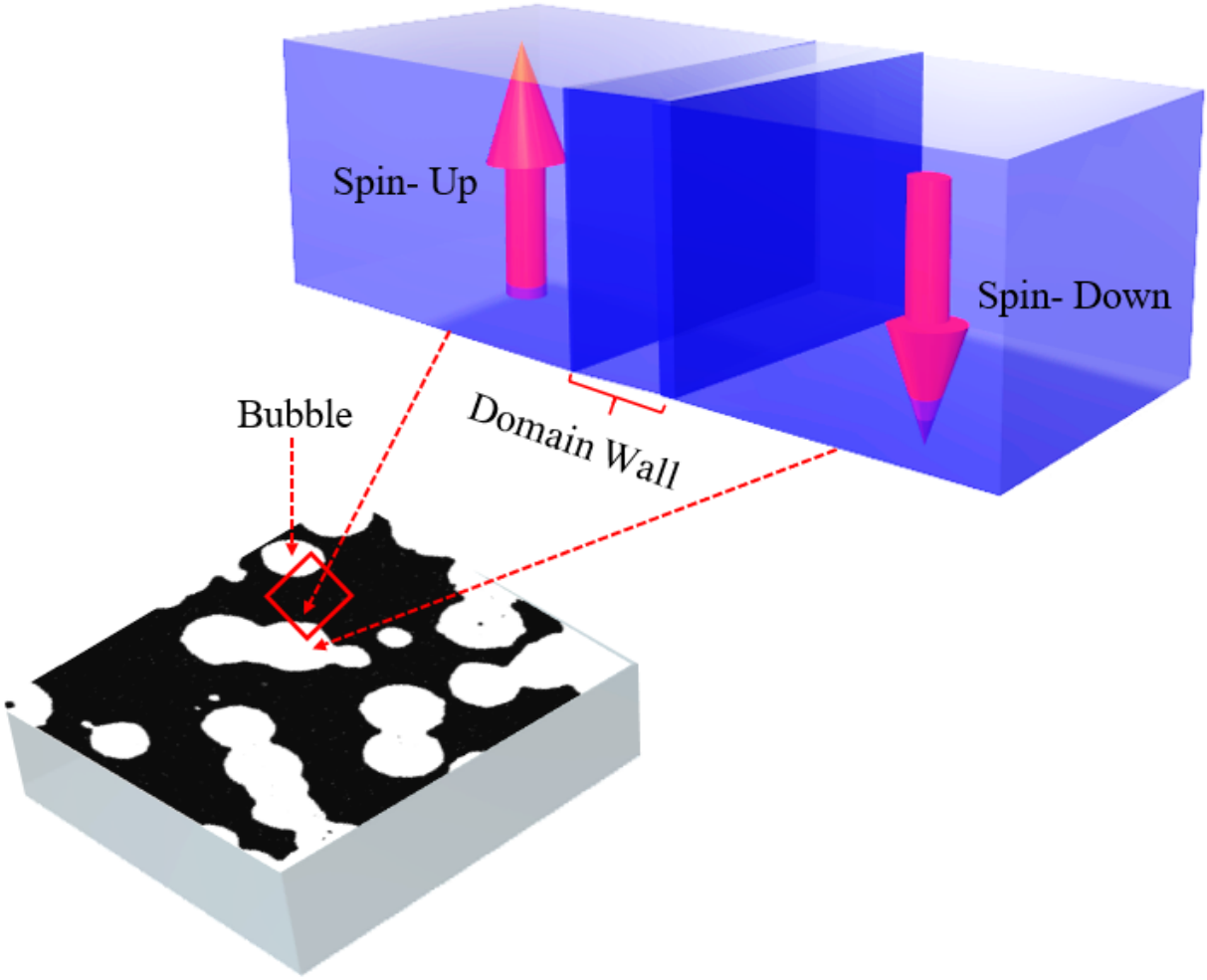

Fig. 2.5 Schematic diagram to illustrate the spin up and spin down that is happen in domain wall, black and white contrast for t_{Pt} (2.0)/t_{Co} (0.5)/t_{Pt} (2.0) nm with a 500 μm cross section at 0.2 Oe.

Fig. 2.5 shows two domains, they are separated by a domain wall which is too small to recognise it on the image. It is proportional to the exchange energy of the conduction electrons. The exchange interaction prefers a large DW width, so that the adjacent magnetic moments are separated by small angles. In contrast, anisotropy leads to a reduction in the number of non-aligned magnetic moments along the easy axis. So, when the anisotropy is large compared to the exchange energy, this leads to a thin domain wall that is opposite to weak anisotropy. Through a domain wall, the magnetic spins transition from one domain direction to another.

Several interactions that play an important role in the behaviour of a magnetic frameworks have been introduced. Each interaction has a relation with it is an energy: magnetostatic, E_{ms}, exchange, E_{ex}, magnetocrystalline and E_{mc} energies respectively. These energies determine the alignment of the magnetic moments , and the various arrangements of magnetization direction alter the energy contributions to the system. The overall energy of the system is described by equation 2.7, and like other physical phenomena, the stable configuration is the case that the overall energy is minimized; which determines the behaviour happening in magnetic materials.

$$E_{tot} = E_{ms} + E_{ex} + E_{mc} \,. \tag{2.7}$$

Competition between energies in a ferromagnetic material is often determined by the exchange and magnetostatic energies. The exchange energy is reduced when magnetic moments are aligned; which saturating the magnetization. However, this will generate the magnetic poles at the edge of the sample producing a large magnetostatic energy contribution. In this situation the overall energy can be minimized by making multiple domains in the system separated by domain walls. Fig. 2.6 shows an example of how the expansion of a bubble has been occurred in case of out-of-plane magnetic anisotropy.

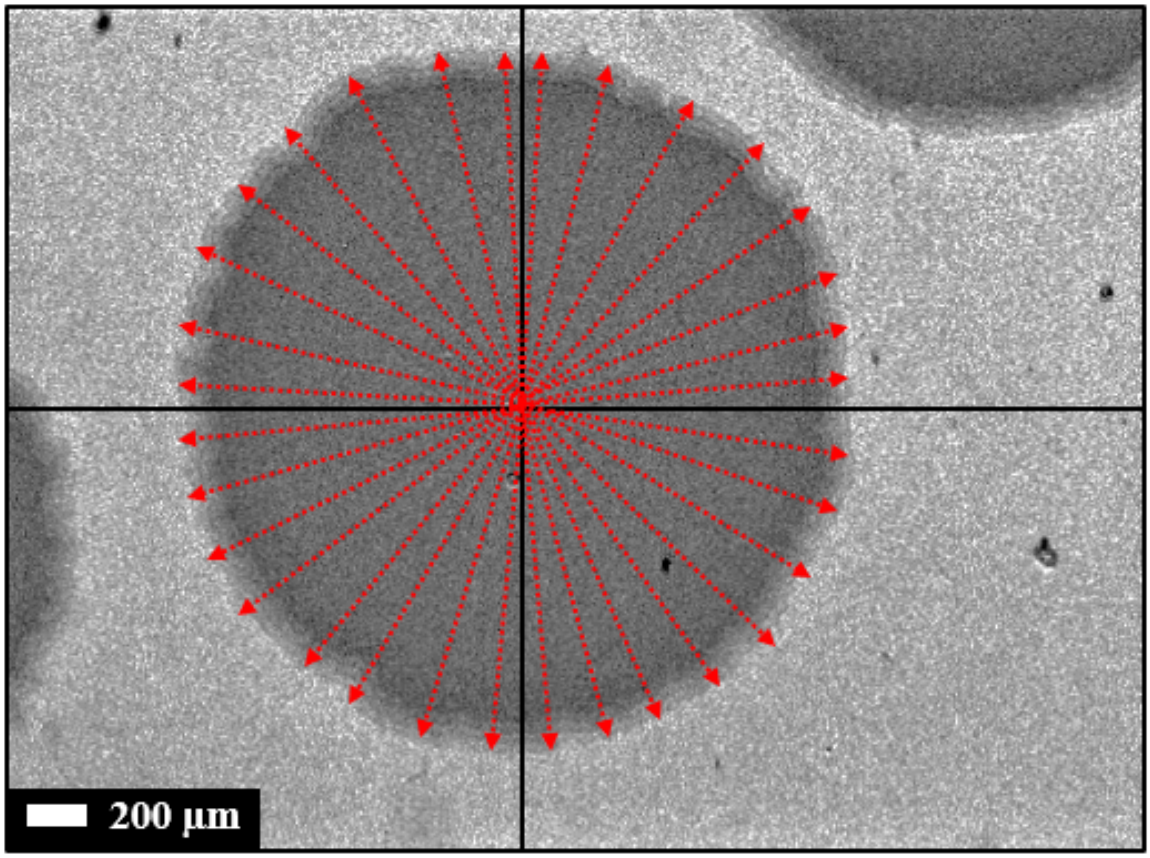

Fig. 2.6 Expansion of bubble for a t_{Pt} 2.0/t_{Co} (0.5)/t_{Pt} 2.0 nm at 80.7 Oe magnetic field.

2.5.1 Bloch and Néel domain walls

In this work, the real focus is on the out-of-plane magnetic systems. Thus, the explanation about the domain wall presented in the next section will focus only on the magnetic systems with out-of-plane magnetic anisotropy.

In this situation, the magnetization of the domains is directed either up or down out of the plane. The magnetization within the domain wall rotates within from up to down. There are two common types of wall: Bloch wall and Néel wall. If the magnetization rotates in the plane that contains magnetization of the two domains, it is known a Néel domain wall. In case of Bloch domain wall, magnetism rotates perpendicularly to this plane [36]. Fig. 2.7 represents a schematic graphs of two types of wall areas Néel and Bloch domain walls.

While Fig. 2.8 shows a schematic figure of two types of a magnetic bubble in case of Néel domain wall and Bloch domain wall as well.

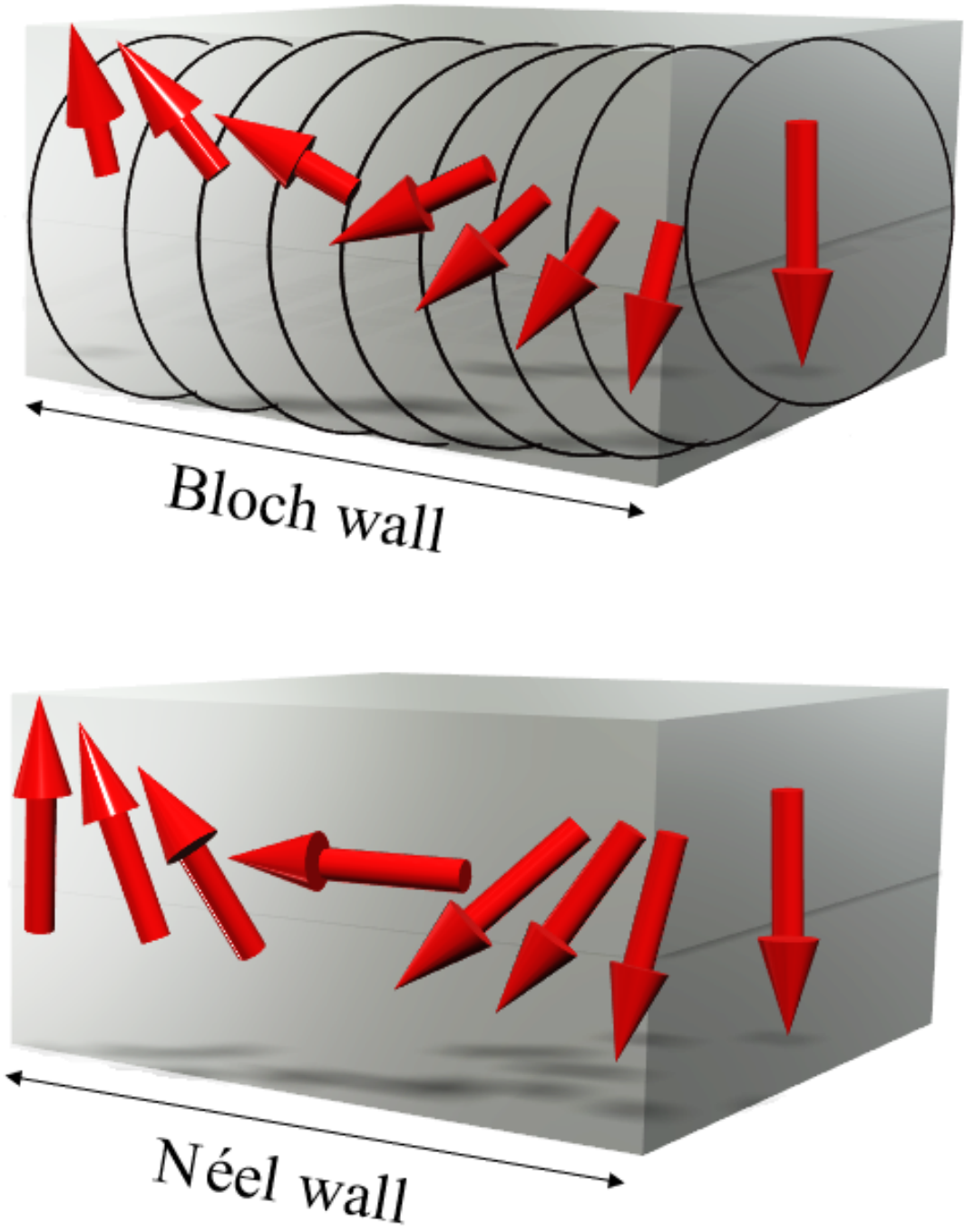

Fig. 2.7 The schematic graphs of two types of wall areas distinguishable Néel and Bloch domain walls with perpendicular magnetic anisotropy. The Néel DW. The magnetization within the domain wall alters its direction along the DW length. While, the Bloch DW. The magnetization rotates out of plane to the DW length.

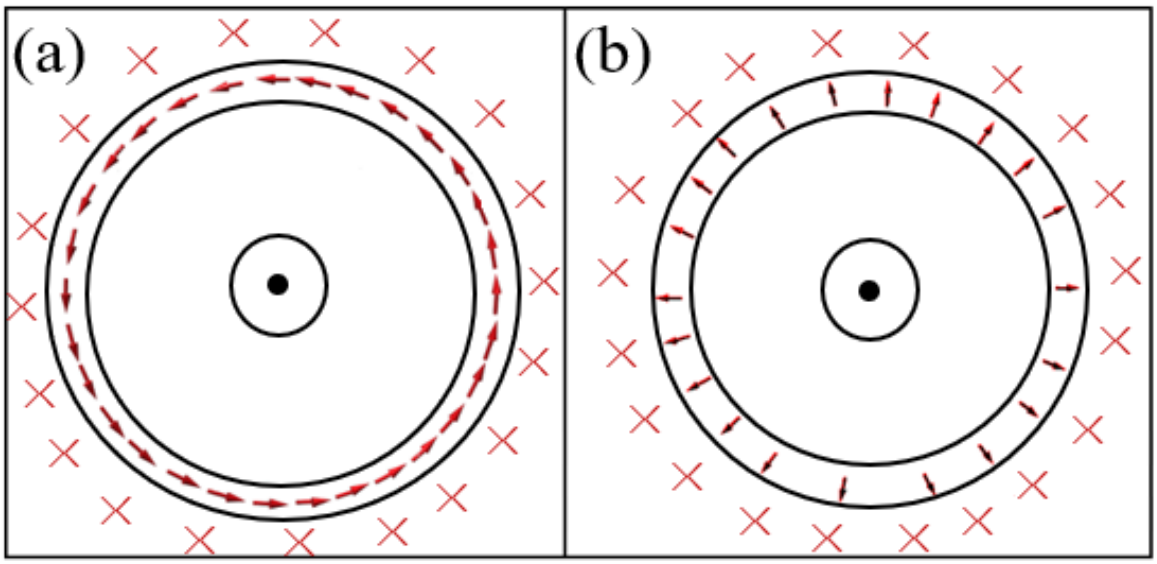

Fig. 2.8 Schematic configuration of a magnetic bubble. (a). [left] in case of bloch wall, the magnetization of the plane, which describes the domain wall between the circular bubble region (magnetization is down) and the outer region (magnetization is up). (b). [right] same as in the left entry but the domain wall is a Néel wall.

2.5.2 Dzyaloshinskii-Moriya interactions

The Dzyaloshinskii-Moriya interaction (DMI) is the antisymmetric exchange interaction at interfaces between ferromagnetic and heavy metal layers with large spin–orbit coupling [37–39]. The combination of DMI and the magnetic field can work together to influence the magnetic structure, for example to make highly stable micromagnetic textures known as skyrmions [40]. DMI creates a chirality between adjacent atomic moments in an interface that has strong spin orbit coupling. The interaction energy of the DMI can be described by the equation [41–45]:

$$H_{DM} = - D_{12} \left(S_i \times S_j \right), \tag{2.8}$$

since D_{12} is the vector of the Dzyaloshinskii-Moriya interaction between, S_i and S_j in the interface layer. Similar spin textures can also result from long-ranged magnetic dipolar interaction in combination with the magnetostatic interaction between two thin film layers

and an applied bias field [41]. The SOI plays a crucial role between NM ions with a close-layer that interacts with the FM atoms [38]. Interfacial DMI happens when a ferromagnet is combined with a non-magnetic heavy metal. This was found in the Pt/Co multilayers [46, 47]. In these systems, the addition of heavy metal, such as Pt, Fig. 2.9 illustrates chirality/canting between adjacent moments, where the preferential direction of the system's magnetisation is out-of-plane.

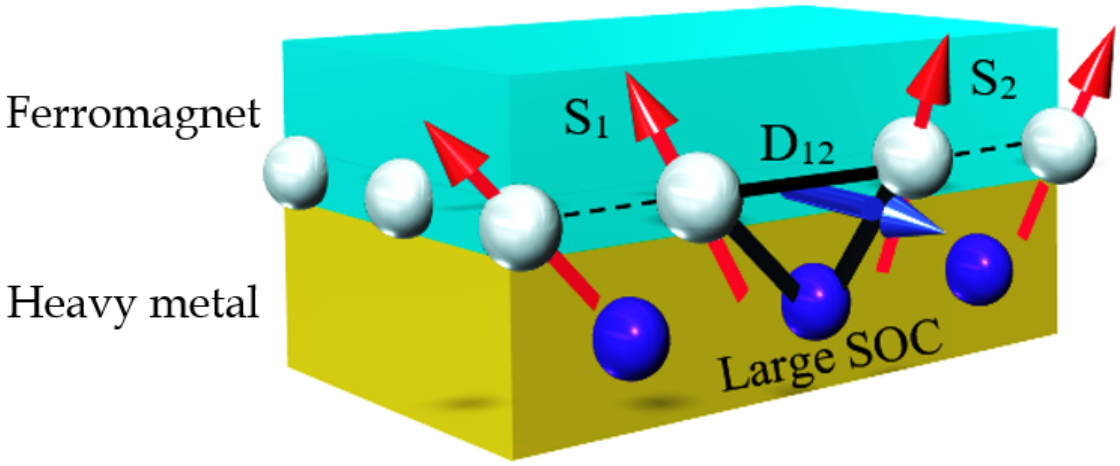

Fig. 2.9 The interfacial Dzyaloshinskii-Moriya interaction.

2.5.3 Chirality of Domain Walls

Relying upon the atoms involved, the strength of DMI can have different magnitudes and signs. This will lead to two possible chiralities of DW$_s$ with sufficiently high DMI contributions [48, 49], as illustrated in Fig. 2.10. The two chiralities of a Bloch wall (Fig. 2.10. (a,b) are degenerated in energy, since both reduce the stray field along an axis of symmetry. Néel walls that are generated by a contribution to a contribution from DMI with a positive (negative) DMI strength, D, and hence in Fig. 2.10 (c,d) a positive (negative) effective DMI field have chiralities that are right-handed (left-handed) [50]. Since the DMI is presented as an effective field, it is worth noting that an applied field of enough strength can set the DW$_s$ chirality configuration.

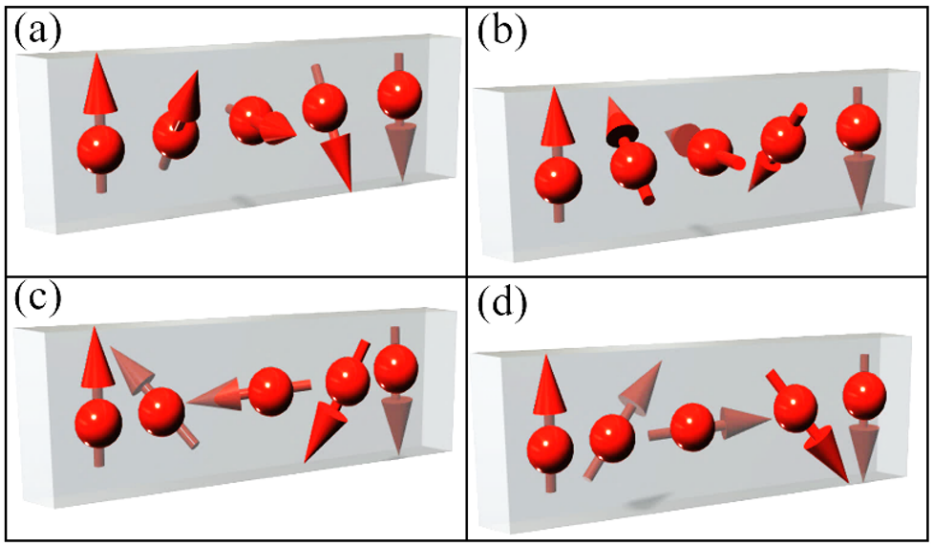

Fig. 2.10 Representation of Bloch (a, b) and Néel (c, d) domain wall congurations. a and c are left-handed (anticlockwise); b and d are right-handed (clockwise).

2.6 Theory of the Hall Effect and the Anomalous Hall Effect

First discovered in 1879 by Edwin Hall [51], the Hall effect consists of the voltage generation in a conductor subject to a current flow and orthogonal magnetic field. This is due to the transverse motion of electrons in a longitudinal current flow due to the magnetic field. This results in a separation of the charges in the transverse direction. Detecting the charge separation can be done by measuring the transverse voltage. The measurement technique used in this work was HE magnetometry that arises due to the Anomalous Hall effect in ferromagnets. The physics of the Ordinary Hall Effect (OHE) and Anomolous Hall Effect (AHE) are presented here.

2.6.1 Ordinary Hall effect

The ordinary Hall effect, OHE, happens in the materials due to the current flowing under the application of a magnetic field [52], see Fig. 2.11.

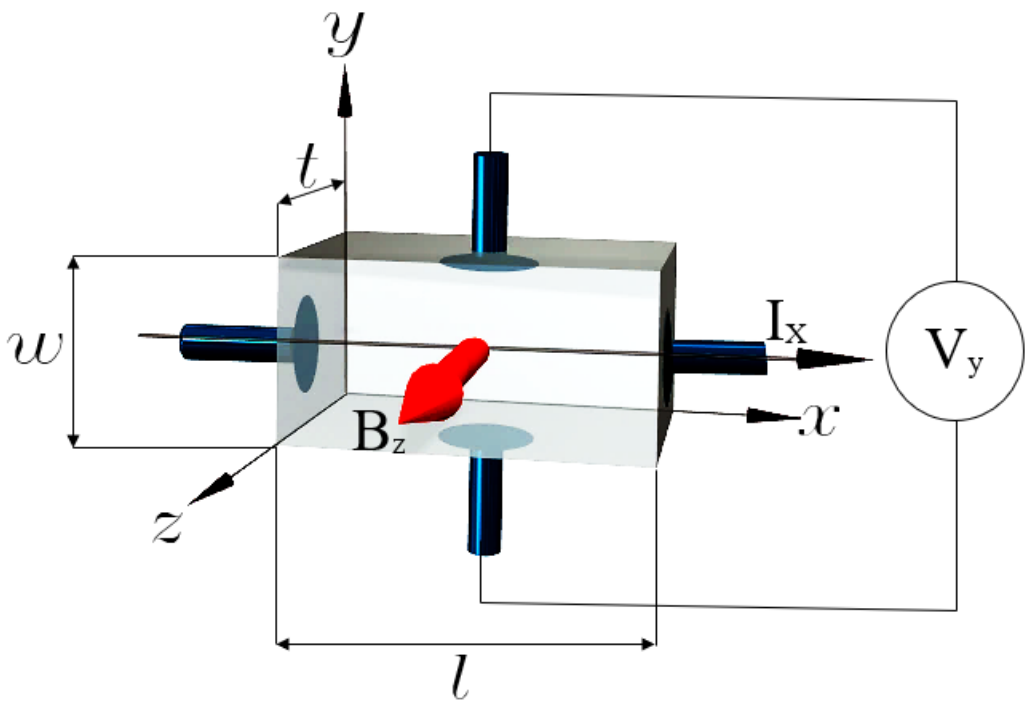

Fig. 2.11 Schematic diagram of a Hall effect measurement. Where l is the length in the x direction, w is the width in the y direction and t is the thickness in the z direction. The current is the current density times the cross sectional area.

It leads to a transverse charge imbalance, and thus a transverse electric field that depends on the direction and amplitude current, and the applied magnetic field. This happens because of the Lorentz force on the charge carriers (electrons or holes) due to their motion in a magnetic field. The Lorentz force F is:

$$\mathbf{F} = q\,(\boldsymbol{E} + \boldsymbol{v} \times \mathbf{B})\,, \tag{2.9}$$

where q is the charge on the carriers, E is the electric field, v_{ex} is the speed of the charge carriers and B is the magnetic field. In a balanced state, as the electric field caused by the charge imbalance leads to an equilibrium of the applied magnetic field, the electrons feel no net force.

$$E_{y=-}\, v_{ex}\, B_z\ , \tag{2.10}$$

taking into consideration $E_y = V_{Hall}/w$ and the current $I_x = qntwv_{ex}$, where w is the width of the material, t is the thickness and n is the density of the charge carrier, the Hall voltage, V_{Hall}, is given by:

$$V_{Hall} = I_x B_z/(nte) = I_x B_z R_{Hall}/t \ , \tag{2.11}$$

where $R_{Hall} = 1/(ne)$ is the Hall coefficient. Thus, the Hall voltage is linearly dependent on the current and the magnetic field, but also it inversely dependent on the density of the charge carriers [53].

$$V_H = R_0 I B_z/t \, . \tag{2.12}$$

2.6.2 Hall resistivity

Since the magnetic field acts perpendicularly to the carrier drift direction, the speed and current density have a different direction for the electric field. The sum of the electric field is the total field applied externally E_{ext} and E_H :

$$\mathbf{E}_{tot} = \mathbf{E}_{ext} + \mathbf{E}_H \, . \tag{2.13}$$

This in turn will lead to generalized resistivity matrix, Where ρ_{xx} and ρ_{yy} equal to the old resistivity ρ, as shown in equation 2.14 and 2.15 respectively. Hence, ρ_{xy} means that the current applied in the x-direction is divided by the voltage measured in the direction y.

$$\mathbf{E} = \rho \, \mathbf{J} + \mathrm{R_o} \, (\mathbf{J} \times \mathbf{B}) \, , \tag{2.14}$$

$$\begin{bmatrix} E_x \\ E_y \\ E_z \end{bmatrix} = \rho \begin{bmatrix} J_x \\ J_y \\ J_z \end{bmatrix} - \mathrm{R_0} \begin{bmatrix} J_y B_z - J_z B_y \\ J_z B_x - J_x B_z \\ J_x B_y - J_y B_x \end{bmatrix} , \tag{2.15}$$

$B_x = B_y = 0$ as field is applied along the z direction as it doesn't show up in standard measurements, giving:

$$\begin{bmatrix} E_x \\ E_y \end{bmatrix} = \begin{bmatrix} \rho & -R_0 B_z \\ -R_0 B_z & \rho \end{bmatrix} \begin{bmatrix} J_x \\ J_y \end{bmatrix} , \tag{2.16}$$

the equation 2.18 is obviously related to 2.12 in the usual relation between resistance and resistivity, and gives a sample-independent quantification of the Hall effect. Since it is appropriate to report the values independently of the current and the thickness of the sample.

$$\mathbf{E} = \boldsymbol{\rho}\,(B)\; \boldsymbol{J} = \begin{bmatrix} \rho_{xx} & \rho_{yx} \\ \rho_{xy} & \rho_{yy} \end{bmatrix} \boldsymbol{J} \;, \tag{2.17}$$

$$\rho_{xy} = -\,\rho_{yx} = \; R_0 B_z \;. \tag{2.18}$$

2.7 Anomalous Hall effect

After the original discovery of the Hall effect [52], it was shown that the Hall effect was 10 times greater in an FM material than for non-magnetic conductors [54]. Fig. 2.12 illustrates the drift current flows in the metal under an applied Hall voltage.

So, the drift current is spin-polarized, when the metal is ferromagnetic such as Co and Ni. Where there are a lot of electrons with spin directed up, this leads to more electrons to be scattered into the left direction than into into the right. The occurrence of this "abnormal" effect was discovered to occur in ferromagnets such as Co and Ni [55]. The magnitude of the transverse voltage was found to be roughly related to the magnetization of M_s. Big [56] and Pugh and Lippert [57] showed that the experimental relationship:

This is applicable to many materials across a wide range of external magnetic fields. The first term is the OHE, where R_0 relies on the type and density of the charge carriers, as described in the previous section. The second term is the AHE, where R_s (the AHE coefficient) is found to be dependent on several specific physical parameters in addition to temperature. The origin of the AHE remains poorly understood. After a lot of theoretical

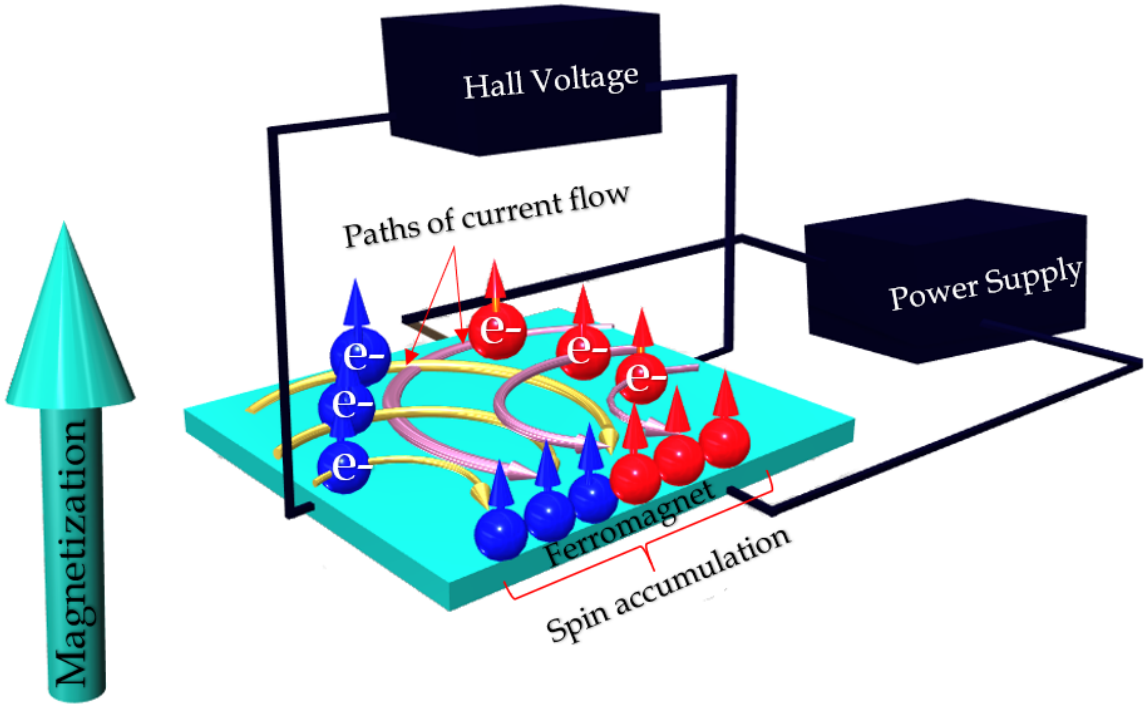

Fig. 2.12 Anomalous Hall Effect Theory. Different colour of electrons refers to the electrons that is coming from both left and right sides in the thin film.

$$\rho_{xy} = \rho_{OHE} + \rho_{AHE} = R_0 B_z + \mu_0 R_s M_z \,. \tag{2.19}$$

and experimental work, the AHE is believed to be occurred due to three basic mechanisms [58]. At their center is the up and down imbalanced spins in the current flow within the FM material.

2.7.1 Anomalous Hall effect mechanisms

Three primary mechanisms are believed to contribute separately to the AHE. One of these mechanisms is called "intrinsic" as the theory predicts that it occurs in an ideal crystal. The other two are referred as “extrinsic” as their causes depend on the presence of defects in the crystal structure [59–61, 58].

Intrinsic deflection

In 1954, Karplus and Luttinger [60], KL, showed that when an electric field is applied to a solid material, electrons gain additional input to their group velocity, which is perpendicular to the electric field.

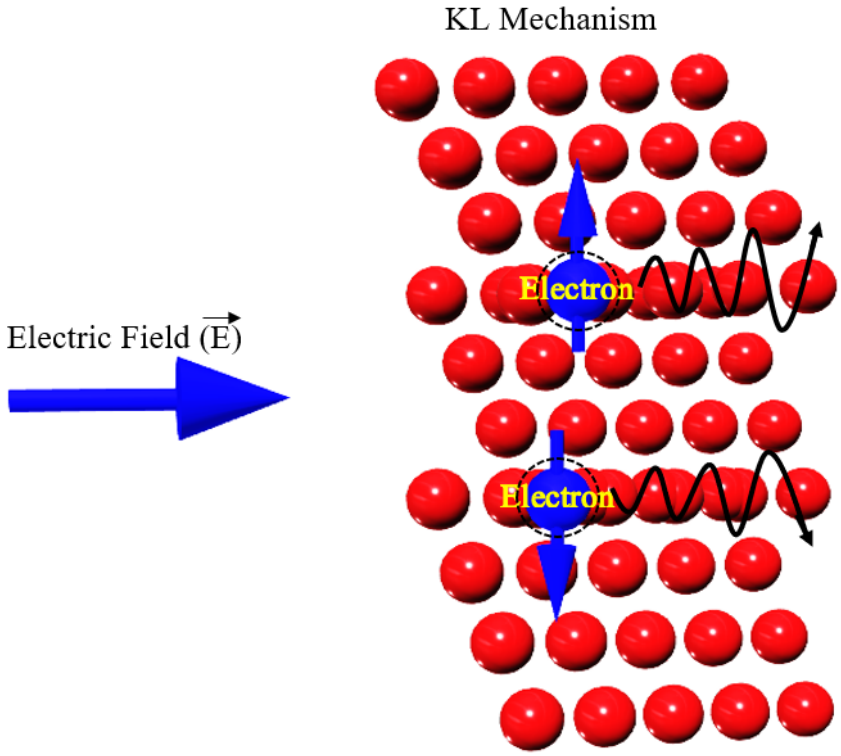

Fig. 2.13 Schematic graph of KL Mechanism of Anomalous Hall Effect.

This anomalous velocity operates in two opposite directions of the different spin electrons, and so as for ferromagnets, where there is a net spin-polarisation of carriers, this leads to a contribution to ρ_{xy}, the Hall conductivity as sketched in Fig. 2.13. This is referred as an intrinsic contribution because it relies only on the band structure; which is largely independent of the scattering. It is expected to be dominant in the AHE for magnetic materials with "moderate conductivity" [the intrinsic anomalous Hall conductivity in itinerant ferromagnets such as Fe and Co]. After the concept introduction of the Berry phase [62], this anomalous velocity is now considered as the Berry curvature, with the cross-section of the electric field

and the arc of the Berry phase causing different electrons to scatter. The intrinsic effect was expected to have a substantial impact in certain metals, e.g., for Pt/Co, large effects were expected [63].

Side jump

The side jump mechanism depends on the same influence that causes intrinsic deviations, but is associated with impurities in the material; when the impurity defect the electron experiences the electric field resulting from that impurity [59, 64]. This leads to a deviation due to the abnormal Karlo-Luttinger speed component shown in Fig. 2.14. Berger explained this as a displacement of the mass center of an electron wave package upon collision, hence the shift direction depends on the spin orientation Fig. 2.14 [59, 64]. The side jump mechanism is expected to be of great importance in moderately conductive magnetism, since the intrinsic deviation is assumed to be a prevalent mechanism in these materials [58].

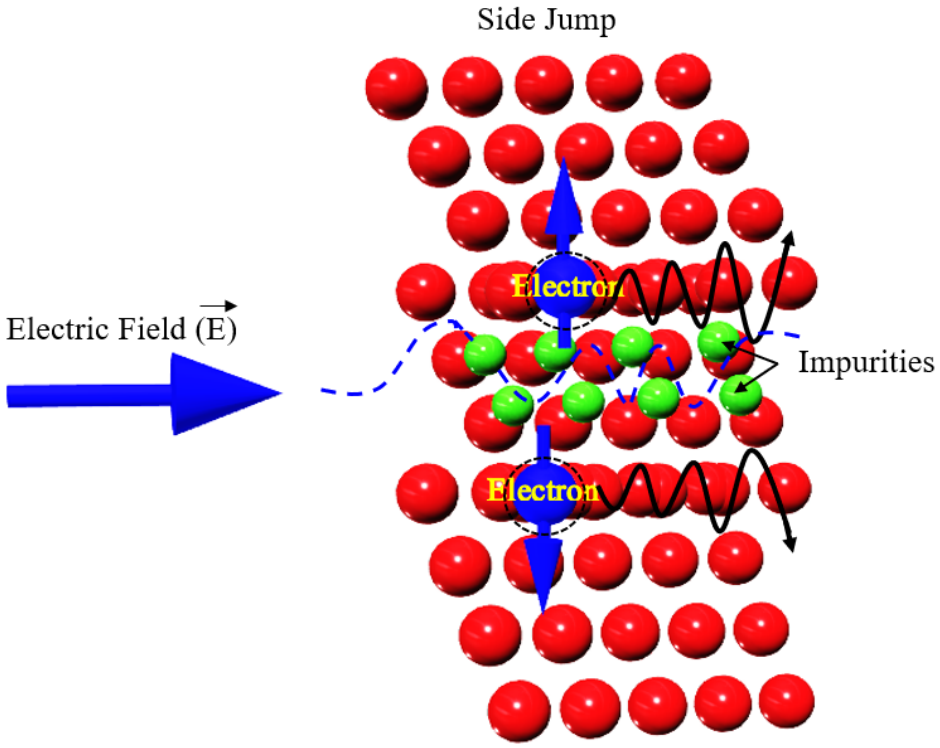

Fig. 2.14 Schematic illustration of side jump scattering process of the Anomalous Hall Effect.

Skew scattering

The third mechanism is the estimated asymmetric scattering because of the influence of the spin-orbit coupling of the electron with defects [65, 61]. This is expected to be prevalent in high-conductivity ferromagnets. The magnetic field B on an electron is inhomogeneous as the scattering potential and the speed of electron are space dependent. This leads to a spin dependent force that is proportional to the gradient of the Zeeman energy acting on the electron [66]. Because of the force direction that relied on the spin orientation of the electron, the spin-up and spin-down electrons are turned in different directions as sketched in Fig. 2.15. Thus, the skew scattering is generated due to a perpendicular conductivity to the incoming particles.

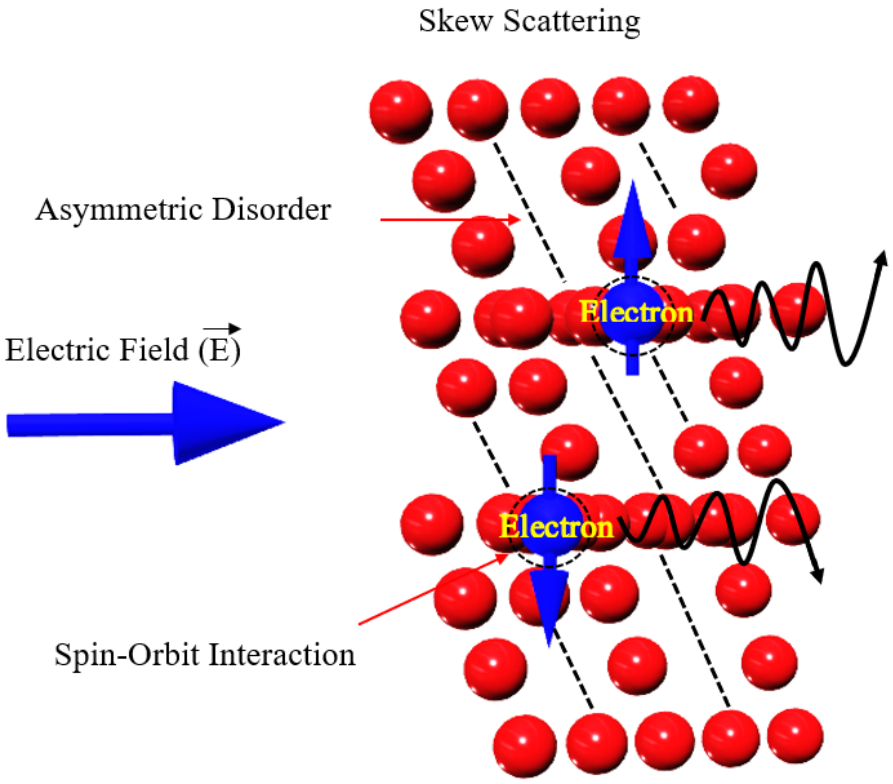

Fig. 2.15 Schematic illustration of the skew scattering mechanism of the Anomalous Hall Effect.

2.8 Summary

The goal of this chapter was to present the basic physics ideas behind ferromagnetism, domain walls DW_s and Anomalous Hall Effect. At first, it has been explained how magnetic domains and DW_s forms. Then, the different magnetic DW structures were discussed. Our experimental studies were mainly focused in magnetic systems with strong spin-orbit interaction, a thorough understanding of the Anomalous Hall Effect mechanism is required to understand the results. Thus, this chapter has focused greatly on the discussions of various aspects behind the AHE mechanism. Finally, the three significant mechanisms that contribute to the Anomalous Hall Effect have been discussed in detail.

Chapter 3

Fabrication of Thin Films: Principles and Methods

3.1 Introduction

An introduction to the processes of sample preparation by sputtering are presented in this chapter. The first section focuses on the physical basis of the sputtering process and particularly magnetron sputtering, while the second section reviews the various growth phenomena and defects resulting from the deposition process of the thin film. Defects can importantly affect the physical properties of the materials.

3.2 Substrate Materials and Preparations

The films studied in this work were grown on two types flexible polymeric substrates and on rigid oxidized silicon wafer substrates for a comparison study. To make good samples, cutting and cleaning of the high quality flat substrates was the first step. The substrate materials were silicon, polyimide and polyethylene naphthalate wafers. The thicknesses of SiO_2 on the silicon, polyimide PI 2611 and polyethylene naphthalate $C_{14}H_{10}O_4$ were 150 μm, 10

μm and 125 μm respectively. The electrical resistance of the substrate is important here and needs to be very high to prevent electrical conductivity through the substrate when the Hall effect measurements are performed.

Returning to the wafer, a diamond tipped scribe was used to produce chips and strips. The dimensions of these chips varied depending on the measurements of the samples that were made [the samples in this project have a length and width of 8×8 mm^2]. In the following section, a full description of the dimensions and the shapes of the samples in relation to the intended measurement is provided. After cutting the wafer into differently shaped chips, the chips were subjected to a cleaning process. The chips were cleaned in acetone. The beaker with acetone and chips was put in an ultrasonic bath for 120 seconds. The chips were removed from the acetone and a similar procedure was repeated but, with isopropan-2-ol (IPA) in the ultrasonic for a similar amount of time. After removing the chips from the isopropan-2-ol, a N_2 gas gun was used to evaporate the remaining IPA. Cleaning and cutting of the substrates were undertaken in the fume cupboard in the laboratory, prior to loading into the vacuum system.

3.3 Thin-Film Deposition

In this study the magnetron sputtering deposition technique was used to grow the thin-films and multilayers. DC magnetron sputtering was used as the technique for producing Pt, Ru and Co thin-films. In the following sections the physical processes involved in magnetron sputtering are explained.

3.3.1 Overview of Magnetron Sputtering

Sputtering is carried out in an initially evacuated deposition chamber. It is different from the evaporation methods as it can deposit all kinds of materials including thin metal or ceramic

films onto a substrate without the need for heating as for thermal evaporation. For sputtering a low-pressure gas is required. In many systems argon gas is introduced and becomes ionised with the formation of a plasma in the chamber that includes the substrate and the target material to be sputtered. The term plasma refers to a gas of electrically charged ions and electrons. The target is kept at a negative potential relative to the positively charged Ar^+ ions [67]. The positive ions accelerate towards the negative charge and hit the target with enough momentum for some of the target atoms to be removed. This Ar^+ impact and removal of target material defines the sputtering process. The liberated material travels within the chamber and settles on all exposed surfaces in the chamber including the substrates. Inside the magnetron the magnets reside behind the target material and the magnetic field pattern enhances the ion interactions with the target, which are restricted to the surroundings of the generating target plasma. There are two main methods for powering sputtering: direct current (DC) and radio frequency (RF). Magnetron sputtering deposition can be performed under both of them.

A schematic diagram is presented in Fig. 3.1 (a) with key features indicated. The main chamber is linked to two turbomolecular pumps and one rotary pump forming a pumping system capable of obtaining a UHV pressure within a reasonable period of time. The Mantis Qprep500 system has five different sputter sources, each with gas injection, cooling water lines and contacts for DC or RF sputtering power, Fig. 3.2 shows the Mantis sputtering system used in this research project. The main chamber is supported with a gas analyzer for monitoring chamber's gaseous environment and detecting pollutants. The location of the substrate is on an upper surface facing down and the substrate is rotated to improve the uniformity of the film. A delicate quartz crystal balance (QCM) is installed locally to measure the rate of film deposition growth. The samples are transferred from a load-lock chamber to the main deposition chamber via a transfer arm that allows the substrates to be moved on the rotating substrate stage. The system is connected to a control computer to

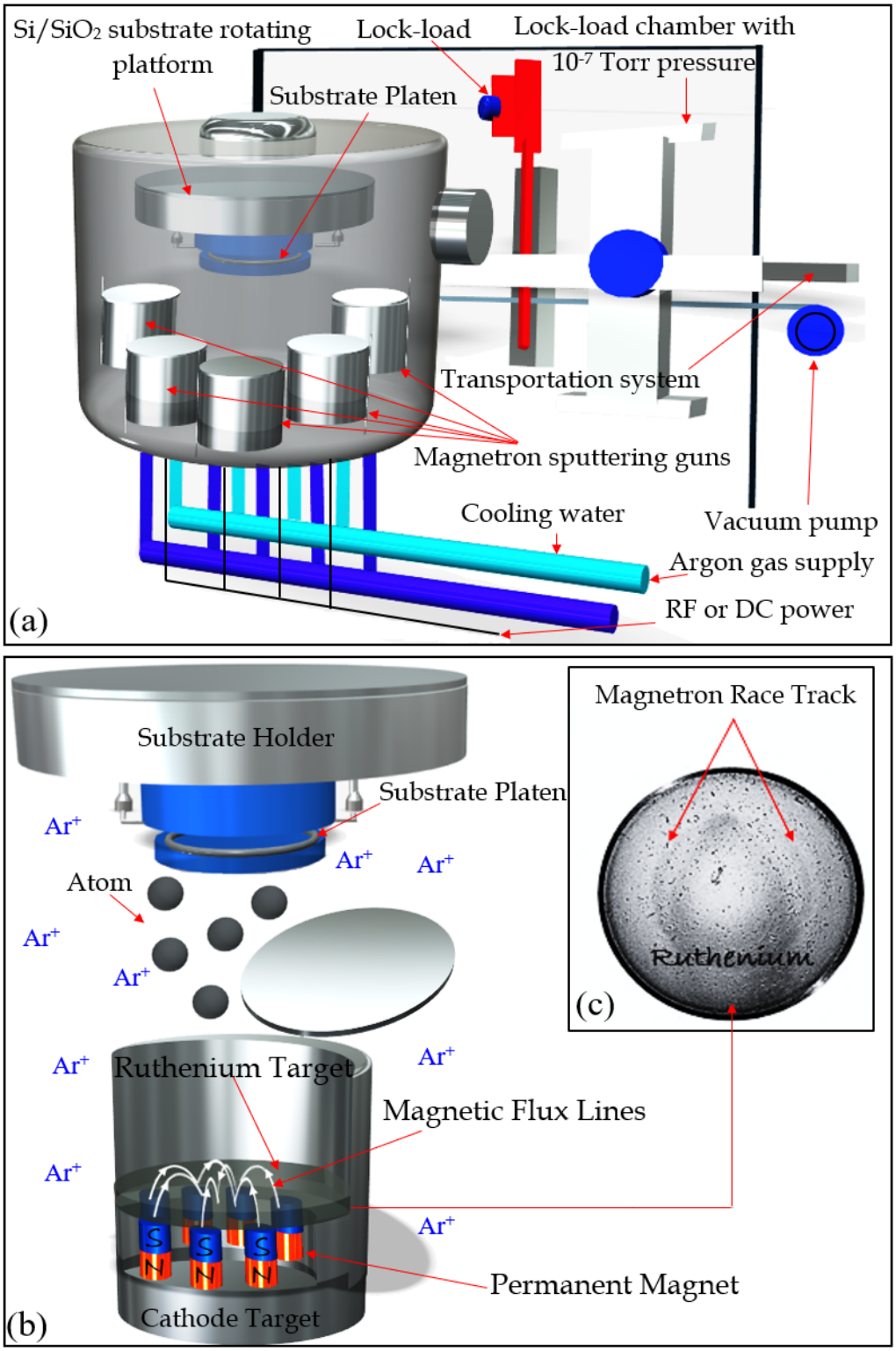

Fig. 3.1 (a, b) schematic images of the sputtering system and sputtering process respectively; (c). image of ruthenium target, in which magnetron erosion leads to a circular race.

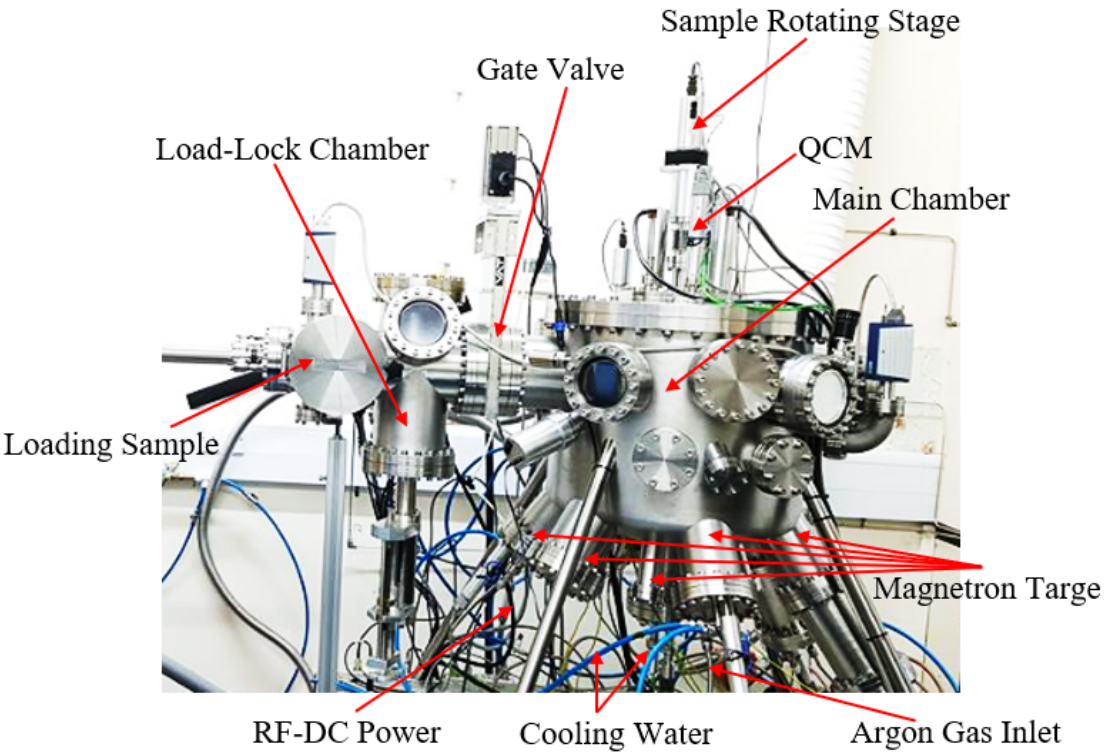

Fig. 3.2 Shows a side view of the Mantis Qprep500 sputtering system in the lab with the main parts indicated.

control the deposition time. To obtain an accurate deposition time requires a known growth rate and accurate control of when the shutters are opened and closed. At all times, the conditions for the deposition of thin-films are controlled and monitored. Record keeping is essential to track the history of thin film manufacturing - and to connect any results with deposition conditions. These conditions are either related to the basic chamber environment, like pressure, temperature or flow rate of argon gas, where the general deposition process can be changed, or connected to the voltage, current and the DC/RF power of each target, which affect the sputtering rate of individual targets. All the ferromagnetic targets need strong magnets in the magnetron sputtering gun to overcome the magnetic flux flow through the sputtering target. While for targets of non-magnetic materials the lower magnetic fields will do in the magnetron gun.

3.3.2 DC Magnetron Sputtering

A continuous negative bias voltage is applied to the deposition target in DC magnetron sputtering, which acts as one electrode while a surrounding earth shield acts as the other electrode. The voltage ionises the precursor gas to create the required plasma and ions for the sputtering process. The target material used for film deposition using DC sputtering must be an electrically conductive material to sustain a plasma at a specific temperature. The Co and Pt targets are usually sputtered in DC magnetron sputtering [68, 69]. The Ar sputtering gas was introduced from a base pressure of 3×10^{-8} Torr and the typical Ar gas pressure was 1×10^{-3} Torr [68].

3.3.3 RF Magnetron Sputtering

In order to sputter non-conducting target materials, a capacitively coupled RF power supply is used within the RF magnetron sputtering. A periodic negative bias is produced on the target electrode; when the RF power frequency is higher than the ion plasma frequency (ion mobility). Typically, the substrate is maintained at room temperature for the synthesis of equiatomic CoPt films by RF sputtering under the Ar pressure of 3 to 10 mTorr [70, 71, 70, 72].

3.4 Film Growth

The growth mode of a layer is determined by the surface energies of the underlying layer, the deposited layer and the interface [73]. However, dynamical processes also affect the growth mode such as the diffusion length of the atoms on the surface. In addition, deposition by sputtering involves high-energy particles impinging on the surface, which can also modify the behaviour. The section below deals with a description of the various growth modes that can arise in thin films and especially multilayer structures.

3.4.1 Thin-Film Growth Modes

The deposition of atoms onto a surface is the first step to forming a material layer on a substrate. Repetition of this step through time will increase the thickness of the layer in general and this will lead to the formation of a thin- film. Forming layers of a thin-film takes place through three growth modes. These three modes are strongly dependent on the interactions between the atoms deposited with other atoms in relation to the bonding force of those atoms and with the substrate atoms [74]. The first mode is Volmer-Weber growth, which is also known as island growth pattern, where the strength of an atom is much stronger than the bonding force of the adatoms to the substrate. This situation begins with a clustering of atoms with each other, forming islands in separate areas on the substrate, eventually these islands grow and join to form a thin layer. See Fig. 3.3. When the atomic bond strength of the adatoms to the substrate is stronger than that of the adatoms to each other, the second situation of deposition occurs. This is the Frank-van der Merwe growth, where layer-by-layer growth occurs, where the deposited atoms are arranged to form a fully covered monolithic layer on top of the substrate. The lattice interface between the substrate and the growing layer has a key role, thus increasing layer-by-layer control.

In the third situation, as shown in Fig. 3.3, layer-by-layer growth competes with island growth, this is called the Stranski-Krastanov growth mode. This starts by with layer-by-layer growth to cover the entire substrate, then the growth of the island occurs to form the rest [74]. In the first and second growth modes the atoms either form their own structural arrangement or follow the structural arrangement of substrate. Whereby, it leads to stress-free film. In the third mode the growth switches to significantly decreases stress, because the energy of the interface increases with the thickness of layer, by changing the growth situation. This indicates that the following deposition layers are strained [75]. With these growth patterns, different surface structures are assumed to be stimulated. Changes in the crystal structure can happen either in one layer or between two layers as a function of the increase of the thickness

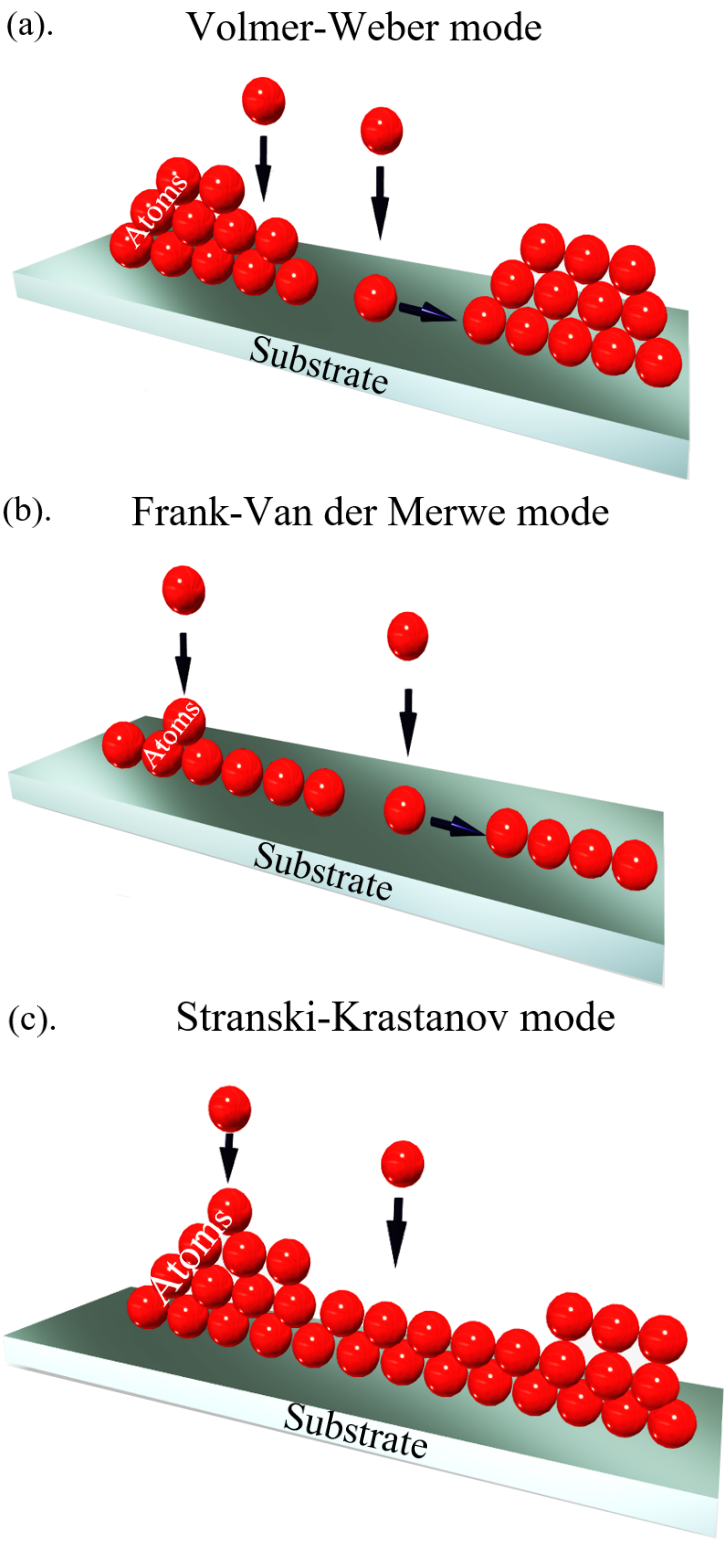

Fig. 3.3 Schematic illustration of the three film growth modes. The spheres is an atoms. Depending on the free energy contributions one finds (a) Volmer-Weber (VW), (b) Frank-van-der-Merwe (FvdM) and (c) Stranski-Krastanov (SK) growth.

of the film [75]. Structural changes indicate the presence of defects in thin films. These defects can happen when two substances with different lattice parameters are adjacent to each other, when the thickness of the substance itself increases to the extent that it weakens the bonding strength of the deposited material. So, the strength of the atom-atom bonding is predominant in the formation of the crystal of material and the arrangement of it.

3.4.2 Crystalline Defects

A real crystalline material can possesses a type of crystallographic structuring known as a mosaic structure [76], which is illustrated in Fig. 3.4. This structuring consists of ideal crystalline grains with axes that are slightly rotated in relation to each other. The ideal crystal regions are then separated by dislocations. To determine the perfect degree of thin film the concepts of in-plane correlation length and out-of-plane swap are introduced. The correlation length in one axis is the average size of the ideal crystalline blocks along this direction. The meaning of mosaicity is the angular spread of the crystalline regions from each other. Defects that make up these features can be created by relaxing the film relative to the substrate, as described above.

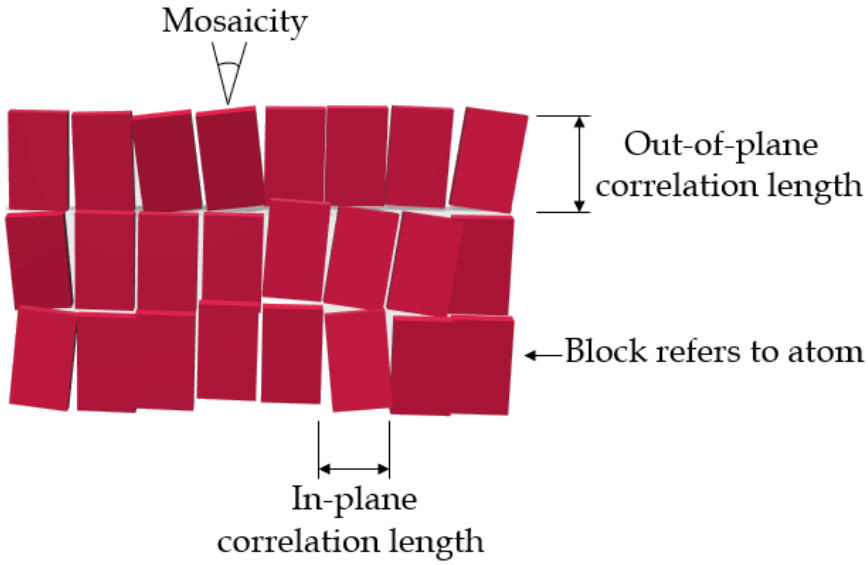

Fig. 3.4 Illustration of crystalline mosaicity and the relevant length scales in the sample.

3.4.3 Layer Imperfections

The growth of films will have some roughness associated because the adatoms will have a limited propagation length. Therefore, all interfaces will display some type of roughness. Moreover, the surface roughness of the underlying layers can be propagated throughout the further film layers. If successive interfaces have the same shapes of interface profiles, they are said to be fully conformal. The other extreme situation of roughness is fully uncorrelated roughness where there is no repetition between the interfaces.

As can be observed in Fig. 3.5, with correlated roughness there will be no thickness fluctuations. On the other hand, films with uncoordinated roughness will have variations in thickness. Another issue that arises between different layers is the interdiffusion of the material. In contrast to topological roughness, which gives a chemically sharp interface, interdiffusion will lead to a diffuse interface [74].

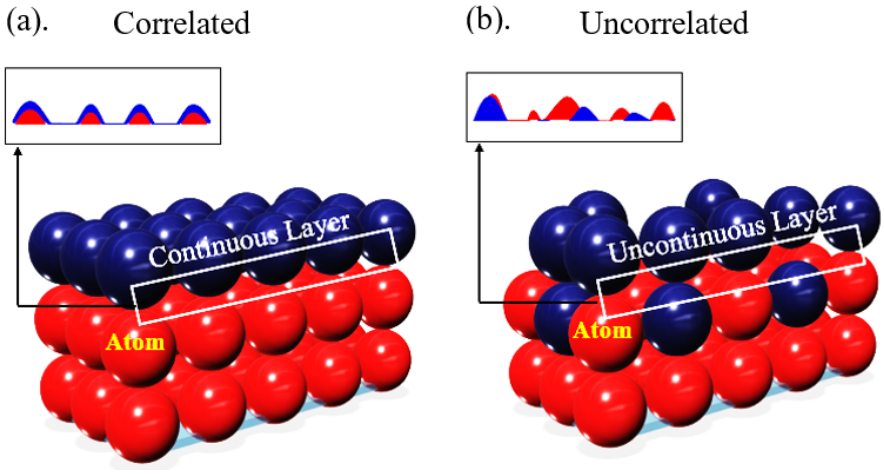

Fig. 3.5 Schematic of structures with correlated and uncorrelated roughness.

3.5 Tables of Film Growth

Examples of the deposition conditions are shown in Table 3.1, which shows the parameters for growth of trilayered samples of pure FM layers combined with NM layers of Pt or Ru. All

film thicknesses were verified by the QCM through deposition and the QCM was calibrated by the measurement of film thickness using x-ray reflectivity (XRR). QCM calibration involves measuring an XRR on a sample that is fabricated with a thickness that is assumed using the QCM growth rate and knowing the deposition time. The assumed thicknesses were compared with the thickness extracted from the XRR and knowing the difference a correction factor was introduced into the QCM as a tooling parameter within the deposition rate monitoring programme.

Table 3.1 Deposition conditions, showing the system parameters of the multi-layer thin films fabrication. Where, [1] refers to buffer layer, while [2] refers to capping layer.

Material,thickness (nm)	Gas rate (sccm)	I (mA)	V (Volt)	Power (W)	Dep. rate ($Å s^{-1}$)	Time (s)
Pt, 3[1]	18.00		153	60	0.28	107
Co, 0.5	18.00	74	340	25	0.28	28
Pt, 3[2]	18.00		155	60	0.28	107
Material,thickness (nm)	Gas rate (sccm)	I (mA)	V (Volt)	Power (W)	Dep. rate ($Å s^{-1}$)	Time (s)
Ru, 15[1]	18.00		129	60	0.17	882
Co, 1.15	18.00	74	341	25	0.18	64
Ru, 3[2]	18.00		127	60	0.17	177
Material,thickness (nm)	Gas rate (sccm)	I (mA)	V (mV)	Power (W)	Dep. rate ($Å s^{-1}$)	Time (s)
Pt, 3[1]	18.00		173	75	0.29	103
Co, 0.5	18.00	74	342	25	0.18	22
Pt, 5	18.00		173	75	0.29	172
Co, 0.5	18.00	74	342	25	0.18	22
Pt, 3[2]	18.00		173	75	0.29	103

3.6 Summary

In summary, introducing all of the physics pertinent to the preparation of the multilayer magnetic thin films investigated in this chapter. Hence, it contains the fundamental theories about structure of sample and crystallography. Also, explaining the mechanisms for formation

of this structure through sputtering system. Where, the focusing on the sputtering system was discussed.

Chapter 4

Magnetic and Hall-Effect Measurements

4.1 Previous Work

This section gives a detailed investigation of previous studies using both of magneto optical kerr effect and Anomalous Hall effect devices. Pt/Co multilayer systems exhibited a great magneto optical Kerr rotation [77, 78], large anomalous Hall effect [79, 80] and perpendicular anisotropy [81] which makes these materials viable for a new generation of storage devices [82]. A lot of experimental studies of the magneto optical Kerr rotation properties of Co/Pt multilayers [77, 78, 81, 83–85] prepared by various techniques. Pt/Co layers have been amongst the most studied [77, 81, 86, 87]. Where these multilayers can show magnetisation out of the plane of the film. In case of the bilayer, the PMA is due to the orbitals hybridising of Pt 5d electron with the 3d orbitals of cobalt at the interface [88, 81, 89, 90], which leads the magnetisation to be out of the plane of the sample with thin thickness of cobalt [91]. Also, in previous studies of AHE in Co/Pt multilayers [92–95] which is an ideal system of strong 3d–5d interface spin-orbit coupling, the AH coefficients were not determined accurately because it was overlooked both of the shunting effect and the equivalent circuit. More information about the contents of this chapter has been illustrated in the introduction section.

4.2 Introduction

The functional magnetic and magneto transport measurements used to understand the magnetic behaviour of the Co-based thin-film samples studied in this work are presented here. Two kinds of measurement were made to study the magnetisation status of the samples. Magneto-optical Kerr effect (MOKE) magnetometry and Kerr effect microscopy measurements represent the first kind. While the second experimental method was the Hall Effect (HE). For all these methods the background related to the basic principles is presented followed by details of the system setup and finally the representation of the data. These measurements give the basic physics needed to understand the results from the different samples that form the basis of this thesis.

4.3 Magneto-Optic Kerr Effect Optical Geometrics and Magnetic Sensitivities

The polar and longitudinal are two of three geometries within MOKE experiments, which are defined by the magnetization axis and magnetic field axis regarding the incidence plane and sample's surface.

The MOKE induces a rotation and an ellipticity (phase shift) in polar, longitudinal and transverse MOKE situations [96]. Fig. 4.1 shows the polarization situation of the light. To illustrate a general elliptic polarization. It is very important to know the meaning of ellipicity ε_a, which is defined as the percentage between the minor, b, and major, a, axes of the polarization ellipse, by tan = b/a. A difference in phase between the electric field elements perpendicular and parallel to the plane of the incident light is defined by the Kerr ellipticity. While, the azimuth θ_a is the rotation angle between the basic axis of the polarization ellipse and the S direction.

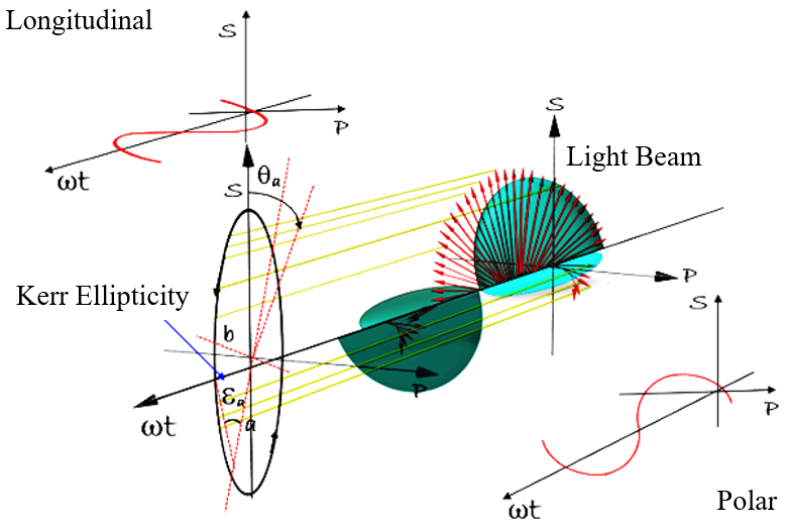

Fig. 4.1 Time evolution of the electric field vector E (ω) at a given spatial position, decomposed along the s (right) and p (left) directions. When looking along the incoming light beam, the extremity of E (ω) describes a polarization ellipse (center). The presented polarization ellipse has a positive azimuth θ_a and a negative ellipticity ε_a.

For more illustrating Fig. 4.2 was drawn, where a vector represents the idea of a Lorentz force that mentions how p and s-polarised light interact in the three magneto optic geometries. The electric field of the plane polarised light which is incident onto the sample. This leads to exciting the electrons so that they vibrate parallel to the incident polarisation. This gives increase to the normal component (EN: E_S, E_P) of light in the reflected light. The extra Kerr component, E_K, originates because of the Lorentz force. The Lorentz force motivates a small component which is perpendicular to both the elementary movement (normal component) and the magnetisation direction [97].

In general, the two components are not in-phase and it is the overlap of those two components which gives increase to a magnetisation that depends on rotation of the polarisation. In case of longitudinal and polar Kerr effects Fig. 4.2 a,b, p or s-polarised light will usually become elliptically polarised with its main axis rotated (Kerr rotation). This is a result of perpendicular electric field component being motivated because of the Lorentz force. The Lorentz force directions, and the motivated components, are shown by the dashed arrows (E_K). The Kerr effect reduces as the incident angle approaches the normal to the plane of

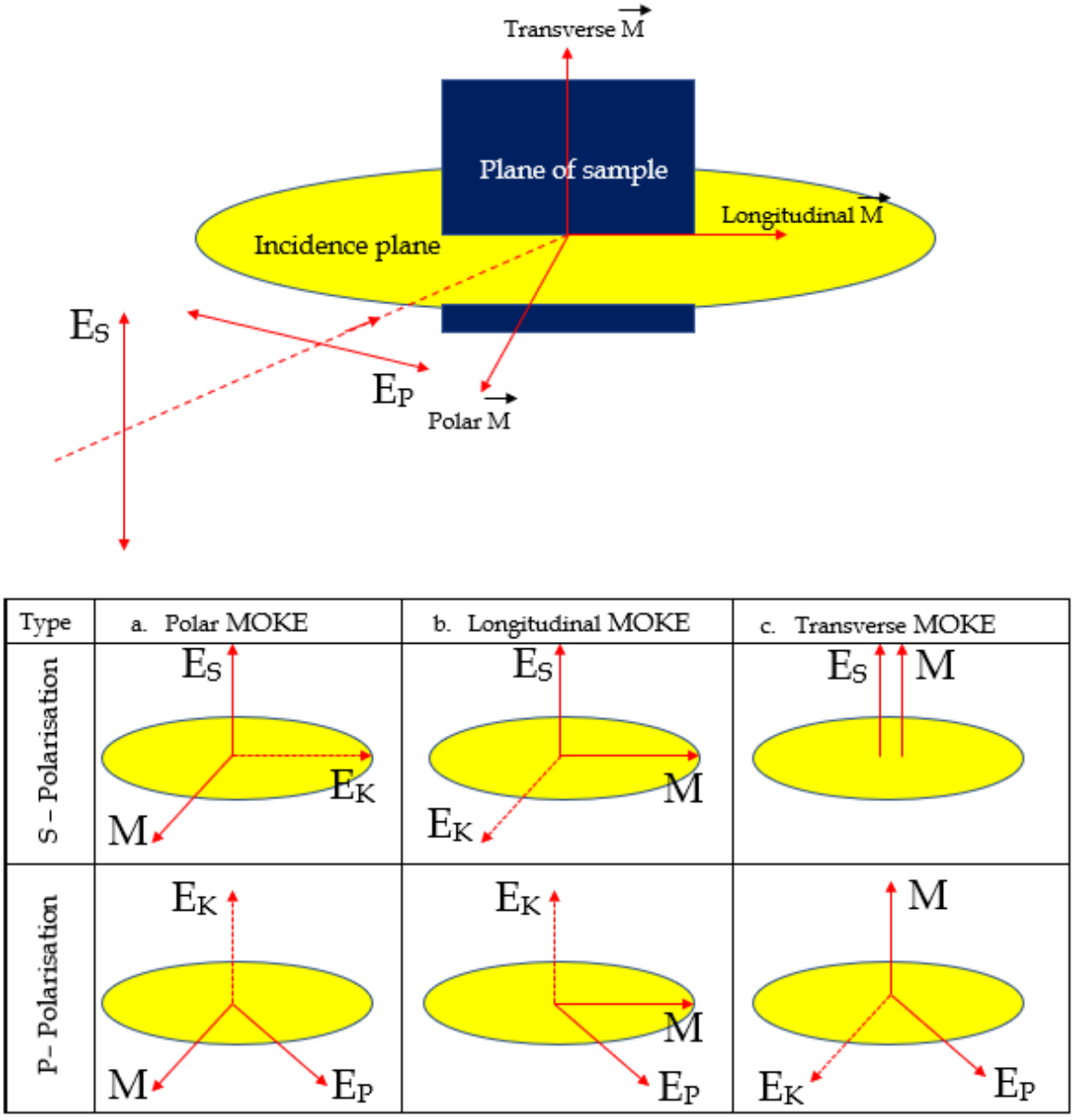

Fig. 4.2 A schematic diagram of the Magneto Optic interaction utilizing the concept of a Lorentz force. The normal component (EN: E_S or E_P) of light is specified by the solid lines, the Kerr component (E_K) and the Lorentz force direction is specified by the discontinuous lines.

sample in the longitudinal effect because neither the Lorentz force disappears (p-polarised) or points along the direction of the s-polarised light. This light is not for the polar Kerr effect because of the magnetisation is out of the sample plane and always a Lorentz force exists at normal incidence [97].

The polar effect is independent of the incident polarisation at normal incidence. In Fig 4.2 (c), the transverse effect include a variation in the light intensity (reflectivity of Kerr). Variation of intensity is dependent onto the element of magnetisation which is perpendicular to the incidence plane. No Kerr ellipticity is found because of M X E motivates the element which is in the incidence plane. Both of the normal element and the induced Kerr element allow rise to an alter in the amplitude. Is is possible to see a Kerr rotation in case when a Lorentz force is present. Generally, either light of s or p-polarised light is utilized. The reason is because any alter in the light polarisation will be a consequence of the magnetisation, because in an ideal case there will be no alter in the light polarisation for either s or p-polarised light [97].

4.3.1 Polar MOKE

In this case, the magnetic vector is perpendicular to the reflecting surface. It is parallel to the plane of incidence in the polar MOKE as shown in Fig. 4.3.

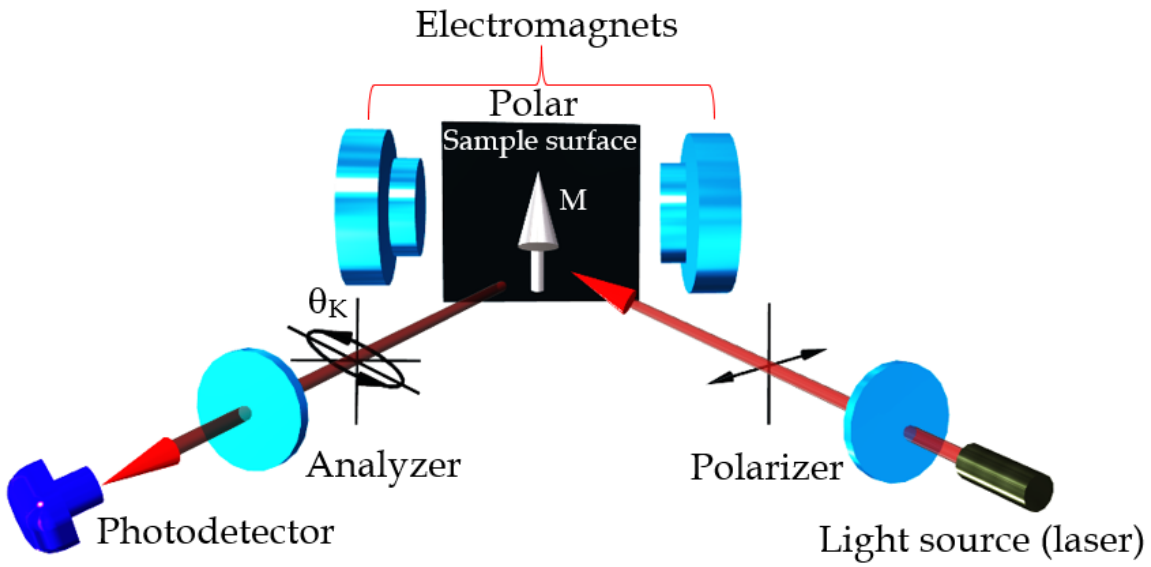

Fig. 4.3 Polar MOKE geometry with magnetic and polarisation indicated (where M is magnetization vector).

Near-normal angles of incidence and reflection from the reflecting surface are most frequently studied in the polar MOKE, because the polar MOKE sensitivity is a maximum at normal incidence and, practically, both beams must pass through a hole in a one-pole magnet. Atkinson [98] demonstrates a schematic of polar MOKE as shown in Fig. 4.3.

4.3.2 Longitudinal MOKE

The magnetic field lies within the plane of incidence and is parallel to the sample surface for longitudinal MOKE. The experimental setup is not identical as polar is reflected at 90^o to the surface and hence requires a beam splitter in the optics path, longitudinal reflection is at 45^o and along the optical path as shown in Fig. 4.4.

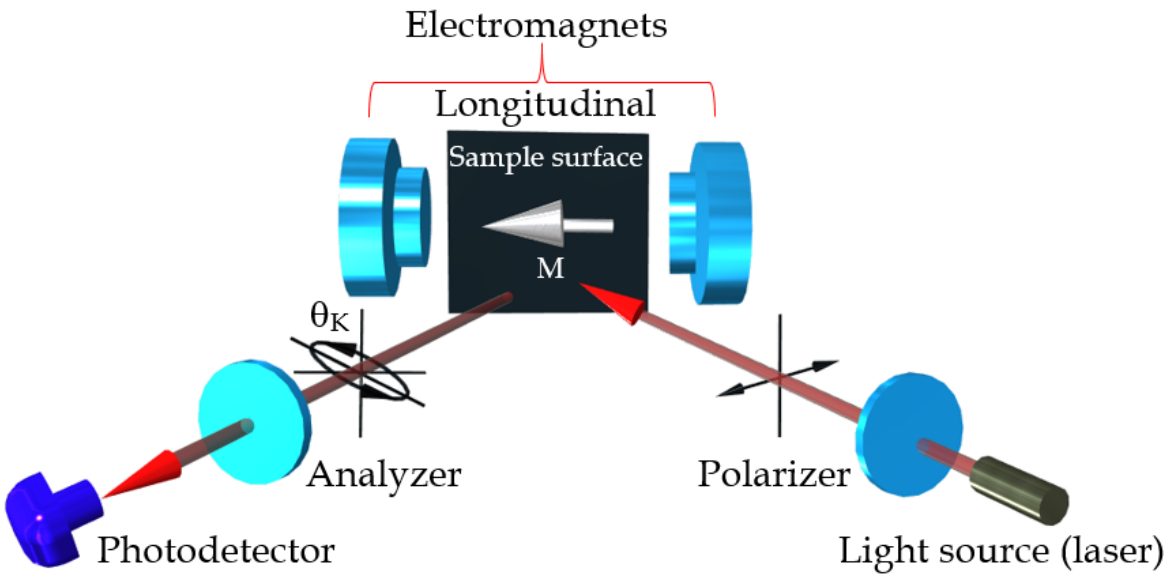

Fig. 4.4 Longitudinal MOKE geometry with polarisation and magnetization (where M is magnetization vector).

There are two cases of incident polarisation that should be taken into consideration, which are S-polarisation and P-polarisation [98]. In the S-polarisation, the electric vector, E, direction is perpendicular to the incidence plane, while in the P-polarisation, the polarisation plane and the incidence plane are parallel. Both cases can be taken into consideration when

the first polariser is placed into a precision rotator by simply changing the first polariser orientation, in which the equations of the polar MOKE can be applicable for the longitudinal MOKE setup [72].

4.3.3 Transverse MOKE

In case of transverse MOKE geometry, the magnetic field will be in-plane but normal to the plane of light incidence as it shown in Fig. 4.5.

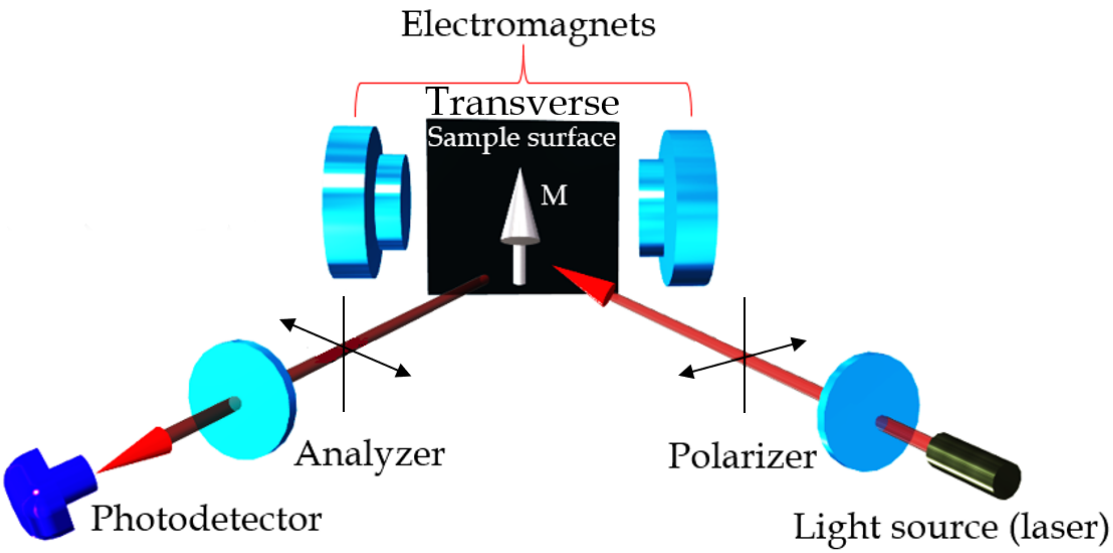

Fig. 4.5 Transverse MOKE geometry with polarisation and magnetization (where M is magnetization vector).

It is quite different from the polar MOKE and longitudinal MOKE effects. Where, a smaller Kerr is generated that is being parallel to the reflected polarization. This increase or decrease in the amplitude in case if polarisation depends on the direction of the magnetic field. Some researchers have been used a Photo-elastic Modulator [PEM] when a very fast response is needed in order to modulate the incident of the laser beam [72].

4.4 The Magneto-optic Kerr Effect

The study of the reflection polarised light by a ferromagnetic material sample that is subjected to a magnetic field is defined as the Magneto-optical Kerr Effect (MOKE). There are several effects occurring from this reflection, such as: 1) the rotation of the plane of the light polarisation, 2) the occurrence of ellipticity of the polarisation within the reflected beam, and 3) an alteration of the intensity of the reflected beam [96]. In this thesis, both polar and longitudinal MOKE were utilized.

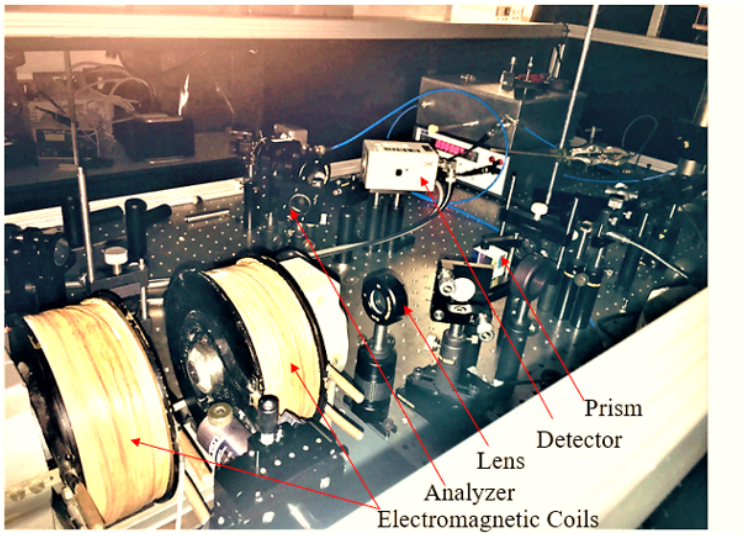

Fig. 4.6 Optical Bench Set-up for polar MOKE with key component indicated.

The experimental setup utilized for polar MOKE and the schematic diagram of polar MOKE measurements are illustrated in Fig. 4.6 and Fig. 4.7 respectively. For the longitudinal MOKE the laser was incident on the sample at an angle of 45^o, whereas for the polar MOKE the light was incident at 90^o. The experimental setup utilized for longitudinal MOKE and the schematic diagram of longitudinal MOKE measurements are illustrated in Fig. 4.8 and Fig. 4.9 respectively.

The following discussion applies to both MOKE setups. Polar MOKE is a technique for studying out-of-plane and was used to examine all samples in this work. Fig. 4.7. shows the actual polar MOKE geometry and set-up used here. A diode laser was used as a light source,

where the wavelength was 658 nm. The laser beam passed through to a beam expander.

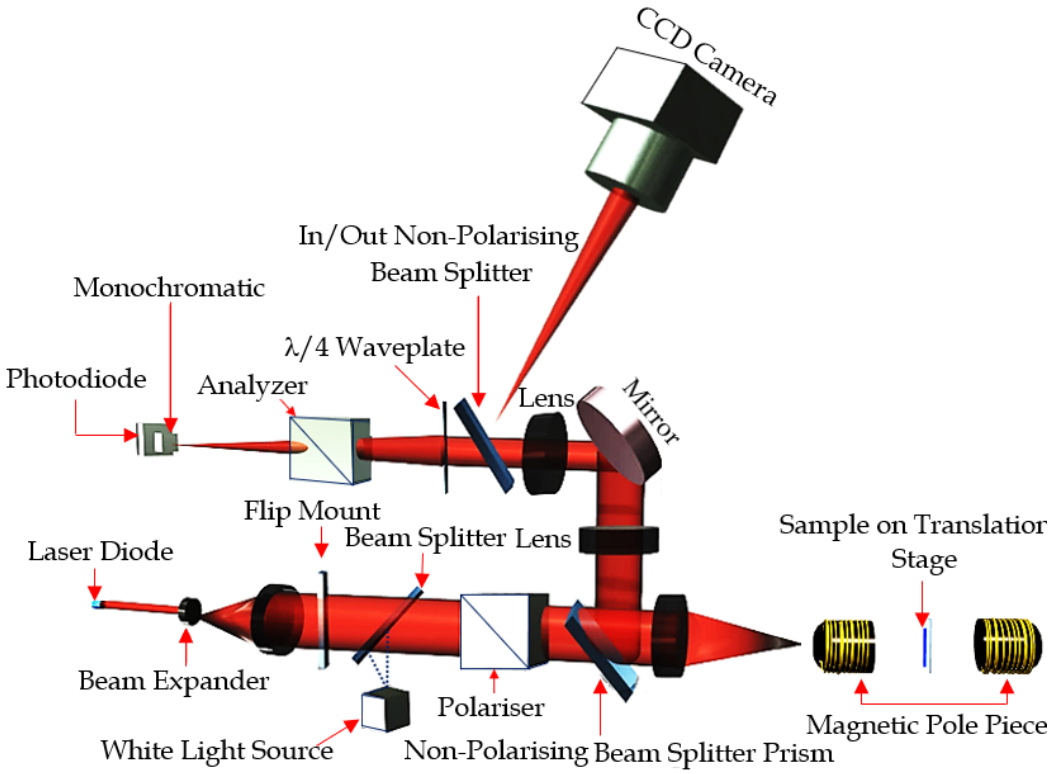

Fig. 4.7 Schematic of the polar magneto-optical Kerr effect magnetometry system with all the principle components showing the light path through the optical enhancement and focusing.

Polarisation was imposed using a Glan-Taylor prism located before a lens focusing the laser beam to a spot size of $\sim 5\ \mu$m on to the sample [75] for the in-plane MOKE, but the spot size will be larger for the polar MOKE as the lens is much farther away and has a longer focal length. Fig. 4.7 shows a schematic diagram of the polar MOKE magnetic system architecture. The maximum range of magnetic fields reaches 1000 Oe. Magnetic fields were provided out-of-plane in the sample by a small electromagnet powered by a Kepco bipolar amplifier; which was driven by a function generator. The figure illustrates the optical method with optical elements and other necessary components. An attenuator was put between the beam expander and the polarising prism to decrease the intensity of the laser when focusing the laser spot and when locating the spot of the laser on the sample using the camera.

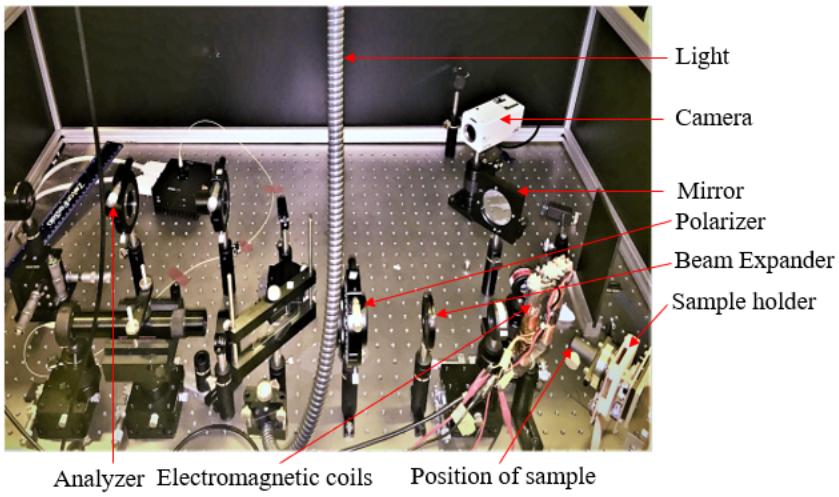

Fig. 4.8 Optical Bench Set-up for longitudinal MOKE with key component indicated.

A movable mirror was put into the beam path to guide the reflected beam to the camera. After reflection from the sample, the laser beam passes through a quarter-wave plate to remove any ellipticity and restore the linear polarisation of the reflected beam. A CCD camera was used with a white light source, to observe the focus of the spot of the laser and the spot location on the sample surface. Measurements as a function of magnetic field were collected using a digital oscilloscope that was controlled by a computer for synchronisation of the full process. The polar MOKE measurement requires an additional beam splitter to detach the incident lighting and reflected lighting from the sample and two lenses to re-focus the light onto the photodiode.

For MOKE measurements both the in/out attenuator and in/out beam splitter were put out of the beam. The laser passes out of a beam expander, thereafter a Glan Taylor polarising prism, which was set to ensure p-polarised light was incident on the sample. The initial lens focused the laser spot to $\sim$ 5 µm upon the sample. The reflected light was concentrated upon the photodiode, having passed through a $\lambda/4$ wave plate and an analysing polariser. As before, the aim of the $\lambda/4$ wave plate was to remove any induced ellipticity in the reflected illumination. The analyser was set to extinction and then offset to between 2^o to 6^o, which was changing dependent on the reflectivity of the sample. The Kerr rotation was thereafter

measured as a variation of intensity at the photodiode due the rotation of the polarisation axis of the reflected illumination proportional to the polarisation axis of the analyser. The photodiode voltage was passed to a Melles-Griot dynamic range amplifier that can amplify small signals, which is representative for the Kerr voltage. The oscillating magnetic field causes the sample magnetisation to cycle through the hysteresis loop, making an oscillating Kerr signal voltage, which was measured by an oscilloscope and time-averaged through hundreds of field cycles to efficiently improve the signal to noise ratio. White light was applied to image the sample to align microstructures with the laser spot. For that purpose, the in/out attenuator and in/out beam splitter were put into the beam. The white light follows the same beam track as the laser beam.

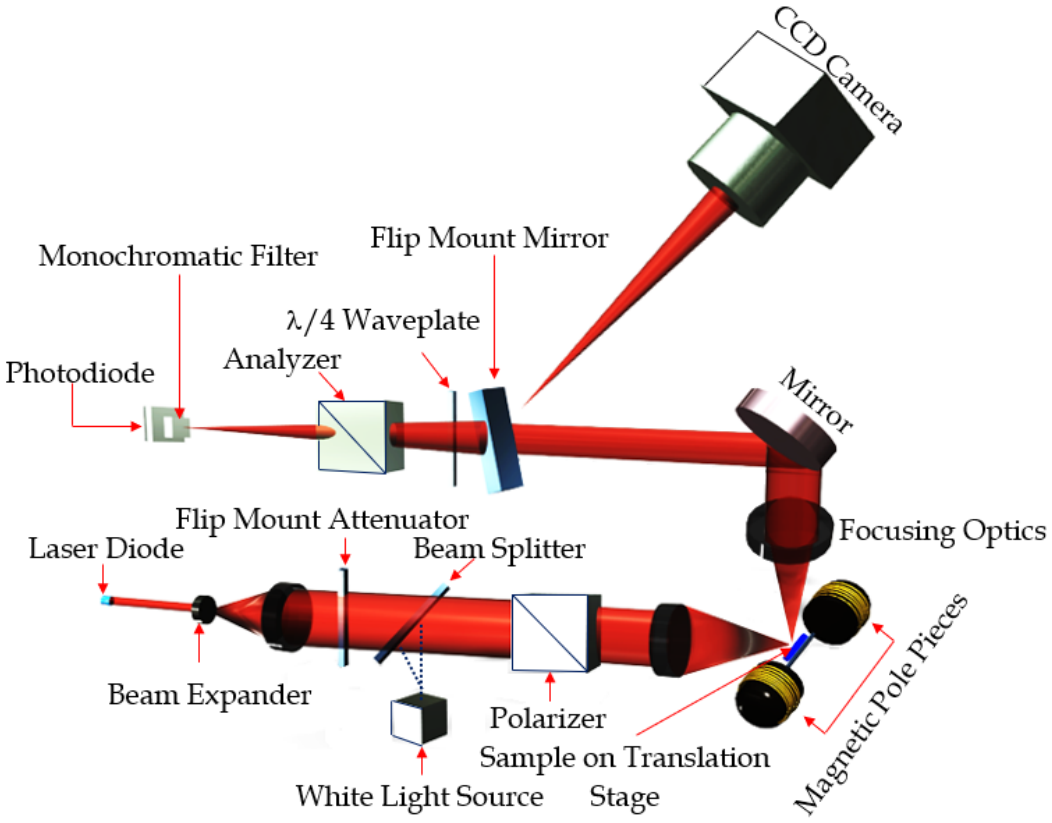

Fig. 4.9 Schematic of the longitudinal magneto-optical Kerr effect magnetometry system with all the principle components showing the light path through the optical enhancement and focusing.

4.5 Magneto-optic Kerr effect microscopy

Magnetic Kerr microscopy and magnetometer systems have been used to visualise magnetic domains and the magnetisation process in various kinds of magnetic materials. With mechanical stabilisation facilities a standard microscope with high-quality optics can obtain high-resolution domain imaging with spot sizes between approximately 100 μm and 5 mm. The light from a source is linearly polarised. It is reflected by a semi-reflective piece to be incident on the sample through the objective. The reflected light returns through the analyser and reaches the camera. Fig. 4.10 (a,b) illustrates the MOKE microscope from Evico Magnetics used in this work [99, 100].

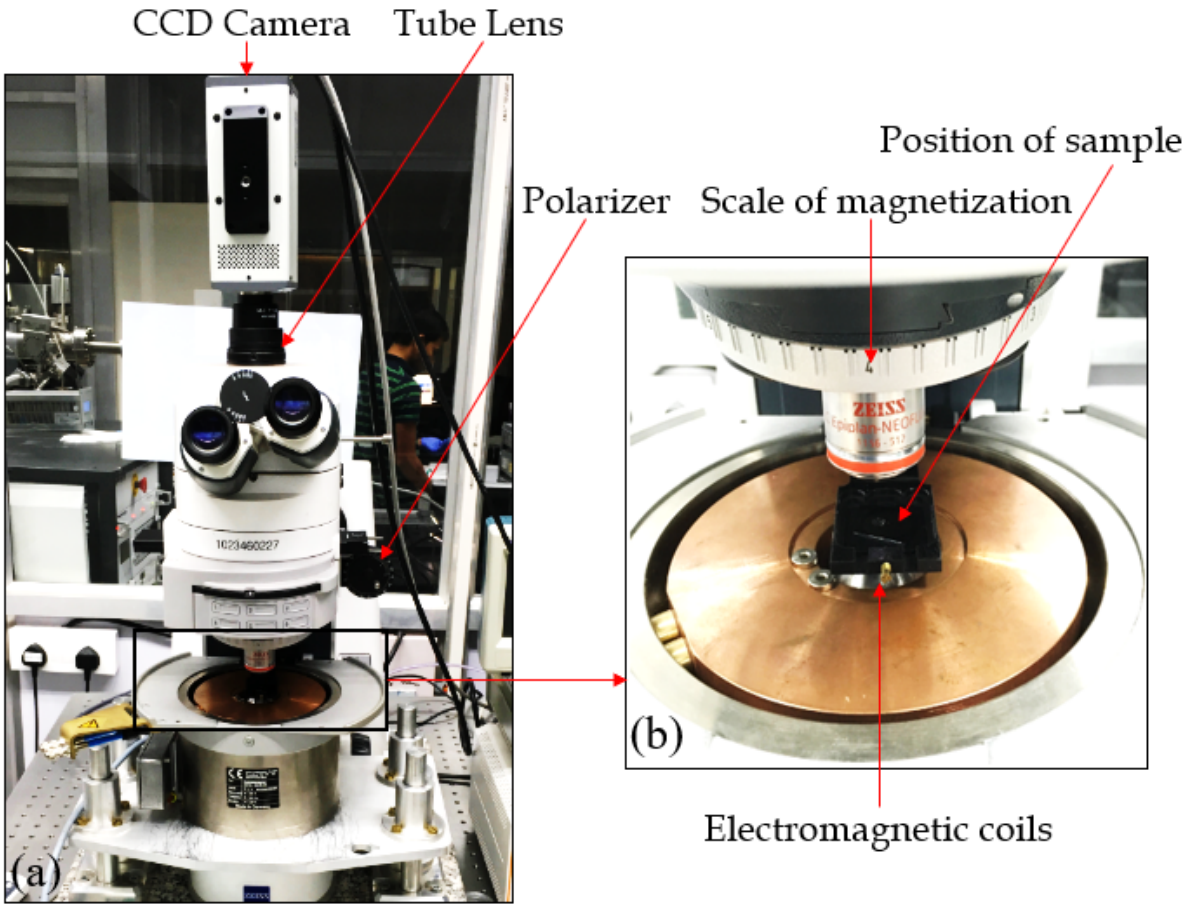

Fig. 4.10 (a). Evico Magneto-Optical Kerr Effect Microscope. (b). Magnification part of (Evico) microscope machine.

In the MOKE microscope, the magnetic state of the material is measured by analysing the change in polarisation of the reflected light from the surface through an appropriate optical microscope. The image contrast depends on the magnetisation state of the sample. The reflected light is recorded on a CCD camera through which a magnetic image can be obtained after subtracting the non-magnetic background that includes topographical features. In Fig. 4.11, the light emitted from a high-intensity lamp is transformed into linearly polarized light to illuminate the sample surface. After reflection, the light is passed through both of compensator and analyser.

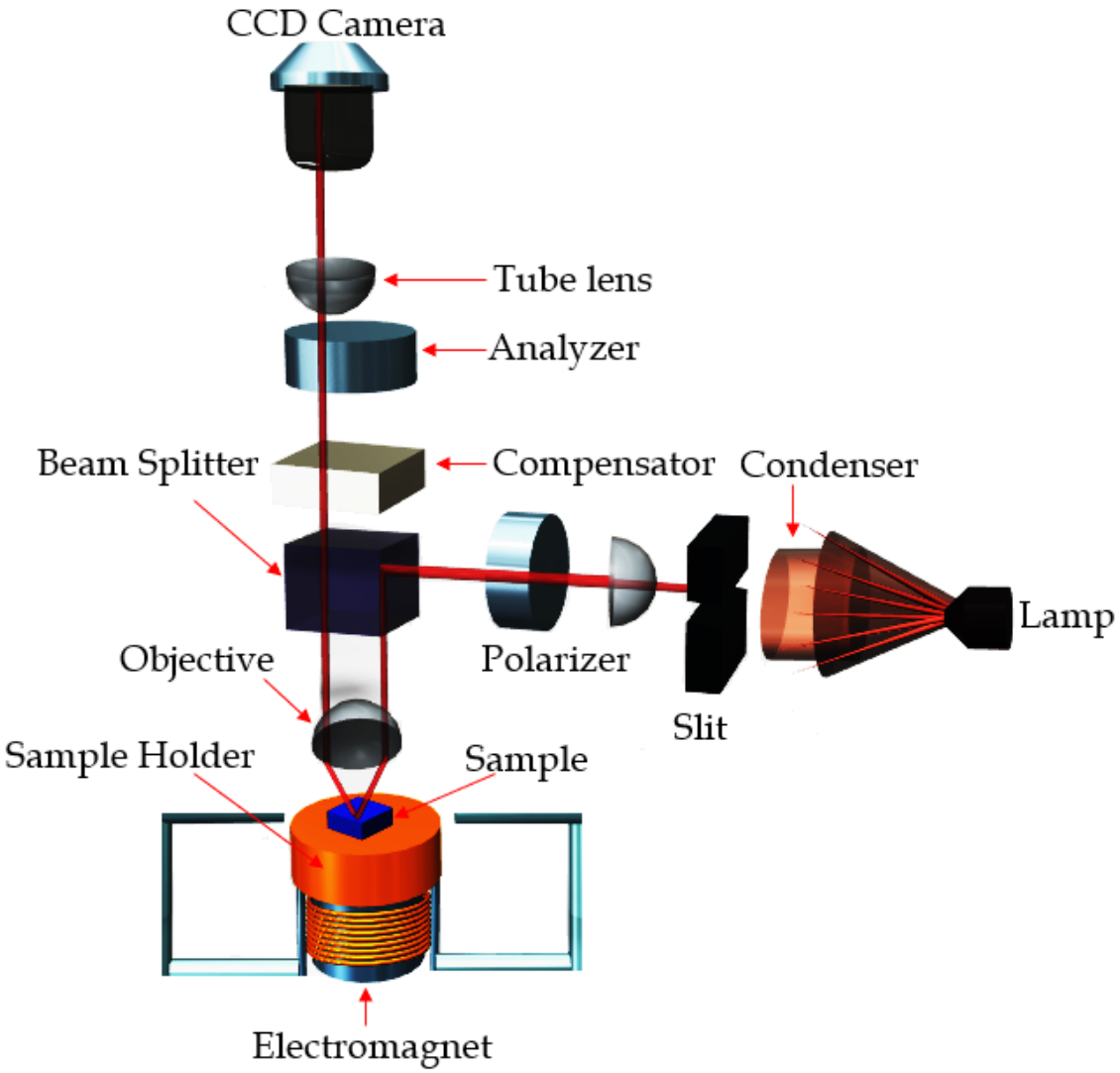

Fig. 4.11 Schematic of the optical diagram of the MOKE microscope.

Fig. 4.12 shows examples of images from multilayers with out-of-plane domain structures for films on SiO_2 and PEN, respectively.

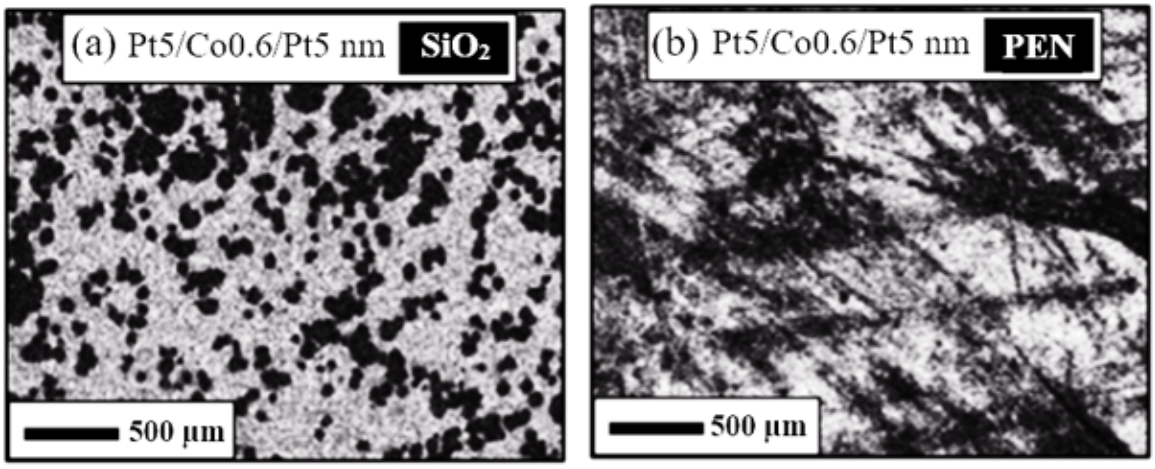

Fig. 4.12 Examples of MOKE microscopy imaging of magnetic films on (a) SiO_2 and (b) PEN using the MOKE microscope.

4.6 Hall effect magnetometry

The experimental aspect of the magnetoresistance device is presented in Fig. 4.13 (a,b). Measuring of the Hall Voltage (V_H) through the sweep of an external magnetic field leads to a voltage hysteresis loop for the material.

The sample holder should be well aligned between the two magnetic poles perpendicular to the magnetic field. Where, the magnetic field was applied perpendicular to the direction of a flow current [101]. A small current I = 0.25 mA was used. The current passing through the sample must not be too large, which leads to heating. Finally, the Hall Voltage (V_H) is measured as a function of the magnetic field while maintaining a proper value for the current.

A schematic design of the sample holder is shown in Fig. 4.14 (a) with all the components, which consists of brass spring-pins, an aluminum arm and a piece to rotate the direction of current and voltage to be longitudinal or perpendicular. Also, the magnetic field was measured using a Gaussmeter. Fig. 4.15 illustrates a diagram of the required measurement

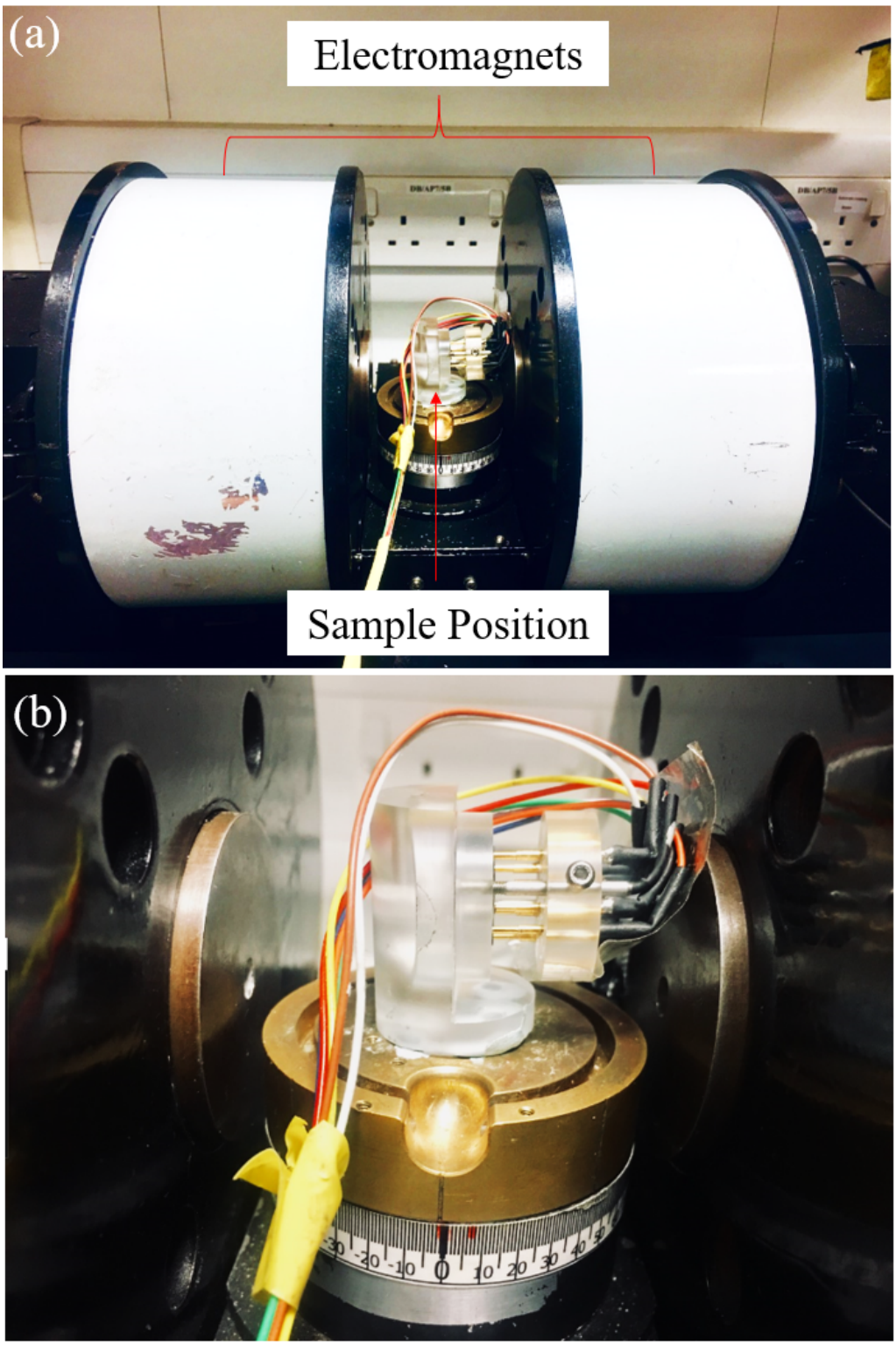

Fig. 4.13 (a). Magnetoresistance machine for Hall measurements. (b). Magnification photo of sample holder.

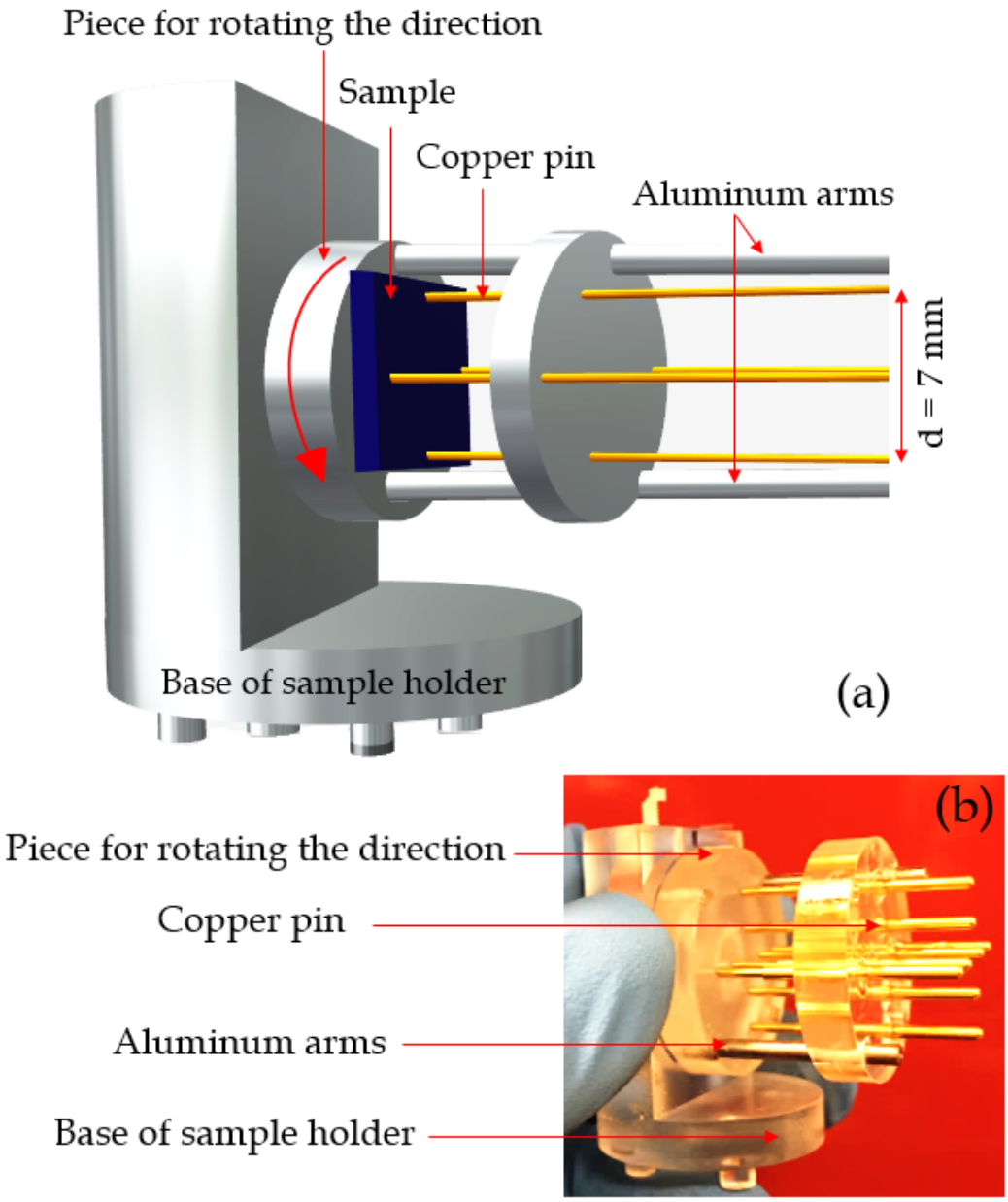

Fig. 4.14 (a) Schematic design for Hall measurements of thin-film samples. (b) Example Hall measurements sample holder. The sample holder was designed by the author Ala Bahaaldin.

system. A sample is put between a pole of an electromagnet so that a out of plane magnetic field can be applied. The arrangement allows the sample to be rotated to do the measurements at different angles. In our measurements the angle was 90^o. Current and voltage pins are attached to the Hall cross so that the current can be applied from the current source. The

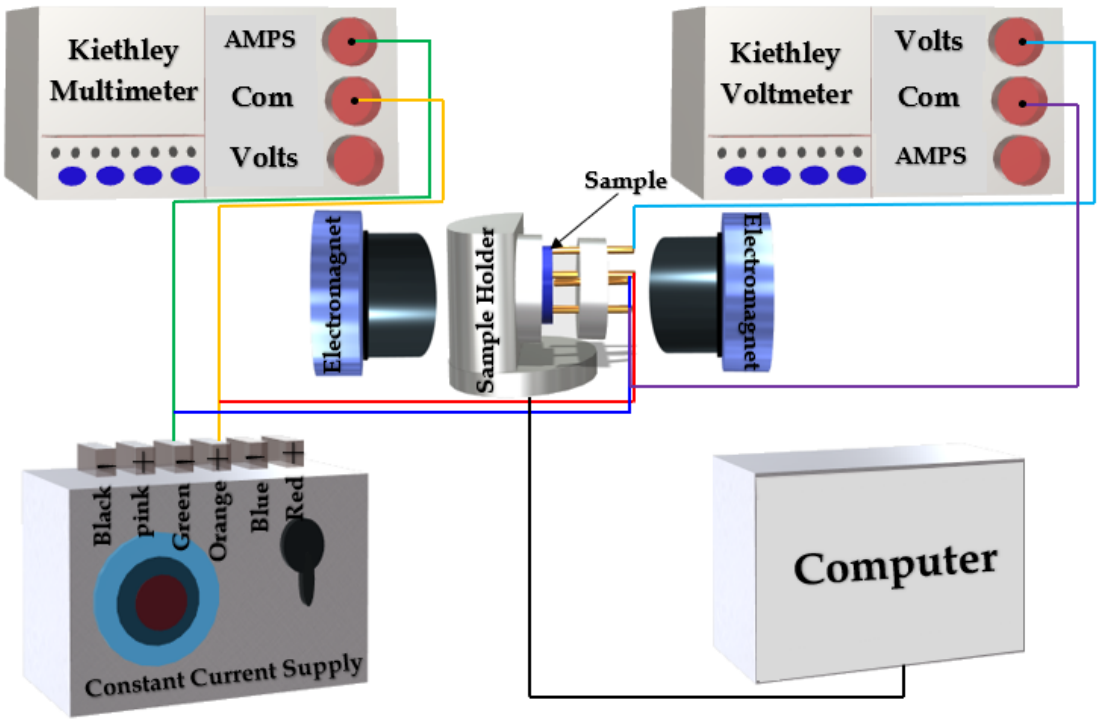

Fig. 4.15 Schematic of Hall Effect electrical connections.

output voltage is measured by the voltmeter (either the lock amplifier or nanovoltmeter). These components are controlled by the software on the control computer. The program then plots the measured voltage against the magnetic field in real-time to construct the hysteresis loop.

4.7 Geometrical sample designs for Hall Effect measurements

At the beginning of the work, to carry out sensitive Hall Effect electrical measurements, shape masks were already manufactured. This engineering design of shape is appropriate for performing thin-film sample measurements. The samples in this project have a length and width of 8×8 mm^2, and it is shown in both geometrical mask that is executed in work shop Fig. 4.16 (a,b).

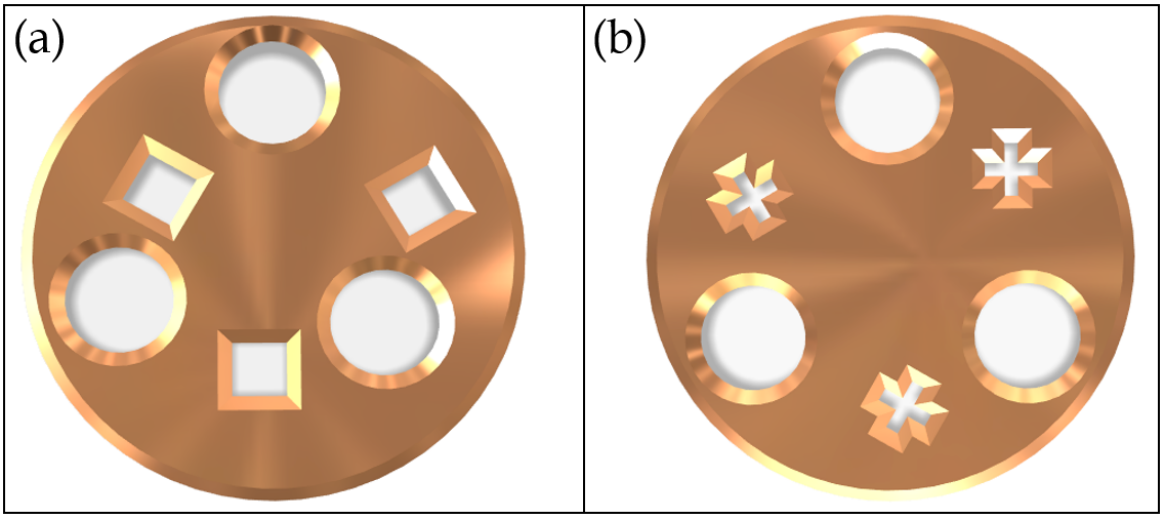

Fig. 4.16 (a,b) Geometry of the shadow mask with different shapes for Hall measurements.

For accurate measurements in this study, using both of the samples cross and square shape samples were investigated. It should be taken into consideration that the thicknesses of samples should be homogeneous, and the pins point contacts placed at the edges of the samples. As described in one study [102], a very satisfactory way of performing Hall effect measurements is that through the van der Pauw method [103], using a "square" sample. Several studies have focused on the effect of inhomogeneous samples using van der Pauw measurements [104–110]. Some disadvantages of Hall effect measurements have been found using circular samples, this may be due to the spreading of the current everywhere in the sample from the current contacts. Van der Pauw introduced how to calculate the resistivity and mobility of a flat sample in the case that the following conditions are met: 1. pin contacts are on the perimeter of the sample, 2. pin contacts are small enough, 3. the sample has a uniform thickness, and 4. the sample is connected individually (does not contain isolated holes).

At the beginning of this work a circular mask was manufactured. A big difference was found in the hysteresis results when compared with the results of the MOKE. So, differently shaped masks were manufactured to study the differences between them and to get accurate

results. For square samples with length sides and d is represented a contact of size in the four corners, if a/d <0.1, the measurement error is less than 10 % [111]. The error is decreased by putting the contacts on square samples at the middle point of the sides. The error of our square shape was approximately 10 %. Since, d is represented the length of deposition film sample while a is the distance between the probe and the edge of sample. Fig. 4.17 (a,b) shows a schematic images of Greek mask and square masks respectively.

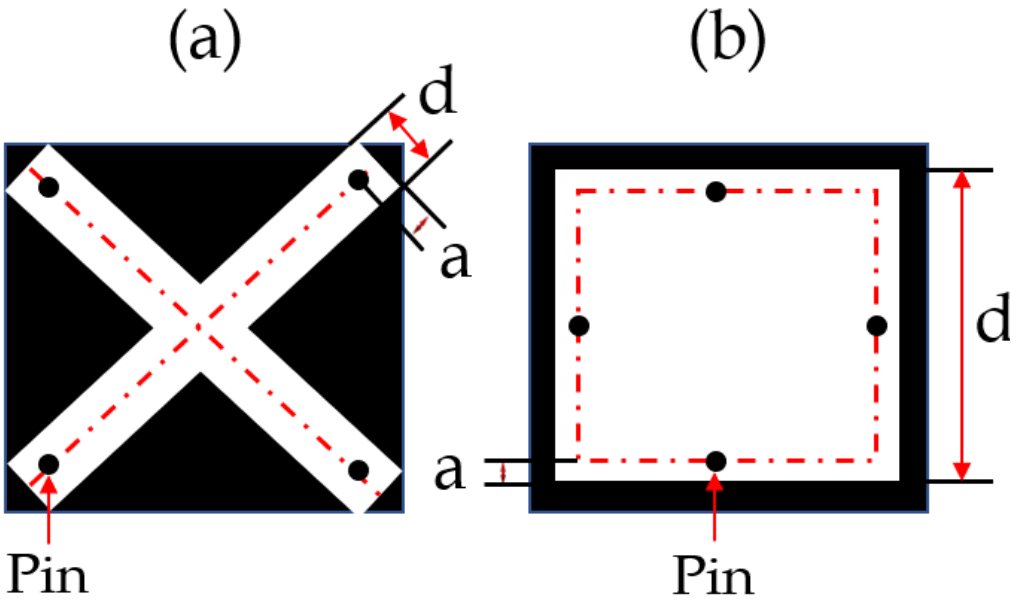

Fig. 4.17 Geometrical of the shadow mask with different shapes for Hall measurements for (a). Greek cross and (b). square shapes. Where, d is the length of deposition film and a is the distance between pin and the edge of deposition film. The white colour represents the deposition film region while the black colour represents the substrate region.

4.8 Summary

In this chapter, different kinds of techniques have been introduced linking to the understanding of the structural and magnetic properties in thin films. It has been included MOKE, Hall magnetoresistance magnetic analysis techniques. Each techniques has features for giving more understanding of the magnetisation behaviour in this study. Also, Magneto optic Kerr

microscopy has been used to visualise magnetic domains and the magnetisation process in various kinds of magnetic materials.

Chapter 5

Structural Characterization of Thin-Films and Substrates

5.1 Previous Work

The structure of thin film samples plays an important role in the dynamics of magnetisation, so that the capability to describe the particular sides of it is pivotal. X-rays gives the opportunity to know the properties of the interior structure of samples, like layer thickness, electron density and interface roughness and interweave [112, 113]. Wells et al. has found that the data of roughness that are taken from the X-ray curves on the first Kiessig fringe exhibited a reduction in the interface roughness with deposition temperature, referring that the peak in whole disorder has resulted due the competition between growing intermixing and lessening of the roughness with temperature [112]. Besides, in this study, the focusing was on increasing the thickness of Pt buffer layer to decrease the roughness of the polymer substrates; in order to improve the preferential orientation of magnetisation to be out-of-plane. Also, x-ray diffraction (XRD) measurements was used because of the grain size of the magnetic material; which represents an important structural factor that has a great impact on the magnetic properties i.e, the magnetic anisotropy. According to other studies, when

the diffraction peaks indicate a high crystal quality, this means the anisotropy was greater compared to broader, or less intense diffraction peaks [114, 115].

Moreover, surface morphology and magnetic structure were studied using atomic force microscopy. In previous study of Kolesnikov [116], it was shown that the surface morphology consideration of Ru films with different thicknesses leads to smoother silicon dioxide substrate. Lower root-mean-square roughness r_q = 0.095 nm was illustrated at t_{buffer} = 15 nm. However, when the thickness of the buffer layer increased from 3 nm to 20 nm, the surface roughness has decreased to less than 10% .

5.2 Introduction

In this chapter, all structural analysis techniques that have been used in this study are discussed in detail. Structural analysis in this work includes x-ray reflectivity (XRR), x-ray diffraction (XRD) and atomic force microscope (AFM), which are used to measure the thickness of the samples, surface and interface structure and crystallization respectively.

5.3 Structural Characterisation

It is known that the functional physical properties and material structure are linked in most materials. The structural characterization is an important aspect of the work in this thesis. Structural analysis of thin films was performed primarily by x-ray scattering techniques and with surface roughness studied using atomic force microscopy.

5.4 X-Ray Reflectivity

X-ray reflectivity is occasionally referred to as x-ray reflectometry. It represents a surface-sensitive analytical mechanism to distinguish between thin films surfaces and multilayers

used in physics ,chemistry and materials science where the thickness of film ranges from less than 1.0 nm up to several tens of nanometers [117–120].

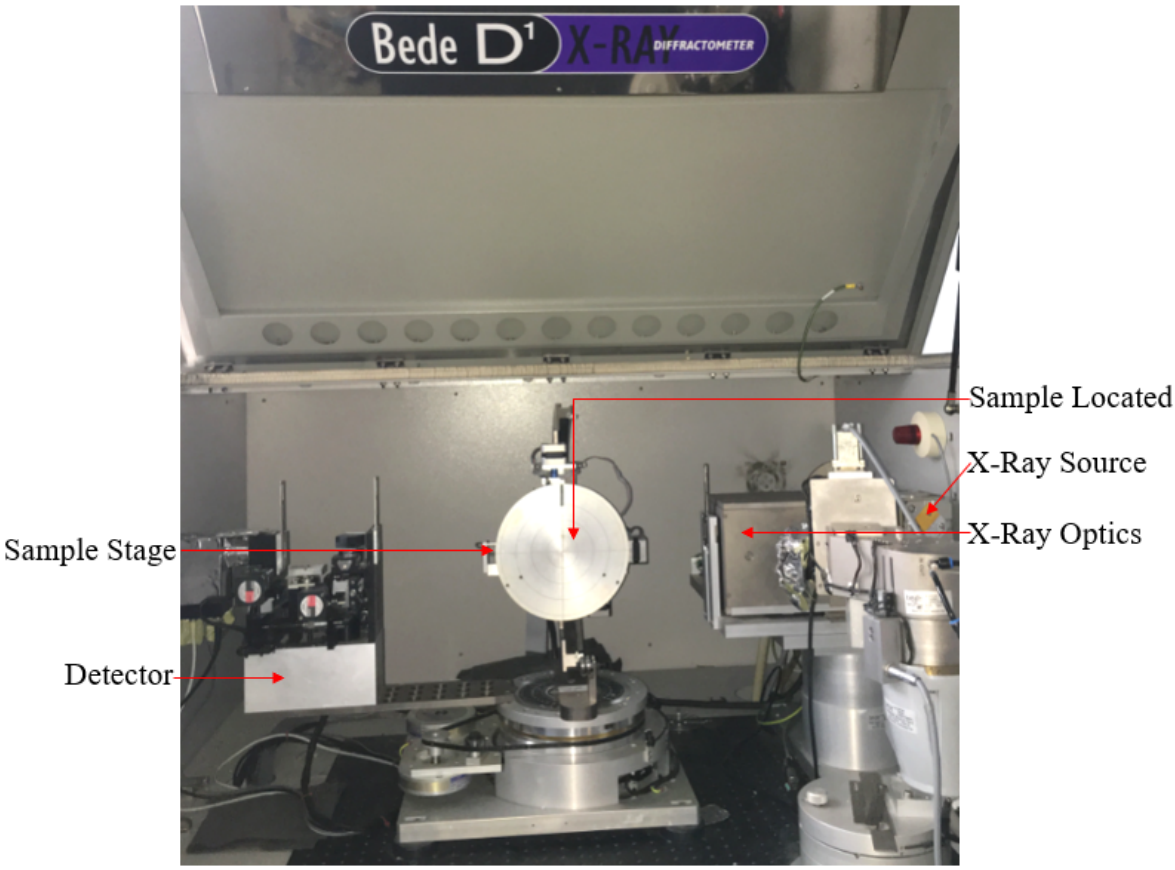

Fig. 5.1 Bede D1 x-ray reflectivity system with key components indicated.

Fig. 5.1 shows the x-ray reflectivity system that was used. The fundamental concept is based on the reflection of an x-ray beam from a surface and interfaces of thin films that determines the intensity of the reflected x-rays in the specular condition i.e. reflected angle = incident angle. The intensity of the reflected beam depends on constructive and destructive interference and is furthers affected whenever the interfaces are not perfectly sharp and smooth according to the law of Fresnel reflectivity. This technique was first implemented with the x-ray by Professor Lyman G. Parratt of Cornell University in an article published in Physical Review in 1954 [113]. The determination of x-ray reflectivity can be measured using a conventional powder diffractometer with very low angle of incident x-rays. The

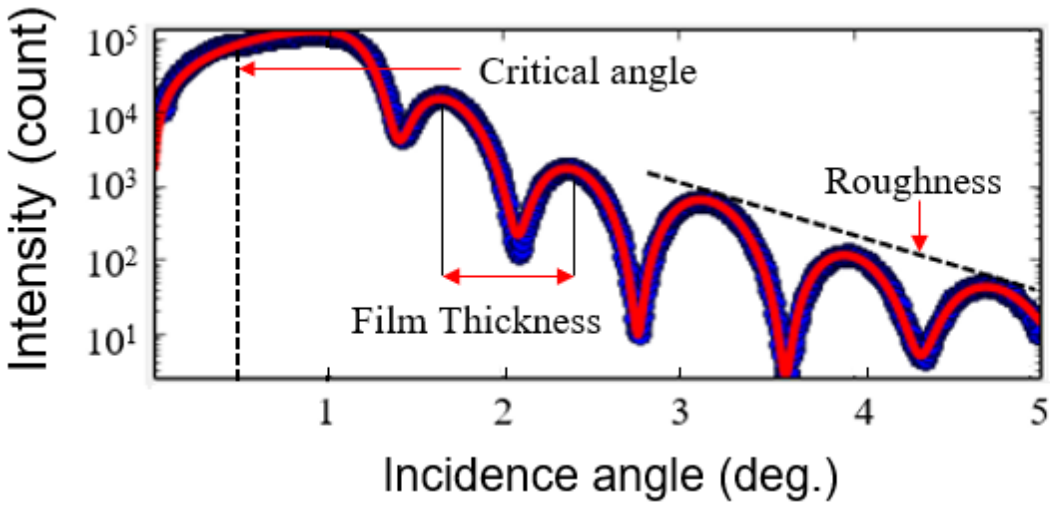

Fig. 5.2 Interpretation of x-ray reflectivity data that is includes critical angle, roughness, film thickness and density.

modified Bragg equation links the interference fringe positions to the film thickness [121–123]. Fig. 5.2 shows x-ray reflectivity as a function of incident angle for t_{Pt} 5.0/t_{Co} 0.5/t_{Pt} 5.0 nm.

5.4.1 X-Ray Reflectivity: Refraction and Reflection

In a medium containing many atoms, many x-ray scattering and absorption events will occur. As a result, x-rays will be refracted and then reflected as they travel due to media with different electron densities. Refraction in thin-films can occur between various materials or when the x-rays propagates through into the surface from the ambient air. The refractive index, n, is

$$n = c/v \ , \tag{5.1}$$

where, c is the speed of light and v is the velocity with material. The x-ray incident interacts with the atoms of every layer. The atoms can be considered to absorb x-rays and emit spherical x-ray waves, propagating in all directions. This is considered as the best description in which the atoms are thought of as the source of the waves. Since the refractive

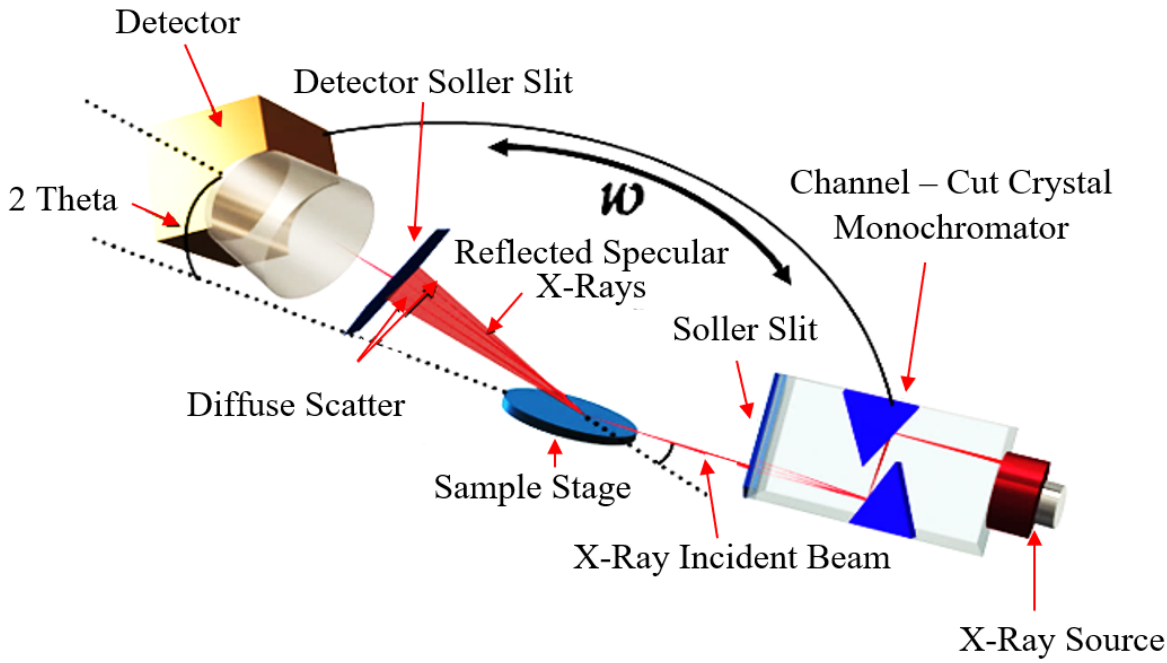

Fig. 5.3 Schematic illustration of x-ray reflection.

index, n, increases with the wave frequency ω, the excitation and spontaneous emission will rapidly repeat. Above the resonance frequency, n reduces the number of electrons transitions. For x-rays the frequencies are very high and this will lead to x-rays with small n propagating into a material with velocity v and vector k. The refractive index n is associated with scattering, the dispersion coefficient δ, connects the incident beam wave vector k, and the density of the electrons in the material. The second factor is the absorption coefficient, β; this is responsible for attenuation of the photon beam. When a beam travels through a material, it will experience attenuation. The refractive index can be written as follows:

$$n = 1 - \delta + i\beta \ , \tag{5.2}$$

the value of β is known to be very small, of the order of 10^{-6} and 10^{-8}, and the value of δ will be approximately to 1. Fig. 5.3 illustrates the x-ray reflectivity geometry. Equations 5.1 and 5.2 mean that n is slightly less than 1, by an amount δ, which is small, and therefore v in the material is greater than the speed of light, c, which cannot be correct except if v represents the phase velocity not the group velocity [124]. The total beam amplitude is equal

to the sum of both the reflected and refracted components. Snell's law is used to find the critical angle which leads to that the total reflection is external is a result of n being slightly less than 1. This law concerns the occurrence of incidence and refraction angles due to the refractive index by:

$$n_o cos\theta_i = n_1 cos\theta_t \ , \tag{5.3}$$

the condition that leads to total external reflection is $\theta_t = 0$, and θ_i is very small. Equation 5.3 can be written as follows:

$$\theta_i = \theta_c = \sqrt{2}(1 - n_1) = \sqrt{2}\delta \cdot \tag{5.4}$$

The critical angle θ_c for the whole reflection is very small, of the order 10^{-2} radians, 10^{-1} degrees is an angle, with scattering vector is in inverse angstroms. Both refraction and reflection occur in the case when the x-ray beam propagates in the medium [124]. Increasing the number of layers in the medium increases the complexity of the equations due to the greater number of the interfaces. These increase the number of scattering events, such as multiple reflections from the top and bottom interfaces within the medium. On top of this, changing the material changes the refractive index, due to additional layers and materials having different electron densities. This change will affect the reflection profile that is determined by the combination of materials.

Reflection from a Thin-Film

The simplest scenario of an x-ray propagating into a medium by single refraction and reflection events is explained here. In thin-films case, these processes can be repeated in each layer, hence each layer has its own refractive index, n. The refractive index of the vacuum around the thin film is n_0 followed by the first layer of the film with the refractive index n_1 and the substrate with n_s. Beyond the substrate there is no contribution to the total intensity of the reflective radiation. When x-rays enter a thin film at a limited angle, a series

of reflections appear from both the top and bottom of each layer within the thin film. Fig. 5.4 illustrates the reflection of the thin-films and the resulting beam components.

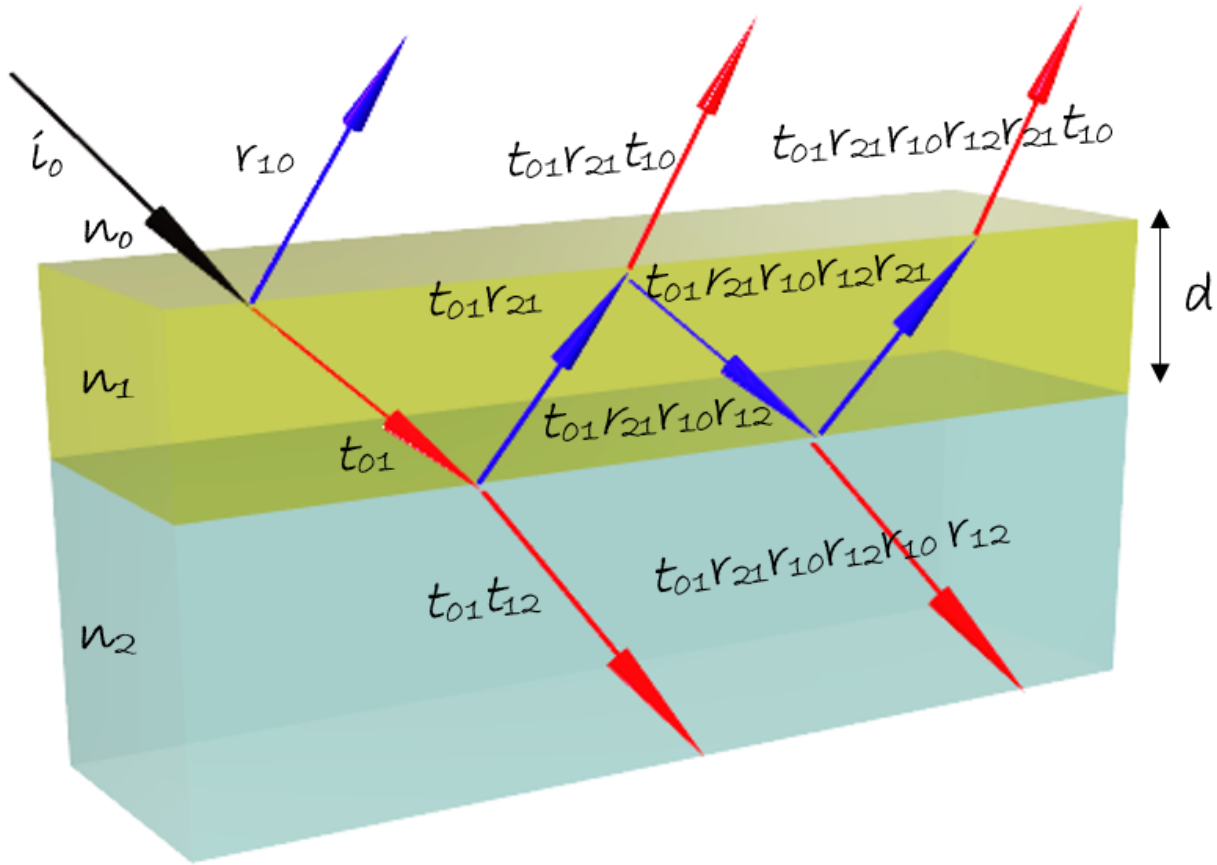

Fig. 5.4 Schematic illustration of x-ray interactions with a single layer above the layer of substrate with the total reflection calculation of the x-ray incident beam. In the case of the reflected or the transmission is towards the thin-film surface then $n > m$, whereas if the transmission is towards the substrates then n $< m$, where n and m = 0,1 or 2 only .

From this schematic, the whole reflected x-ray intensity (r_{tot}) can be calculated, beginning with the x-ray beam incident to the final reflected, r, and transmitted, t, beams:

$$r_{tot} = r_{10} + t_{01}\, t_{10}\, r_{12} p^2 \sum (r_{10}\, r_{12} p^2)^m \ , \tag{5.5}$$

in this equation, the layer density is homogeneous, making the calculation easier. In addition, reflectivity is associated with the phase factor, p, where the phase difference can be

calculated by $P^2 = \mathrm{Exp}^{(idq)}$. The layer thickness, d, and the wave number, q, are linked to the wavevector, k_1, of the incident beam θ_i by the equation:

$$q = 2k_1 sin\theta_i \cdot \tag{5.6}$$

The critical angle can also be calculated from thin films using Snell's law. This term is used for calculating the amplitude of both reflectivity and transmissivity. This equation leads to a relationship between reflected amplitude, α_R, the transmitted amplitude, α_T, and the incident amplitude, α_I.

$$\alpha_T = \alpha_I + \alpha_R \cdot \tag{5.7}$$

5.5 Influence of Thin-Film Thickness, Density and Surface or Interface Roughness

The reflected x-ray intensity from a thin film is affected by several factors, such as: number of layers, the thicknesses and the interfaces between the layers. When the thin-films have more than one layer, equation 5.8 governs the reflected intensity of the nearest layer of the substrate. Considering N layers will add more to the equation.

$$r_{N-1,N} = \frac{r_{N-1,N} + r_{N,\infty} P_N^2}{1 + r_{N-1,N} r_{N,\infty} P_N^2} \cdot \tag{5.8}$$

The recursive equation of Parratt's 5.8 [113] can be used to obtain the intensity of the overall reflected x-rays for the thin-film system. As mentioned above, when the x-rays move through a thin -film, the x-ray intensity will be attenuated in relation to the thin-film thickness d. This intensity attenuation is by the factor of $e^{-\mu d}$, but the attenuation of amplitude will be by the factor $e^{-\mu d/2}$. The increment of the incident angle beyond the critical angle will

increase the path travelled through the thin-film, thus the intensity of x-rays will decrease with increasing angle of incidence to the angle of the incident [124].

Thickness influence of Thin-Film

Changes in reflection intensity as a function of thin-film thickness are shown in Fig. 5.5.

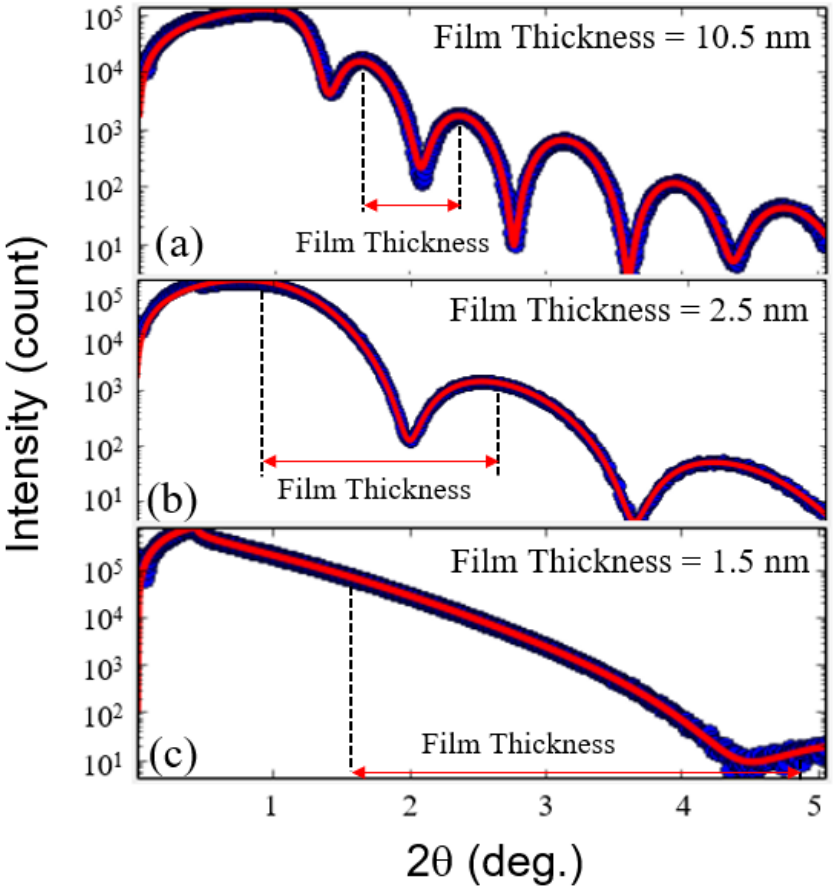

Fig. 5.5 Reflectivity of Pt/Co/Pt film with different values of film thickness (a). t_{Pt}Pt5.0/t_{Co}0.5/t_{Pt}5.0 nm, (b). t_{Pt}2.0/t_{Co}0.5/t_{Pt}2.0 nm and (c). t_{Pt}1.0/t_{Co}0.5/t_{Pt}1.0 nm respectively deposited on SiO_2 substrate. The blue symbols indicate the measured data and the red lines the best fitting simulations.

Fig. 5.5 illustrates the x-ray reflective curve of a Pt/Co/Pt film deposited on a SiO_2 substrate. In general, the y-axis of the curve of x-ray reflectivity appears in a logarithmic scale of the measured I/I_0. A logarithmic scale is used to account for the wide range of reflected x-ray intensity. The occurrence of interference between the x-rays reflected from the

surface of the Pt/Co/Pt thin-film and interface between Pt/Co/Pt film and substrate appears the profile as oscillations known as Kiessig fringes caused by x-ray interference. Those oscillations were observed firstly in 1931 by Kiessig and have shorter period oscillations for thicker films [121].

Influence of density on Pt and MgO buffer layers

The influence of film density on the x-ray reflectivity curve is explained below. Fig. 5.6 illustrates two reflective curves of 10.8 nm thin-films with different densities deposited on the SiO_2 substrates. In this case, the films are deposited using different deposition parameters. A shift in the whole reflection edge is apparent which leads a change in density. The thin film sample with the lowest density [lowest reflection edge] exhibits interference fringes in a shorter angular range than the thin film sample with highest density.

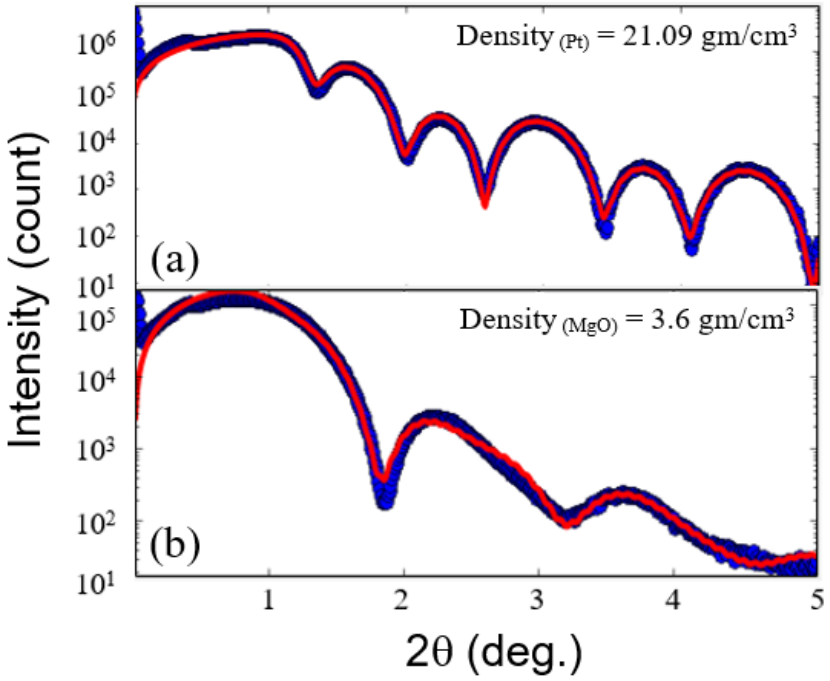

Fig. 5.6 X- ray reflectivity curves of different structure for both (a). $t_{Pt}5.0/t_{Co}0.8/t_{Pt}5.0$ nm and (b). $t_{Pt}5.0/t_{Co}0.8/t_{Mgo}5.0$ nm respectively on SiO_2 substrates (film thickness 10.8 nm). The blue symbols indicate the measured data and the red lines the best fitting simulations.

Pt and MgO films are used in the figure as examples of large and small densities, respectively. The results show that the amplitude and wavelength of the oscillation and the critical angle are affected by the film density, with the amplitude of the oscillation depending on the difference between the substrate and the electronic density of the film [121].

Surface and interface roughness

The thickness shown above is estimated by calculating the reflectivity using the recursion method of Parratt. This method assumes that the interface between each layer in the thin layer is completely flat or smooth and there is no mixing in the interface [121].

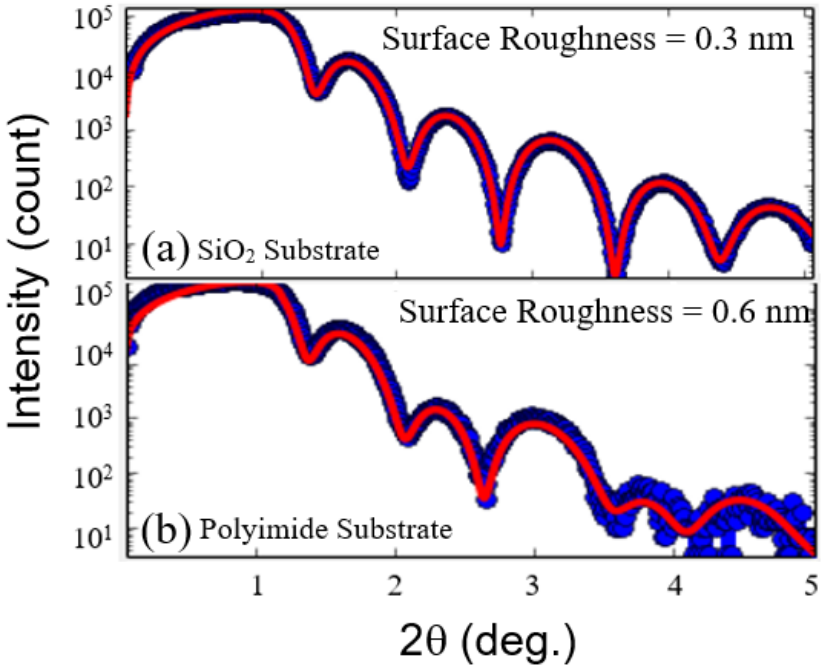

Fig. 5.7 X- ray reflectivity curves of $t_{Pt}5.0/t_{Co}0.5/t_{Pt}5.0$ deposited on both (a). SiO_2 and (b). polyimide substrates with two different values of surface roughness (film thickness 10.5 nm). The blue symbols indicate the measured data and the red lines the best fitting simulations.

This is not typically the state of real thin-films, in which the interfaces will have a finite amount of roughness. The interface width can be composed of topographical roughness and/or chemical grading or intermixing. The specular reflectivity is influenced by the width of the interface structure. Fig. 5.7 illustrates the reflectivity for SiO_2 and polyimide substrates

with two different values of surface roughness. The results indicates that reflected x-rays decrease more rapidly with greater surface roughness. Surface roughness includes an uneven physical interface and a transition boundary layer that constantly changes in density.

5.6 X-Ray Diffraction

X-ray diffraction is used to obtain information on the crystal structure. High intensity x-ray peaks occur when constructive x-ray interference results from scattering from the electrons of periodically arranged groups of atoms. When x-rays are diffracted from various planes in the lattice, constructive interference occurs for a path difference. This was explained mathematically in Bragg's law [125].

$$n\lambda = 2d_{hkl}sin\theta\,, \tag{5.9}$$

where: λ is the x-ray wavelength of the incident, n: is a positive integer, d_{hkl}: is the spacing between the plane, θ: is the angle between the x-ray of the incident and the relevant lattice planes hkl are Miller's indices, which are linked to reciprocal lattice parameters [124]. Fig. 5.8 illustrates the Bragg case of structural interference of x-rays, which are diffracted from atoms separated by d spacing. The relationship between the angles of incidence and reflection and the path difference is given by Bragg's law [126]. With the diffraction of x-rays from different planes in the grid, an interference occurs:

$$d_{hkl} = a_0/\sqrt{h^2 + k^2 + l^2}\,. \tag{5.10}$$

In cubic material, they are associated to spacing between plane levels. In Bragg's Law, when x-rays interfere constructively, the difference between path lengths of the two waves must be equal to nλ. Diffraction pattern refers to vertices which can be identified by measuring the scattered x-ray intensity as a function of the incident and the detector angle. So, every peak is associated with certain planes where the atoms are arranged.

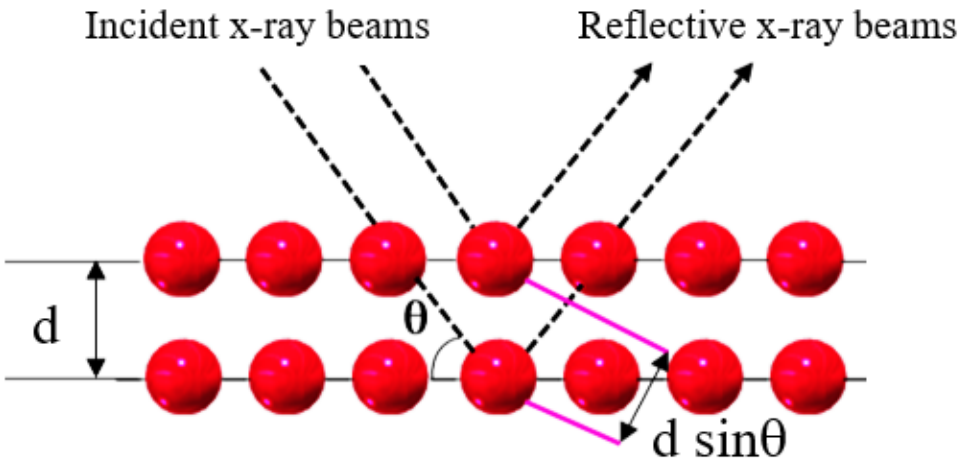

Fig. 5.8 Schematic figure showing x-ray diffraction, the condition of the constructive interface between the incident and the reflective x-ray beams.

5.6.1 Crystallite size

Experimental diffraction peaks can be compared to those in the JCPDS (Joint Committee on Powder Diffraction Standard) database for phase identification [127]. The peak broadening of the experimental diffraction peak can also give information of the material dimensions. The grain size can be calculated from the Scherrer formula, using the full-width-half-maximum (FWHM) values of indexed peaks in the X-ray pattern [128–130]. For conventional XRD this is the out-of-plane grain size D, given by the Debye-Scherer equation:

$$D = 0.9\lambda/\beta cos\theta_B\,, \tag{5.11}$$

where, λ is the wavelength of the incident X-ray beam, θ_B is the diffraction angle and β is the FWHM at θ_B in radians. The grain size can only be determined by means of XRD measurements.

5.7 Atomic Force Microscopy (AFM)

Scanning probe microscopies can provide very high spatial resolution structural and functional information. Atomic force microscope (AFM) measures the local surface characteris-

tics by means of scanning a sharp probe tip, which is usually mounted on a cantilever, across a surface.

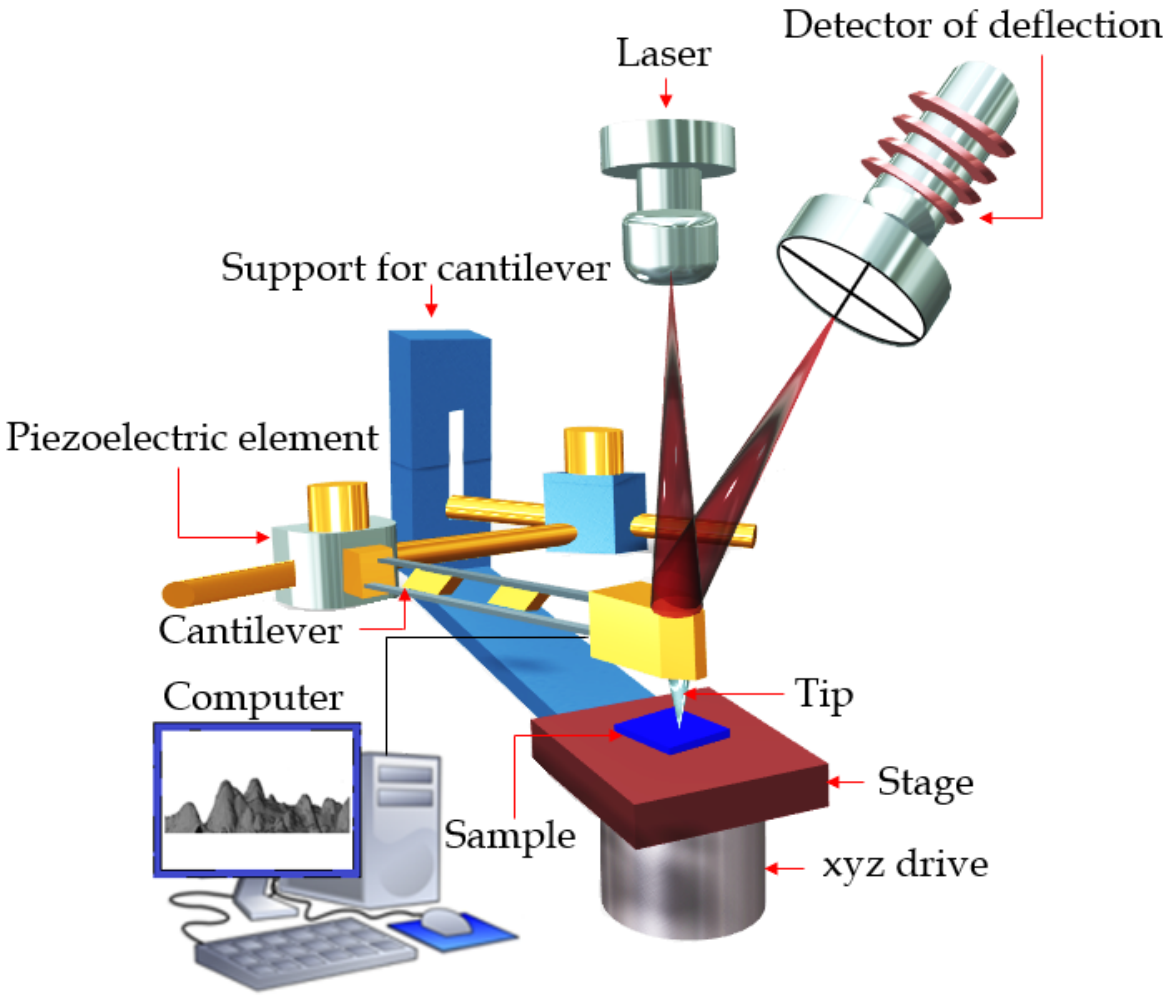

Fig. 5.9 Schematic of a atomic force microscope.

The small displacements of the cantilevers are detected by the reflection of a laser beam from the upper surface of the cantilever onto a detector. The beam is focused on the back part of a cantilever by means of a four-piece optical detector. Fig. 5.9 illustrates a schematic atomic force microscope, which usually consists of a small spring cantilever a piezoelectric element cantilever. The sharp tip is located at the free end of the cantilever, and the detector records the deflection of the cantilever. The sample is placed on the sample stage. An xyz piezoelectric drive moves the sample stage in x, y, and z directions relative to the tip. As

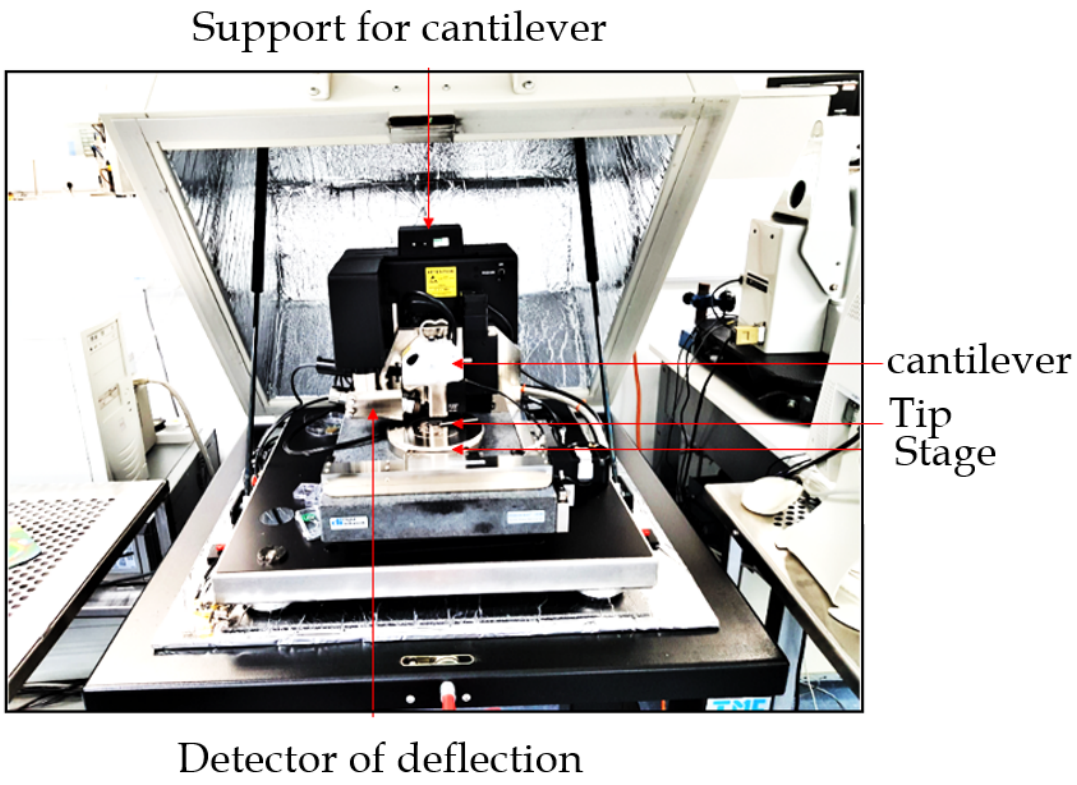

Fig. 5.10 Image of the atomic force microscope used in this study.

illustrated in the schematic, the interaction between the tip and the sample allows detection of features down to the atomic scale. Many aspects of the cantilever movement can be used to determine the interaction between the tip and the sample, the detector of AFM measures the deflection of the cantilever and transforms it into an electrical signal. AFM signals, like sample height or cantilever deflection, are recorded on a computer as a function of x-y scan position. The data are displayed a pseudocolor images, where each pixel represents the x-y position on the sample, and the color refers the recorded signal [131]. Fig. 5.10 shows an actual atomic force microscope. To survey the surface, the cantilever is scanned along the surface by a piezoelectric actuator [132]. Examples of atomic force microscope topographical scans of silicon dioxide (SiO_2) and polyethylene naphthalate (PEN) substrates are shown in Fig. 5.11. The micro and nano-scale features of the both substrates can be

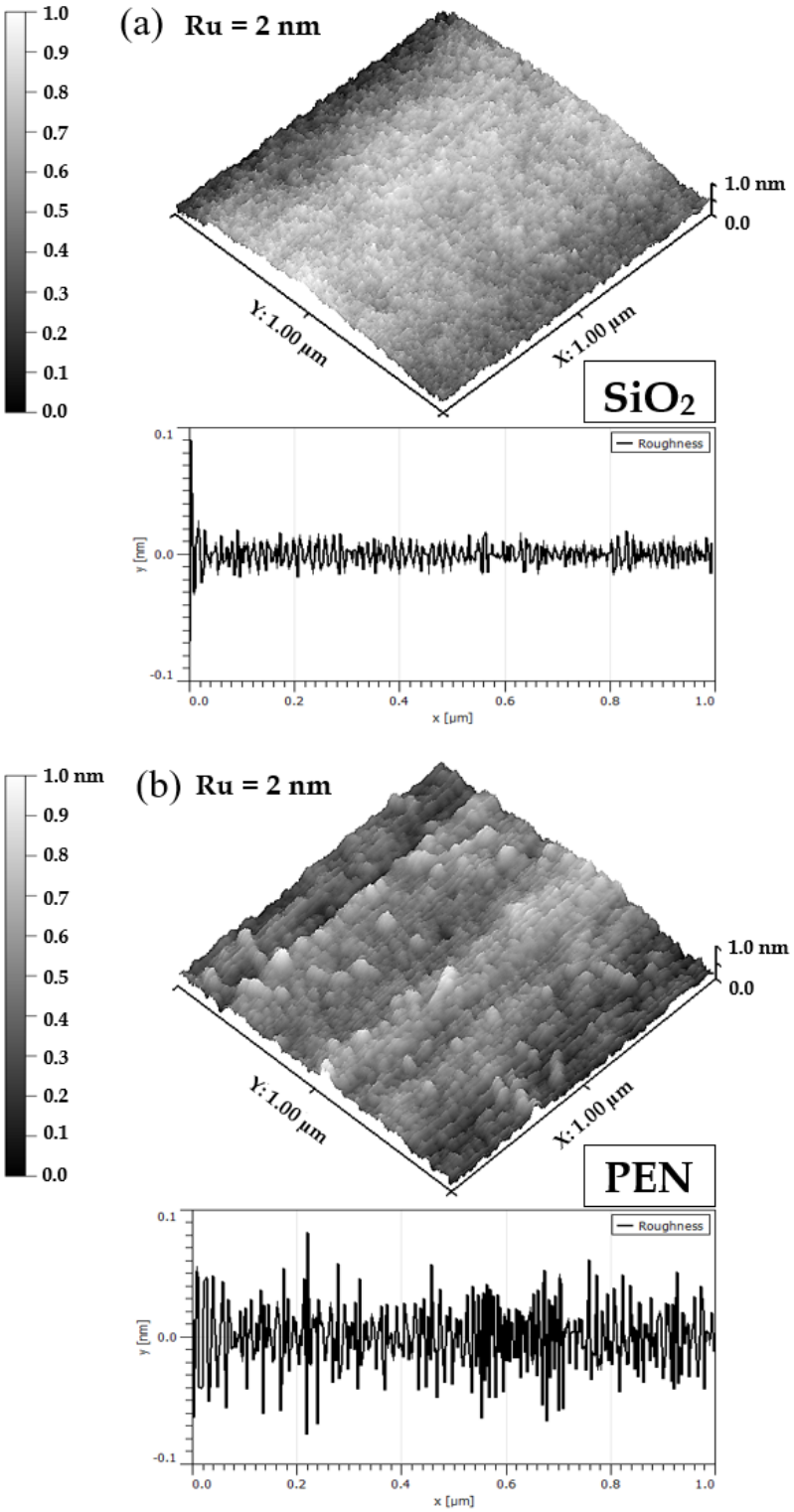

Fig. 5.11 Image illustrates the topography of 2.0 nm ruthenium grown on both (a). SiO_2 and (b). PEN substrates using atomic force microscopy machine.

observed, portraying the roughness of the material. The image space is (x,y,z) = (1 μm x 0.37 μm × 2 nm).

5.8 Summary

This chapter detailed the investigation of the structural studies by x-ray reflectivity, atomic force microscope and x-ray diffraction as well. X-ray reflectivity (XRR) gives insight into the thickness of each layer in thin films and interfaces between them. Both atomic force microscope measurements (AFM) and x-ray diffraction (XRD) techniques give more details about morphology of nano scale structure, in particular for buffer layers, in the case of using AFM, and the crystallisation of thin films for multilayer thin films for XRD.

Chapter 6

Influence of Pt buffer layer on magnetic behaviour of Pt/Co/Pt thin films on flexible substrates

6.1 Previous Work

Perpendicular anisotropy magnetic materials have an important role in the storage media of hard-disk drives [133], applications of newer spintronic concepts that involve DMI domain walls for memory applications, spin-orbit torque switching and interfacial skyrmions. For some future applications, there is much interest to move away from expensive, rigid substrates, such as silicon, to lower cost flexible polymeric substrates [134]. Such a thing is driving an interest in controlling the behaviour of magnetic multilayers on plastic substrates for device applications. It has been shown recently that the functional GMR structures with in-plane magnetisation can be fabricated on plastic substrates[135]. The spin orbit coupling that was discovered and leads to the switching exploits a spin accumulation at the Co/Pt interface, which imposes a torque on the Co magnetization[136]. Buffer layer such as Pt and Ta are often used to reduce interstitial surface roughness [137], in order to stimulate out-of-plane

layers from anti-ferromagnetic layer [138], and to release the inherent stress of magnetic films [139]. A lot of the earlier work focused on the impact of buffer layers on the magnetic properties of magnetic thin films which has been performed on rigid substrates [137]-[140]. Over the previous years, magnetic and spintronic systems are growing on flexible substrates that have gained a great deal of interest because of the exciting new applications offered by geometric surface after manufacturing [141]. Fabricating flexible spintronic devices as a priority, then a certain buffer layer needs to be introduced in order to decrease the roughness of flexible substrates, enhancing the orientation of crystal of magnetic thin films, also releasing the residual stress [92]. The rotation and vertical polarization of Pt/Co can be explained by the current in the plane caused by torque rotation, owing to the effect of the torque phenomenon [142, 143].

In this study, it has been demonstrated the out of plane voltage/current that causes magnetization switching in a perpendicularly polarized Pt/Co/Pt by assembling the heterostructure on a flexible/rigid substrate at room temperature. Studying the magnetism of Pt/Co/Pt trilayers and interfacial roughness took the great attention, because the magnetic characterization of these trilayers system relate strongly on the change of the interface composition. This change has been done using different kinds of substrates.

6.1.1 Properties of flexible material substrates

Polyethylene Naphthalate (PEN-Teonex Q65H)

PEN is a high-transparency film and it is suitable for optical and electronic applications. The treat of film is done on one side to provide improved adhesion, handling and winding properties. It contains high temperature resistance and it can be used continuously at 160 °C (320 °F). It has high mechanical strength and high-strength insulation. PEN is also considered an excellent resistance to solvents and chemical materials [144, 145].

Polyamide (PI 2611)

Polyimide film contains the perfect thermal properties of films available. The range of temperature can be used from -269 °C to 350 °C (-450 °F to 660 °F). The material properties are excellent and contains a high resistance and abrasion, solvents and high tensile strength. It is considered as an ideal insulating material, because it has a high dielectric strength for using it with high voltage. Polyimide film has a resist to radiation and ultraviolet light [145].

6.2 Introduction

This chapter includes the investigation of the structural properties and the magnetic properties of multi-layered thin-films measured by using an atomic force microscopic and both MOKE and Hall-effect measurements for the magnetic properties. It is found that the film structure and interfacial roughness of SiO_2, polyimide and PEN substrates can be influenced by the nature of the buffer layer; which is likely to be affected by the substrate. This structural influence of the substrates correlates with the structure of thin films and influences the anisotropy developed.

It is known that the Hall effect has two contributions; the first contribution is coming from the Lorentz force effect and the second anomalous contribution is coming from spin-dependent scattering. The magnetic measurements focus in this chapter on the analysis studying of magnetization that is coming from the effect of spin-dependent scattering while the Hall resistivity calculations were done through of Lorentz force effect. Hence, all the calculations was done through of using Hall effect measurements.

6.3 Experimental Work

The multi-layer Pt/Co/Pt samples were deposited on Si/SiO_2, Polyimide and PEN substrates respectively at room temperature using DC magnetron sputtering. Fig. 6.1 shows the

deposition time that was taken to grow different thickness of platinum buffer layers from 1.0 nm to 5.0 nm the growth rate was constant (linear slope).

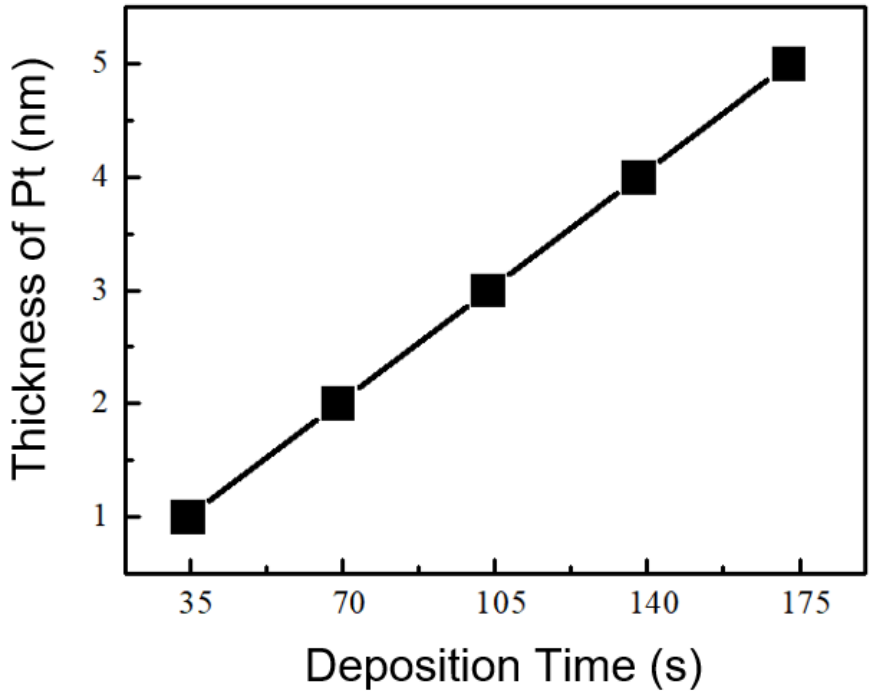

Fig. 6.1 Deposition time as a function of thickness of platinum started from 1.0 - 5.0 nm that was used for the growing buffer layer by sputtering system.

The base pressure of the sputtering system was typically 1.13 x 10^{-7} Torr. Magneto hysteresis loop measurements have been performed in a polar geometry (i.e. with field out-of-plane). The topography of the deposited samples was measured by atomic force microscopy.

6.4 Influence of Pt buffer layer on perpendicular magnetic anisotropy using rigid/flexible substrates

For fabricating rigid/flexible magnetic films, a suitable buffer layer will be necessarily to be inserted to reduce the roughness of rigid/flexible substrates and enhance the crystal orientation of magnetic films. Therefore, the buffer layers are highly important in determining

the features of rigid/flexible magnetic films, such as magnetic anisotropy and coercivity [133]. A schematic diagrams of cross masked sample structure used for Hall measurements with the different substrates is shown in Fig. 6.2.

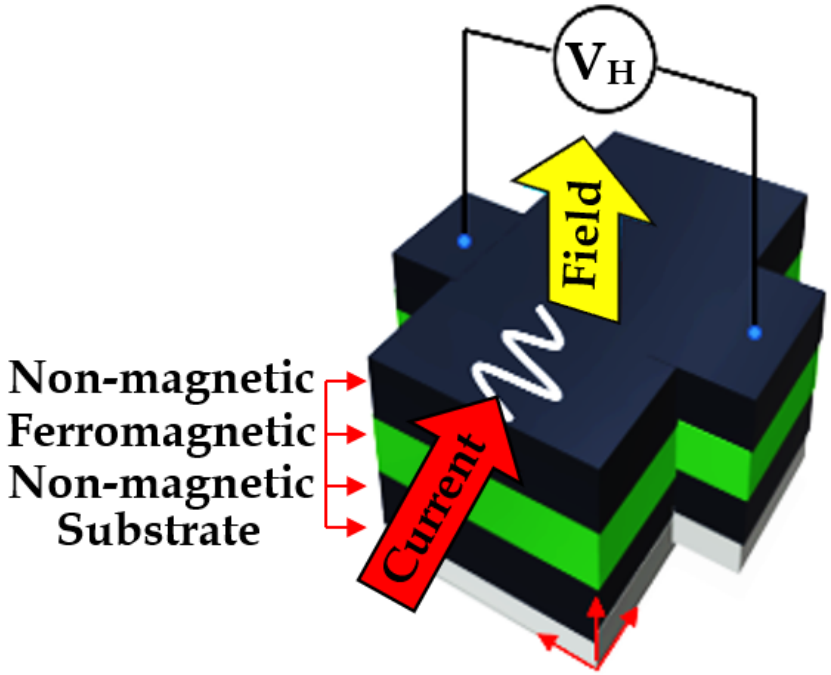

Fig. 6.2 Atomic force microscopy image of a silicon dioxide surface.

6.4.1 Influence of Pt buffer layer on perpendicular magnetic anisotropy on SiO_2 substrate

Before investigating PMA on flexible polymer substrates the developments of PMA on conventional rigid SiO_2/Si substrates is described first. The effectiveness of using the buffer layer thicknesses t_{Pt} was studied by using different thickness of Pt buffer layers t_{Pt} = 1.0 - 5.0 nm. First the surface structuring is discussed. In Fig. 6.3, the AFM micrographs shows that the Pt buffer layer can effectively reduced the roughness of magnetic film grown on silicon dioxide substrate. Fig. 6.3 shows the surface roughness morphology of silicon dioxide

without adding any platinum. Where, the rms roughness was 0.3 nm. The line signal of roughness shows smaller fluctuations.

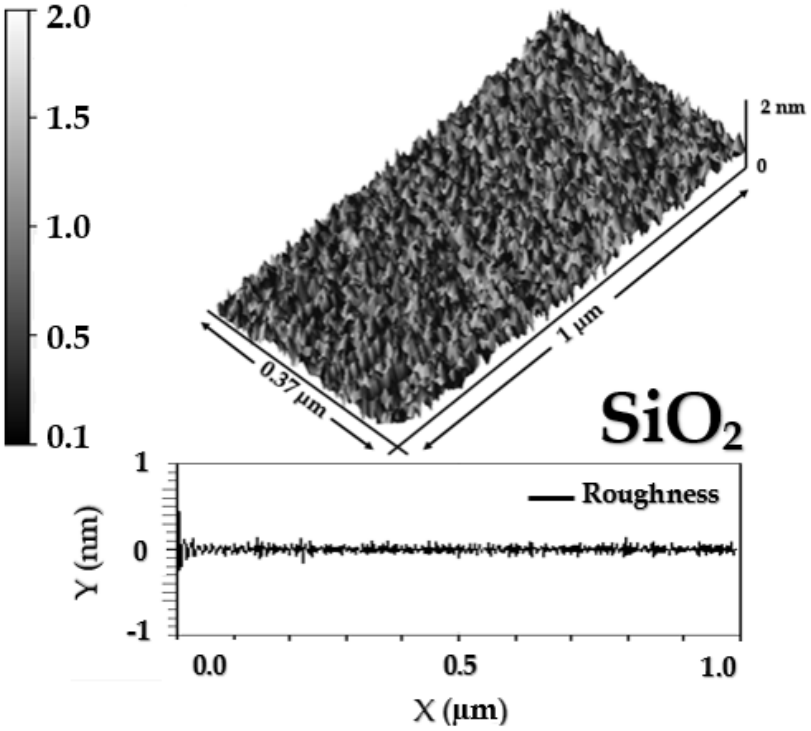

Fig. 6.3 Atomic force microscopy image of a silicon dioxide surface.

Co/Pt has a strong PMA when the Co layer is thin enough ($t_{Co} \leq 1.0$ nm), and the layer of Pt has (111) texture. In Fig. 6.4, the trend indicates that with increasing Pt buffer layer from 1.0 nm to 5.0 nm, reduced the roughness gradually, the films became smooth and the RMS roughness of the films was decreased gradually from 0.5 nm at Pt = 1.0 nm to reach a constant value 0.22 nm at Pt = 5.0 nm. Therefore, it was found that a Pt buffer layer can effectively reduced the roughness of magnetic film grown on silicon dioxide substrate and can therefore be applied to enhance the film structure. For the manufacture of magnetic film on flexible substrates, an appropriate insulating layer has often been needed to reduce the roughness of the flexible substrate that then ensure a continuous and functioning layer of magnetic materials [7–9]. Fig. 6.5 shows that the root mean square roughness reduced with increasing Pt thickness from 1 nm to 5 nm.

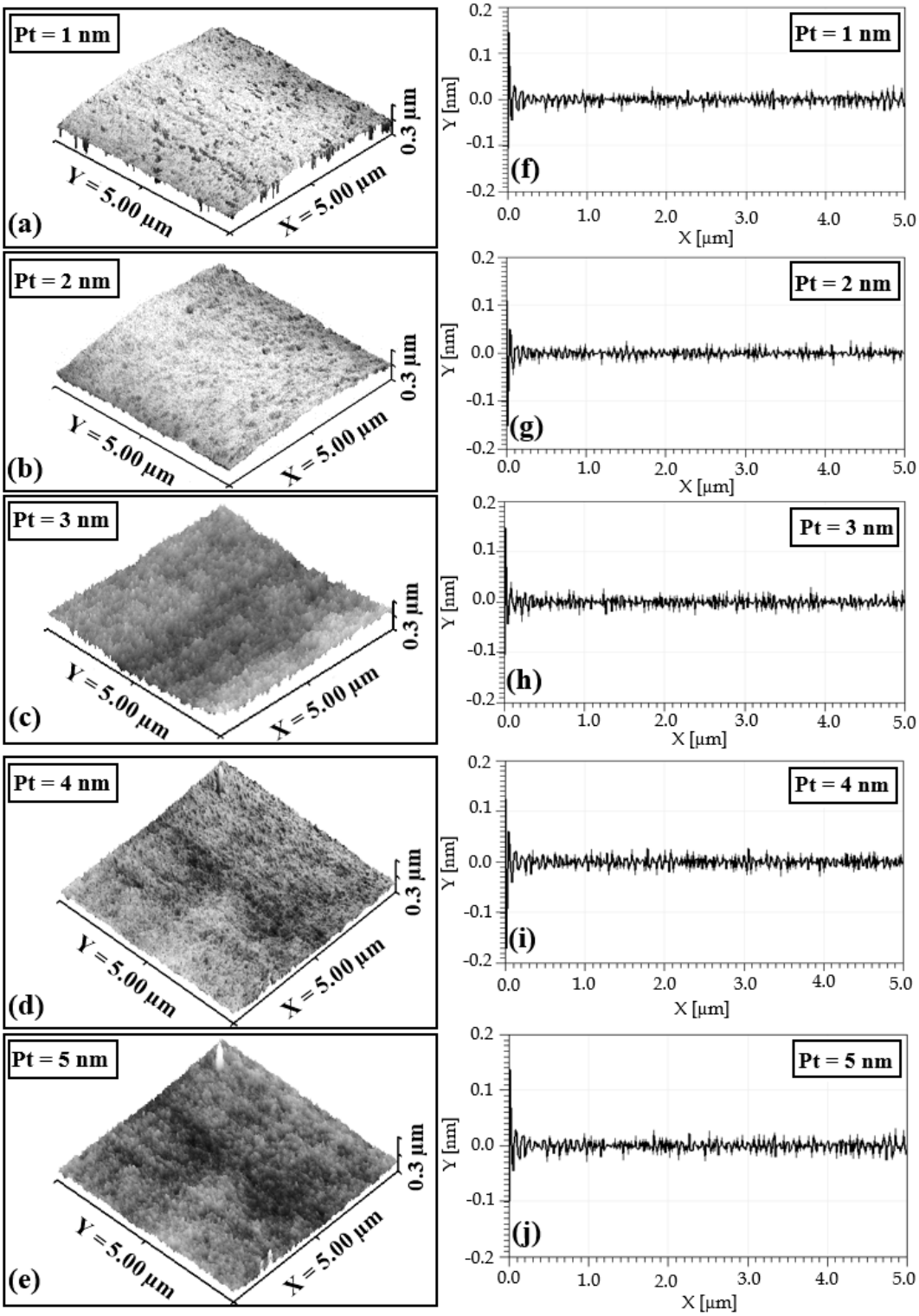

Fig. 6.4 Graphs showing the topography of the Pt 1.0 - 5.0 nm buffer layers that is grown on a SiO_2 substrate.

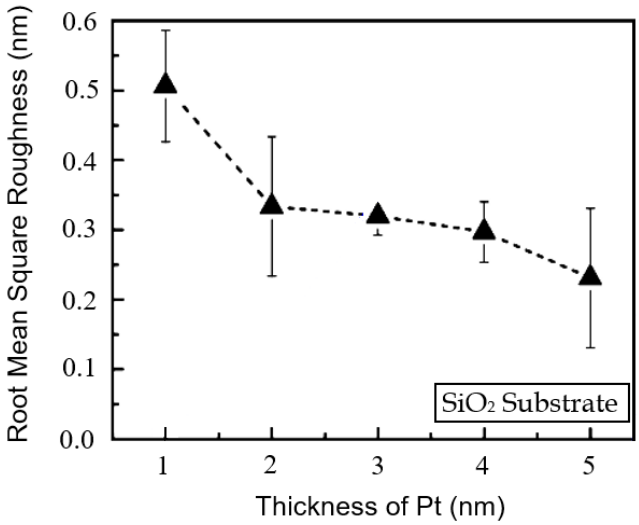

Fig. 6.5 Graph shows the trend of roughness as a function of increasing Pt buffer layer thickness for t_{Pt} film sputtered on SiO_2 substrate.

6.4.2 Influence of Pt buffer layer on out-of-plane anisotropy on Pt/Co on flexible Polyethylene Naphthalate substrate

Fig. 6.6 shows the surface topography for a PEN substrate.

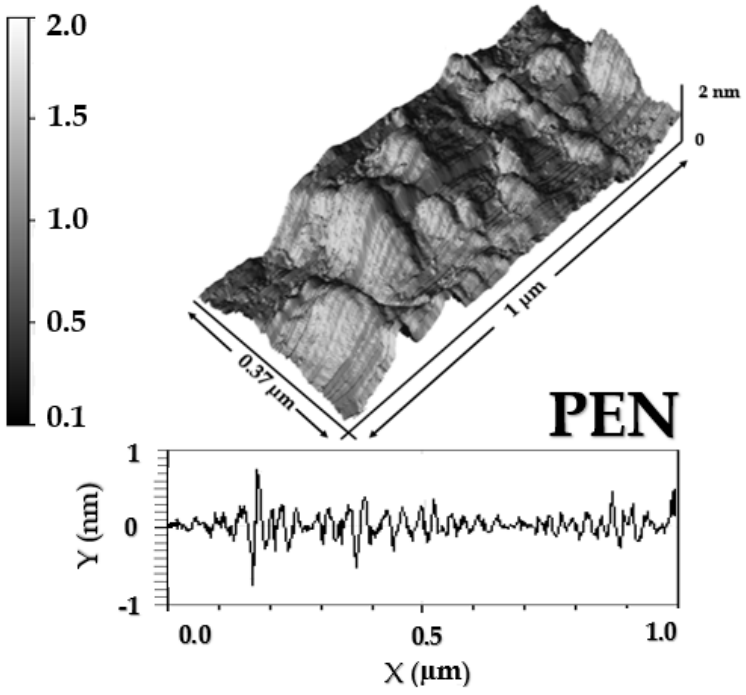

Fig. 6.6 Atomic force microscopy image of a Polyethylene Naphthalate substrate.

The root-mean-square RMS roughness was 7.0 nm, which was obtained from a scan area of $1 \times 0.37\ \mu m^2$ by atomic force microscope. In other work [146] it was found that PEN had a value of roughness RMS= 6.3 nm, which was closed to the roughness that was found in this studying.

Fig. 6.7 (a,b,c,d,e) shows AFM 3D height images for Pt buffer layers, deposited on PEN substrate using identical process conditions, showing clear variations in roughness details. The averaging of surface roughness values (RMS) on a $5 \times 5\ \mu m^2$ area are significantly decreased from 4.0 nm at t_{Pt} = 1.0 nm to 2.5 nm at t_{Pt} = 5.0 nm with increase in deposition time as it shown in Fig. 6.1. It is clear that as for rougher films, the distinguished of smaller grains could not easily seen by AFM; basically, they are being hidden because the surface roughness scale is far bigger than the size of these features. In Fig. 6.7 (f,g,h,i,j) more exhaustive 2D roughness profiles shows that deposition time period for Pt buffer layer which was grown on PEN substrate leads to much larger peak heights, with increasing Pt thickness (where, cluster formations represent higher root mean square roughness).

In Fig. 6.7, the AFM micrographs indicates that the Pt buffer layer can effectively reduce the roughness of magnetic film grown on flexible plastic substrates and can therefore be applied to improve the film structure in the fabrication of flexible magnetoelectric devices. After growing the Pt layer on PEN started from 1.0 - 4.0 nm, the films became smooth and the RMS roughness of the films was decreased slowly to a constant value of 1.5 nm at Pt = 4.0 nm as shown in Fig. 6.8. With further increasing of the Pt thickness until 5.0 nm, the roughness was increased. Inserting a buffer layer of a Pt between Co and PEN substrate can effectively improve the growth condition and reduced the roughness of layers. For the manufacture of magnetic film on flexible substrates, an appropriate insulating layer has often been needed to reduce the roughness of the flexible substrate that then ensure a continuous and functioning layer of magnetic materials [7–9]. The growth mechanism that has been

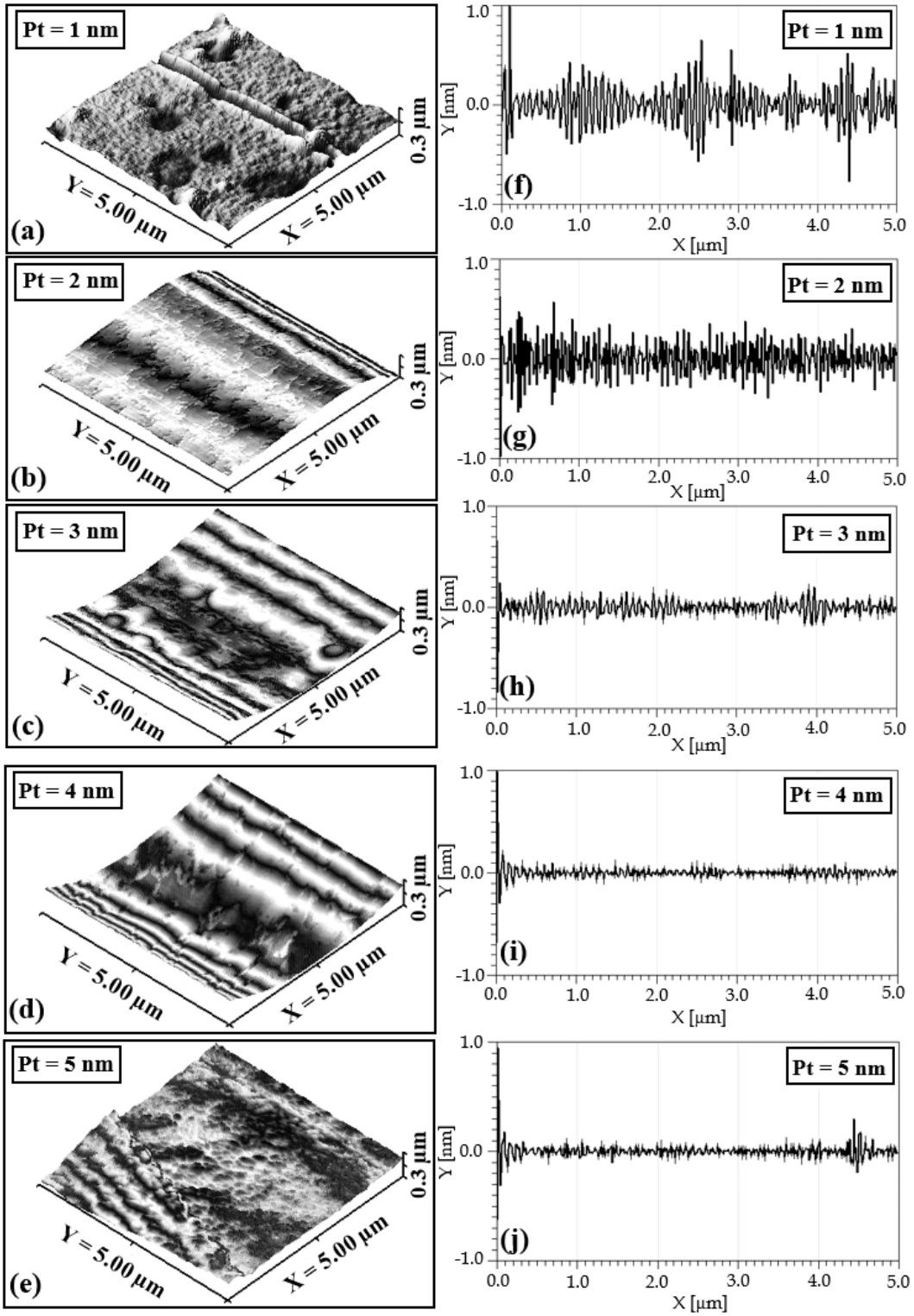

Fig. 6.7 Graphs showing the topography of the Pt 1.0 - 5.0 nm buffer layers that is grown on a polyethylene naphthalate substrate.

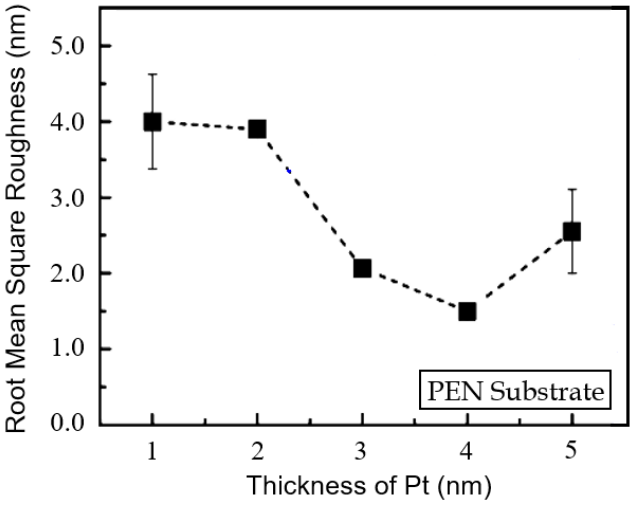

Fig. 6.8 Graph shows the trend of roughness as a function of increasing Pt buffer layer thickness for t_{Pt} film sputtered on a polyethylene naphthalate.

occurred by deposition Pt buffer layer on PEN substrate is Stranski-Krastanov growth mode.

Also, the increasing of roughness at Pt = 5.0 nm is due to the higher interface energy.

6.4.3 Influence of Pt buffer layer grown on polyimide substrate

Atomic force microscopy imaging of the polyimide substrate surface is shown in Fig. 6.9.

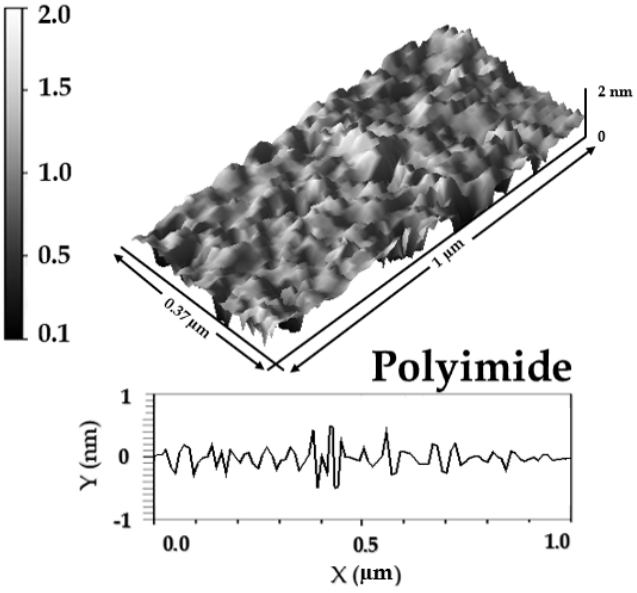

Fig. 6.9 Atomic force microscopy image of a polyimide substrate surface.

The root-mean-square RMS roughness was 1.5 nm, which was obtained from a scan area of $1 \times 0.37\ \mu m^2$ by atomic force microscope. Moreover, as shown in Fig. 6.10 (a,b,c,d,e), the roughness was decreased until reaching to t_{Pt} = 4.0 nm then it was increased at t_{Pt} = 5.0 nm ,where the roughness was increased to about 0.6 nm. Also, a thin Pt capping layer was used to prevent oxidation.

Fig. 6.10 (f,g,h,i,j) shows a 2D AFM image of a photoresist line. This images were taken by scanning in the direction over the line using Gwyddion software. This images show informations with high resolution for surfaces. Higher roughness and protrusion from surface were shown very visible by of the photoresist line at lower Pt buffer thicknesses, but the surfaces at higher Pt buffer thicknesses are much smoother.

The profiles of single line on the top surface could be extracted from the higher resolution 3D AFM images. Where, Fig. 6.10 shows the profiles of single line at various surface of the photoresist. These profiles line also clearly display that the surfaces of lower Pt buffer thickness are much rougher than the surfaces of greater Pt buffer thickness. Taken together, these analyses can elucidate the differences in the structural properties of the Pt buffer layers films. Since inserting a buffer layer of a Pt between Co and polyimide substrate can effectively improve the growth condition and reduced the roughness of layers. After growing the Pt layer on polyimide started from 1.0 - 4.0 nm, the films became smooth and the RMS roughness of the films was decreased slowly to a constant value of 0.29 nm at Pt = 4.0 nm as shown in Fig. 6.11. With further increasing of the Pt thickness until 5.0 nm, the roughness was increased. Inserting a buffer layer of a Pt between Co and polyimide substrate can effectively improve the growth condition and reduced the roughness of layers. It seems that in both cases PEN and polyimide substrates at Pt = 5.0 nm the roughness increased, and this may be related to increase in the interface energy due to stranski-krastanove growth mode.

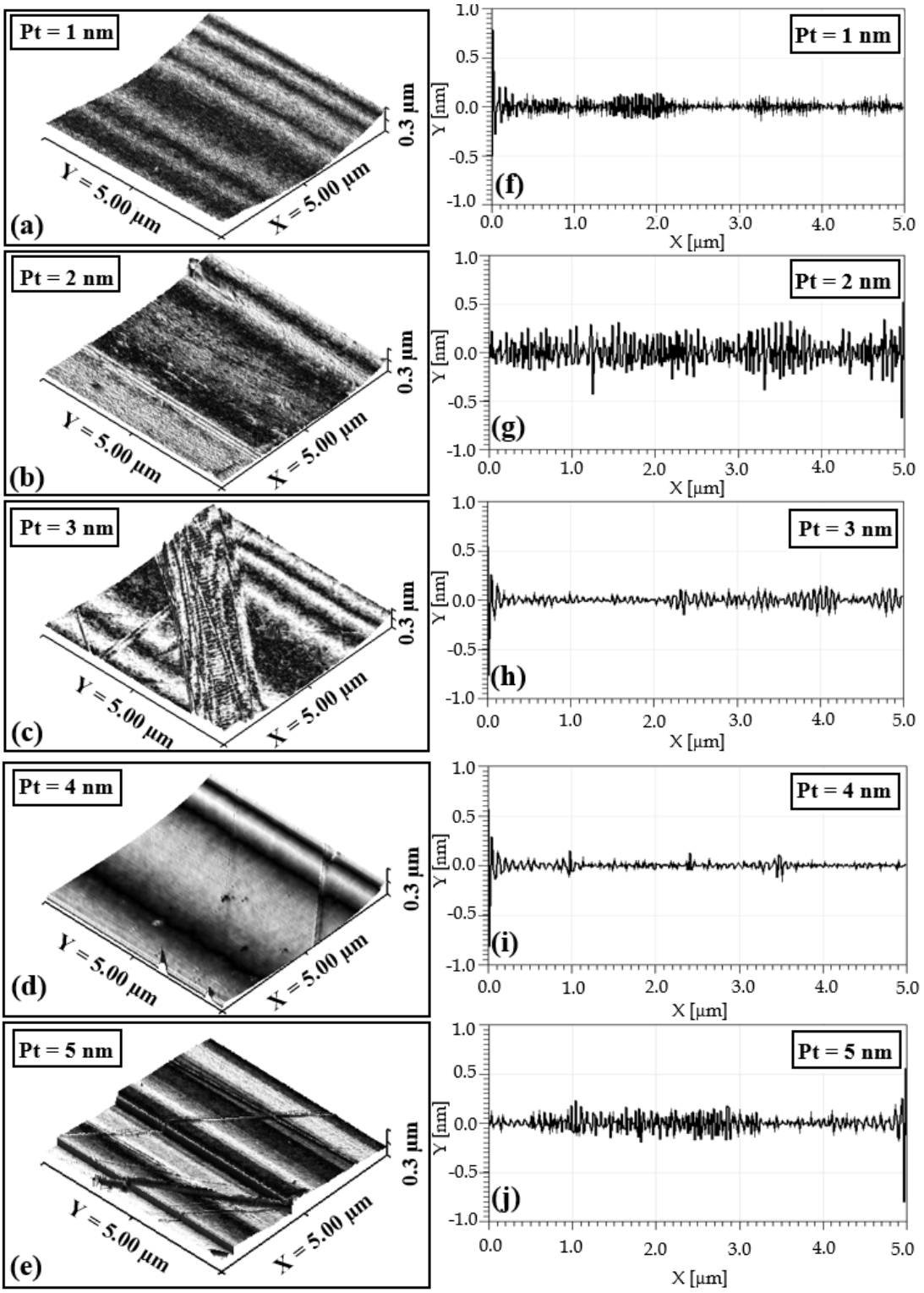

Fig. 6.10 Graphs showing the topography of the Pt (1.0 - 5.0) nm buffer layers that is grown on a polyimide substrate.

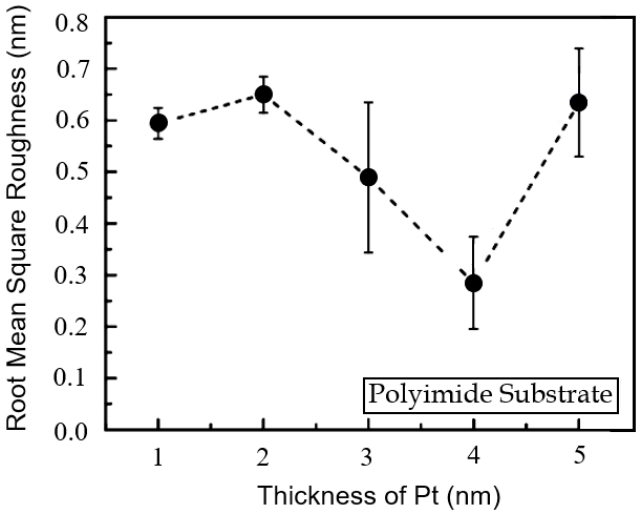

Fig. 6.11 Graph shows the trend of roughness as a function of increasing Pt buffer layer thickness for t_{Pt} film sputtered on a polyimide substrate.

6.5 Coercivity of Pt/Co/Pt trilayers thin-films on rigid and flexible substrates

For realizing a higher recording density based on having high coercivity, high PMA and high remenant squareness, Pt/Co multilayer thin-films deposited on rigid/flexible substrates were shown in this section and comparing between them.

6.5.1 Coercivity of Pt/Co/Pt trilayer thin-films on SiO_2 substrate

Fig. 6.12 Hall effect hysteresis loops for different Pt thicknesses from 1.0 nm to 5.0 nm with a fixed Co layer thickness of 0.5 nm. In Fig. 6.13, the values of coercive field were increased with the increment of Pt thickness. An increase of the coercive field was associated with an improvement in the fcc (111) texture [147] because of the reduction in the RMS roughness. XRD diffraction measurements in chapter 8 confirmed the enhancement in the fcc (111) texture.

The coercivity was increased with increase in Pt thickness. It can be concluded that the increase of the perpendicular magnetic anisotropy, indicated by the increasing coercivity,

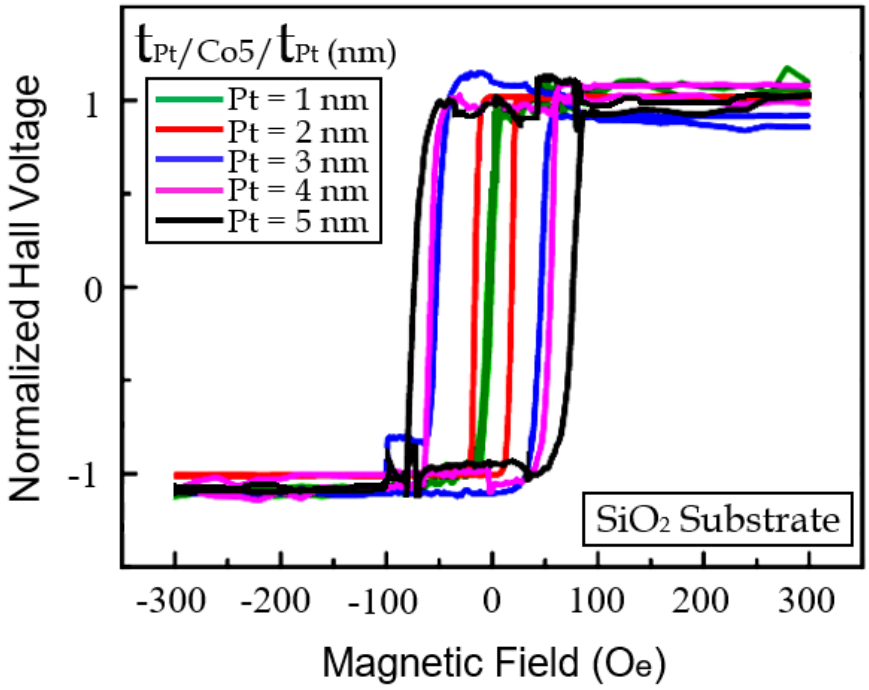

Fig. 6.12 Hysteresis loops of t_{Pt}/Co0.5/t_{Pt} nm using different thickness of platinum grown on SiO_2 substrate.

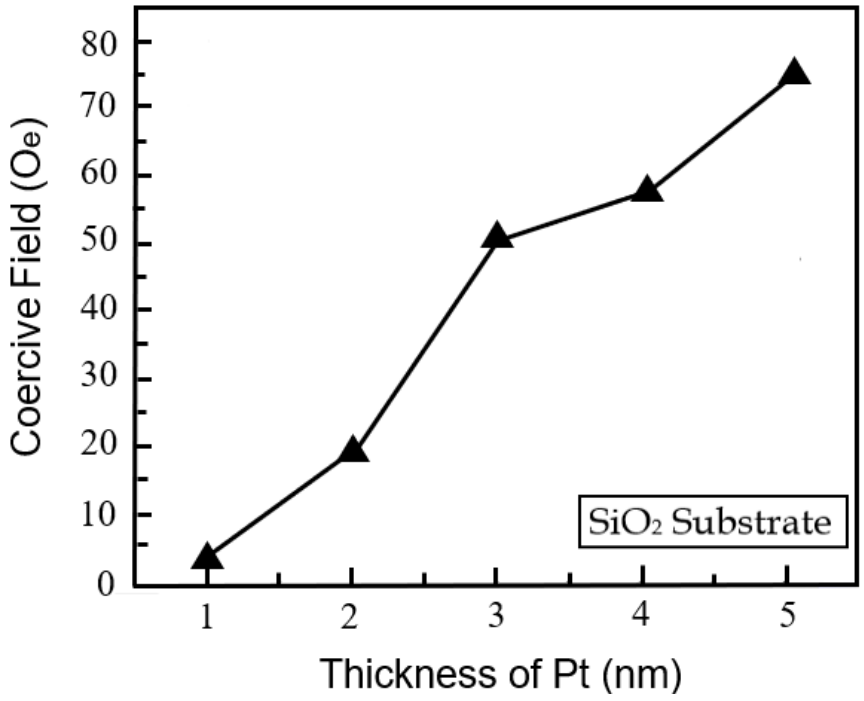

Fig. 6.13 Coercive field of t_{Pt}/Co0.5/t_{Pt} nm as a function of platinum thickness grown on SiO_2 substrate. The error bar is very small.

with the increasing Pt thickness was related to the modification of the Pt surface roughness. It has already been observed in the case of Co/Pt (upper) multilayers grown on a Pt buffer [148, 149] that increasing the buffer thickness increases the multilayer anisotropy and coercive field; due to the smoother top Pt surface of larger buffer thicknesses coming from the improvement of the (111) texture and the larger grain size [147].

6.5.2 Coercivity of Pt/Co/Pt trilayer thin-films on Polyimide substrate

Fig. 6.14 shows the hysteresis loops was increased gradually with the increase of Pt thickness.

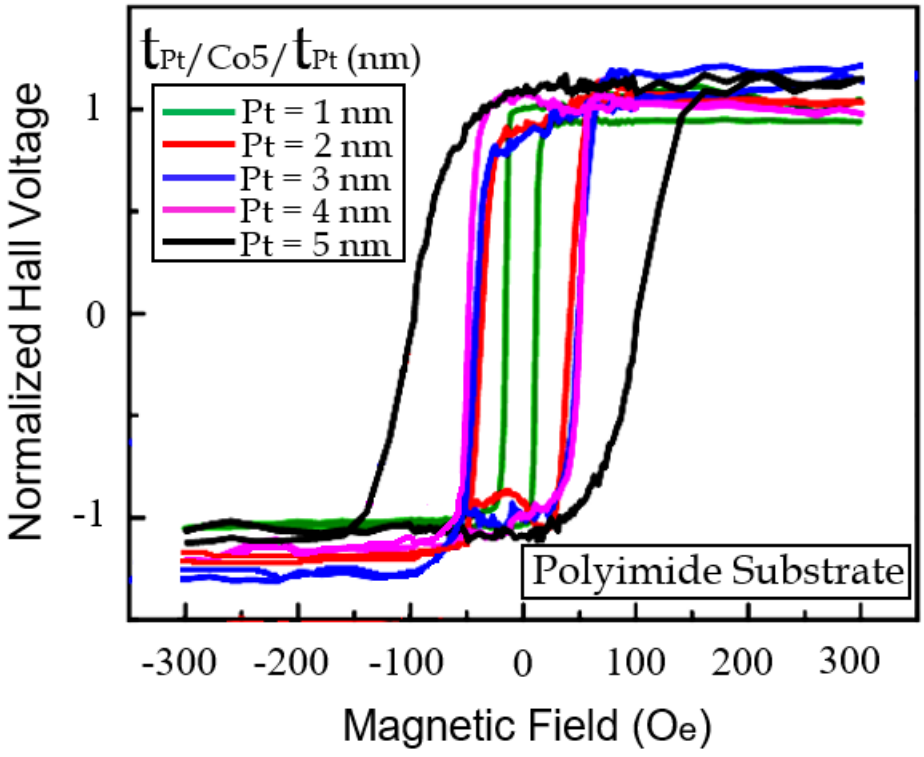

Fig. 6.14 Hysteresis loops of t_{Pt}/Co 0.5/t_{Pt} nm using different thickness of platinum grown on polyimide substrate.

In the case of polyimide, it was shown here that the coercive field increase gradually with increase platinum thickness until t_{Pt} = 5.0 nm as it shown in Fig. 6.15. This was associated with the enhancement of the fcc texture [147].

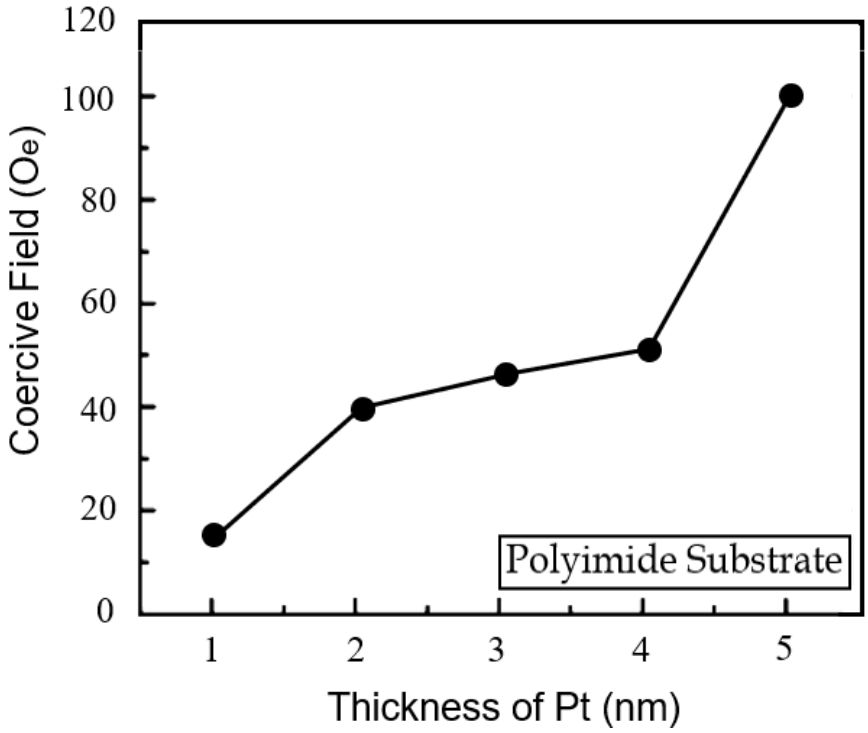

Fig. 6.15 Coercive field of t_{Pt}/Co 0.5/t_{Pt} nm as a function of platinum thickness grown on polyimide substrate. The error bar is very small.

6.5.3 Coercivity of Pt/Co/Pt trilayer thin-films on Polyethylene Naphthalate substrate

Fig. 6.16 shows the hysteresis loop for Pt/Co/Pt films on PEN with increasing thicknesses of the Pt buffer layer from 1.0 nm to 5.0 nm. In the case of PEN, it was shown here that the coercive field increase gradually with increase platinum thickness until t_{Pt} = 4.0 nm as it shown in Fig. 6.17. This was associated with the enhancement of the fcc texture [147]. Fig. 6.18 illustrates the Pt/Co/Pt trilayer structures; which was consisted of a fixed ferromagnetic Co layer 0.5 nm and a varying Pt layer 1.0 - 5.0 nm using different kinds of substrate, rigid SiO_2, flexible Polyethylene Naphthalate and rigid Polyimide. The Pt/Co/Pt system contains an ultrathin Co film, with Pt used as a buffer layer to motivate (111) texture and enhance the perpendicular magnetic anisotropy (PMA) while the usage of a Pt capping layer was to prevent oxidation [150]. In general, magnetic films on rough surfaces can also exhibit a

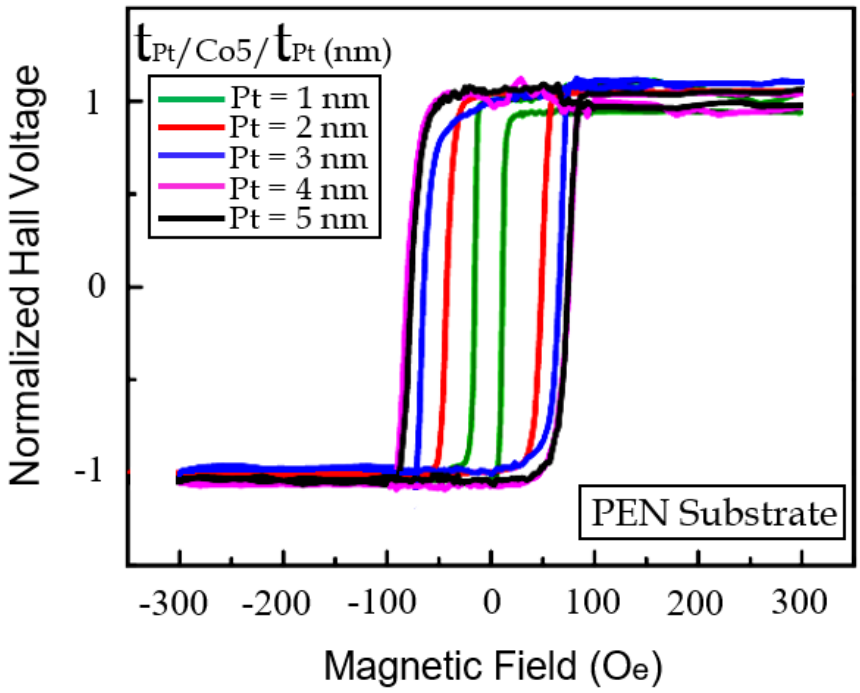

Fig. 6.16 Hysteresis loops of t_{Pt}/Co 0.5/t_{Pt} nm using different thickness of platinum grown on PEN substrate.

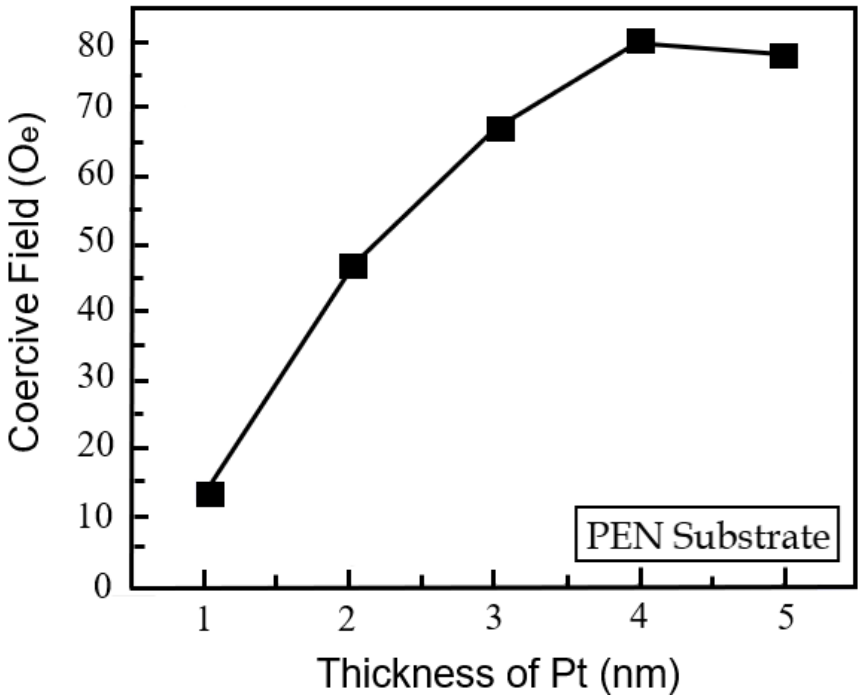

Fig. 6.17 Coercive field of t_{Pt}/Co 0.5/t_{Pt} nm as a function of platinum thickness grown on PEN substrate. The error bar is very small.

higher H_c than smooth films. This was attributed to the pinning of the magnetic domains. But since applications such as micro-structuring or hard disks need a smooth surface (danger of head crashes or a too large read/write distance), an increased roughness is not suitable.

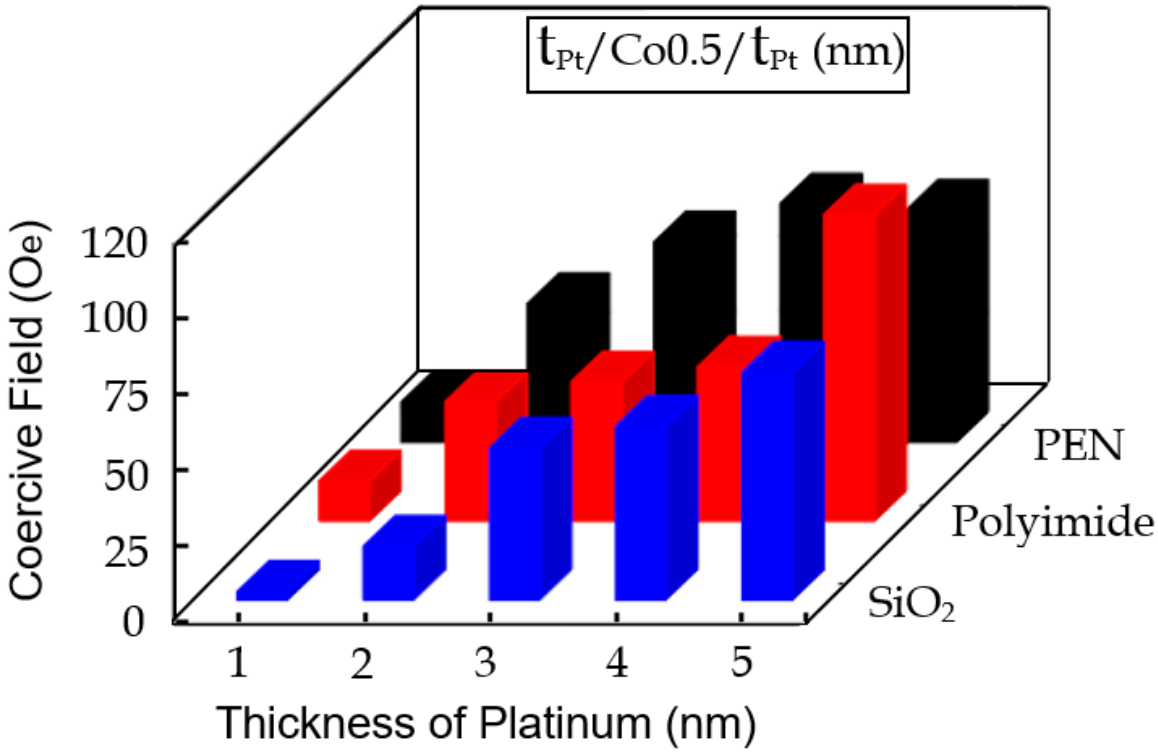

Fig. 6.18 Graph shows the coercive field values of t_{Pt} 1.0 - 5.0/Co 0.5/t_{Pt} 1.0 - 5.0 nm trilayers thin-films grown on different substrates.

6.6 Correlation between roughness and coercivity using rigid/ flexible substrates

This section is focused on the important role of the substrate in supporting the development Perpendicular Magnetic Anisotropy (PMA) and coercive field shape in the Pt/Co/Pt system for the application of these materials in flexible spintronic applications. The film structure and interfacial roughness are expected to play a role as they can influence structure of the Pt

buffer layer; which in turn will affect the interface and growth of the Co layer. Silicon chips are used extensively in the manufacture of electronic devices. However, the silicon chips are rigid, while some applications are growing that require electronics that are soft, elastic and bendable. Technology for assembling the electronic circuits and devices on flexible substrates depends on the flexible electronics that are much less expensive, more compact and lighter, when compared to the traditional electronic devices although component density and device speeds are much lower.

In Fig. 6.19 (a), SiO_2 case, it was shown that the coercive field was increased with decreasing of root mean square roughness. While, in Fig. 6.19 (b), PEN case, it was shown that the coercive also increased with decreasing of root mean square roughness from 1.0 nm to 4.0 nm Pt thickness, then at 5.0 nm there was an increase in roughness which was associated with decrease coercive field a little bit from 80 Oe to 79 Oe. Finally, in Fig. 6.19 (c), polyimide case, the coercive field increase with increasing of root mean square roughness from 1.0 nm to 2.0 nm Pt buffer layer. Finally at 5.0 nm Pt, the coercive field was increased and it was associated with increase roughness. It seems that in both cases PEN and polyimide substrates at Pt = 5.0 nm the roughness increased and this may be related to increase in the interface energy due to stranski-krastanove growth mode. Where, it was very clear that when the thickness of platinum at 5.0 nm, the differences between the root mean square roughness [RMS] of polyethylene naphthalate and polyimide were 2.5 nm and 0.65 nm respectively.

It was found that there is an inverse correlation between root mean square roughness and coercive field i.e, [R_q proportional to $1/H_C$]. Therefore, according to these results, it was found that there was a highly correlated between increasing of coercivity and decreasing of roughness in a lot of Pt buffer layer thickness and this relationship between increasing of coercive field and decreasing of roughness as it has been shown in this work which was similar to the study of Wang et. al. [151].

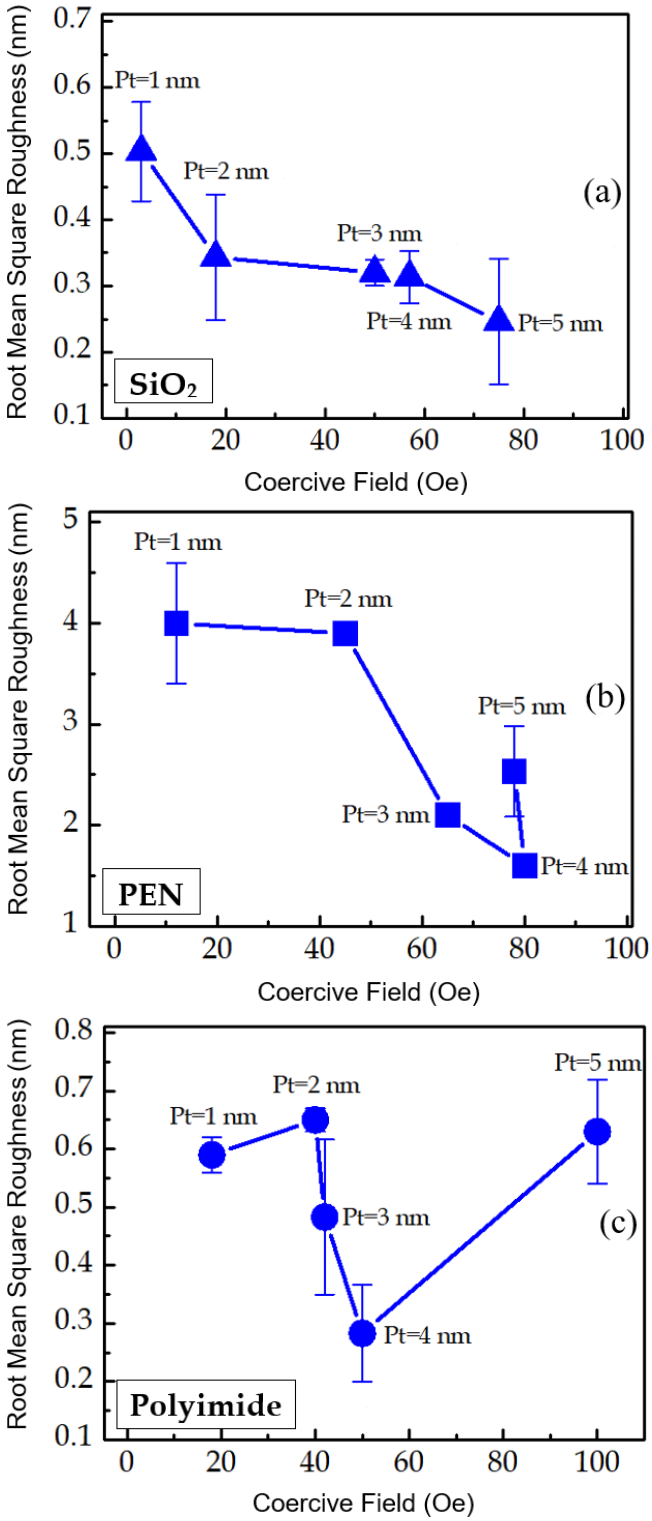

Fig. 6.19 (a,b and c) Graphs show the root mean square values as a function of coercive field for various Pt buffer layers grown on SiO_2, PEN and polyimide substrates.

6.7 Magnetic reversal behaviour in Pt/Co multilayers using rigid/flexible substrates

Studying of the influence of ferromagnetic Co layer thickness separated by non-magnetic layer on the magnetic properties of multilayers will be explained in this section by using different kinds of substrates. The combination of magnetic layers with different switching field was investigated. The [Co/Pt]n ML has strong perpendicular anisotropy when the Co thickness layer is thin enough and the layers of Pt have the (111) texture. As it is considered as an important member of the magnetic systems with perpendicular magnetic anisotropy, it has the applications in recording media with higher-density perpendicular magnetic storage. The expection of the presence of AF coupling across the Pt spacer had been shown theoretically [152], comprehensive studies on [Co/Pt]n multilayers with perpendicular magnetic anisotropy had just detected the FM interlayer coupling [153–155]. Magnetic tunnel junctions that used perpendicular magnetic anisotropy have highly interested because of their potential for higher storage densities with higher capacity magnetic memory applications. Fig. 6.20 shows a schematic diagram of multilayer thin-films grown on different substrates.

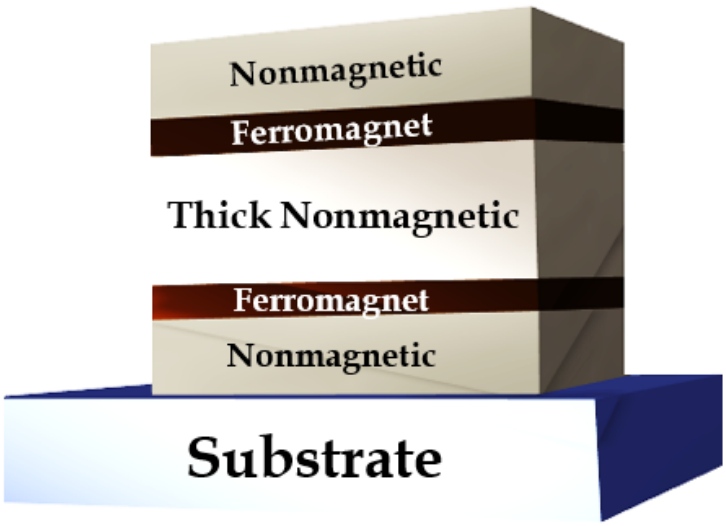

Fig. 6.20 Graph shows configuration of multilayer thin-films grown on different substrates.

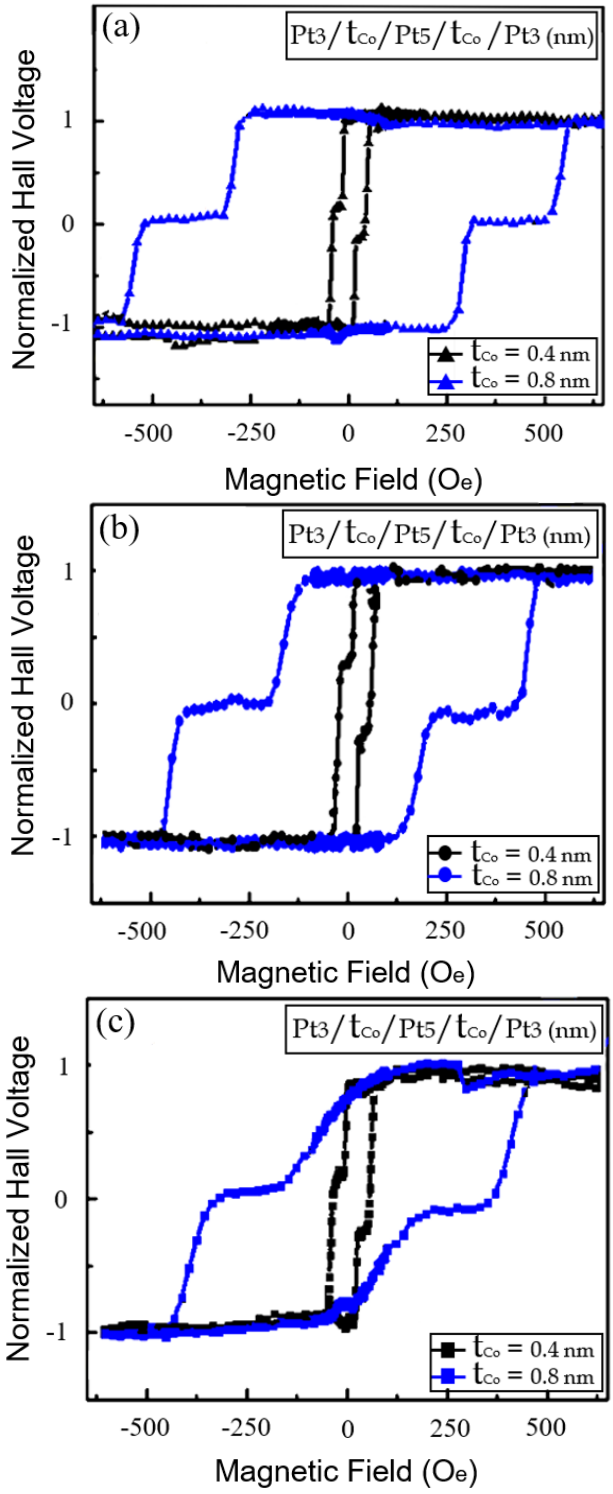

Fig. 6.21 (a,b and c) Graphs show two steps of hysteresis loops using different thickness of cobalt 0.4 nm and 0.8 nm respectively grown on (a). SiO_2, (b). polyimide, and (c). PEN substrate.

Fig. 6.21 shows the Hall measurements of multi-layered sample with using different cobalt thickness 0.4 nm and 0.8 nm. In Fig. 6.21 (a,b and c), in case of black colour of hysteresis loop [t_{Co}=0.4 nm] using SiO_2 substrate, the hysteresis loops alternate between stepped loop. It was shown that in case of using SiO_2 substrate the smaller density of nucleation sites that were appearing on hysteresis loop in comparison with polyimide and PEN substrates.

In Fig. 6.21 (a,b and c), in case of blue colour of hysteresis loop [t_{Co}=0.8 nm] using SiO_2 substrate, the hysteresis loops alternate between stepped loop. It was shown that in case of using SiO_2 substrate the smaller density of nucleation sites that were appearing on hysteresis loop in comparison with polyimide and PEN substrates. In PEN substrate, higher nucleation sites were seen in the blue hysteresis loop; which was correlated with $M_r/M_s < 1$. Also, it was very clear that the reaching of saturation magnetization in case of using SiO_2 substrate was faster than polyimide and PEN as it shown in Fig. 6.21 (c). Fig. 6.21 (a,b and c) shows that with increasing cobalt thickness from 0.4 nm [black loops; which contains two steps of loops] to 0.8 nm [blue loops; which contains two steps of loops] the areas enclosed by the hysteresis loops were increased. The Hall hysteresis loop showed an ideal sample, which was a perfectly symmetric square of homogeneous material at a constant (room temperature). Referring to Fig. 6.21; it was shown the hysteresis loops, as a function of increasing the thickness of the cobalt between t_{Co} = 0.4 nm to t_{Co} = 0.8 nm. Both films show a significant increase in the width of area enclosed by the hysteresis loop for 0.8 nm. Also, the shape of hysteresis loops was not very sharp squareness at t_{Co} = 0.8 nm. This might be happened due to the large value of root mean square roughness of polyethylene naphthalate at t_{Pt} = 3.0 nm and 5.0 nm respectively.

In the case of using a polyimide, Fig. 6.21 (b) illustrates that the increasing in the thickness of cobalt from 0.4 nm to 0.8 nm was resulted in an increase in the coercive field. Also, the shape of hysteresis loops was shown to be more improved than in case of using

PEN. This might be happened due to the small value of root mean square roughness [RMS] of PEN at t_{Pt} = 3.0 and 5.0 nm respectively.

6.8 Comparison of the influence of the Pt buffer layer on magnetization behaviour of Pt/Co/Pt on flexible and rigid substrates

Studying the influence of thicker and thinner Pt buffer layer thicknesses on improvement magnetization were focused in this section. Samples with varying thickness of the Pt buffer (15.0 and 5.0) nm layers, the top Pt layers (3.0 and 5.0) nm and varying thickness of cobalt (0.3-0.7) nm were deposited on SiO_2, Polyimide and PEN substrates by sputtering system.

In the measurements, the highest maximum coercive field reached for Pt15.0 nm buffer layer case was about 1000 Oe. While, the highest maximum coercive field reached for Pt5.0 nm buffer layer case highest 300 Oe. Magneto Optical Kerr Effect measurements of the films show hysteresis loops with comparable coercive fields and saturation fields for the in-plane and perpendicularly magnetized films. With increasing thickness of the Pt buffer layer, the magnetization and the squareness of the Pt/Co/Pt trilayer thin-films significantly change as shown in Fig. 6.22 (a-e), (f-j) for cases when t_{Pt} = 5 nm and 15 nm. The results show that the coercive field increased with increasing of cobalt thickness from 0.3 nm to 0.7 nm. The shape of hysteresis loops is also very square, indicating sharp switching and approximately full remanence.

Fig. 6.23 shows the values of coercive field at 5.0 nm and 15.0 nm platinum thickness. For t_{Co} = 0.3 nm to 0.7 nm the coercivity increased with increasing cobalt thickness. In Fig. 6.22 (j) at t_{Co} = 0.7 nm the shape of hysteresis loop was not full square. But, it was very obvious that at t_{Pt} = 15 nm, the values of coercive field was higher than in the case when the platinum thickness was 5.0 nm. Examples of hysteresis loops are shown in Fig.

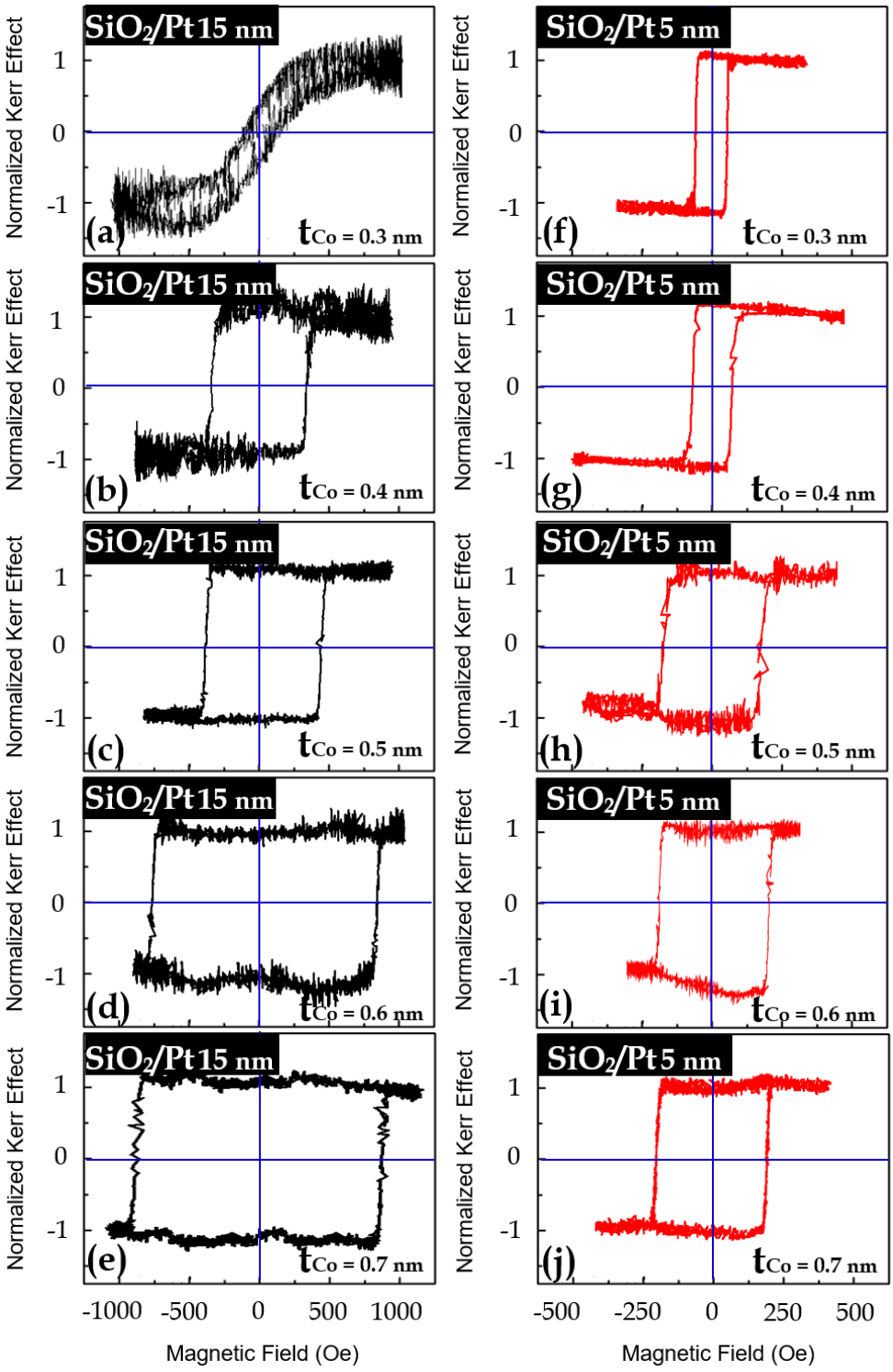

Fig. 6.22 Out-of-plane polar MOKE hysteresis loops for Pt/Co/Pt films with different thicknesses of Pt buffer layer of 15.0 nm and 5.0 nm grown on silicon dioxide substrates. The Pt top layer was 3.0 and 5.0 nm.

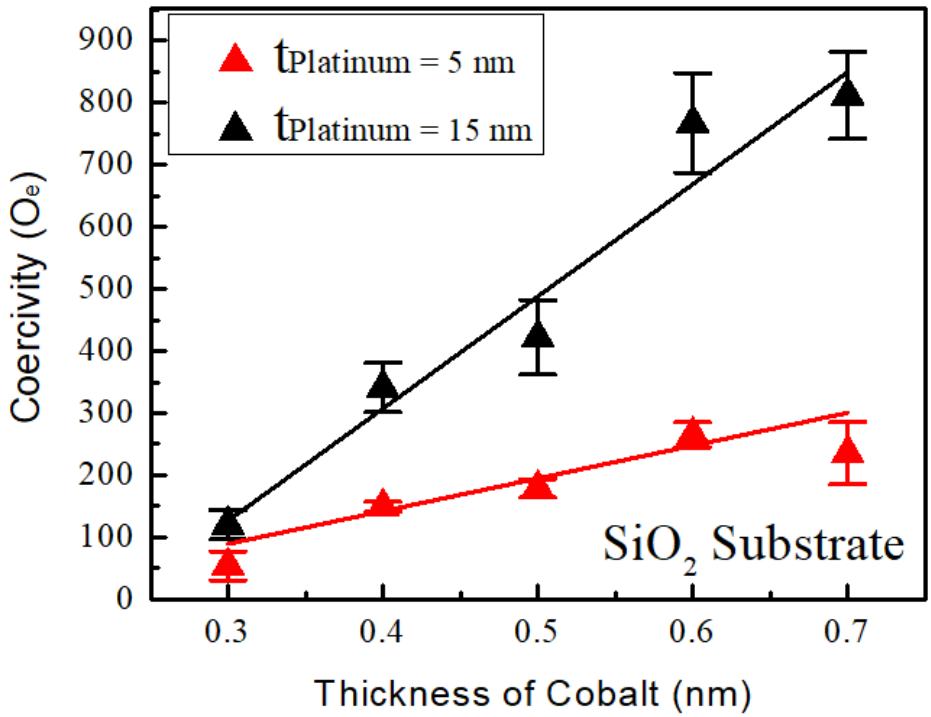

Fig. 6.23 Comparison between different values of Pt buffer layers on coercive field as a function of Co thickness. The red and black lines are linear fits.

6.24 (a-e), (f-j) for films on polyimide substrates with t_{Pt} = 15.0 nm and 5.0 nm respectively. The variation of the coercive field as a function of Co thickness is shown in Fig. 6.25. The coercivity increased with increasing cobalt thickness from 0.3 nm to 0.7 nm. However, the larger values of coercivity were obtained for t_{Pt} = 15.0 nm.

Fig. 6.26 (a-e) shows the hysteresis behaviour and the (f-j) values of coercive field are shown in Fig. 6.27 as a function of Co thickness for two Pt buffer layer thickness using PEN substrate. The coercivity increased with increasing cobalt thickness from 0.3 nm to 0.7 nm. In Fig. 6.26 (j) at t_{Co} = 0.7 nm the shape of hysteresis loop was not square. For all cases using SiO_2, polyimide and PEN, the coercivity values at t_{Pt} = 15.0 nm was higher than the coercivity values at t_{Pt} = 5.0 nm. The increment of coercive field has been shown in Fig. 6.23, 6.25 and 6.27. In Fig. 6.27, the coercivity increased with increasing cobalt thickness from 0.3 nm to 0.7 nm. However, the larger values of coercivity were obtained for t_{Pt} = 15.0 nm.

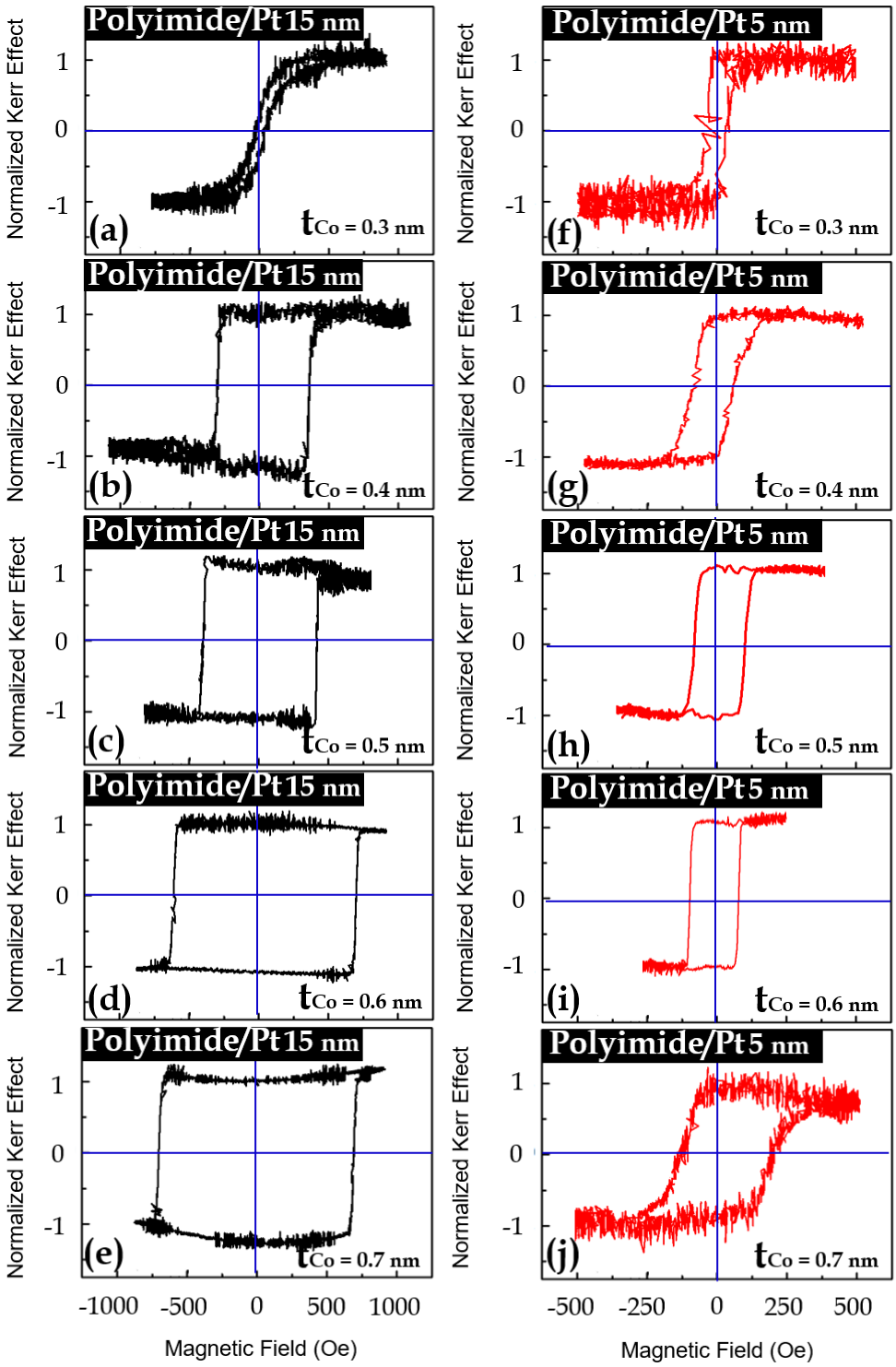

Fig. 6.24 Out-of-plane polar MOKE hysteresis loops for Pt/Co/Pt films with different thicknesses of Pt buffer layer of 15.0 nm and 5.0 nm grown on a polyimide substrate. The Pt top layer was 3.0 and 5.0 nm.

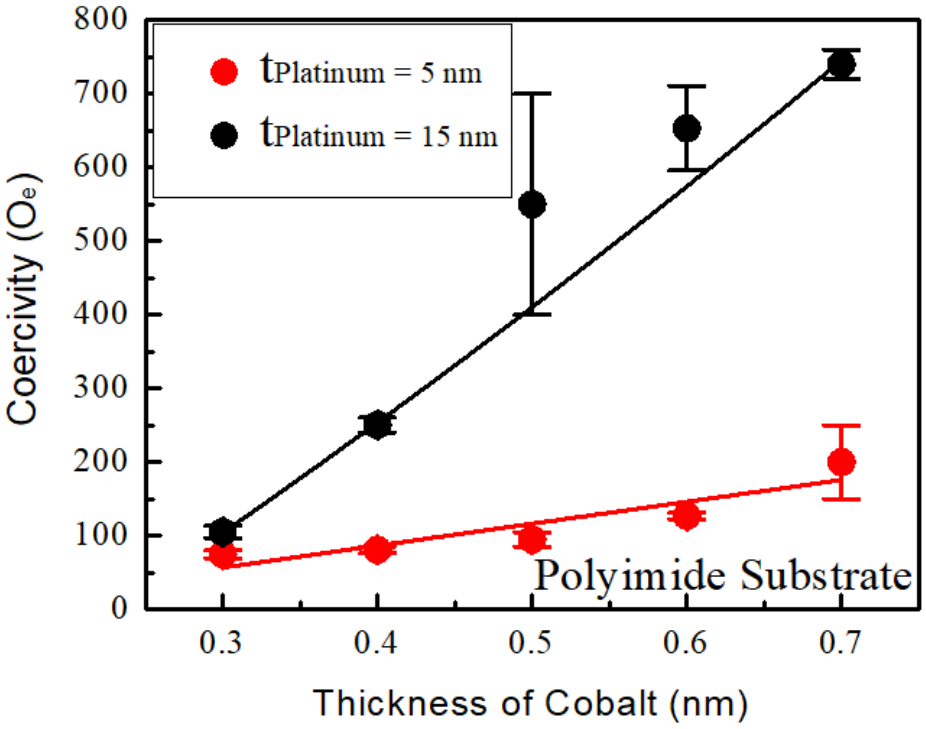

Fig. 6.25 Comparison between different values of Pt buffer layers on coercive field as a function of Co thickness. The red and black lines are linear fits.

From the results of t_{Co} ranged from (0.3-1.15) nm using different kinds of substrates as shown in Fig. 6.28 at t_{Pt} = 15 nm, the coercive field was increased gradually. Then, the coercive field decreased gradually until reaching a 1.15 nm. In general, higher coercivity was found for all cases SiO_2, polyimide and PEN at t_{Pt} = 15 nm with increasing cobalt thickness from 0.3 to 0.7 nm in comparison when t_{Pt} = 5.0 nm.

From Magneto Optical Kerr Effect (MOKE) measurements, the films show hysteresis loops with comparable coercive field and saturation field for both the multilayers with in-plane and perpendicular magnetization. The increase in thickness of Pt buffer layer substantially improved the PMA with higher coercive fields and the squareness of the Pt/Co/Pt trilayer thin-films [151]. The highest remenance M_r/M_s =1 was shown in case of using silicon dioxide because of the root mean square roughness of Pt buffer at 5.0 nm was 0.2 nm. Then, the medium remenance of hysteresis loop was shown in case of using polyimide substrate because of the root mean square roughness of the Pt buffer layer at 5.0 nm was 0.6 nm. In

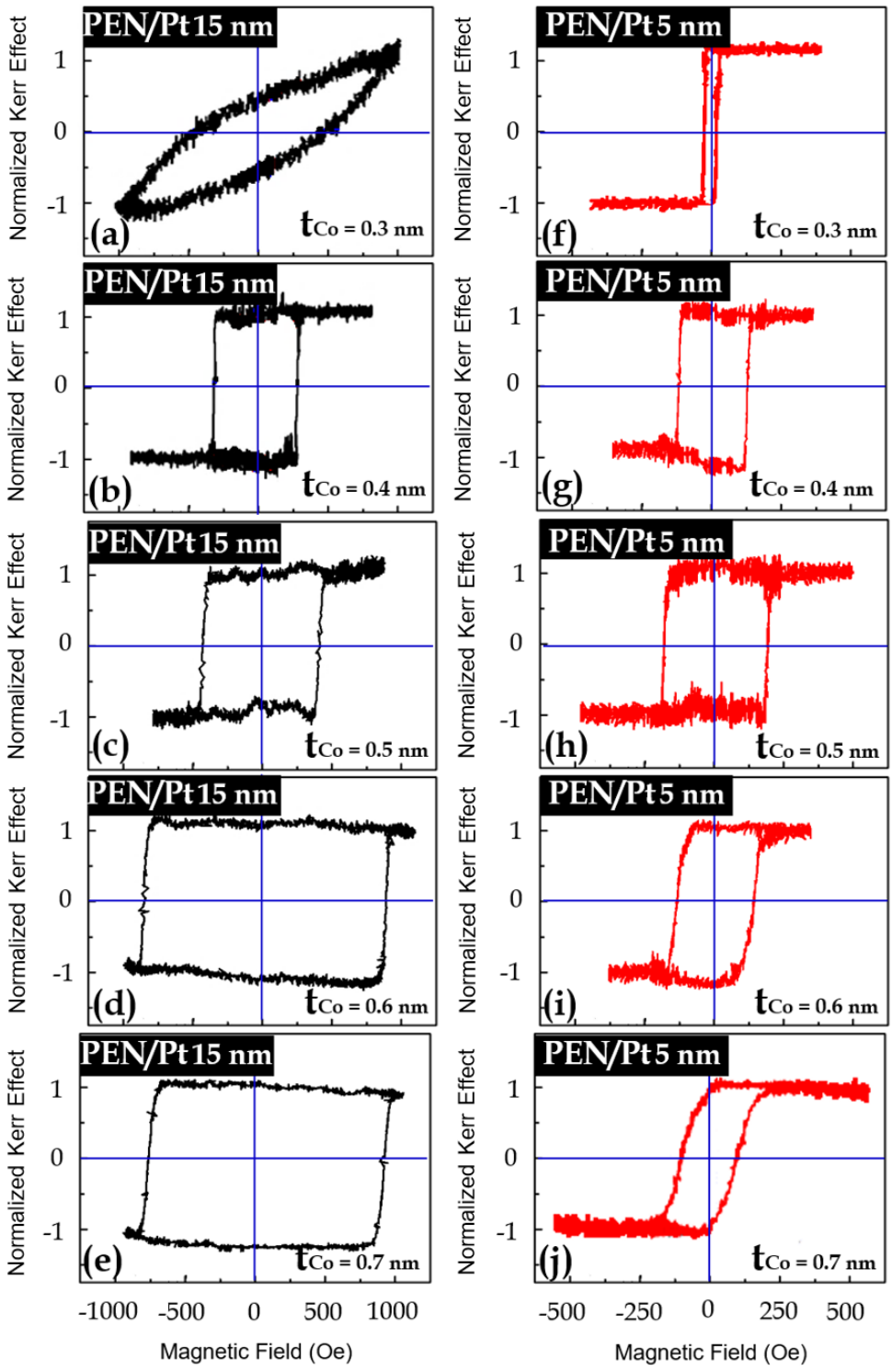

Fig. 6.26 Out-of-plane polar MOKE hysteresis loops for Pt/Co/Pt films with different thicknesses of Pt buffer layer of 15.0 nm and 5.0 nm grown on a PEN substrate. The Pt top layer was 3.0 and 5.0 nm.

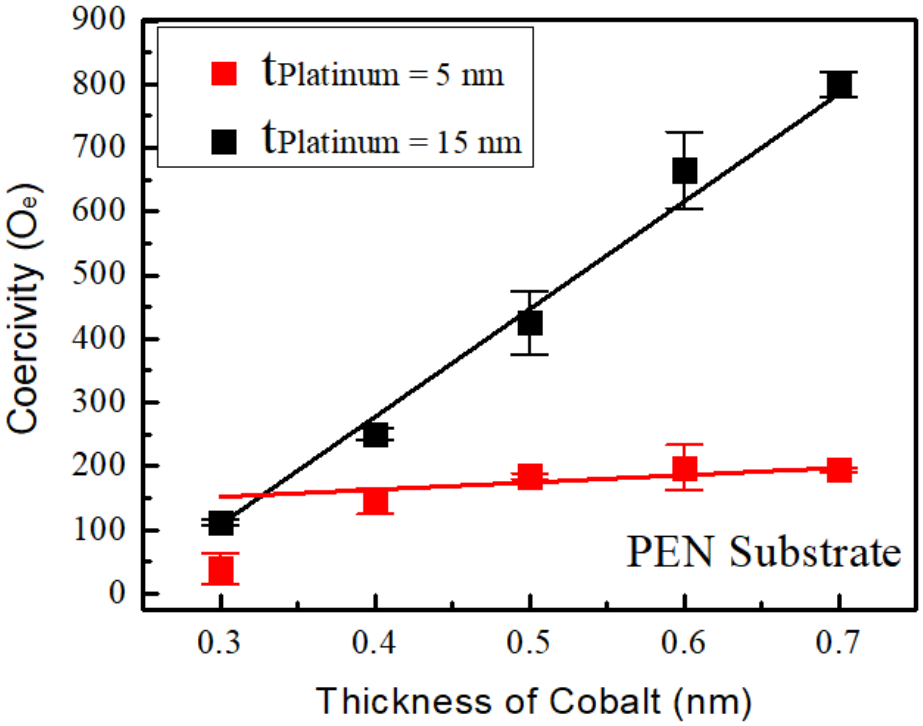

Fig. 6.27 Comparison between different values of Pt buffer layers on coercive field as a function of Co thickness. The red and black lines are linear fits.

the polyimide case, it appears from Fig. 6.24, at t_{Pt} = 5.0 nm, that there was a transformation from out-of-plane to in-plane. The reason for this transformation may be the increasing of roughness to 0.6 nm, as shown in t_{Pt} = 5.0 nm, also as it was referred to in chapter 5, the roughness from x-ray reflectivity at t_{Pt} = 5.0 nm was 0.6 nm, which agrees with the result from atomic force microscopy. Finally, the lowest remenance of hysteresis loop was shown in case of using PEN substrate because of the root mean square roughness of Pt buffer at 5.0 nm = 2.4 nm. According to this result, it is illustrated that the smooth roughness of Pt buffer layer plays an important role to enhance the perpendicular magnetic anisotropy.

The very small out-of-plane remanence ratio in these samples of high thickness means that their magnetisation was almost completely in-plane. Interestingly, a sharp maximum value appeared in the out-of-plane coercive field at a Co thickness of 0.7 nm. Although, it could be associated to the small anisotropy near the spin reorientation thickness, or the effect

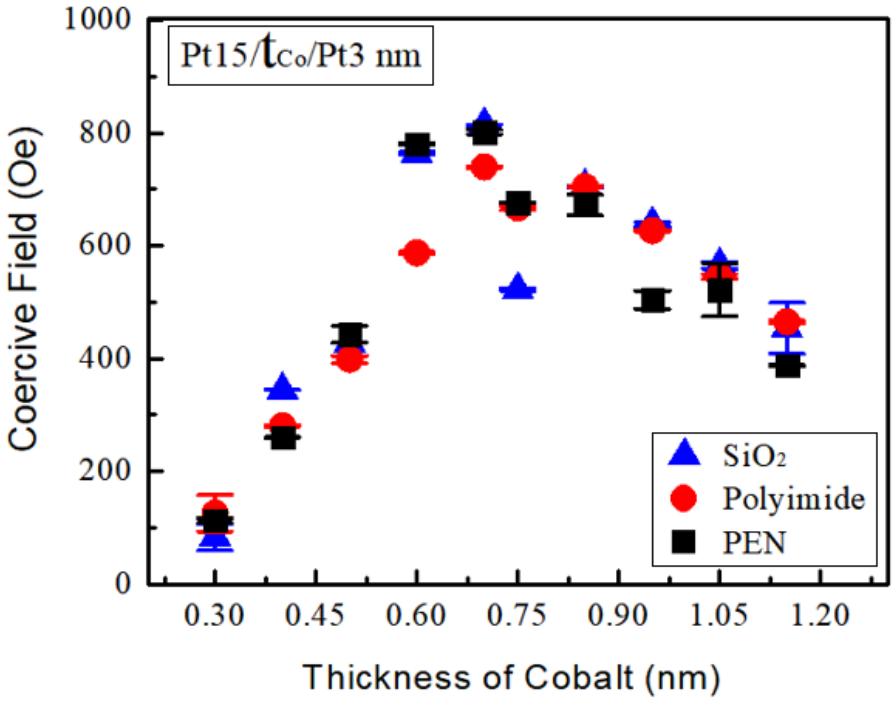

Fig. 6.28 Graph shows the comparison between using different values of Pt buffer layers on coercive field with the error bar for t_{Pt}/Co(0.3-1.15)/t_{Pt} nm.

of stronger DW pinning (switching becomes somewhat broader at larger Co thicknesses) [156, 157].

6.9 Comparison of Hall Resistivity (ρ_{Hall}) of Pt/Co/Pt tri-layers on rigid and flexible substrates

Measurements of the Hall resistivity considered as an important techniques to directly know the charge concentration and mobility of a thin film. Figure 6.29 shows the resistivity decreased with increasing of Pt thickness from 1.0 nm to 5.0 nm for both SiO_2 and PEN. While, the resistiviy in the case of polyimide was smaller than SiO_2 and PEN. It is very clear that the decreasing of resistivity of the platinum layers showed a significant thickness dependence most likely due to increased interface scattering when the thickness was reduced [158–160]. Also, when the thickness of Pt layer is not thick enough, the interfacial roughness,

defects and pinholes in the Pt layers lead to prompt the magnetostatic interactions. Hence, it will increase the exponential decay of the interlayer coupling strength of Co/Pt with increase the thickness of Pt layer [154]. Therefore, the reason of lower resistivity of using polyimide in comparison with higher resistivity for SiO_2 and PEN came from the reducing of interface scattering when the thickness was increased [161, 162]. Hence, this might be associated with a fluctuation of roughness with increasing thickness of platinum in comparison with no fluctuation in roughness happens in case of using SiO_2 and PEN substrates. Due to the hybridization of the Co 3d and Pt 5d orbitals at the Co/Pt interface, the Pt layers are polarized [85]. It is well known that the polarization depth of the Pt layer was only several monolayers at room temperature.

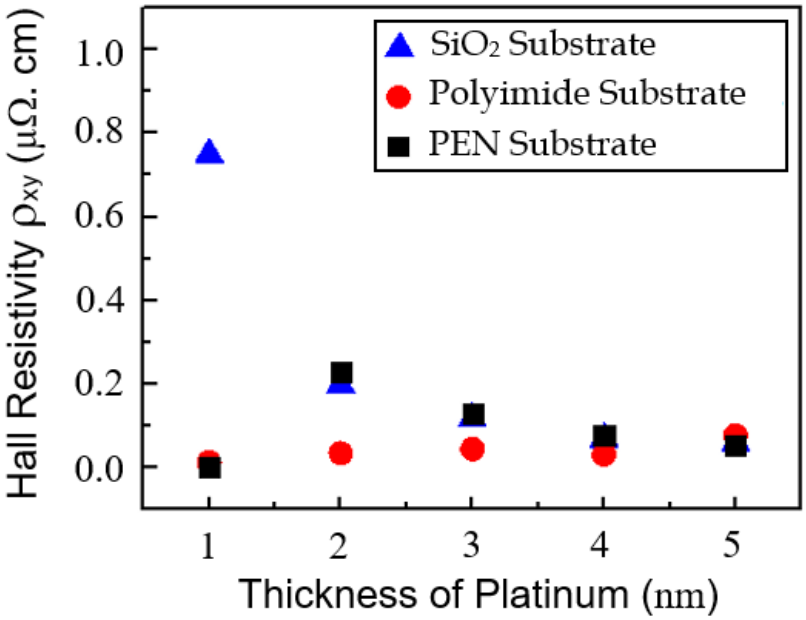

Fig. 6.29 Graph shows the trend of t_{Pt}/t_{Co} (0.5)/t_{Pt} nm of the Pt (1.0 - 5.0) nm buffer layers that was grown on a SiO_2, Polyimide and PEN substrates. The error bar is very small.

Figu. 6.30 shows the Hall resistivity as a function of Co thickness. The cobalt plays an important role for increasing the Hall resistivity and also because of the layer of cobalt does not fully complete, so the polarisation will lead to increase the resistivity. The Hall resistivity increased with increasing cobalt thickness from (0.3-0.7) nm for silicon dioxide, polyimide

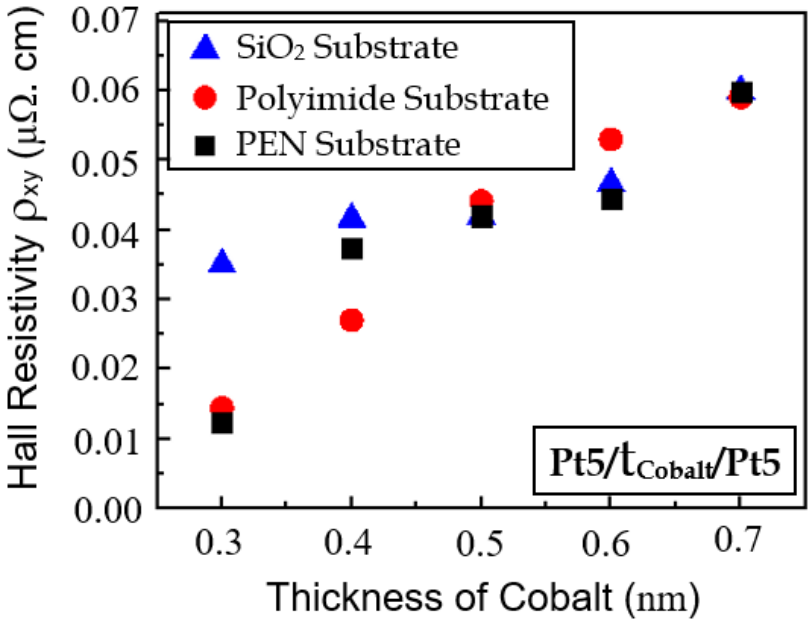

Fig. 6.30 Graph shows the Hall resistivity of t_{Pt} 5.0/t_{Co}/t_{Pt} 5.0 nm as a function of the Co layer thickness on a SiO_2, Polyimide and PEN substrates. The error bar is very small.

and PEN substrates respectively. Fig. 6.30 shows that the Hall resistivity increased with increasing cobalt thickness from 0.3 nm to 0.7 nm. Hence, the resistivity dependence on the Pt and Co layer thickness. The roughness of surface was shown here to be strongly dependent on the thickness of buffer layer and the preparation conditions. In Co/Pt multilayers that were sputtered, the roughness of the surface increases with increasing thickness of Co layer [163, 164]. This leads to increase scattering which is associated to increased resistivity due to Lorentz effect.

6.10 Influence of bending on magnetization behaviour of Pt/Co/Pt trilayers on PEN substrates

The effect of strain on Pt/Co/Pt layers on flexible substrates was also studied. The aim from this section is to know the influence of tension and compression of flexible substrate on increases or decreases the coercivity due to the reversal magnetization. Controlling of

magnetic properties by mechanical strains of flexible magnetic films is considered as an interesting subject from the viewpoint of both essential researches and potential applications [165]. Fig. 6.31 illustrates a photo of samples deformed such that the magnetic thin-films a brought into tension or compression.

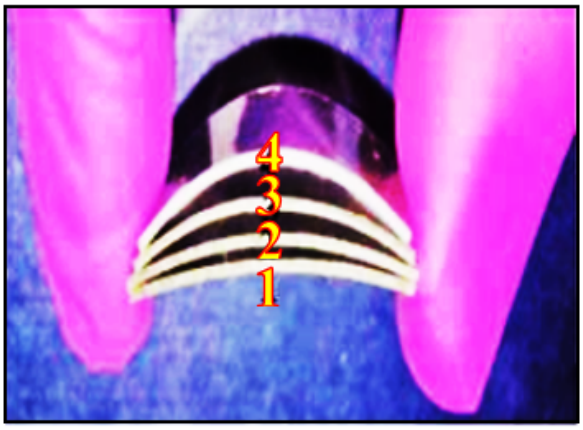

Fig. 6.31 Photo illustrates aluminum pieces used to bend the PEN samples.

Fig. 6.32 shows a schematic diagram of a two typical cases: compression and tension for a bending magnetic plastic substrate. The magnetic properties of PEN/Pt/Co/Pt were investigated by bending the PEN substrates to different degrees of curvature as shown in Table 6.1.

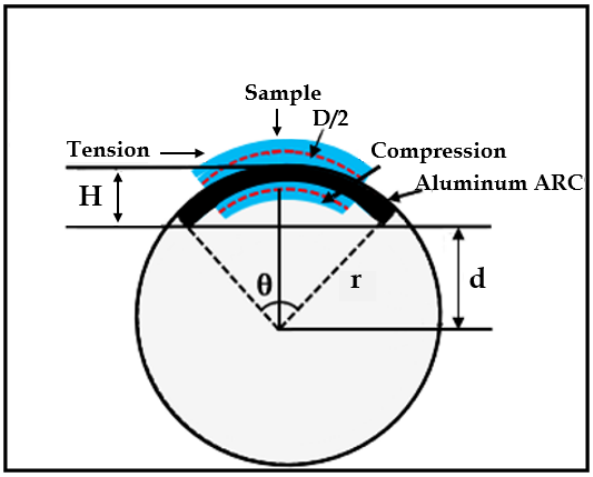

Fig. 6.32 Schematic of a PEN flexible plastic substrate for the calculation of the tensile and compressive strains.

Equations 6.1, 6.2, 6.3 and 6.4 [166] show the tensile strain ε and compressive strain ε_0 that appear within the films. r represents the curvature radius of bending of the the substrate from the neutral plane, ε represents strain; while ε_0 represents compressive strain. Where, D defines the thickness of a sample; in which it equals to 125 μm. Also, d is the height measured from the center of a circle to the middle of a sample and θ is the angle of radius curvatures of samples.

$$R_{strain} = r + D/2 \tag{6.1}$$

$$\varepsilon = \varepsilon_{strain} = D/R_{strain} \tag{6.2}$$

$$-R_{compressive} = r + D/2 \tag{6.3}$$

$$\varepsilon_o = \varepsilon_{compressive} = D/-R_{compressive} \tag{6.4}$$

Fig. 6.33 shows a real photo of PEN thin film that have been used for position bending of flexible magnetic thin films in both sides; which the top side represents the tensile strain while the other side represents the compressive strain.

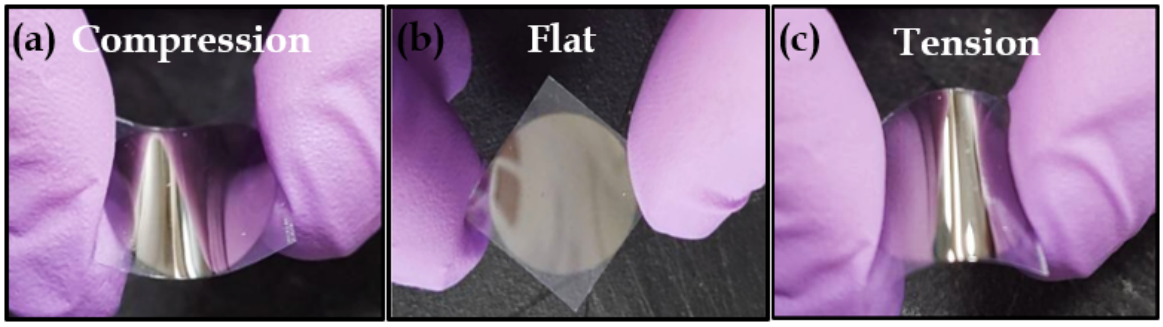

Fig. 6.33 (a,b and c) photo illustrates compression,flat and tension of Pt/Co/Pt trilayer magnetic thin film deposited on PEN flexible substrate.

In Fig. 6.34 the PEN/Pt/Co/Pt samples were bended to different ε (tension) and ε_0 (compression) for introducing various effects on the sample. The strains ε and ε_0 have been

Table 6.1 A comparison of parameters for varies bending strains for the PEN samples.

No.	Radius (r) (10^{-3}m)	R_{strain},-$R_{compressive}$ (10^{-3}m)	d (10^{-3}m)	θ (deg.)	ε (10^{-3})	ε_0 (10^{-3})
1	33.5	33.50,-33.43	31.0	29.0	3.73	-3.73
2	32.5	33.12, -31.87	31.0	35.0	3.77	-3.92
3	22	22.62,-21.37	24.0	35.0	5.52	-5.84
4	15	15.62,-14.37	14.5	48.0	8.0	-8.69

applied to Pt/t_{Co}0.5/Pt nm multilayers which have different thicknesses of Pt. The range of Pt thicknesses t_{Pt} is 1.0 - 3.0 nm.

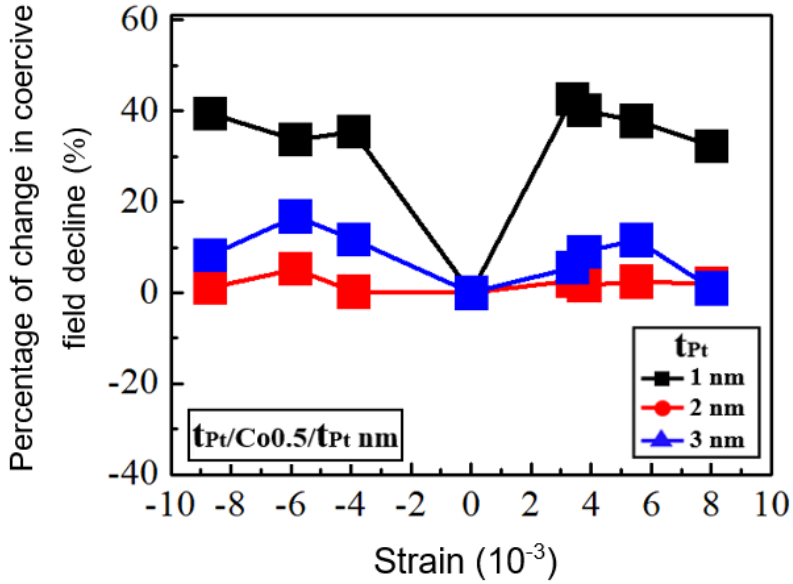

Fig. 6.34 Percentage of coercive field changing after bending as a function of tensile strain and compressive strain sides for PEN flexible plastic substrate using different kinds of structures.

Fig. 6.35 shows the change of the coercive field due to a given strain as a function of Pt thickness. It shows the decline of coercive field as a function of different platinum thickness. It shows that the highest changing in ε was equal to 68 % for Pt1.0/Co0.4/Pt1.0 nm and 39 % for Pt1.0/Co0.5/Pt1.0 nm. Moreover, there was a gradual decreasing in the coercive field with increasing thicknesses of Pt which ranges from 2.0 to 5.0 nm, with a thickness of (t_{Co} = 0.4 nm). Also, there was a sudden increase when the (t_{Co} = 0.4 nm) at Pt thickness

range from (3.0 - 4.0) nm, then it falls again. The ε and ε_0 of Pt/t_{Co}0.5/Pt nm was studied for different thicknesses of Pt.

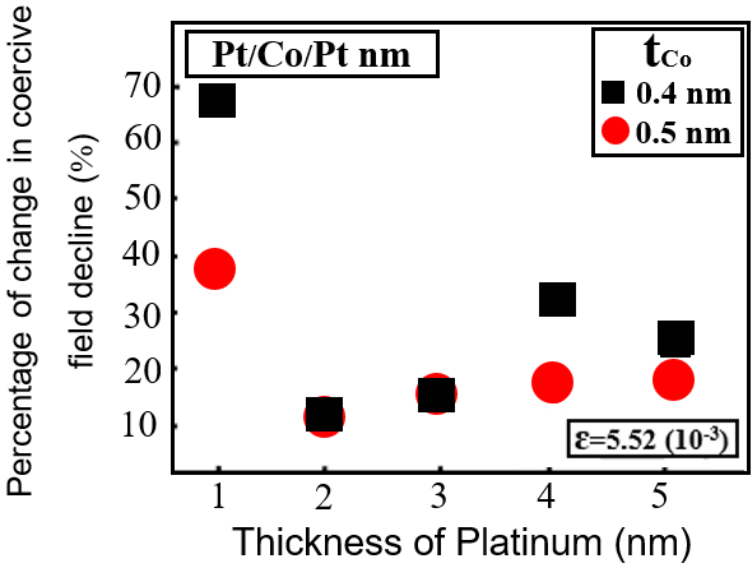

Fig. 6.35 Percentage of coercive field changing as a function of thickness of Pt in nm. The error bar is very small.

The greatest change occurred when the Pt thickness t_{Pt} was equal to 1.0 nm. When the Pt/Co/Pt was stretched, there must be an effective compression along the z-direction in the layers, which decreases the distance between the Pt an Co layers [167]. This behaviour may come from changing in the perpendicular magnetic energy; which is due to orbital hybridization at the Pt/Co interface. It was found that the highest impact of bending occurred at the lowest thickness of t_{Pt} = 1.0 nm. So, it were supposed that the increment in the intermixing between layers was led to an enhancement in the effective saturation magnetization; which in turn was led to an improvement in the interface at lower thickness of (t_{Pt} = 1.0 nm). [168] showed that the strain will lead to a reduced coercive field. Here, the highest change in coercivity was 68 % for Pt1.0/Co0.4/Pt1.0 nm [from 20 Oe to 7 Oe] and 39 % for Pt1.0/Co0.5/Pt1.0 nm; due to the ease of movement of a few spin magnetic moments through the thin film. It is clear that the presence of interfaces can cause a perpendicular magnetic anisotropy which is a feature for high density hard disk media and required for

magneto-optical recording. Platinum is important for the magnetism of these systems, since the late d-transition elements can be significantly magntically polarized ferromagnetically ordered atoms [162]. An extensive studying was focused on the perpendicular magnetic anisotropy that is associated with strain. Hence, the interface of Pt atoms became polarized by common atoms in its vicinity [169, 170].

6.11 Conclusion

It was found the important of using a Pt buffer that grown on SiO_2, Polyimide and PEN substrates in the development of PMA. Hence, it would allow the readers to distinguish between the advantage and disadvantage of using both flexible plastic/rigid substrates. Where, it depends on the surface roughness that will effect on the strength of perpendicular magnetic anisotropy (PMA). Also, it was found that with increasing Co thickness, the resistvity has been increased due to increasing of roughness and scattering from 0.3 nm to 0.7 nm.

Moreover, decreasing the root mean square roughness of the Pt buffer layers plays an important role to improve the shape of hysteresis loop and this will be correlated to improve perpendicular magnetic anisotropy with decrease resistivity. In case of Pt/Co/Pt/Co/Pt trilayers, because of the higher roughness of PEN, the squareness shape of hysteresis loop seems to be not very squareness. Hence, it was appeared that there was a transformation from out-of-plane to in-plane direction. Here, the most significant difference in the magnetic behaviour was found to depends on the variation of the roughness of substrates; which represents of the needing to more time for reaching to saturation magnetization. The variation was the main subject of the discussion.

Chapter 7

Perpendicular magnetic anisotropy in Ru/Co and Pt/Co trilayer thin-films on flexible substrates

7.1 Previous Work

The advantages of using Perpendicular magnetic anisotropy (PMA) in device applications is due to the thermal stability and decreasing of the current density for magnetization switching; which in turn will enhance the low power consumption operation of spintronics devices like the magneto-resistive random access memories (MRAMs) [171, 172]. Also, the structure of PMA in ferromagnetic multilayer has been studied thoroughly; due to its significant effect on the performance enhancement of electronic devices like the storage devices, magnetic read-heads, and random access memory. In the nano-structure, the increase in the magnetic density is resulting from the larger PMA; which in turn will develop the efficiency of electronic devices. According to such studies, there are multiple elements that fabricate the thin films like the Co/Pt or Pt/Co/Pt, or more complicated nano-structures using thin or

ultra-thin films like the Pt/Co/MOx/Pt; which have an important role in the orientation an MA [151, 173–177].

7.1.1 Pt/Co structures

Cobalt and Platinum have focused on the magnetism society for decades [178, 179], specifically in the form of an alloy. But gained great popularity when, in 1988, Carcía et al. [180] PMA has found found in multiple thin layers of Pt/Co. Perpendicular magnetic anisotropy (PMA) is inversely dependent on the thickness of Co, so its interpretation of this is something Neel presented in his 1954 paper on the contrast of the facade [181], once the application is proposed by Zipper et al [77], from the recording of optical magnetism, the research on the system has grown considerably. The regime was a major candidate for such a request, not only because of the PMA, but also due to the because of the enhanced Kerr effect. In 1991, Lin et al [81]. posted some major work on the super lattices of Pt/Co, not only the different thickness of the layer, but also, the direction of crystal, follow-up from Den Broeder et al [182]. They showed that the variation and coercion of samples were more dependent on Co thickness of Pt and more significantly, a sharp contrast to the crystalline orientation, PMA presentation of Pt (111) and strong variability of the plane to Pt (110) were affected. This indicates that the variation was originally magnetic. At this period, Bruno [183] published a theoretical work to discuss the relationship between the magnetic-magnetic variation and the orbital moment in the traveling iron magnets.

7.1.2 Ru/Co structures

In Ru/Co films the reasons for the cration of PMA are still not obviously defined, and remain a dialectical issue. In some researches, the PMA origin is demonstrated from the point of view of strains relaxation in films —in other states, it is clarified as a conclusion of surface contribution [184], hybridization of d orbitals by spin–orbit coupling [185], or even like a

catalyst-resulted manipulation of the interfacial electronic structure through an ultra-thin Ru layer [186]. In this study, we explore the influence of ruthenium (Ru) buffer layers of various thicknesses on coercive field, magnetic anisotropy and Hall resistivity in ultrathin Ru/Co/Ru trilayers. It must be noted that, in contrast to the plurality of prior investigations on epitaxial Ru/Co systems with a very thin Ru buffer (thickness of buffer layer up to a small nm) [187, 188, 184, 189, 190], this research has studied the polycrystalline Ru/Co/Ru trilayers with a buffer thickness of up to 15 nm and compared to the Pt/Co structures. PMA has been experimentally observed in a diversity of ultrathin films [191, 192, 173] and multilayers like Co/Ru [187] and Co/Pt [115]. Theoretical studies have exhibited that PMA in thin films may occur due to various reasons. The fundamental models leads to spin–orbit interaction, and demonstrates the appearance of PMA in terms of: (i) magnetocrystalline anisotropy consequent to loss of atomic bonds on the surface [181]; (ii) the contribution of orbital moment to the magnetocrystalline anisotropy of transition metals [183]; and (iii) magnetoelastic anisotropy growing as a consequence of tensile distortion of the film [193].

7.1.3 Physical properties of materials

Physical properties of ferromagnetic material Cobalt

In bulk, Co has an (HCP) structure of hard, brittle and magnetic properties [68].It is widely utilized in magnetic recording media. In addition, it goes through an allotropic transformation and adjusts itself upon the face centred cubic (FCC) structure at temperature of 425^{o} C. In ultra-thin films, it can also be face centred cubic (FCC). Perpendicular Magnetic Anisotropy (PMA) decreases with the increase of Co thickness [68].

Physical properties of ruthenium and platinum elements

Ruthenium is the 44th element in the periodic table, just below the iron and above the Osiumium in the eighth group, but its properties are closer to the osmium compared with

iron [194]. Fig. 7.1 shows the electrical resistivity and the electrical conductivity of metals as a function of rank from smallest to largest.

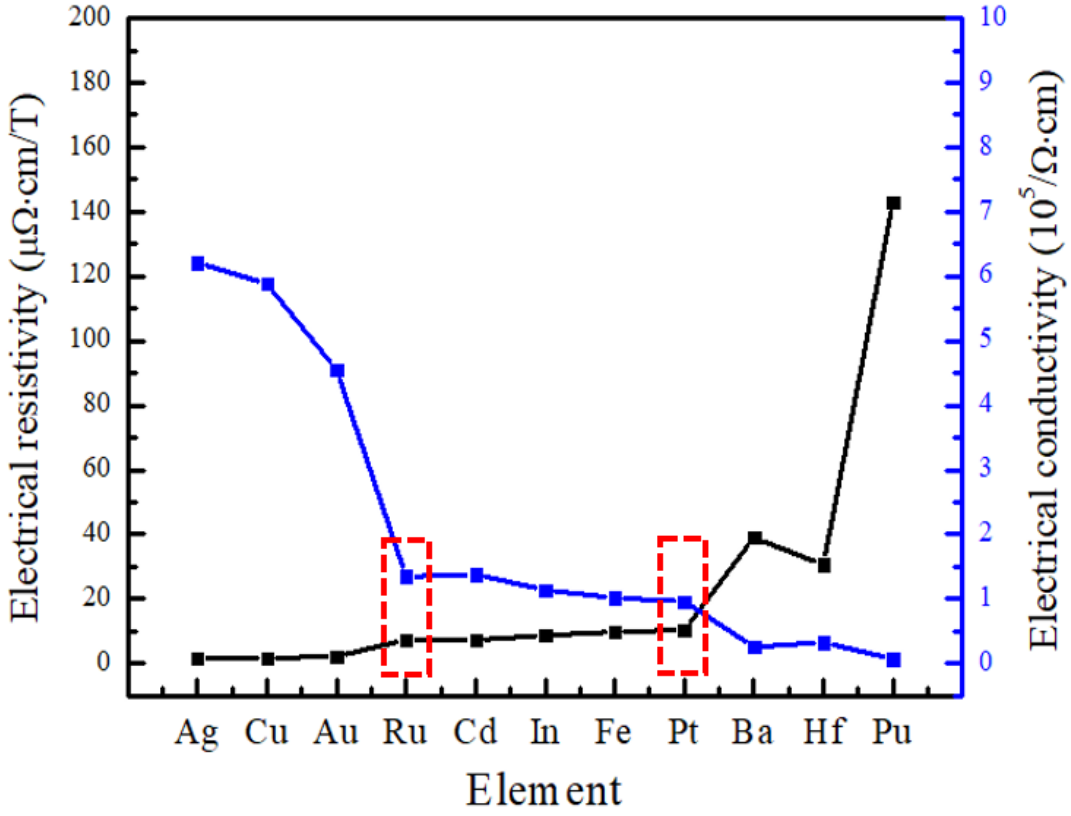

Fig. 7.1 Resistivity and electrical conductivity of metals at 295 K as a function of rank from smallest to largest.

There are four stable stages with having a low temperature phase. Its high melting temperature reachs to 2334 °C. Also it has a resistance to chemical attack on a wide broad of temperatures. Moreover, it is used as a hardener in metal alloys and in industrial as a catalyst [195]. Ruthenium is a transitional metal with equal electrons that occupies more than one shell (4d7, 5s1) [196]. Less than 1000 °C, Ruthenium shows a closed hexagonal structure packed (hcp), where successive atomic levels follow the A-B-A stack sequence. Ruthenium is a resistant to magnetism and is a reactive metal of the type p [197]. It contains approximately five times the resistivity of silver at room temperature and is considered as a very good conductor of heat and current [198]. While Pt doesn't have a magnetic characteristic, it can

be proximity polarised, and thin-films on ferromagnetic layers have a big effect on damping and can lead to interface DMI. Co/Pt showed large PMA at room temperature. Also, it has been regarded as the best candidate for the dielectric layer and can be utilized in the capacitor applications to improve the storage capability.

7.2 Introduction

In this chapter, the effect of using different thickness of ruthenium and platinum buffer layers on the crystal structure and the surface roughness in the development of PMA for ultrathin Ru/Co/Ru, Pt/Co/Pt trilayers was studied. X-ray diffraction data for Ru15.0/(t_{Co})/ Ru3.0 nm and Pt15.0/(t_{Co})/Pt3.0 nm with different cobalt thickness (t_{Co} = 0.75, 0.85, 0.95, 1.05 and 1.15 nm) was studied.

The data obtained during the experiments were related to the microstructural features of thin-films and their relationship to the measured magnetic properties. The surface structural analysis was supplemented using x-ray diffraction studies. The grain size was calculated from the XRD data and Hall resistivity was calculated from the Hall measurements and film thickness measurements. The details of experimental data and the results obtained from this formation of thin-films are presented in the following sections.

7.3 Experimental work

Ru/Co/Ru and Pt/Co/Pt multilayered films were sputtered on to SiO_2, Polyimide and PEN substrates at room temperature. The base pressure was 1.0×10^{-8} Torr. The growth pressure during deposition was 1.1×10^{-3} Torr. The cobalt thickness (t_{Co}) ranged from 0.75 nm to 1.15 nm. The thickness of the Ru and Pt buffer layers (t_{Buffer}) was 15.0 nm.

A capping layer of 3.0 nm of either Ru or Pt was used to prevent oxidation of the Co layer and to aid the development of PMA. The magnetic properties of the films were examined

using magneto - optical Kerr effect magnetometry. The surface morphology was studied using atomic force microscopy and the crystal structure studied using x-ray diffraction.

7.4 Structural characterization of Ru and Pt buffer layer on SiO_2, Polyimide and PEN substrates

The results of the AFM surface morphology of single-layer films is displayed for similar thicknesses of ruthenium and platinum in Fig. 7.2, Fig. 7.3 and Fig. 7.4. The area of thin-film measured was 5.0 μm $\times$ 5.0 μm. The surface ripples were very small in Fig. 7.2 (a,b). Hence, the smooth substrate surface of SiO_2 gave low roughness for both Ru and Pt seed layers. The root-mean-square roughness was 0.25 nm for 15.0 nm thick films of both Ru and Pt seed layers respectively.

Fig. 7.3 (a,b) shows the surface structure of 15 nm Pt and Ru on polyimide. Values for the root mean square roughness of 1.4 nm for Pt and 1.35 nm for Ru were obtained on polyimide.

The AFM images shown in Fig. 7.3 (a,b) shows that the morphology of the films is complex, including large scale surface features. The area of thin-film was taken from a different part of the film surface, which is of an area of 5 μm $\times$ 5 μm. It can be observed that there are large ripples and peaks in the case of ruthenium compared with platinum.

Nano structural features are observed when using PEN substrate. Fig. 7.4 (a,b) illustrates the AFM images of PEN/Pt and PEN/Ru thin films with similar buffer layer thicknesses of 15.0 nm. The measured area of thin-film was 1 μm $\times$ 1 μm.

The AFM image of PEN/Ru (15.0 nm) thin-film shows the discontinuous nature of the films that were deposited. However, the AFM image of PEN/Pt (15.0 nm) thin-film sample was consistent with both layer by layer and island types of growth. RMS roughness of

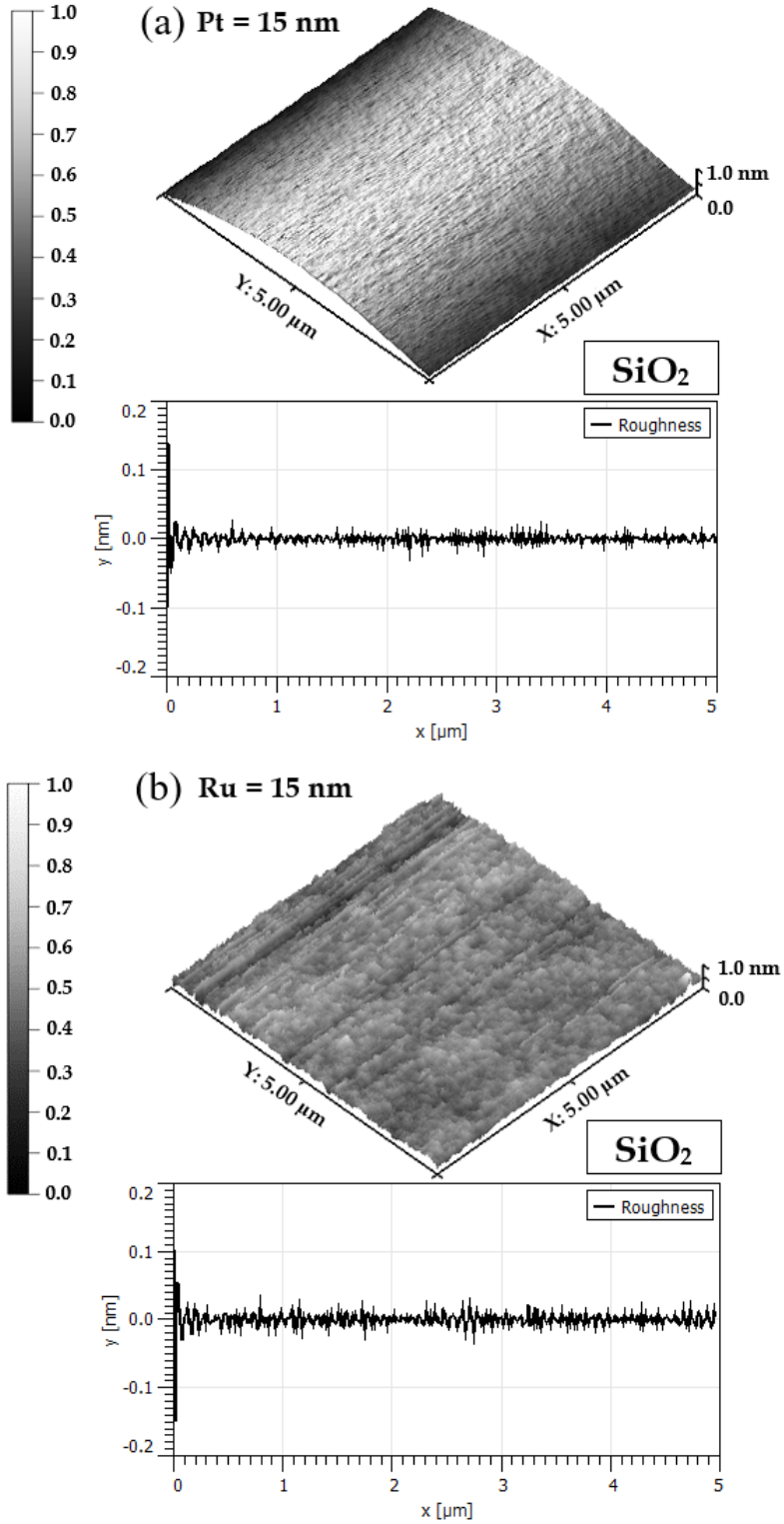

Fig. 7.2 (a,b) Surface morphology for both Pt 15.0 nm and Ru 15.0 nm seed layers grown on SiO_2 substrate. Area and line scans are shown.

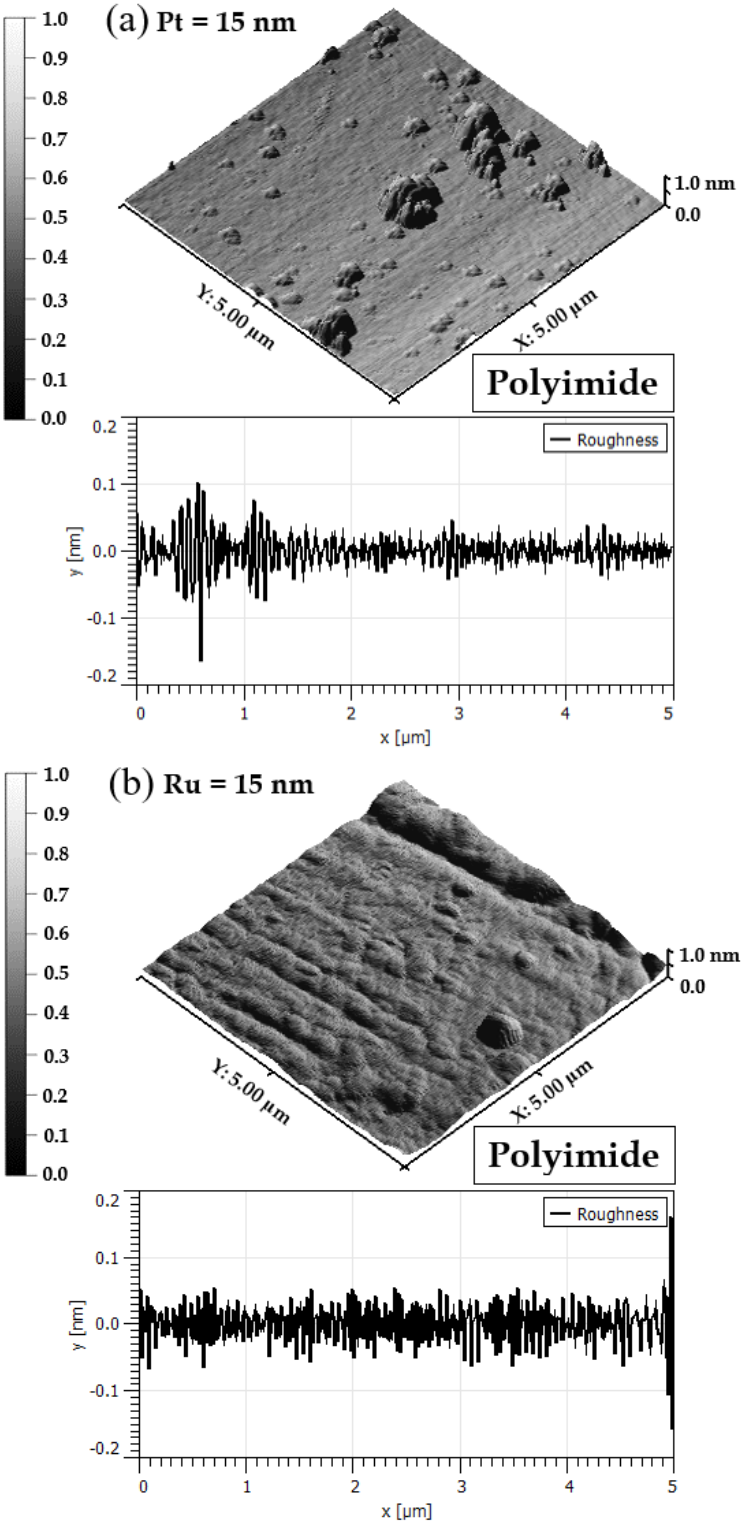

Fig. 7.3 (a,b) Surface morphology for both Pt 15.0 nm and Ru 15.0 nm seed layers grown on polyimide substrate. Area and line scans are shown.

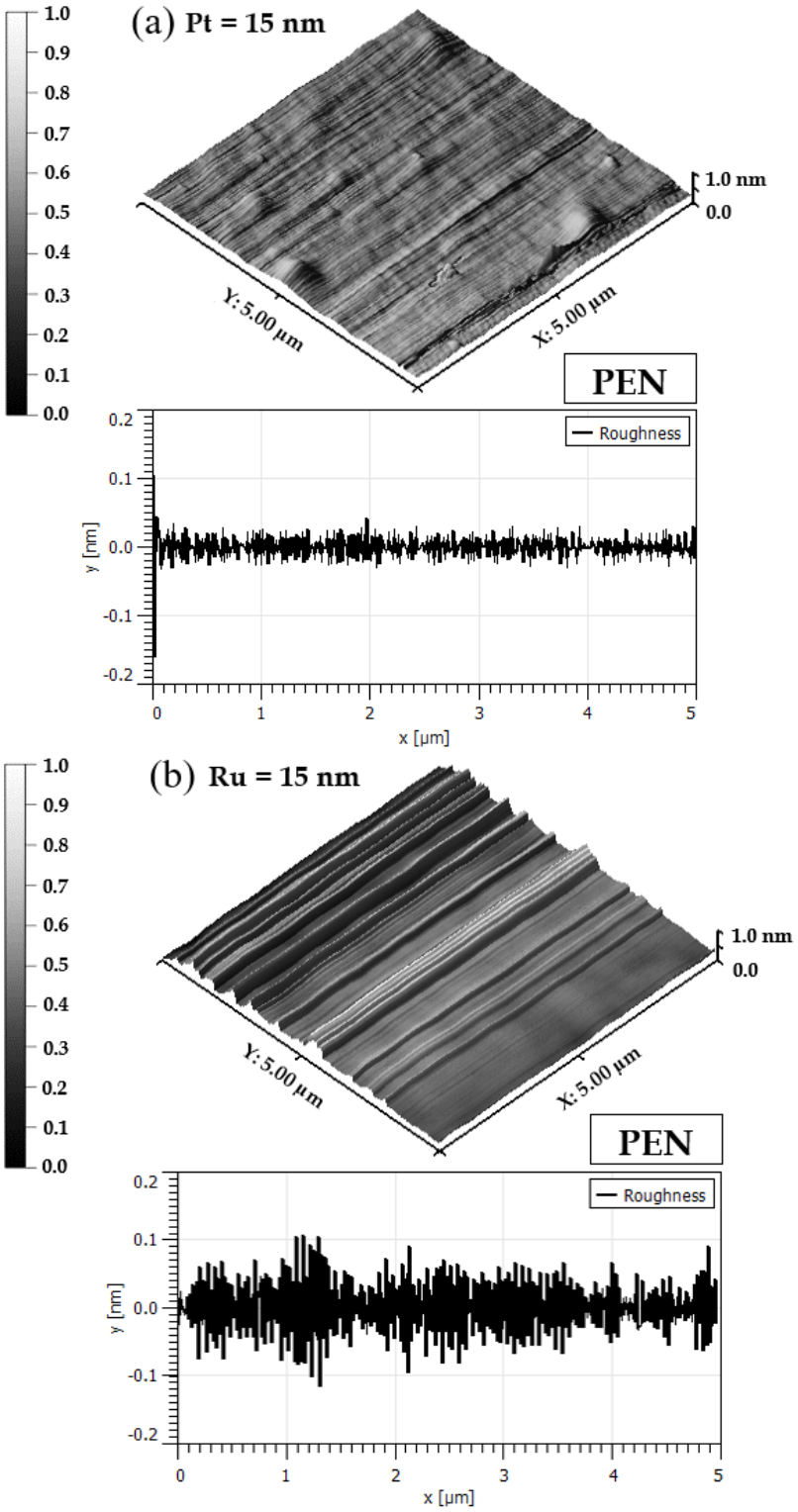

Fig. 7.4 (a,b) Surface morphology for both Pt 15.0 nm and Ru 15.0 nm seed layers grown on PEN substrate. Area and line scans are shown.

the surface increased from 0.9 nm to 1.6 nm for PEN/Pt (15.0 nm) and PEN/Ru (15.0 nm) thin-films respectively.

Maximum and minimum root mean square roughness obtained are shown in Fig. 7.5.

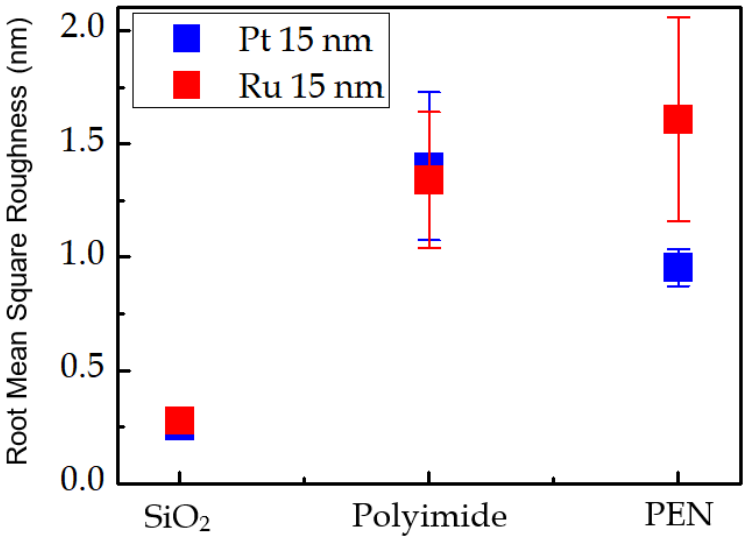

Fig. 7.5 Root mean square roughness for 15.0 nm ruthenium and 15.0 nm platinum deposited on rigid/flexible substrates.

By using the Gwyddion program [199] it was taken different cross section parts of the sample surface were analysed in order to calculate the error bar. It was obvious that in cases of SiO_2 and polyimide substrates, the root mean square roughness of Pt was similar, but the root mean square roughness of Ru was different. In case of using PEN substrate, it seems that the root mean square roughness of Pt is significantly lower than with a Ru base layer.

7.5 X-Ray diffraction for films on SiO_2, Polyimide and PEN substrates

XRD scans of trilayer thin-films are shown in Fig. 7.6 (a,b) and (c,d). The Pt/Co/Pt trilayer with t_{Co} = 1.05 nm grown on SiO_2 substrate, showed Co/Pt (111) texture with multiple peaks that appeared at a range of theta values along with a weak appearance of peaks

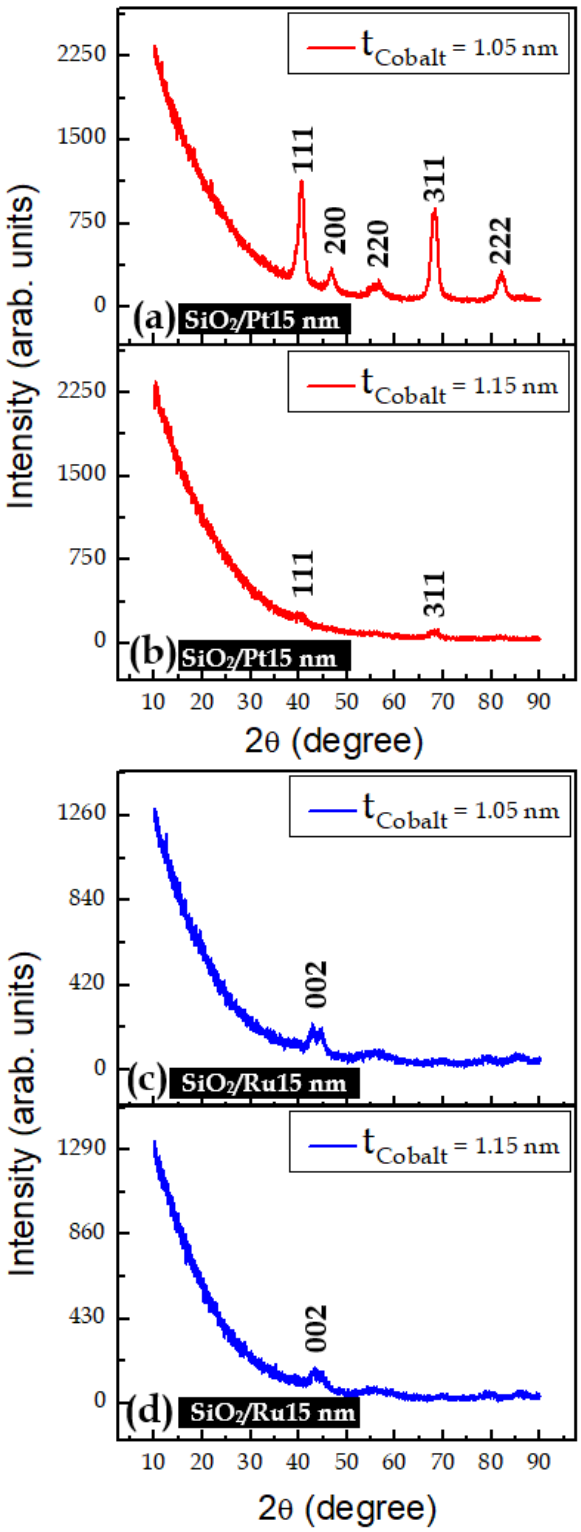

Fig. 7.6 X-ray diffraction scans of the (a,b) Pt15.0/(t_{Co})/Pt3.0 nm and (c,d) Ru15.0/(t_{Co})/Ru3.0 nm trilayer thin-films grown on SiO_2 substrate.

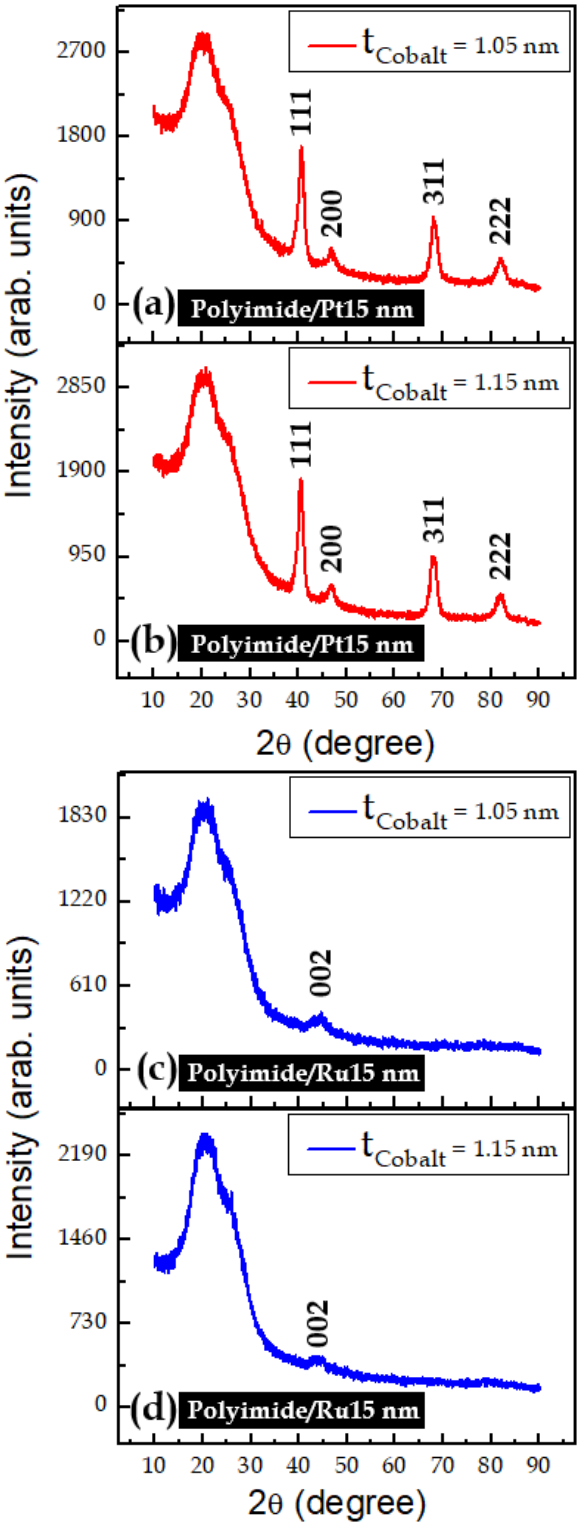

Fig. 7.7 X-ray diffraction scans of the (a,b) Pt15.0/(t_{Co})/Pt3.0 nm and (c,d) Ru15.0/(t_{Co})/Ru3.0 nm trilayer thin-films grown on polyimide substrate.

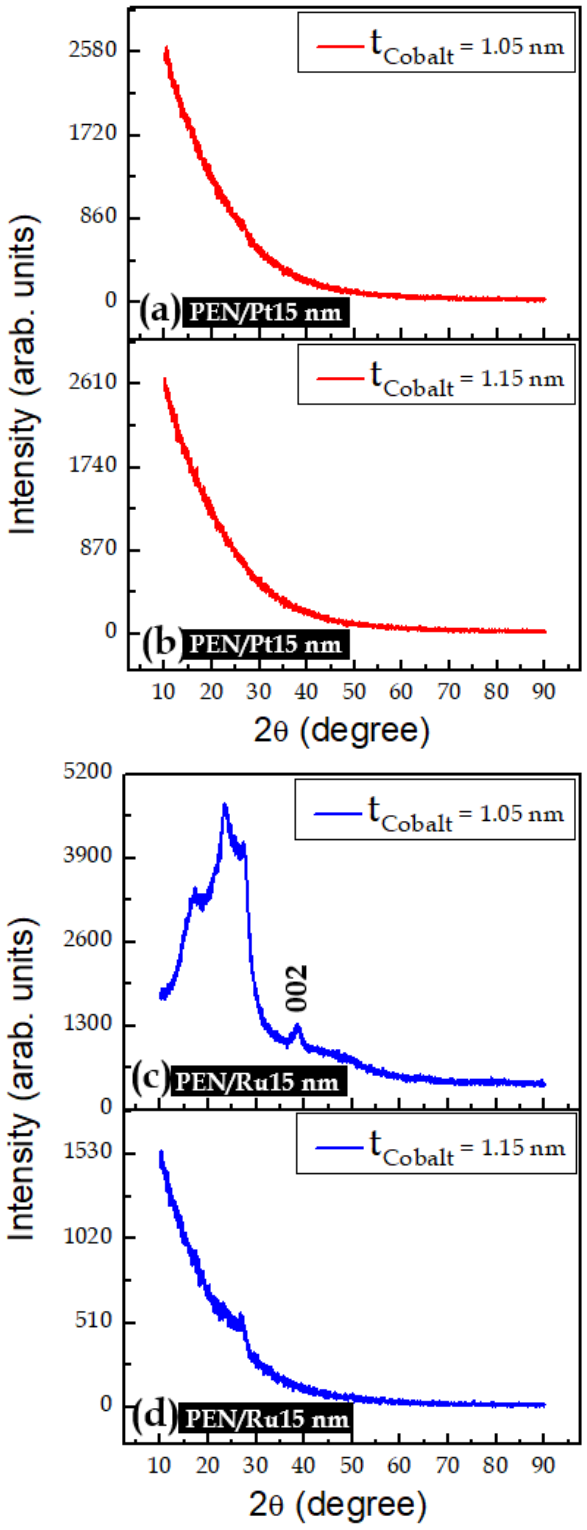

Fig. 7.8 X-ray diffraction scans of the (a,b) Pt15.0/(t_{Co})/Pt3.0 nm and (c,d) Ru15.0/(t_{Co})/Ru3.0 nm trilayer thin-films grown on PEN substrate.

of Ru/Co/Ru using 1.05 nm thickness of cobalt. Sharp peaks in XRD patterns indicated good crystalline structure. The beginning of the curve profile that starts of the XRD profile within the region $2\theta = 10^o$ to 30^o may be coming from the SiO_2 substrate as it shown in Fig. 7.6 (a,b) and (c,d).

Fig. 7.7 (a,b) and (c,d) show x-ray diffraction pattern of the Pt15.0/Co(1.05-1.15)/Pt 3.0 nm and Ru15.0/Co(1.05-1.15)/Ru 3.0 nm trilayer thin-films respectively that were grown on polyimide substrates. The sharpness of the (111) peak for both Pt15.0/Co1.05/Pt3.0 nm and Ru15.0/Co1.05/Ru3.0 nm was improved, where, all the peaks appeared in comparison with silicon dioxide especially at t_{Co} = 1.15 nm. The higher peaks that is shown in the region between $2\theta = 10^o$ to 30^o may be coming from the polyimide substrate as it shown in Fig. 7.7.

Fig. 7.8 (a,b) and (c,d) show the diffraction pattern of the Pt15.0/t_{Co}/Pt3.0 nm and Ru15.0/t_{Co}/Ru3.0 nm trilayer thin-films respectively using the polyethylene naphthalate, where the thickness of cobalt was 1.05 nm and 1.15 nm respectively. In Fig. 7.8 (a,b), the $t_{Pt}/t_{Co}/t_{Pt}$ thin-film shows the disappearance of the peaks while in case of $t_{Ru}/t_{Co}/t_{Ru}$ thin-film, the Ru (002) peak appeared. The curve and the broad peak that appear in Fig. 7.8 7.7 (a,b) and 7.7 (c,d) respectively may be coming from the PEN substrate. The reason of the higher quality films of Pt compared to the Ru came from the difference of surface energy roughness for both Pt and Ru (non-magnetic) materials.

Where, in general, the surface energy of a metal is proportional to the number of broken bonds at the surface. In case of Pt fcc (111) and Ru (200) surfaces, it is clear that the surface energy increase along with the corrugation of the surface, being lowest value for the Pt (111) surfaces and highest value for the Ru (200) surfaces. Moreover, the growth mode of Pt grown on substrate is Volmer Weber while the growth mode of Ru grown on substrate is Stranski-Krastanove [higher interface energy].

7.6 Influence of Ru and Pt buffer layer on the magnetisation using Hall effect on rigid/flexible substrates

To determine the optimised materials and thicknesses for the establishment of the PMA, the effects of t_{Co} and t_{Buffer} thicknesses on magnetic behaviour was comparatively studied in Ru/Co/Ru and Pt/Co/Pt thin films. Fig. 7.9 illustrates the measured Hall hysteresis loops with the applied magnetic field out-of-plane, for both ruthenium and platinum buffer layers. These results show that the coercive field (H_c) varied with increasing cobalt thickness. The deposited films all show out-of-plane magnetisation, with the remanence ratio of $M(H)/M_S$ = 1, which indicates a dominant PMA.

In Fig. 7.9 (a-e), the hysteresis loop width increased with increasing cobalt thickness from 0.75 to 0.85 nm and then decreased from 0.95 to 1.15 nm. While in the case of Fig. 7.9 (f-k), the width of the hysteresis loops increased with increasing thickness of cobalt from 0.75-1.05 nm [to be out-of-plane] and then decreasing at t_{Co} = 1.15 nm [to be in-plane]. The values for the coercive field as a function Co thickness for Ru and Pt buffer layers are compared in Fig. 7.10.

It is shown that the coercive field in case of Ru/Co/Ru thin-films was significantly smaller than that of Pt/Co/Pt thin-films [the values has been illustrated in Figs. 7.9, 7.11 and 7.12]. In Ru/Co/Ru thin-films, H_c increased when the cobalt thickness increased from 0.75 nm to 0.95 nm and the reduced at 1.15 nm cobalt thickness. In Pt/Co/Pt thin-films, the increase in H_c was shown from t_{Co} = 0.75 nm to 0.85 nm and then decrease from 0.85 nm to 1.15 nm. For Co layer thickness, larger than 0.75 nm, in-plane anisotropy was indicated from the in-plane M-H loops shown as inset in Fig. 7.9 in case of Pt/Co/Pt films.

Fig. 7.11 shows the experimental field dependence of the normalized magnetization M/M_S(H) for Ru15.0/t_{Co} (0.75-1.15)/Ru3.0 nm and Pt15.0/t_{Co} (0.75-1.15)/Pt3.0 nm thin-

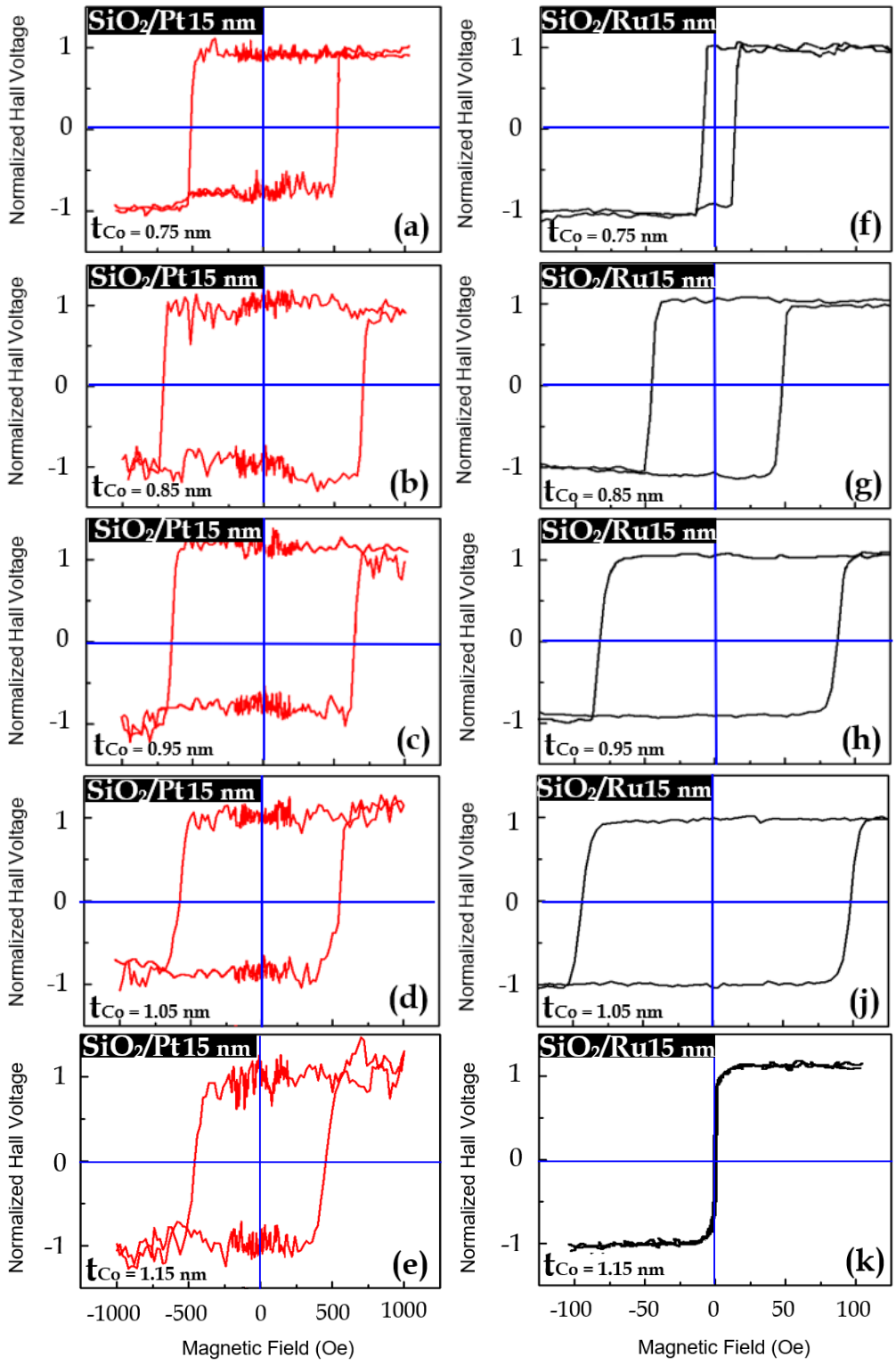

Fig. 7.9 Hysteresis loops for both Ru15.0/(t_{Co})/Ru3.0 nm and Pt15.0/(t_{Co})/Pt3.0 nm using SiO_2 substrate. Note different magnetic field scales for Pt and Ru data.

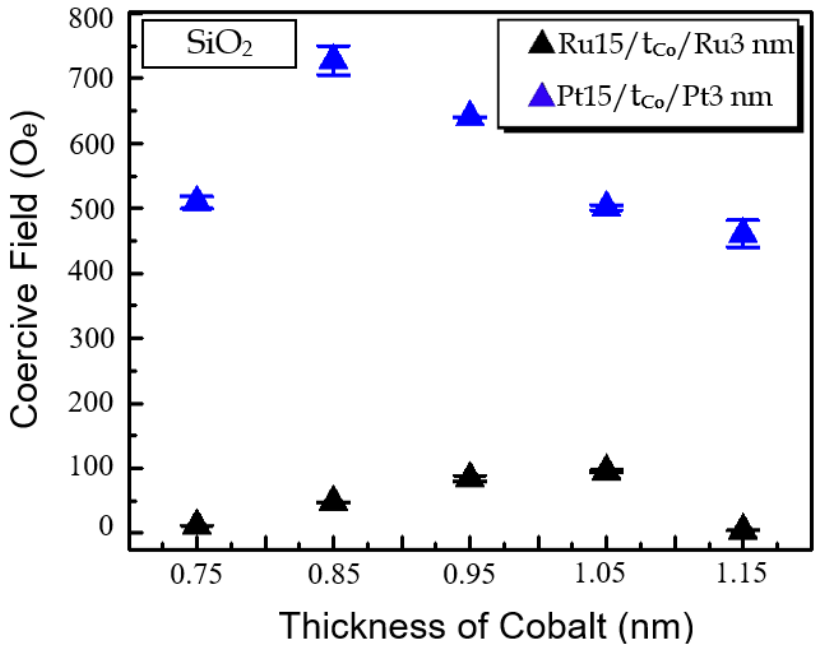

Fig. 7.10 Comparison of coercive field values with error bars for Ru15.0/(t_{Co})/Ru3.0 nm and Pt15.0/(t_{Co})/Pt3.0 nm on SiO_2 substrates as a function of Co thickness.

films on polyimide substrates, measured in an external magnetic field H applied in the direction normal to the film surface.

For the Ru buffer layer, it is clear from Fig. 7.11 (g-j) that the coercivity of the hysteresis loops increased gradually until t_{Co} reaches 0.95 nm, and then decreased as the Co thickness increased from 1.05 nm to 1.15 nm. In Fig. 7.11 (a-e), for the Pt buffer layer, when t_{Co} increased from 0.75 nm to 0.85 nm, the hysteresis loops increased then it decreased gradually until reaches to 1.15 nm. The reason behind the study of out-of-plane anisotropy was to understand how spontaneous magnetism can be vertically oriented on a surface, while the film shape tends to direct the magnetization strongly in the plane of the film. The Pt/Co/Pt system displays a perpendicular magnetic anisotropy at room temperature for a variety of thicknesses of cobalt. The coercivity increased with increasing Co thickness and the magnetisation remains perpendicular until the t_{Co} reaches 1.15 nm. Fig. 7.12 illustrates the coercive field for both Ru and Pt trilayer thin-films as a function of cobalt thickness on polyimide substrates. In the Ru case, H_c increased from t_{Co} = 0.75 nm to 0.95 nm then it was reduced up to 1.15

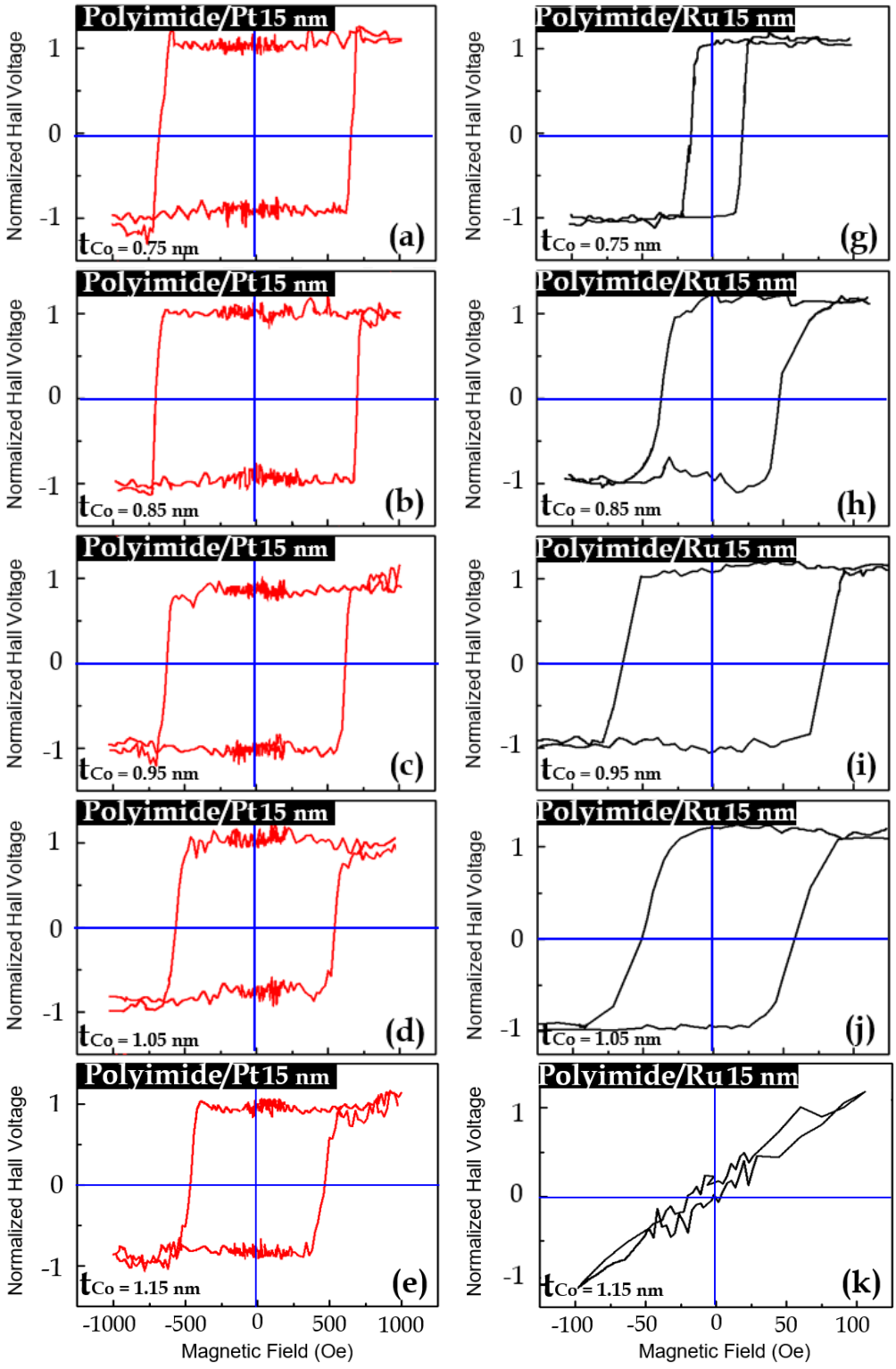

Fig. 7.11 Hysteresis loops for both Ru15.0/(t_{Co})/Ru3.0 nm and Pt15.0/(t_{Co})/Pt3.0 nm using polyimide substrate. Note different magnetic field scales for Pt and Ru data.

nm cobalt thickness. In contrast, for Pt trilayer thin films, from t_{Co} = 0.75 nm to 0.85 nm H_c increased slightly then decreased more significantly and approximately linearly from 0.85 nm to 1.15 nm cobalt thickness.

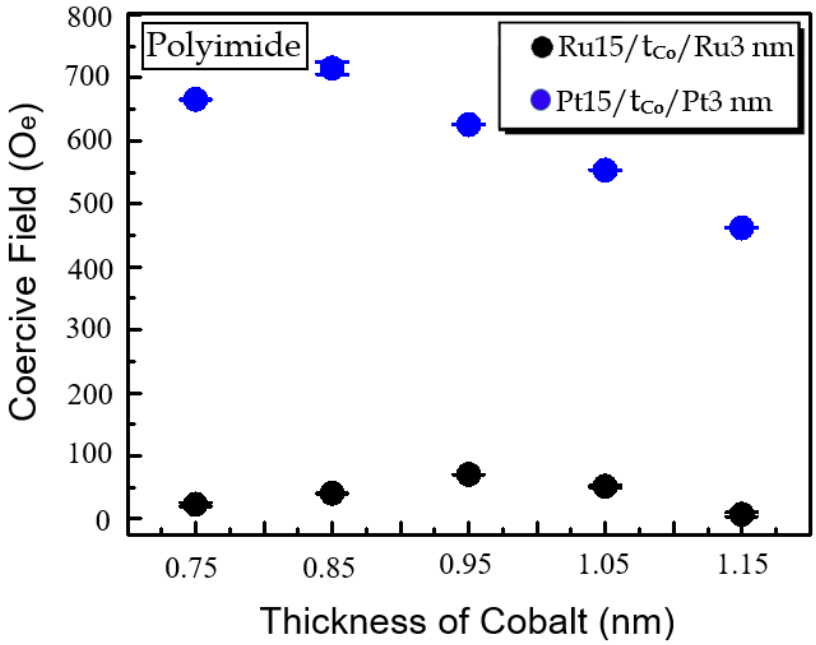

Fig. 7.12 Comparison between coercive field values with error bars for Ru15.0/(t_{Co})/Ru3.0 nm and Pt15.0/(t_{Co})/Pt3.0 nm using polyimide substrate.

Typical Hall hysteresis loops that were measured on multilayer samples deposited on PEN substrates are shown in Fig. 7.13. These samples have different thicknesses for the seed layer 15.0 nm and the capping layer 3.0 nm and show a range Co thicknesses. The loops show in most cases clear perpendicular magnetic anisotropy with a remanence ratio of 1.0. In Fig. 7.13 (a-e), for the Pt buffer layer, the hysteresis loop decreased with increasing Co thickness from 0.75 nm to 1.15 nm. While for the Ru buffer layer, the loops increased from t_{Co} = 0.75 - 1.05 nm then it decreased at t_{Co} = 1.15 nm as it shown in Fig. 7.13 (f-j).

Fig. 7.14 summaries the change of coercivity as a function of cobalt thickness. For the case of Pt15.0/t_{Co} (0.75-0.85)/Pt3.0 nm, the coercive field decreased with increasing cobalt thickness, before reaching a constant value above t_{Co} = 1.05 nm. In Fig. 7.14, in the case

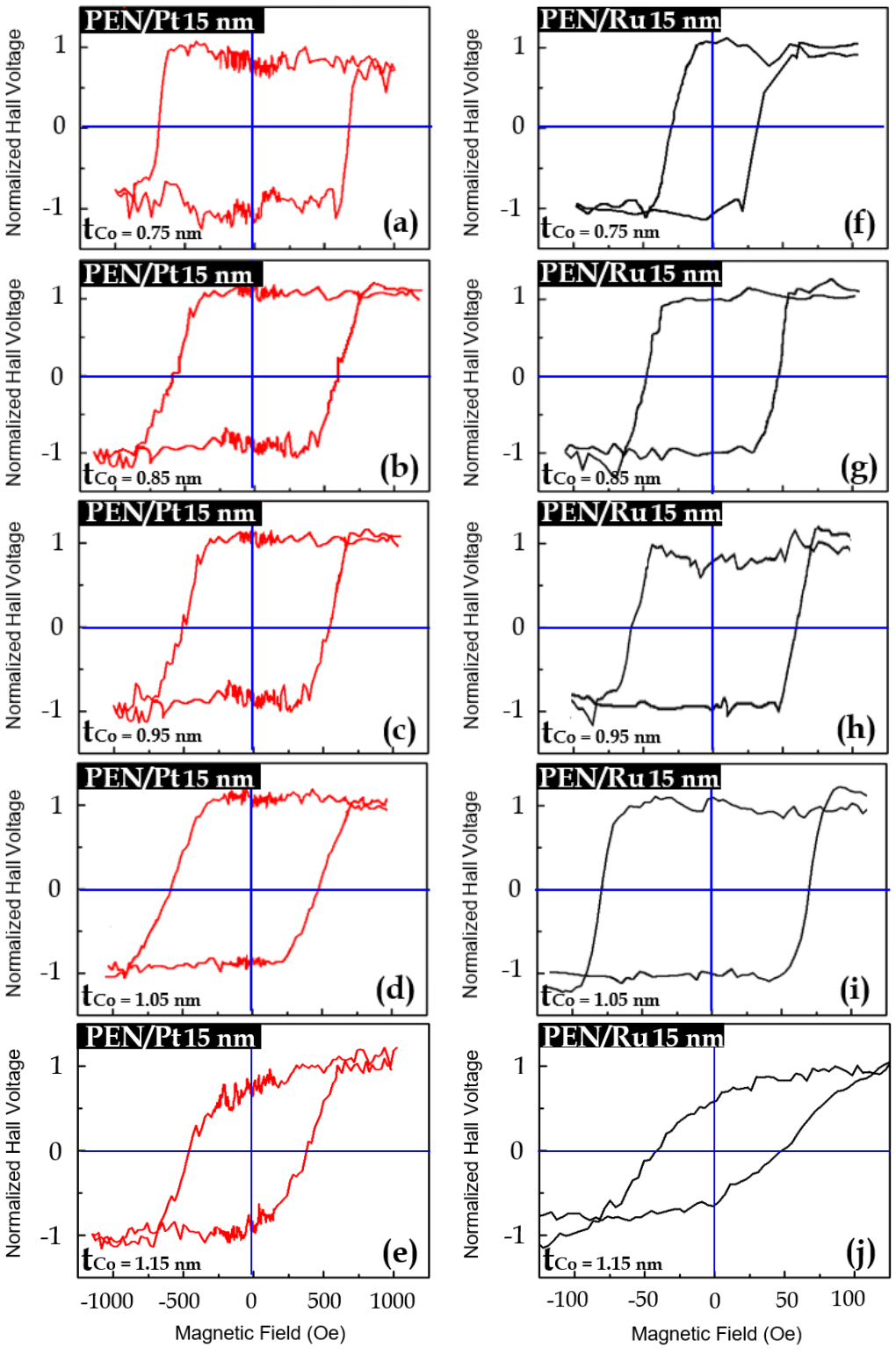

Fig. 7.13 Hysteresis loops for both Ru15.0/(t_{Co})/Ru3.0 nm and Pt15.0/(t_{Co})/Pt3.0 nm using PEN substrate. Note different magnetic field scales for Pt and Ru data.

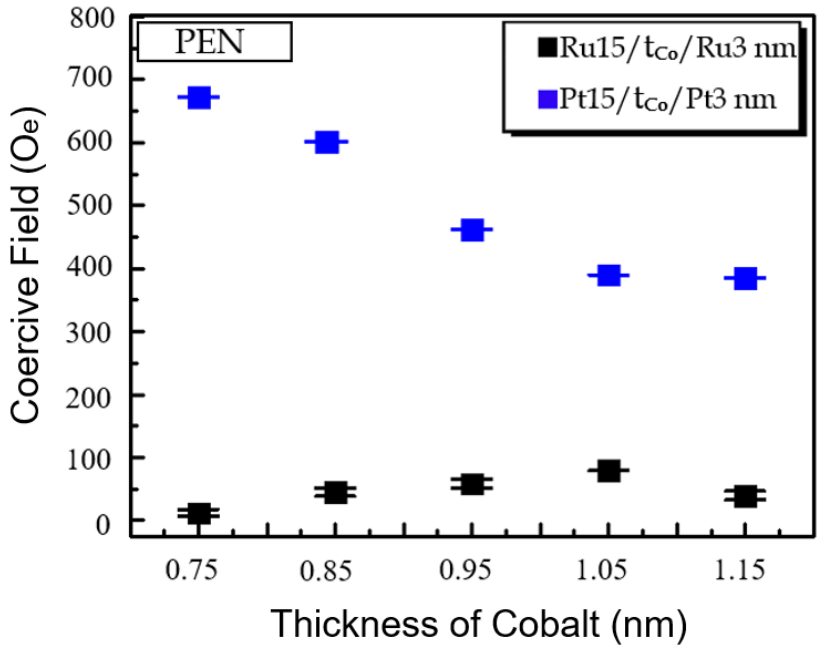

Fig. 7.14 Comparison between coercive field values with error bars for Ru15.0/(t_{Co})/Ru3.0 nm and Pt15.0/(t_{Co})/Pt3.0 nm using PEN substrate.

of Ru trilayer thin films, the coercive field increased from 0.75 nm up to 1.05 nm cobalt thickness then fell for 1.15 nm thick cobalt.

7.7 Dependence of the coercive field on Ru and Pt buffer layers on rigid/flexible substrates

Typical Hall hysteresis loops that were measured on multilayer samples deposited on SiO_2, polyimide and PEN substrates are shown in Fig. 7.15 (a,b). In Fig. 7.15 (a), the Ru/Co/Ru system displays a perpendicular magnetic anisotropy at room temperature for a variety of thicknesses of cobalt. The coercivity increased with increasing Co thickness and the magnetisation remains perpendicular until the t_{Co} reaches 1.15 nm. Fig. 7.15 (b) illustrates the coercive field for both Pt/Co/Pt trilayer thin-films as a function of cobalt thickness on SiO_2, polyimide and PEN substrates. In the Ru case, H_c increased from t_{Co} = 0.75 nm to 0.85 nm then it was reduced up to 1.15 nm cobalt thickness.

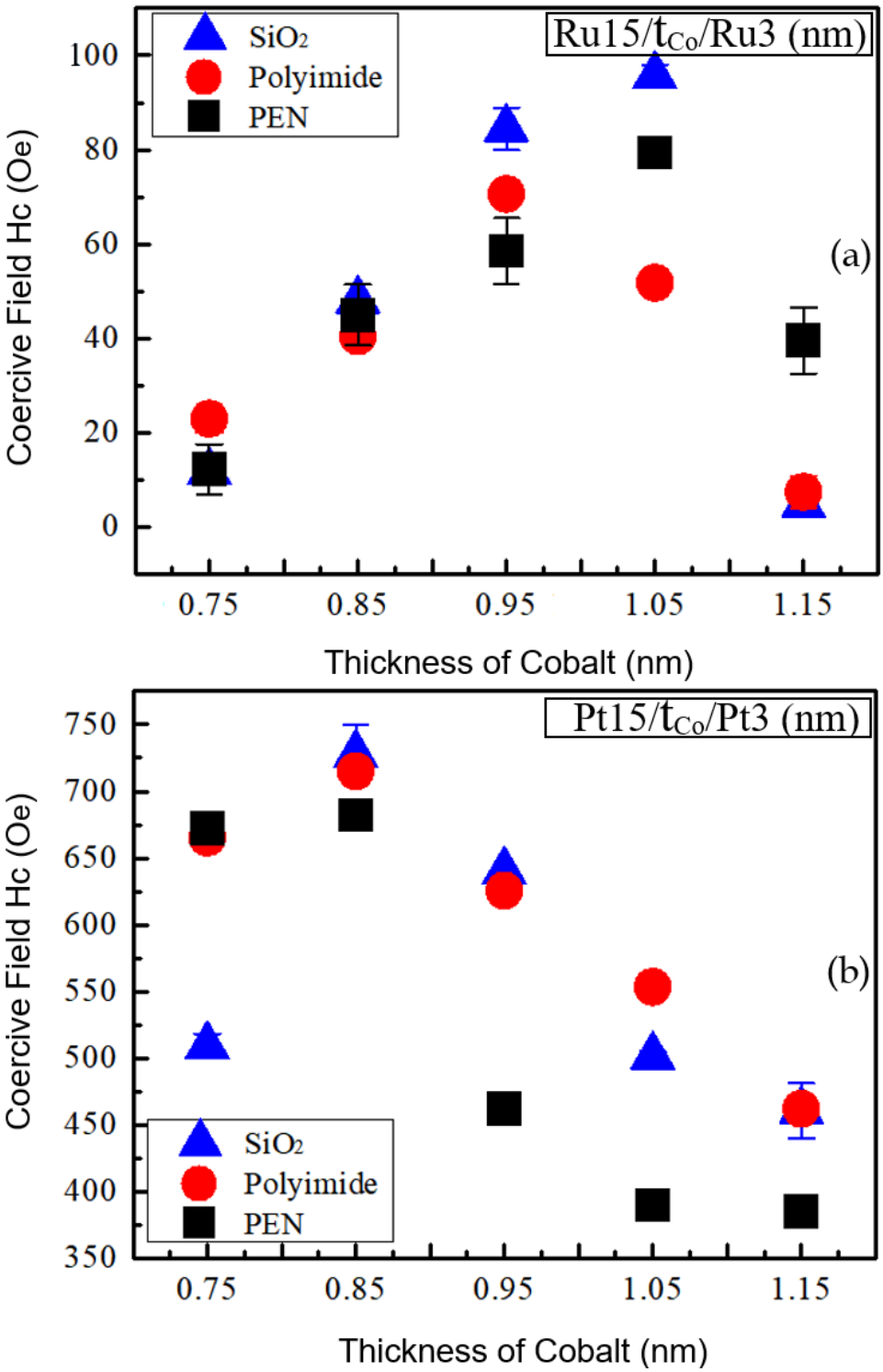

Fig. 7.15 (a,b) Coercive field for both Ru15.0/(t_{Co})/Ru3.0 nm and Pt15.0/(t_{Co})/Pt3.0 nm on SiO_2, polyimide and PEN substrates respectively as a function of the cobalt thickness. The error bars are very small.

7.8 Dependence of the Hall Resistivity on Ru and Pt buffer layers on rigid/flexible substrates

This section focus on the determination of longitudinal resistivity for both Pt/Co and Ru/Co trilayer thin films. It is well known that there is a major correlation between longitudinal resistivity and grain size [200]. The grain size and also the film morphology are important to determine the resistivity of film. Therefore, in order to have a comprehensive understanding this study is focus on showing the link between the resistivity and film morphology.

The Hall resistivity with Ru and Pt buffer trilayers on SiO_2 substrates is presented and it was calculated using $\rho_{xy} = R_0$ B, where R_0 is Hall coefficient and B is magnetic field. Fig. 7.16 shows the variation of Hall resistivity with varied thickness of cobalt t_{Co} for Ru15.0/t_{Co}/Ru3.0 nm and Pt15.0/t_{Co}/Pt3.0 nm thin-films.

For the Ru case on SiO_2 substrate, the Hall resistivity increased slightly with cobalt thickness increased from 0.75 nm to 1.05 nm and then decreased at 1.15 nm cobalt thickness. For Pt/Co on SiO_2, the Hall resistivity is roughly constant with increasing cobalt thickness. The Hall Resistivity with Ru and Pt buffer on polyimide substrates for thicknesses of the cobalt layer in NM/t$_{Co}$/NM multilayers at room temperature are shown in Fig. 7.16 (b). The Hall resistivity increased with increasing cobalt thickness for Ru layers within the Co thickness range 0.75 nm to 1.05 nm and then fell dramatically for t_{Co} = 1.15 nm. While, in the Pt case, the resistivity increased up to a Co thickness of 1.05 nm and then fell slightly for Co thickness of 1.15 nm.

The Hall resistivity with Ru and Pt buffer on PEN substrates for thicknesses of the cobalt layer in NM/t_{Co}/NM multilayers at room temperature are shown in Fig. 7.16 (c). For Ru15.0/t_{Co}/Ru3.0 nm the Hall resistivity decreased with increasing cobalt thickness. However, it was always larger than Pt15.0/t_{Co}/Pt3.0 nm sample series, where it appears that

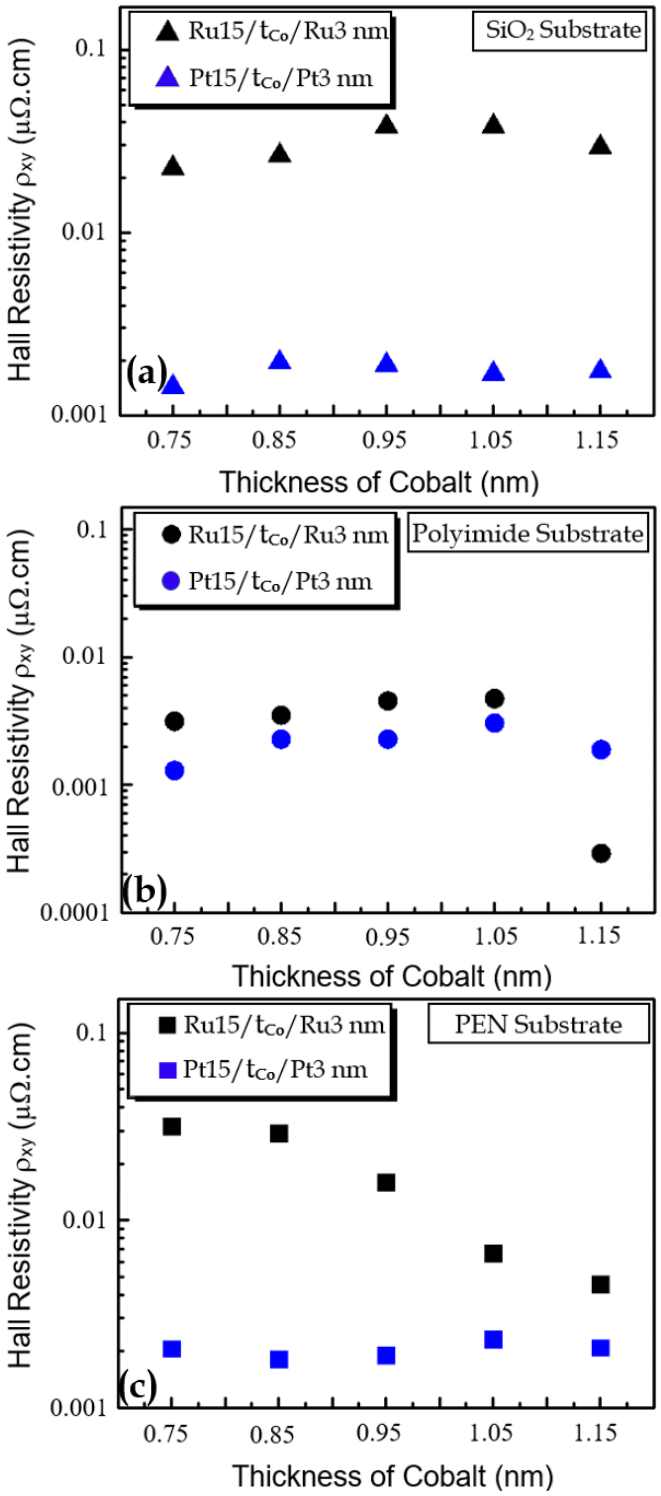

Fig. 7.16 (a,b,c) Hall resistivity for both Ru15.0/(t_{Co})/Ru3.0 nm and Pt15.0/(t_{Co})/Pt3.0 nm on SiO_2, polyimide and PEN substrates respectively as a function of the cobalt thickness. The error bars are very small.

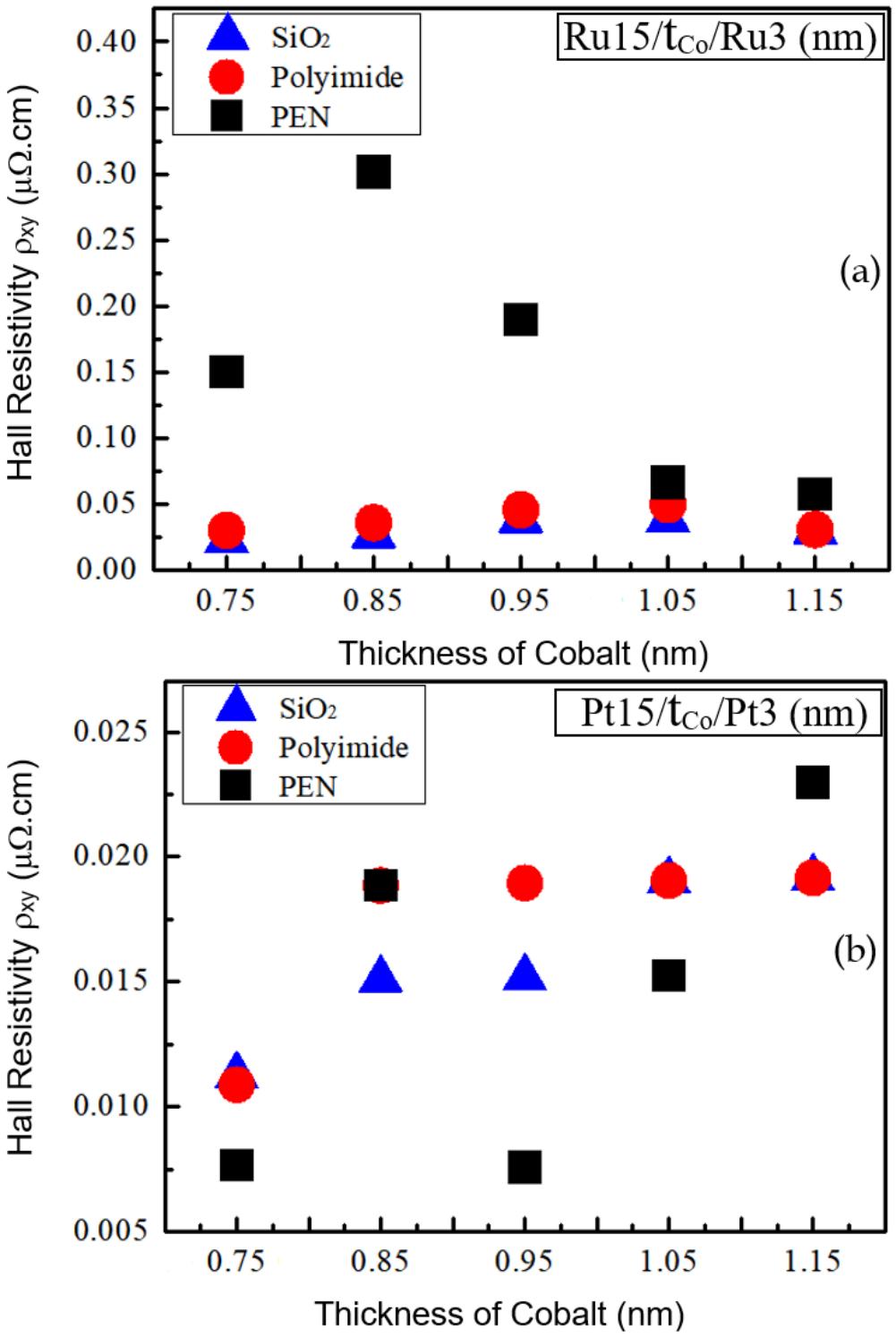

Fig. 7.17 (a,b) Hall resistivity for both Ru15.0/(t_{Co})/Ru3.0 nm and Pt15.0/(t_{Co})/Pt3.0 nm on SiO_2, polyimide and PEN substrates respectively as a function of the cobalt thickness. The error bars are very small.

the Hall resistivity is approximately stable for Co thicknesses from 0.75 nm to 0.95 nm, which later increases at t_{Co} = 1.05 nm and decreases at t_{Co} = 1.15 nm.

In Fig. 7.17 (a), in case of using PEN substrate, the increase in resistivity was shown from t_{Co} = 0.75 nm to 0.85 nm and then decrease from 0.85 nm to 1.15 nm. While similar trend was shown for both SiO_2 and polyimide substrates. The resistivity increased from t_{Co} = 0.75 nm to 1.05 nm then it reduced at t_{Co} = 1.15 nm. In Fig. 7.16 (b), the Hall resistivity increased from t_{Co} = 0.75 nm to 1.15 nm for all cases SiO_2, polyimide and PEN substrates.

7.9 Analysis of results and discussion

The focus of this chapter is to compare the role of Ru and Pt in the formation of PMA in NM/Co/NM multilayers. This comparison combines structural analysis using Atomic force microscopic and x-ray diffraction with magnetic measurements from the Hall Effect. In thin-film systems, such as Co/Pt [81] and Co/Pd [201], out-of-plane remnant magnetisation is associated with the perpendicular magnetic anisotropy that occurs over a limited range of ultra-thin thicknesses of the ferromagnetic layer. The physical origin of this PMA is linked to the increasing importance of the ferromagnet surfaces in the ultrathin limit. The anisotropy is also sensitive to the details of the surface structure, the crystallographic orientation and interfacing with other thin-film materials, such as Pt or MgO [201]. The ferromagnetic film structure and interfacial roughness can be influenced by the buffer layer, which is likely to be affected by the substrate which may influence the difference between Ru/Co and Pt/Co thin-films.

To understand the structure, the results from using atomic force microscope are combined with a structural investigation using XRD. The XRD results from the films are illustrated in Fig. 7.18 for Pt/Co/Pt. Where it is clear that the XRD data showed only one peak at 40^o for Pt (111). This indicates the coherent growth of the trilayered (TL) Co/Pt (111) structure. For Pt/Co/Pt thin-film sample an intense peak at $2\theta = 40^o$ corresponds to (111) fcc Pt. The

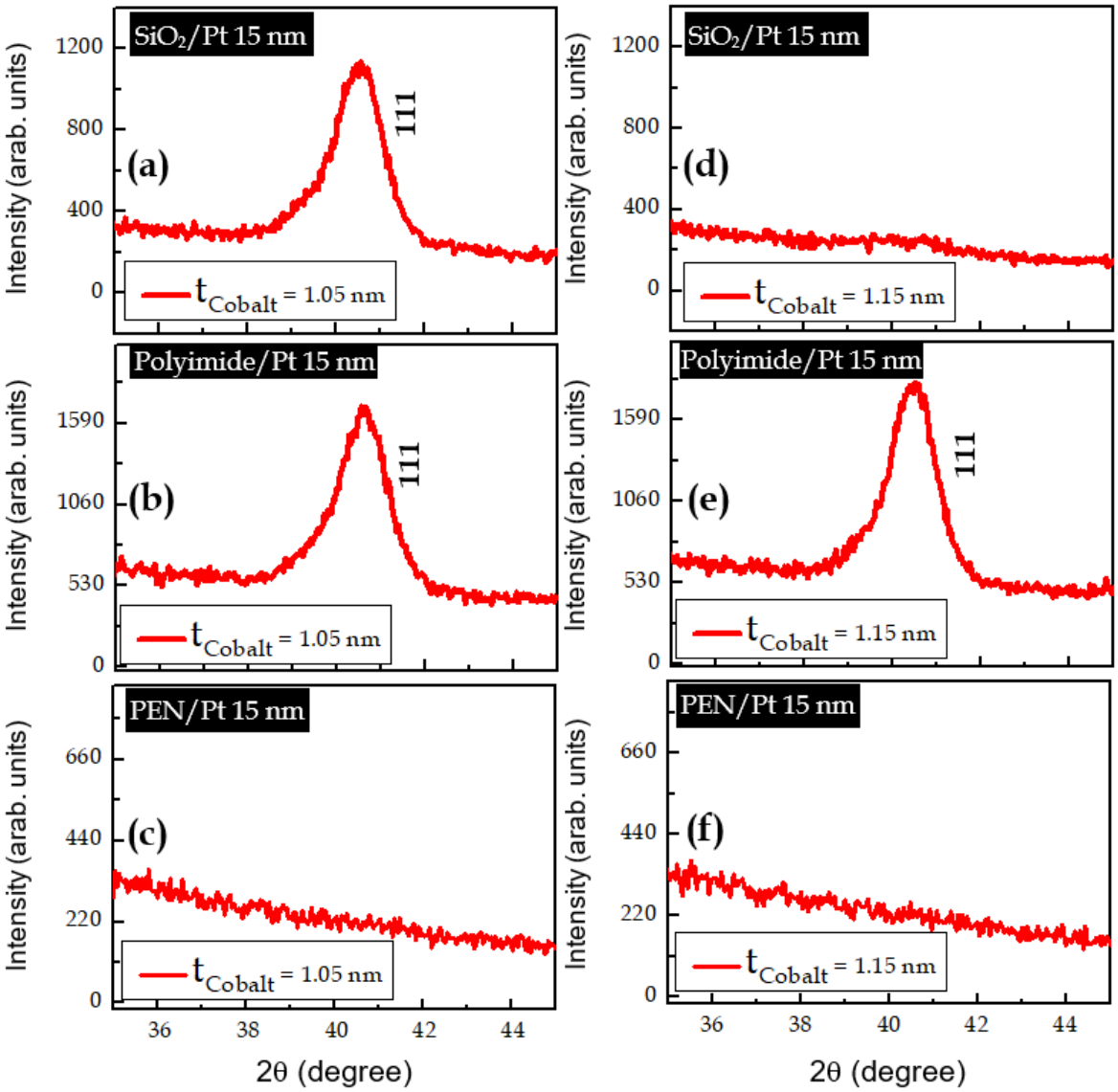

Fig. 7.18 (a,b,c). XRD patterns with 15 nm t_{Pt} with t_{Co} = 1.05 for SiO_2, polyimide and PEN respectively. (d,e,f). XRD patterns with 15 nm t_{Pt} with t_{Co} = 1.15 for SiO_2, polyimide and PEN respectively.

2θ position was consistent with the value reported for fcc Pt. The intense Pt (111) peak shows a high crystal quality at t_{Co} = 1.05 nm as it shown in Fig. 7.18 (a,b,e). In the situation of Pt/Co thin-films, the growth was more like Volmer-Weber (VW) [202], which leads to stress-free thin-film. In Fig. 7.18 (a), due to the good PMA observed previously, an intense Pt (111) peak would be expected due to the correlation between structural and magnetic properties i.e. magnetic anisotropy [203, 115]. The reason behind the absence a significant

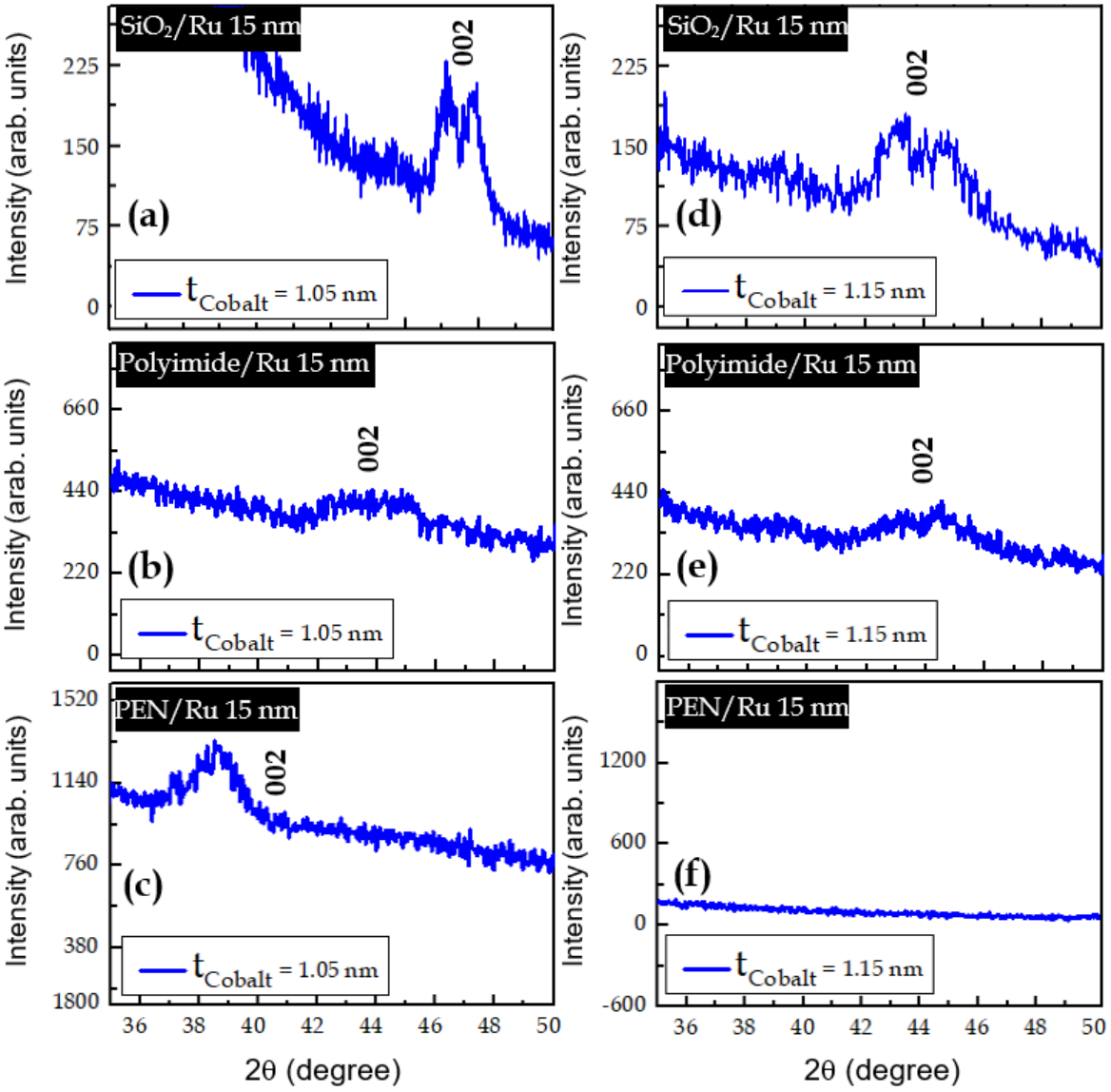

Fig. 7.19 (a,b,c). XRD patterns with 15 nm t_{Ru} with t_{Co} = 1.05 for SiO_2, polyimide and PEN respectively. (d,e,f). XRD patterns with 15 nm t_{Ru} with t_{Co} = 1.15 for SiO_2, polyimide and PEN respectively.

Pt (111) peak in Fig. 7.18 (d) to may be some mistake in the measurements that was done. Also, in Fig. 7.18, in the case of SiO_2 a slight change in intensity may be an artefact of the alignment procedure again (flatter substrate is more prone to this problem). In case of polyimide Fig. 7.18, the peak has shifted compared to SiO_2 case and is less intense and there is no significant difference with Co thickness as expected. While, in the case of PEN as

it shown in Fig. 7.18, the peak has shifted further to lower angle, no peak for thicker Co probably also a measurement alignment artefact. Also, in Fig. 7.18 (c,f), in case of PEN, the higher roughness of buffer layer may be linked to the disappearance of peaks and suggests a poor crystal quality of structure. This may be related to the large average maximum RMS roughness for PEN of 1.4 nm. On the other hand, in Fig. 7.18 (b,e), in case of polyimide at t_{Co} = 1.15 nm, it was found that there was an improvement of anisotropy due to a higher crystal quality of structure, confirming that there is a correlation between a magnetic property [i.e, anisotropy] and structural characterization [203, 115]. It was found that there was no significant change in the texture of peaks, that means the anisotropy was approximately same or close to each other at t_{Co} = 1.05 nm and 1.15 nm respectively and the anisotropy seems to be enhanced more in case of polyimide substrate at t_{Co} = 1.15 nm.

In the situation of Pt/Co/Pt that was grown on polyimide substrate, it appears that there was a slight shifting; where the intensity of peak was decreased. This may be linked to a decrease of anisotropy. Moreover, according to the results of roughness of Ru buffer layer, it was found that the corrugation was higher than in Pt case. The analysis of these differences might be due to the result of growing Ru/Co in a structure similar to Stranski-Krastanov mode which was explain in chapter 3. Several studies have looked at the deposition of Co on Ru, showing that it can lead to the formation of islands in a Stranski–Krastanov growth mode [189, 204–206]. The surface interface energy increases in this mode leading to lattice strain, which is due to the distortion of cobalt lattice due to the mismatch between Co and Ru and may also be affected by the higher roughness in the case of using Polyimide and PEN substrates.

In Fig. 7.18 (c,f), for thin Pt/Co films that were grown on PEN substrate, the peaks disappeared consistent with decreasing of anisotropy and with increasing surface roughness. Surface/interface roughness was shown to have an important influence on the demagnetizing field [207]; When the thickness of cobalt was 1.05 nm and 1.15 nm respectively, the dis-

appearance of the peaks Pt/Co/Pt thin-film was due to the poor crystal quality of thin-film. Moreover, this may be coming from the higher roughness of polyethylene naphthalate as is noted in the section on atomic force microscope measurements. In the case of Ru/Co/Ru thin-film, the Ru (002)/Co was present. According to Kolesnikov[116], it was found that the lattice mismatch on the Ru/Co due to the strain leads to distortion of the Co lattice. The average maximum root mean square roughness for Ru grown on PEN substrate is 1.5 nm and this caused to a shifting in the peak angle as it shown in Fig. 7.19.

In Fig. 7.19, in case of Ru buffer layer grown on PEN, it is shown that there is a shifting of the Co/Ru lattice peak position at 2θ with different substrate material, which may suggest that the roughness leads to increase the strain of the film. Also, it is very interesting to note that the intensity of the peak decreased and that there was an appearance of small peak at 2θ = 46.25^o for the higher roughness of the 15 nm Ru buffer. Hence, this is because of the loss of lattice correlations of the structure [114] where the maximum average root mean square roughness was 1.5 nm. The conclusion of this result that the increasing of roughness plays an important role in defining the decreasing of anisotropy for Co/Ru trilayers and also it was reduced the quality crystal with coherent Co/Ru trilayers structure.

The grain sizes in Fig. 7.20 were calculated from the XRD peaks using Scherrer formula [208]. For conventional XRD this is the out-of-plane grain size D, given by the Debye-Scherer equation D = 0.9 λ/β Cosθ_B, where, λ is the wavelength of the incident x-ray beam, θ_B is the diffraction angle and β is the FWHM at θ_B in radians. In Fig. 7.20 (a.c), it is shown that the grain size in the case of using a Pt buffer layer was bigger than in case of using Ru buffer layer as it shown in Fig. 7.20 (b.d). The anisotropy is higher in case of SiO_2 which was associated with high crystal quality due to smooth surface [lower RMS roughness = 0.25 nm]. With increasing of the full width half maximum the perpendicular magnetic anisotropy was decreased [209]. Also, the higher values of FWHM appeared in Ru samples in comparison with Pt samples.

The grain size of the magnetic material constitutes an important structural factor that affects decisively the magnetic properties i.e, the magnetic anisotropy. Some investigations were conducted on the impact of microstructure on magnetic properties of magnets, where the impact of the improvement of the grain size is linked with the measured M-H Hall hysteresis behaviour that is related to the anisotropy [209] K_{eff}, which increases linearly with t_{Pt} [115]. According to these studies, when the diffraction peaks indicate a high crystal quality, this means the anisotropy was higher compared to broader, or less intense diffraction peaks [23, 114, 115]. The increase in peak intensity relates to the increase in grain size of the thin-film and any shift in peak mode is due to stress as the film thickness increase. It is well known that very thin film contain different defects points [210].

In Fig. 7.10, 7.12 and 7.14, the use of Ru buffer layer, lowers coercive field values were found due to decrease in grain size, which leads to decrease in perpendicular magnetic anisotropy. While, in the case of using Pt buffer layer, the highest value of coercive field shown because of the bigger grain size. Almost all the deposited films showed the out-of-plane loops with a remanence ratio of $M_R/M_S = 1$, which indicates the dominant PMA. The higher coercive field in Pt/Co/Pt compared to Ru/Co/Ru appears to be generally related to the improved crystallinity of the Pt (111) buffer layer over that of the Ru (002) buffer layer, which in turn appears to be correlated to the increased surface roughness of Ru over that of Pt buffer layers. This is considered here as the first reason for why the coercive field of Ru/Co/Ru trilayer thin-film is smaller than the coercive field of Pt/Co/Pt trilayer thin-film. The second reason suggested is the smaller grain size of Ru/Co TL, which is linked to lower coercive field.

For more clarification, the broken bonds at the surfaces of a thin-film or interface in a multilayer leads to a change in the crystal fields and energies of dipole of the atoms at these surfaces [24]. These interfaces will usually cause uniaxial anisotropy. Where, it is clear that the energy of surface increased along with corrugation of the surface which is being lowest

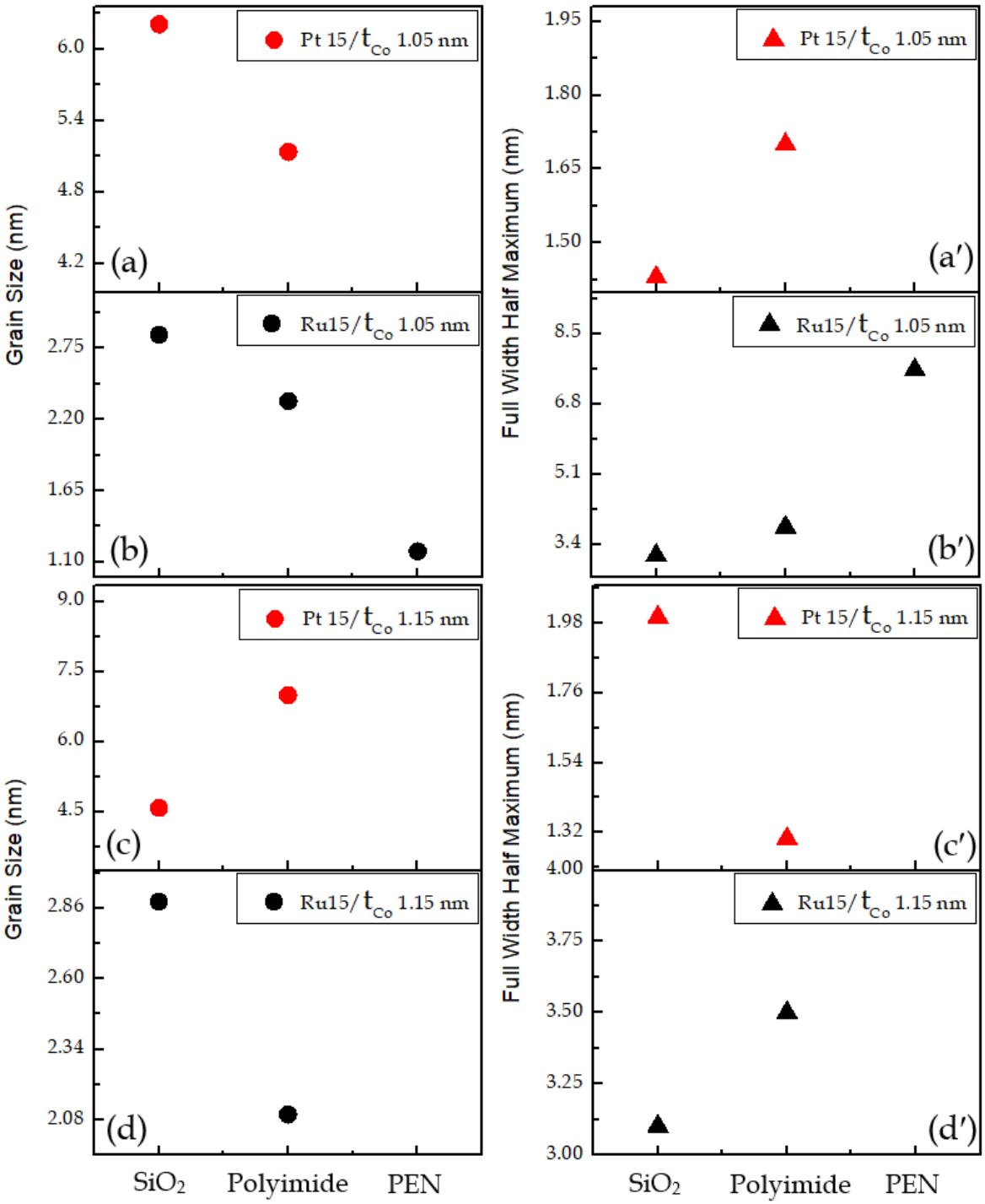

Fig. 7.20 (a,b,c,d) Grain size for t_{Pt} 15.0/t_{Co}/t_{Pt} 3.0 nm and t_{Ru} 15.0/t_{Co}/t_{Ru} 3.0 nm values at t_{Co} = 1.05 nm and 1.15 nm respectively. (a',b',c',d'). Diagrams illustrate the comparison between the full width half maximum for both t_{Pt} 15.0/t_{Co}/t_{Pt} 3.0 nm and t_{Ru} 15.0/t_{Co}/t_{Ru} 3.0 nm trilayer thin-film using different kinds of substrates.

for the fcc (111) surfaces [24] because of smooth surface. While, In case of Ru (002) the energy of surface was higher due to higher strain and roughness/corrugation.

It was shown that ultrathin cobalt films containing a few thick monolayers have an out-of-plane easy axis, transform to in-plane direction with an increasing film thickness [151]. Where the transformation from out-of-plane to in-plane was shown in the range of (t_{Co}) = 0.95 to 1.15 nm for Pt15.0/(t_{Co})/Pt3.0 nm. Rough surfaces/interfaces of thin films lead to scattering of electron and hence to electrical resistivity of the film. In the case of Ru15.0/(t_{Co})/Ru3.0 nm and Pt15.0/(t_{Co})/Pt3.0 nm, it was seen that Hall resistivity decreased with increasing of cobalt thickness (t_{Co}). However, it was still higher than the case of using Pt15.0/(t_{Co})/Pt3.0 nm. The reason for higher Hall resistivity of Ru/Co may be related to increase of roughness which can increase scattering. It was shown that the Hall resistivity increased with increase cobalt thickness and this was associated with a decrease of the anisotropy with increasing cobalt thickness from 0.75 to 1.15 nm. Hence, fcc cobalt-films of a few monolayer thick have a perpendicular easy axis, which transforms to in-plane as the film thickness increases. This anisotropy was extremely dependent on the details of the surface structure, and hence affected by the impurity adsorption, surface reconstruction, relaxation, segregation, and other properties [24].

In general, to give more insight on the structural role for both Pt and Ru buffer layers, XRD measurements were carried out. The MLs grown on Pt and Ru buffer layers showed out-of-plane hysteresis loops at t_{Co} = 1.05 nm. With further increase of cobalt thickness t_{Co} = 1.05 nm, the PMA decreases and this was identical with Kulkarni [209], where PMA decreases at t_{Co} = 1.05 nm. Cobalt thickness more than 1.15 nm is the transition point from out-of-plane to in-plane easy axis direction. This result might be coming from the formation of many crystal grains at the interface which leads to poor quality of crystalline structure.

The result of the surface morphology investigation of single-layer Pt and Ru films by means of AFM showed that the buffer layer smoothen the surface of the naturally oxidized

SiO_2 substrate. The root mean square roughness was observed at t_{Buffer} = 15.0 nm. However, increasing surface roughness is observed to be greater in Ru compared with Pt for all substrates. PMA in Co films may be attributed to large strain due to an in-plane expansion of cobalt, and in increase of the contribution for the interface between Co and Ru nonmagnetic metal. This contributions have been made to link between the magnetic anisotropy with atomic structure by estimating the energy of magnetoelastic anisotropy from the strain in the films [211, 212, 25, 213, 214]. Beyond the thickness of the layer, the growth and strain of a coherent layer can no longer be absorbed, and the strain was expected to be relaxed with increasing cobalt thickness [188]. In the case of a Ru buffer layer, the strain has been shown to be higher than the case of using a Pt buffer layer. A Ru buffer layer 15.0 nm thick was suggested to have a less homogeneous surface, so Ru/Co trilayer thin films have a poorer crystal quality and a weaker PMA. This comes from increased roughness of Ru 15 nm that contributed to the decrease in the quality of the crystal structure and PMA.

According to Fig. 7.16 (a,b,c), it was shown that the Hall resistivity in the case of using 15 nm Pt buffer layer is smaller than in case of using 15 nm Ru buffer layer. This is because, in Pt15.0/t_{Co}/Pt3.0 nm case the grain size was larger, and the scattering leading to resistivity was lesser. On the other hand, higher Hall resistivity was found in the case of Ru15.0/t_{Co}/Ru3.0 nm with smaller grain sizes. Increasing Hall resistivity with 15.0 nm high seed layer of Ru can be linked to shortness of the effective free path. In contrast, lower Hall resistivity and smaller variation with increase of thickness of cobalt were found in case of using Pt seed layer because of longer mean free path. In general, the grain boundaries had an effect on the Hall resistivity. The reduction in grain size, increases the probability of dispersion at grain boundaries and increases resistivity [200]. This situation occurred when the Ru buffer was used.

7.10 Conclusion

This study compared the viability of Ru and Pt as a buffer layers for producing high - quality Pt/Co TLs with PMA. In comparison to the TLs sputtered on Pt buffer layer the TLs using Ru buffer layers exhibited lower PMA. It was found that with increasing cobalt thickness from 0.75 nm to 1.15 nm the PMA samples with Pt buffer layer was significantly higher than Ru buffer layer. The enhancement of the PMA using Pt buffer layers was attributed to smooth of layer growth with pronounced (111) fcc crystallographic orientation. This was seen by using silicon dioxide substrate rather than the roughes polyimide and PEN substrates. The perpendicular magnetic anisotropy was higher in the case of SiO_2 in comparison with Polyimide and PEN. Even though, the use of polyimide substrates showed Pt (111) textured layers a XRD and a significantly decreased mean island height. A minimum roughness [0.25 nm] was achieved with 15 nm thick Pt (111) buffer layers on SiO_2. It was found that the effective anisotropy and coercive field of the Co layer were very sensitive to the buffer layer material. The coercive field values increased approximately from 10 Oe of Ru in comparison to about 1000 Oe for the Pt case. This was associated with the larger grains growth of Pt while Ru has a smaller grains growth. The impact of surface roughness on the Hall resistivity of the films was also found. Higher Hall resistivity was found in the case of Ru/Co/Ru in comparison with lower Hall resistivity in the case of Pt/Co/Pt. This study was focused on the interaction between morphology and magnetic properties of thin films. Moreover, it provided a simple but powerful instrument, based on the buffer layer engineering, to enable significant enhancement of PMA and coercivity of Ru/Co/Ru trilayers, making them suitable for wide range of spintronic applications. The trilayers sputtered with Pt exhibited improvement of PMA in comparison to trilayers with Ru layers. In particular, the Pt/Co/Pt buffer layers allow to maintain magnetization out-of-plane up to cobalt thickness of 1.05 nm in the case of SiO_2 substrate, which was a significant increase compared to the maximum cobalt thickness exhibiting PMA of 1.05 nm attained with Ru buffer layers. The improvement of PMA using

Pt buffer layers was due to the growth of a layer with clear crystalline (111) orientation and a coherent strain at t_{Co} = 1.05 nm.

Silicon dioxide wafers had the lowest surface roughness and were used in the fabrication of Pt/Co/Pt and Ru/Co/Ru TLs characterized by strong PMA. The AFM characterization of Si/SiO_2 under specific systems confirms the flattening of overlapping areas on the surface of the thin-films compared with the use of polyimide and polyethylene naphthalate, leading to smoothed morphology of the Pt/Co/Pt and Ru/Co/Ru films. The phase composition of thin-films studied by XRD demonstrates the crystallinity of Pt/Co and Ru/Co thin-films. The Hall effect hysteresis loops recorded under an external magnetic field orthogonal to the sample surface reveal the PMA in these thin-films. The coercive field and effective anisotropy field can be considerably enhanced by the thickness variation of the buffer layer. This study was focused on the interaction between morphology or topography and magnetic properties of trilayer thin films. This gives a simple but strong instrument dependence on the buffer layer, which gives a significant improvement of PMA, making them appropriate for a broad range of spintronic applications. The trilayers that were grown on Pt buffer layers showed enhancement of PMA in comparison to trilayers that were grown on metallic Ru buffer layers. The improvement of PMA using Pt buffer layers was due to the growth of a layer with clear crystalline (111) orientation.

Chapter 8

Understanding magnetization reversal in Pt/Co/Pt trilayer thin films on Silicon Dioxide and Polyethylene Naphthalate substrates

8.1 Previous Work

The dynamics of a domain wall (DW) is considered as the significant topic for multilayer thin films of perpendicular magnetic anisotropy (PMA). Where, these magnetic objects can be used in the binary information as carriers in the super density for storage systems. However, the perpendicular magnetic anisotropy with high anisotropy have captured the attention of many researchers recently [215–222]. Hence, there are many advantages of the growing domain, and the motion steps have been found in ultra thin magnetic films of vertical anisotropy. The reflection properties of multilayers are determined by the interlayer coupling through a non-magnetic separator and the response of the magnetic layers of the applied

magnetic field. Various magnetization reversal advantages occurred in such structures that may be caused due to the advantages of magnetization reversal in single films, while others occur due to the interlayer coupling. Observing a detailed study was not found yet for the nucleation and growth of domain walls in Pt/Co/Pt ultra-thin structures having an equal Co thickness layers and various Pt spacer thickness, while the magnetic field is vertical in reverse. Micromagnetic calculations [39] were obtained in 2012; which confirmed empirically that the important role of Dzyaloshinskii-Moriya interaction (DMI) [223, 37, 38] at interfaces between ferromagnetic (FM) and heavy nonmagnetic elements [50, 224–231] spontaneous, skyrmion, and a higher velocity has been obtained in asymmetric t_{Pt} 2.0/t_{Co} 0.5/t_{Pt} 2.0 nm. The dynamics of magnetization reversal have been studied in ultrathin cobalt films [232–235, 156, 236]. It was shown that the reversed domains have grown at the same locations and grow isotropically. Also, the velocity of domain wall in ultrathin cobalt films were measured for a vast range of magnetic fields and temperature. Moreover, in other studies of [Co/Pt]n multilayers, the magnetisation reversal has been found after many different repetitions of ultrathin cobalt films [237–245]. This study present the magnetic domain-wall velocity measurements. It also showed experimentally that the magnitude of domain wall velocity is sensitive to the environment of the interfaces including the Pt layer thickness. In this study, the magnetization of domain wall structure has been presented using the polar Kerr microscopy.

8.2 Introduction

With regards to the previous chapters that examined the effect of the thicknesses of the ferromagnetic and nonmagnetic layers on the perpendicular magnetic anisotropy, this chapter presents the magnetization reversal behavior of $t_{Pt}/t_{Co}/t_{Pt}$ thin-films observed using polar Kerr effect microscopy. An explanation about the nucleation of reversal domains, bubbles and domain wall propagation in the presence of an out-of-plane field for $t_{Pt}/t_{Co}/t_{Pt}$ thin

films has been explained here. This chapter also reviews the various studies reported in the literature and compare these studies with the experimental results obtained in this work.

8.3 Experimental work

For this study, $t_{Pt}/t_{Co}/t_{Pt}$ films with perpendicular magnetic anisotropy were deposited on an Si substrate with a 150 μm thick SiO_2 layer and on a 125 μm polyethene naphthalate by DC magnetron sputtering. Prior to deposition, the substrates were cleaned with acetone and isopropanol. The $t_{Pt}/t_{Co}/t_{Pt}$ thin-film trilayers were deposited at room temperature by DC magnetron sputtering from a base pressure of 1.0 x 10^7 Torr. Argon with a purity of 99.998 % was introduced as a working gas. The deposition rates of Pt and Co were 0.1 Å /S and 0.2 Å /S respectively measured using a quartz crystal monitor calibrated from thickness measurements using x-ray reflectivity. The diameter of circular shape masked samples was 16 mm. The images of magnetic domain structures were obtained using a magneto-optical Kerr effect microscope magnetometer systems from (Evico), with a vertical field electromagnet. The mechanical stabilization tools for a standard microscope with a high-quality optics, assist in obtaining a high-resolution domain imaging.

8.4 Results of experimental study of field induced magnetisation reversal

Because of the importance of the ferromagnetic/nonmagnetic trilayer thin films for various technological applications fundamental properties, such as magnetization reversal have been a major key focus area of active research through several decades [246–250]. However, in spite of of the large amount of studies, a lot of aspects are still not well understood as magnetization reversal is a collective phenomenon [251], just as ferromagnetism is, but moreover it is also

very sensitive in nature to changes in structure or composition. Magnetization reversal is a dynamic phenomenon that predict the states of magnetization correctly. After reversal it should be taken the account of the dynamic behaviour of the system. Symmetry bubbles means the process of magnetization reversal, starting with the ”white” status through the emergence of a limited number of ”black” irregular areas these images show that up-to-down and down-to-up reversals of the magnetisation are very similar. While asymmetric bubbles mean the changing of the bubble domain structure, decreasing the threshold of magnetization reversal and asymmetrical of bubbles for both up/down and down/up direction of magnetization. Therefore, this study focus on imaging of magnetization reversal in $t_{Pt}/t_{Co}/t_{Pt}$ TL thin-films on rigid and flexible substrates as a function of Co and Pt thickness. For more understanding of the symmetric and asymmetric bubble expansion, this study was performed in the presence of a magnetic field. The Domain Wall of $t_{Pt}/t_{Co}/t_{Pt}$ TL thin-films was studied using (MOKE) microscopy.

8.4.1 Imaging magnetic domain structure as a function of Co thickness

In this study the nucleation and growth of domains was studied in $t_{Pt}/t_{Co}/t_{Pt}$ trilayer with different Co thicknesses. The magnetic field induced magnetic reversal for $t_{Pt}/t_{Co}/t_{Pt}$ trilayers using wide field Kerr microscopy was observed as a series of domain images captured at a constant time interval. Examples of differential MOKE microscopy images (i.e. with structural background subtracted as a function of Co thickness are shown in Fig. 8.1 (Pt thickness 5.0 nm) and Fig. 8.2 (Pt thickness 3.0 nm) respectively. These images were obtained by averaging several successively acquired images as the magnetic field was swept, and thus, each single image shows some domains expanding in time. It is observed that when the out-of-plane field was applied, a number of magnetic domains are nucleated and these then grow rapidly. Fig. 8.1 (a,a’-b,b’-c, c’,d,d’) and Fig. 8.2 (a,a’-b,b’-c, c’,d,d’) illustrated the process of magnetization reversal, starting with the ”white” status through the

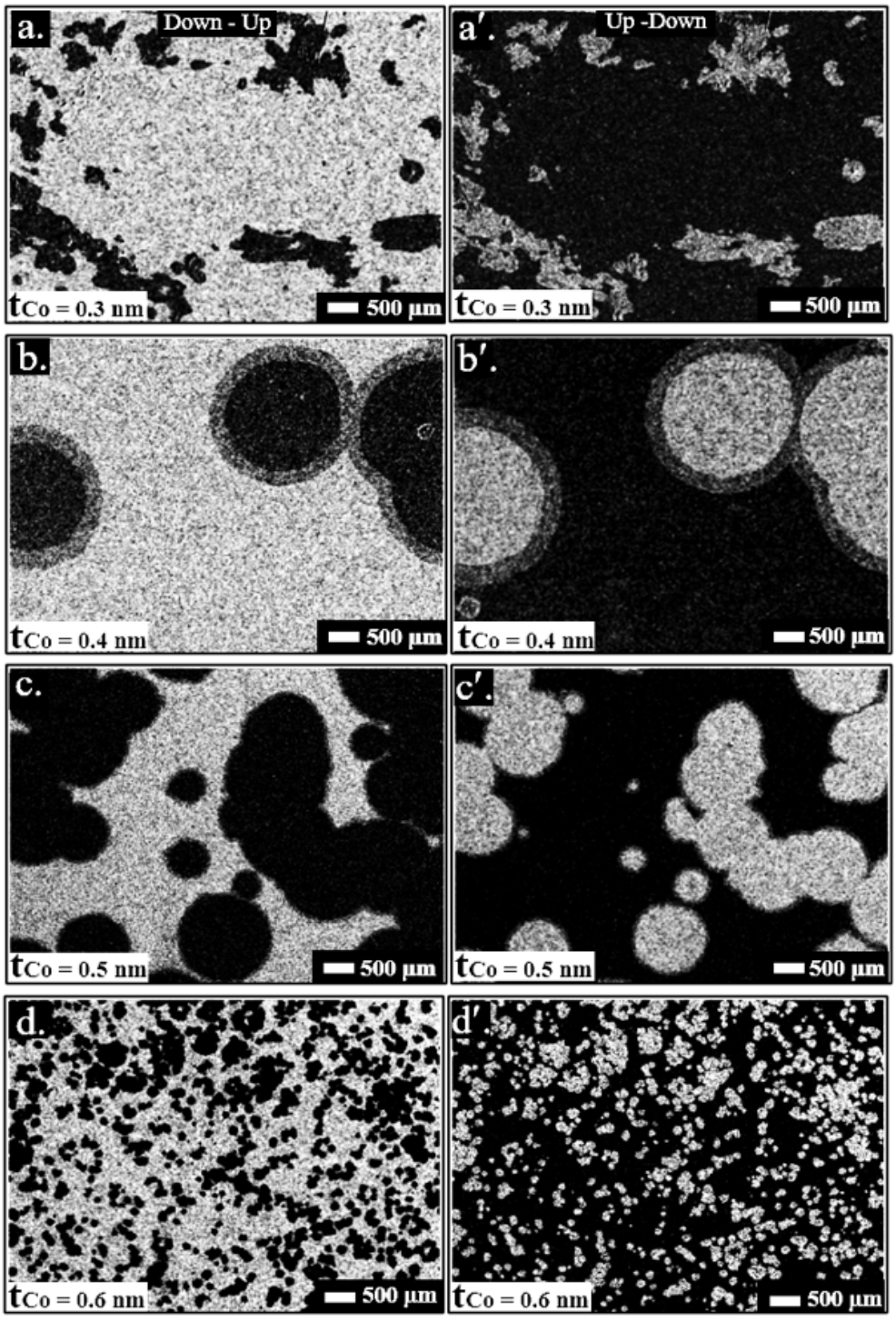

Fig. 8.1 MOKE images of the evolution of domain structure in the ultra thin cobalt as a function of Co thickness for $t_{Pt}5.0/t_{Co}/t_{Pt}5.0$ nm (a, a'). with H = +451 Oe and -334 Oe, (b, b'). with H = +169 Oe and -170 Oe, (c, c'). with H = +280.7 Oe and -278 Oe and (d, d'). H = +468 Oe and -464.9 Oe.

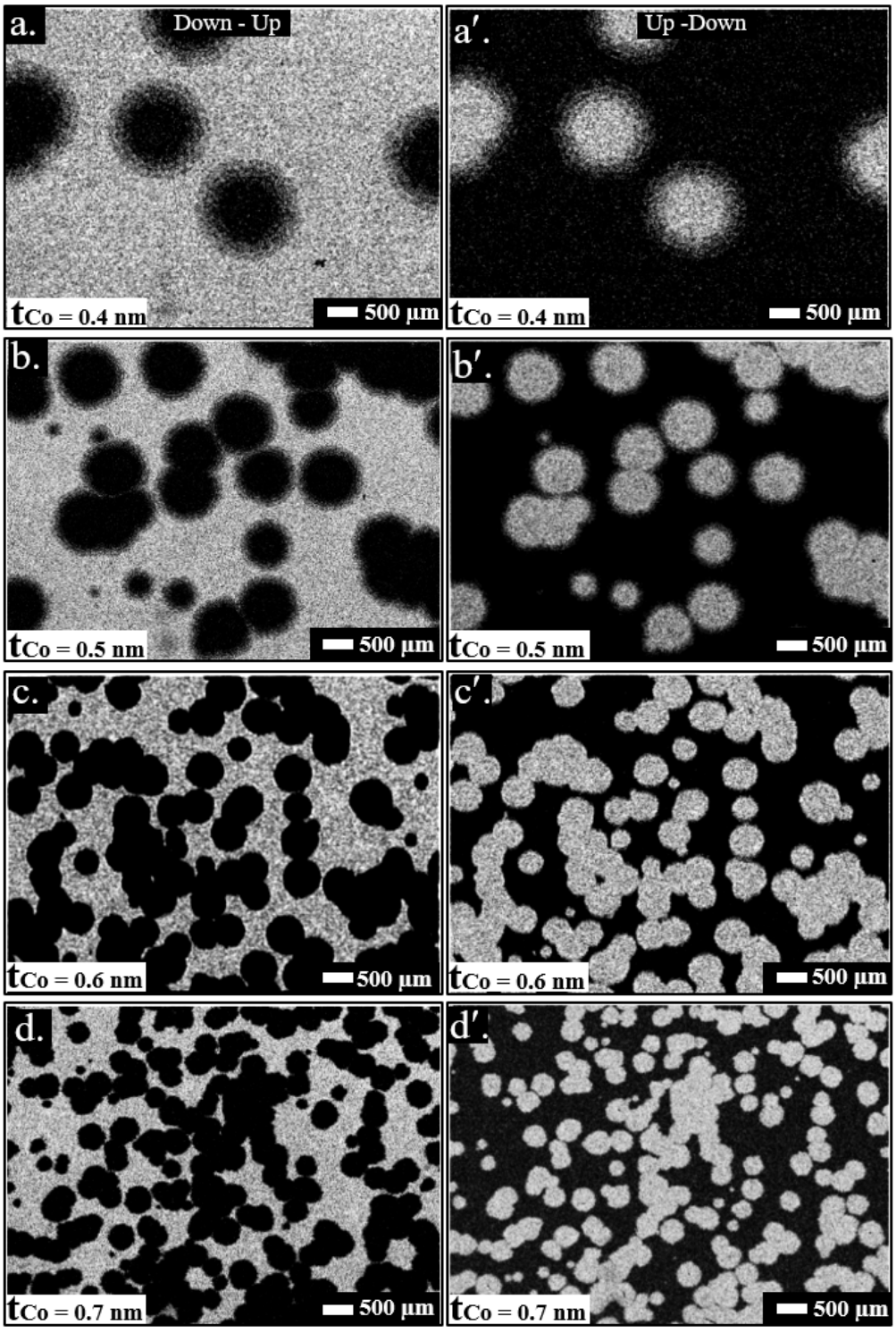

Fig. 8.2 MOKE images of the evolution of domain structure in the ultra thin cobalt as a function of Co thickness for $t_{Pt}3.0/t_{Co}/t_{Pt}3.0$ nm, (a, a').with H = +148.8 Oe and -148.2 Oe, (b, b').with H = +274 Oe and -271.2 Oe, (c, c').with H = +254 Oe and -251.9 Oe and (d, d').with H = +367.1 Oe and -368.3 Oe.

emergence of a limited number of ”black” irregular areas these images show that up-to-down and down-to-up reversals of the magnetisation are very similar. The influence of cobalt thickness on the magnetic properties of $t_{Pt}/t_{Co}/t_{Pt}$ nm trilayer is described below.

Reversal domains were observed for all cobalt thicknesses. For the thickness Pt/Co film the domains were irregular in shape but for all other films circular "bubble" domains were observed. The number of bubbles increased with an increase in the Co thickness from (t_{Co} = 0.3 to 0.7 nm) in Fig. 8.1 and from (t_{Co} = 0.4 to 0.6 nm) in Fig. 8.2. Also, when the cobalt thickness increases the mean size of the domains observed decreases.

In Figs. 8.1 and 8.2, for a different range of cobalt thickness, the formation and spreading of bubble domains were observed under variation of the magnetic field magnitude. Figs. 8.1 and 8.2 clearly show that when a circular domain expands under an out-of-plane magnetic field, the center of the circular domain did not shift.

By increasing the cobalt thickness a reduced of bubble domains was obtained. Through the analysis of the Kerr microscopy images for the bubbles of trilayer thin films with t_{Co} larger than 0.4 nm (after applying of magnetic field), the number of bubbles domain nucleated increased in number but the grew less with further increase in magnetic field.

8.5 Imaging of magnetic domain structure as a function of Pt thickness

The influence of the buffer layer thickness t_{Pt} on the magnetisation reversal was analyzed by using different thickness of Pt layer (t_{Pt} = 2.0 nm, 3.0 nm and 5.0 nm), where the Co layer has a thickness of 0.5 nm in all samples.

Fig. 8.3 (a, a’) showed that a Pt buffer layer equal to 2.0 nm changes the bubble domain structure, decreasing the threshold of magnetization reversal and asymmetrical of bubbles for both up/down and down/up direction of magnetization. While Figs. 8.3 (b, b’) and (c,c’)

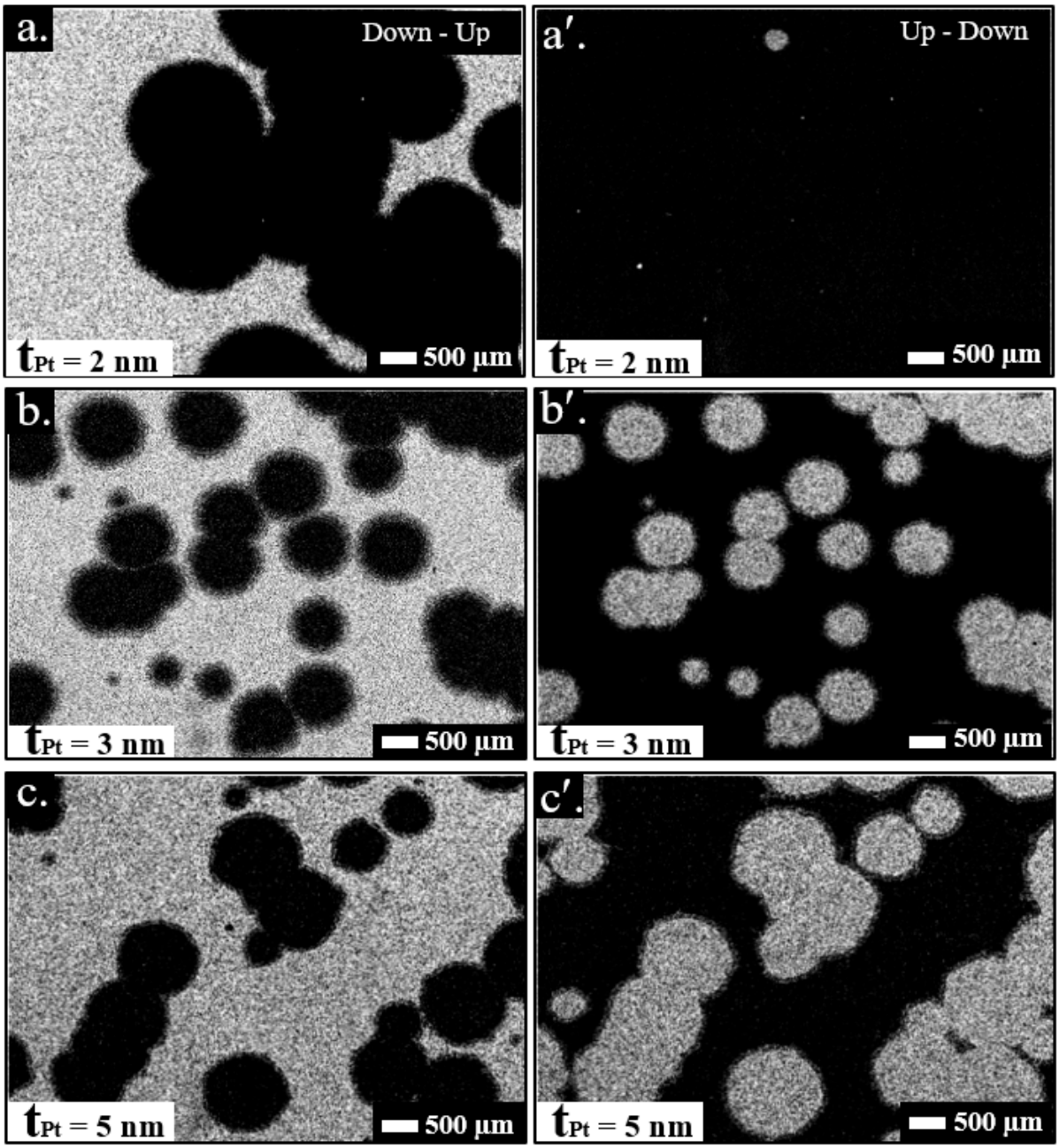

Fig. 8.3 MOKE images of the evolution of domain structure in t_{Pt} 2.0/t_{Co} (0.5)/t_{Pt}t 2.0 nm (a, a'). with H = +179 Oe and after subsequent magnetic field switch to H = -179 Oe. For t_{Pt} 3.0/t_{Co} (0.5)/t_{Pt} 3.0 nm (b, b'). with H = +274 Oe and after subsequent magnetic field switch to H = -274 Oe. For t_{Pt} 5.0/t_{Co} (0.5)/t_{Pt} 5.0 nm (c, c'). with H = +169 Oe and after subsequent magnetic field switch to H = -169 Oe.

showed an increase in a number of bubbles domains nucleated in comparison to the thinner Pt in Fig. 8.3 (a, a').

8.5.1 The domain nucleation site density vs cobalt and platinum thickness

The magnetic domain nucleation site density can simply be found by taking the total number of nucleation sites and dividing by the total image area.

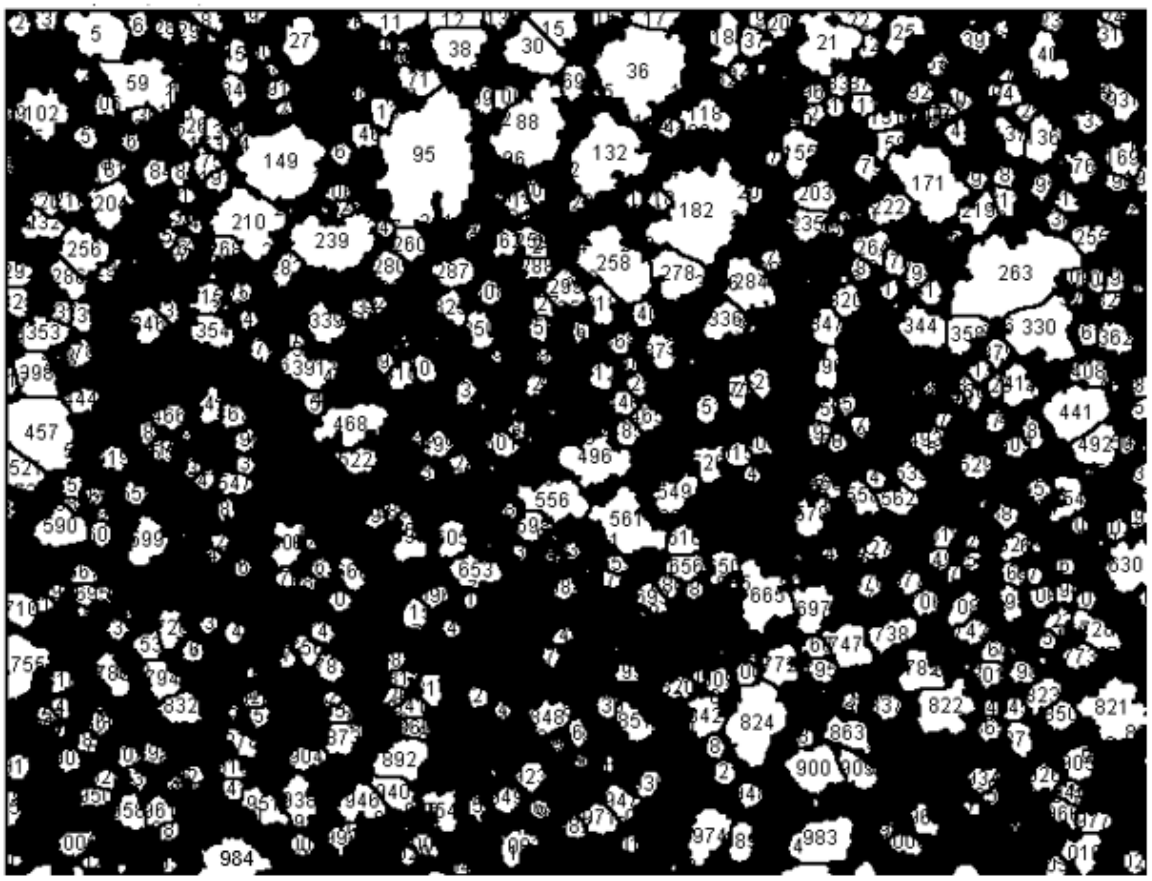

Fig. 8.4 Domain walls by Evico Kerr microscope images for t_{Pt} 5.0/t_{Co}0.6/t_{Pt} 5.0 nm as a function of the direction of applied magnetic field H = -464.9 Oe using SiO_2 substrate.

Each site was selected by using ImageJ program. Fig. 8.4 shows the number of reversal (white) domains that was observed during reversal for a t_{Pt} 5.0/t_{Co} 0.6/t_{Pt} 5.0 nm trilayer thin-film, the domains are identified by using the ImageJ software. The area in ImageJ appears in pixel units, so it was necessary to convert from pixel units to μm units. The measured nucleation site densities versus cobalt thickness (0.3-0.6) nm is presented in Fig. 8.5 (a,b). While, the nucleation site densities versus cobalt thickness (0.4-0.7) nm is presented

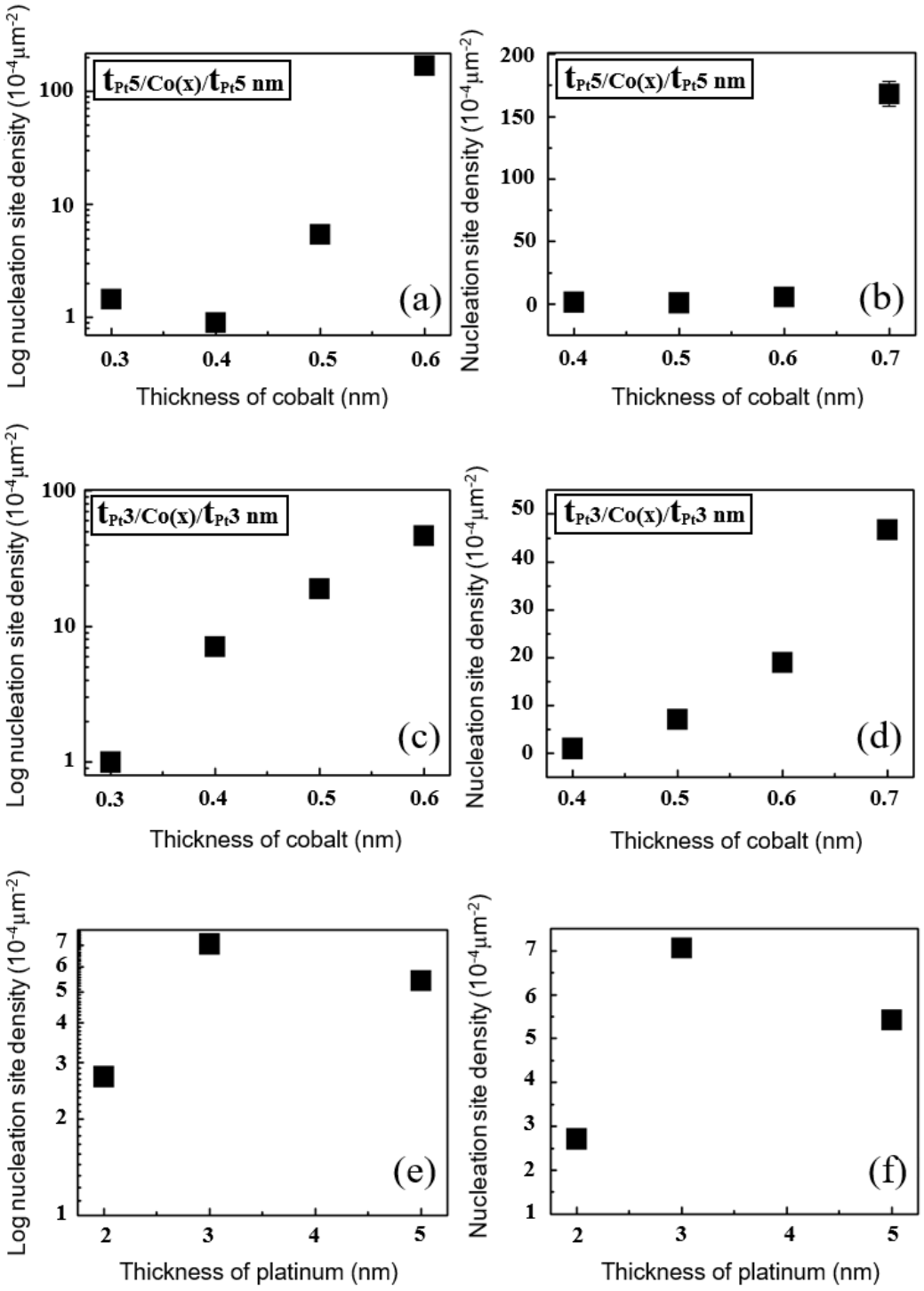

Fig. 8.5 (a,b) and (c,d) showed Log and linear nucleation site densities scales as a function of the cobalt thickness for t_{Pt} = 5.0 nm and t_{Pt} = 3.0 nm respectively. While, (e,f) showed Log and linear nucleation site densities scales as a function of the platinum thickness at t_{Co} = 0.5 nm.

in Fig. 8.5 (c,d). In both cases linear scale and log scales were presented in order to give more clarity of the trend for numbers that were very near to zero. Fig. 8.5 (e,f) shows the reverse domain nucleation site density as a function of the platinum thickness. Here, a low nucleation site density was observed at 2.0 nm Pt thickness and it increased at 3.0 nm then decreased a slightly for 5.0 nm platinum thickness with the cobalt thickness at 0.5 nm. It was shown that the nucleation site density increased with increasing cobalt thickness. The bubbles are pinned by using similar thickness of platinum in the top and buffer layers. While, in another case by using different thickness of Pt with similar thickness of cobalt.

8.6 DW velocity as a function of Co and Pt thickness

Magnetization reversal occurs here via nucleation of domains with reverse magnetization and growth of those domains by domain wall motion.

The movements of the domain walls were analyzed to study the domain wall velocities as a function of cobalt and platinum thickness. The velocity of the domain wall (DW_s) was calculated from the time lapsed domain structure imaging. From the circular domains imaged, the DWs velocity (v) was measured from the change in radius with a constant time step. The radius of a bubble domain was calculated through the program Gwyddion. In the present experiment, v was determined from 4 repeated measurements for each sample. Based on a number of bubble domains, the variation of the DW velocities has been determined.

The DW_s bubbles experience different effective fields $+H_z$ and $-H_z$, leading to differences in their velocities. In Fig. 8.6, a summary of the domain wall velocity is presented. Each data point in these figures represents the average values of all bubbles radius per the growth time of the single nucleation site in (second) over $5.521 \times 10^4 \mu m^2$ area in all captured images. The start of bubble growth simply corresponds to the time at which the field of the nucleation site begins to decline. The time at which bubble growth stops is set at the time when saturation magnetization in a region is reached. Fig. 8.6 (a) summarized the results of

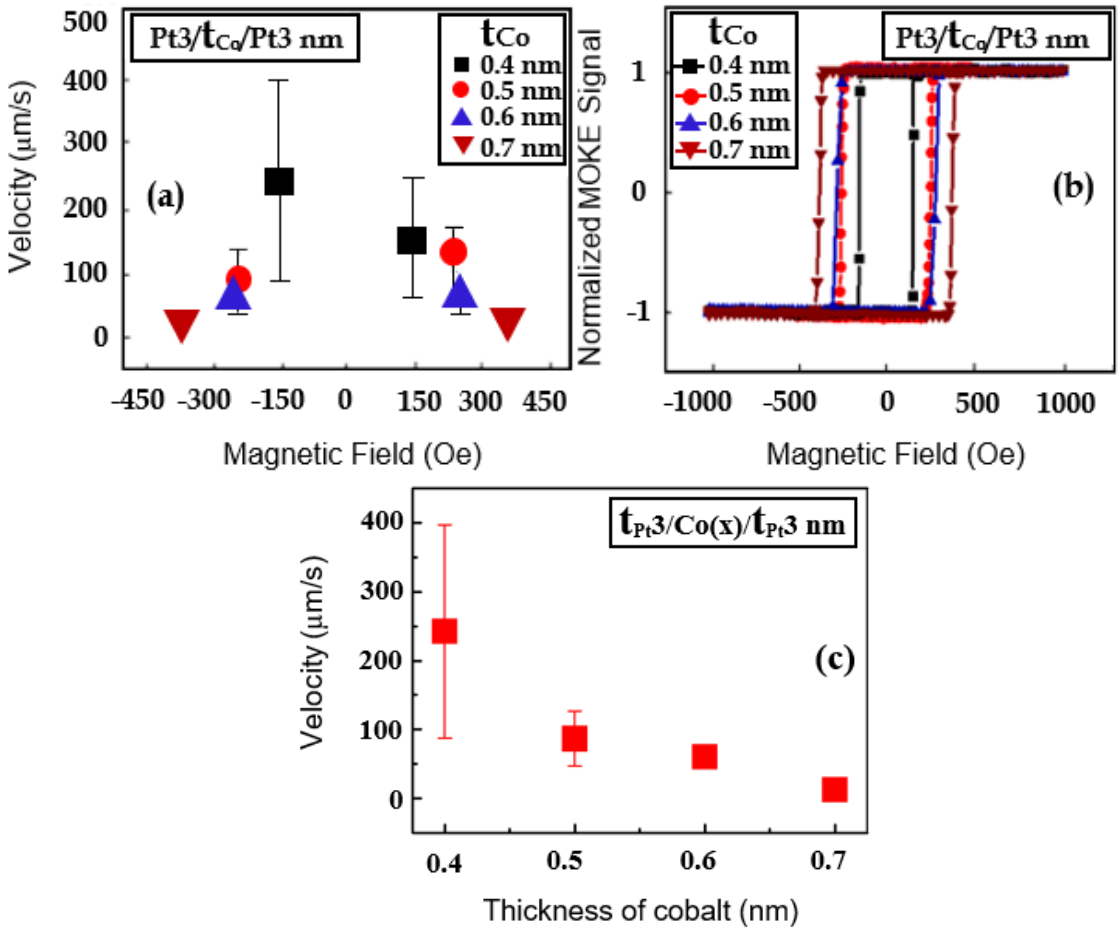

Fig. 8.6 a. Domain wall velocity of a t_{Pt} 3.0/t_{Co}/t_{Pt} 3.0 nm multilayers as a function of magnetic field. b. coercivity of a t_{Pt} 3.0/t_{Co}/t_{Pt} 3.0 nm multilayers as a function of magnetic field. c. Domain wall velocity of a t_{Pt} 3.0/t_{Co}/t_{Pt} 3.0 nm multilayers as a function of thickness of cobalt.

DW velocity for different Co thickness for a fixed 3.0 nm Pt thickness. The field at which the DW velocity is measured depends on the Co thickness because this determines the reversal field and coercivity, which increases with Co thickness. However, the domain wall velocity falls with increasing Co thickness, even though the magnetic field is higher. Fig. 8.6 (b) shows typical (MOKE) loops measured on trilayer samples of the same Pt buffer layer and capping layer (3.0 nm).

Fig. 8.6 (c) shows that the DW velocity decreases with increasing thickness of cobalt. Fig. 8.7 (a) summarizes the DW velocity with different cobalt thicknesses and a fixed Pt thickness

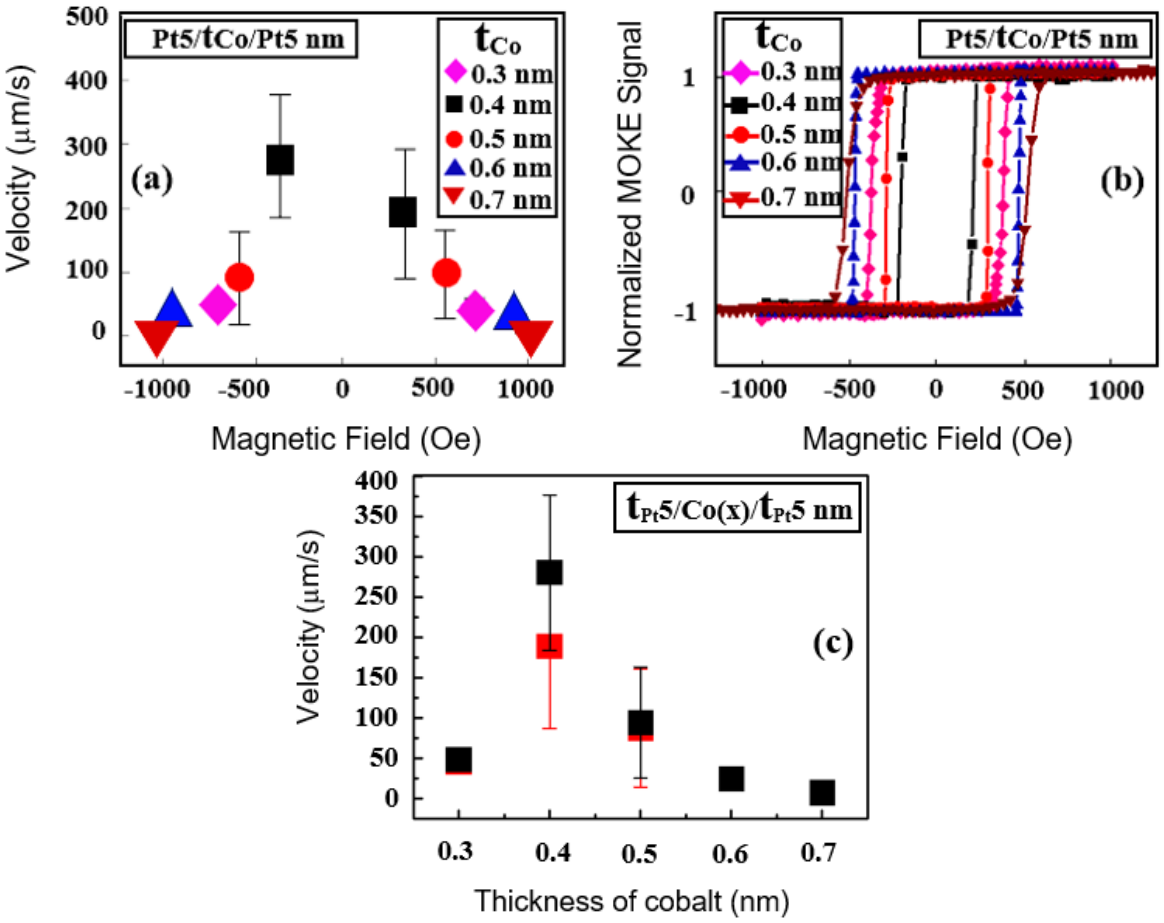

Fig. 8.7 a. Domain wall velocity of a t_{Pt} 5.0/t_{Co}/t_{Pt} 5.0 nm multilayers as a function of magnetic field.b. coercivity of a t_{Pt} 5.0/t_{Co}/t_{Pt} 5.0 nm multilayers as a function of magnetic field.c. Domain wall velocity of a t_{Pt} 5.0/t_{Co}/t_{Pt} 5.0 nm multilayers as a function of thickness of cobalt. The black and red symbols refer to the down-up and up-down reversal magnetization respectively.

of 5.0 nm. The behavior shows similar behavior to the samples with 3.0 nm Pt thickness, as is shown in Fig. 8.6 (a) except for the thinnest Co sample, for which the reverse domains are not circular bubbles. It is clear that the velocity decreased with increasing magnetic field. Fig. 8.7 (b) shows typical (MOKE) loops measured on trilayer samples of the same Pt buffer layer and capping layer (5.0 nm). Fig. 8.7 (c) shows the DW velocity as a function of cobalt thickness for 5 nm thick Pt samples. At the lowest cobalt thickness, 0.3 nm, the DW velocity is low. The velocity increased at 0.4 nm and then start to decrease with the increase of cobalt thickness following a similar trend to the 3 nm Pt samples.

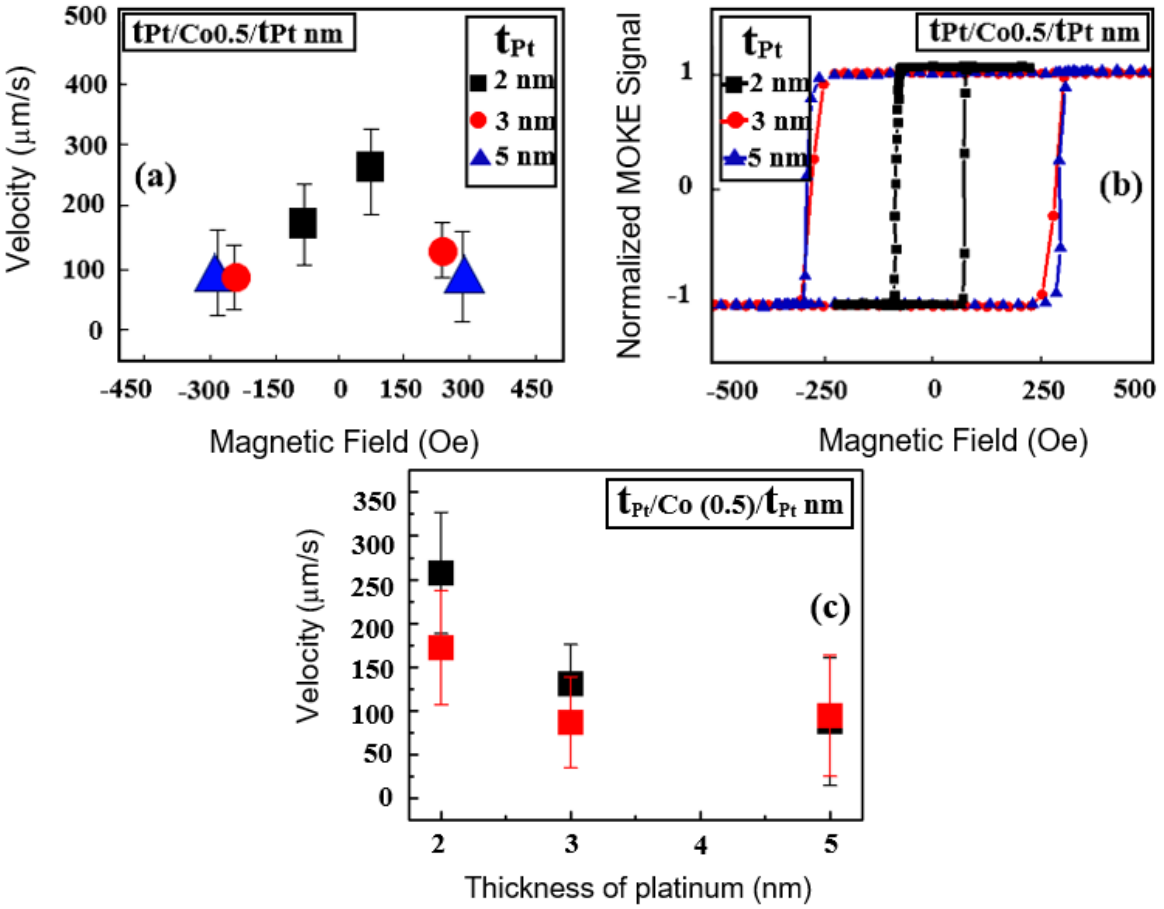

Fig. 8.8 a. Domain wall velocity of a t_{Pt}/t_{Co} (0.5)/t_{Pt} nm multilayers as a function of magnetic field.b. coercivity of a t_{Pt}/t_{Co} (0.5)/t_{Pt} nm multilayers as a function of magnetic field in (Oe).c. Domain wall velocity of a t_{Pt}/t_{Co} (0.5)/t_{Pt} nm multilayers as a function of thickness of platinum. The black and red symbols refer to the down-up and up-down reversal magnetization respectively.

Fig. 8.8 (a) summarize the results of DW velocity for different platinum thicknesses for 0.5 nm Co thickness. Fig. 8.8 (a) shows that the velocity of the domain walls decreased with increasing Pt thickness. The MOKE hysteresis loops for these samples are presented in Fig. 8.8 (b). All loops showed a very square loop; which indicates a good perpendicular magnetic anisotropy (PMA) which increased with the thickness of Pt from 2.0 nm to 5.0 nm. It is also noted that an asymmetry in velocity was obtained in the t_{Pt} 2.0/t_{Co} 0.5/t_{Pt} 2.0 nm sample, with a higher velocity for DW reversal in one direction than the other. The DW velocity was

reduced in sample with 3.0 nm to 5.0 nm of Pt. Fig. 8.8 (c), shows the DW velocity as a function of Pt layer thickness.

8.7 DW mobility vs Co thickness and Pt thickness

Magnetization reversal occurs via nucleation of domains with reverse magnetization and growth of these domains by domain wall motion. The velocity was analysed, and it was noted that the wall motion occured at different magnetic fields.

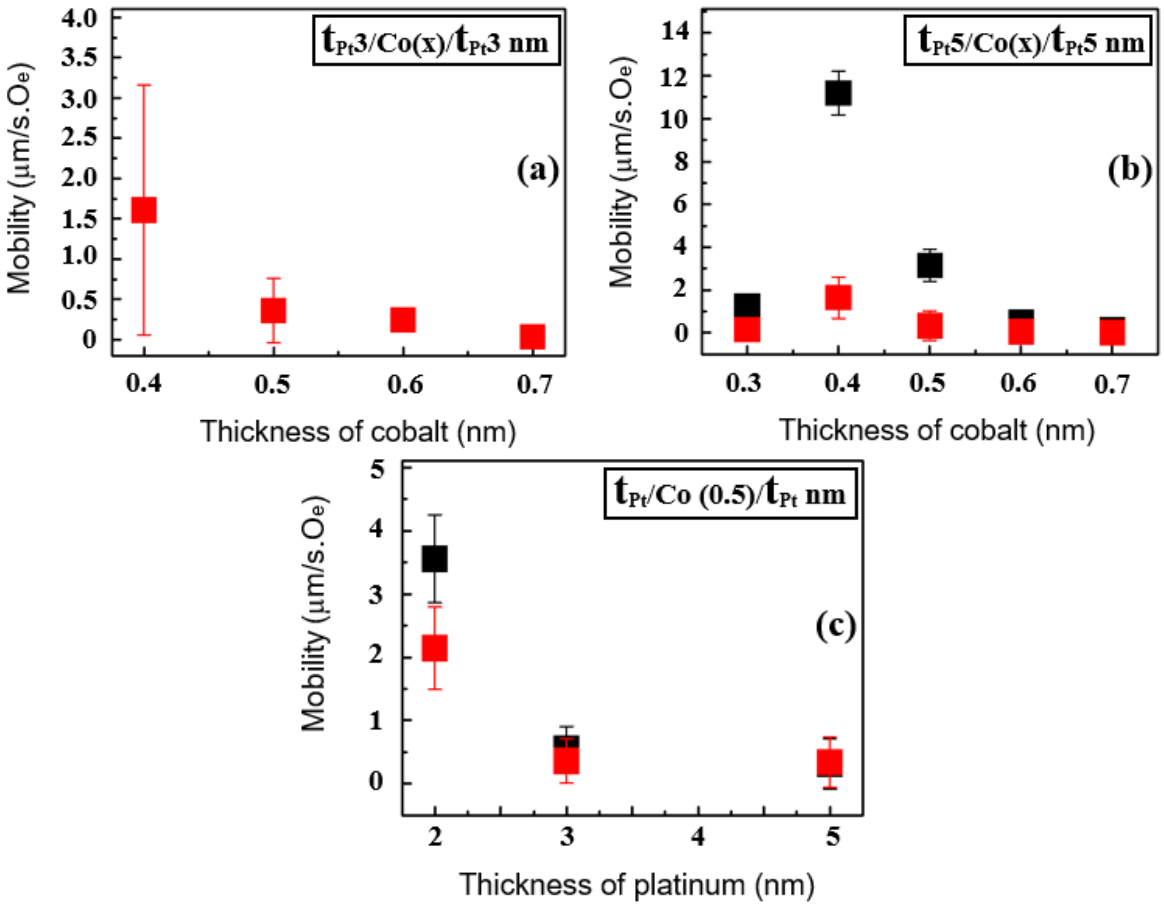

Fig. 8.9 a. Domain wall mobility of a t_{Pt} 3.0/t_{Co}/t_{Pt} 3.0 nm multilayers as a function of thickness of cobalt (nm). b. Domain wall mobility of a t_{Pt} 5.0/t_{Co}/t_{Pt} 5.0 nm multilayers as a function of thickness of cobalt (nm). c. Domain wall mobility of a t_{Pt}/t_{Co} (0.5)/t_{Pt} nm multilayers as a function of thickness of platinum (nm). The black and red symbols refer to the down-up and up-down reversal magnetization respectively.

To more directly compare the DW velocity between samples the domain wall mobility was calculated. The mobility is defined as the DW velocity divided by the magnetic field at which the velocity was measured. The DW mobilities as a function of cobalt and Pt thickness are compared. The general trend for mobility as a function of thickness of cobalt and platinum are shown in Fig. 8.9 (a, b) respectively. While, the DW mobility was at t_{Co} = 0.3 nm. Fig. 8.9 (c) showed the mobility was decreased from 2.0 nm to 3.0 nm and then it was approximately stable at 5.0 nm platinum thickness.

8.8 Imaging Magnetisation reversal behaviour in Pt/Co/Pt as a function of Pt thickness on flexible PEN substrate

To understand the effect of using different thickness of platinum on magnetic properties microscopically, it is necessary to image the magnetic domain structures under magnetic field. Fig. 8.10 (a,b and c) presents the magnetization reversal behavior of $t_{Pt}/t_{Co}/t_{Pt}$ multilayers on PEN substrates observed using the polar Kerr microscopy. In contrast to $t_{Pt}/t_{Co}/t_{Pt}$ films on SiO_2, a huge smaller number of nucleation sites was found at the t_{Pt} = 3.0 nm as shown in Fig. 8.10 (b). Fig. 8.10 (a',b' and c') showed the associated magnetization loops of the t_{Pt}/t_{Co} (0.6)/t_{Pt} nm trilayer thin films on PEN. It was shown that the coercive field increased with increasing the thickness of platinum from 1.0 nm to 3.0 nm to 5.0 nm.

The loop in Fig. 8.10 (b') showed a very squareness shape with a relatively high remanance which a magnetic easy axis at t_{Pt} = 3.0 nm. While in contrast to films on PEN, Fig. 8.10 (c') shows the loop was not very square at t_{Pt} = 5.0 nm. Fig. 8.11 a to f and Fig. 8.11 g to l show images of the out-of-plane domain structures for films on SiO_2 and PEN, respectively. For the $t_{Pt}/t_{Co}/t_{Pt}$ films on SiO_2, magnetization reversal proceeds via the nucleation of small reversed domains followed by rapid uniform growth of these bubbles via domain wall motion. The locations of the nucleation points appear randomly for any given

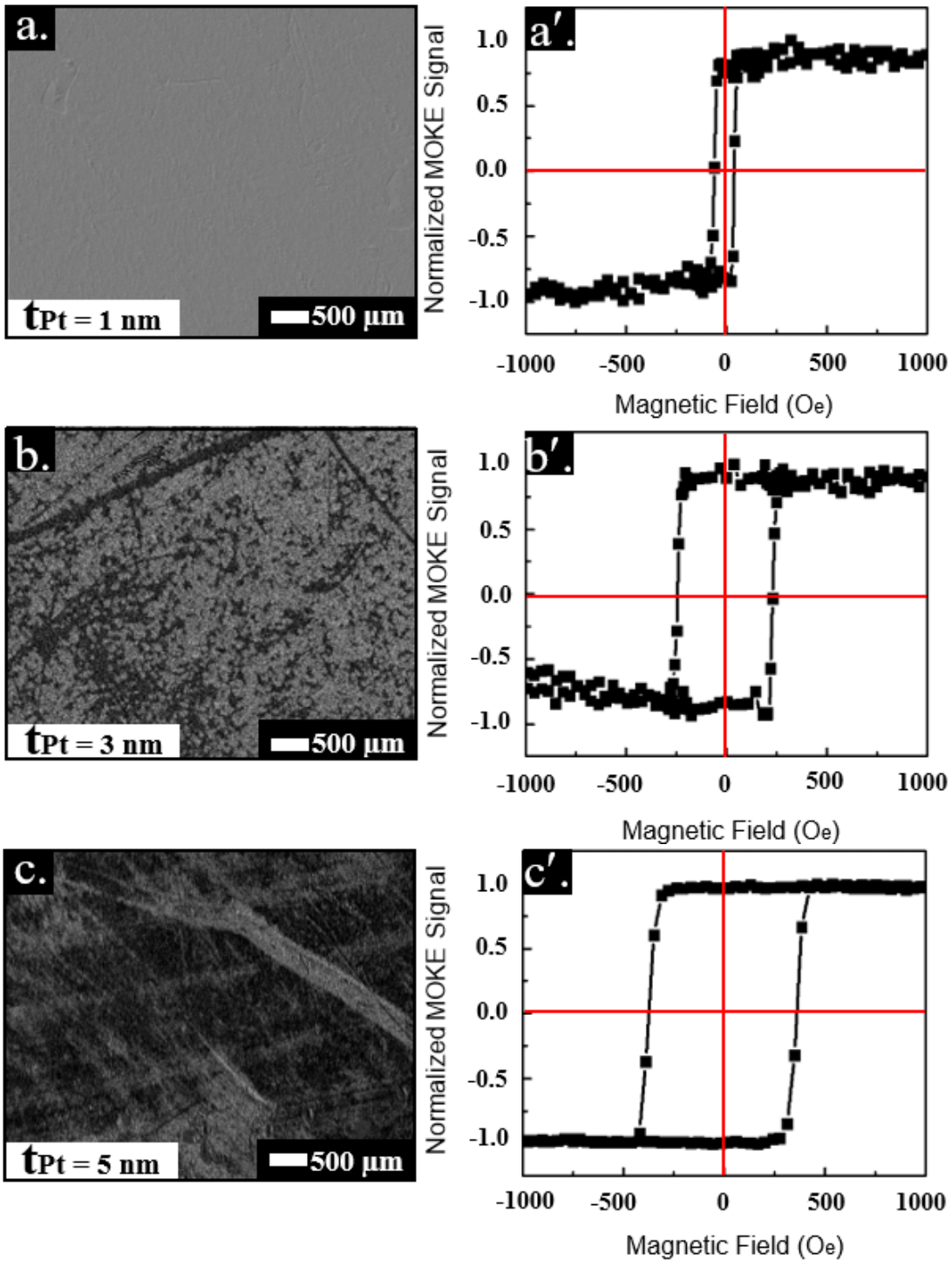

Fig. 8.10 (a,b and c). Magneto-optic kerr effect microscopy images for a t_{Pt}/t_{Co} (0.6)/t_{Pt} nm multilayers on PEN as a function of the Pt thickness at H = 351.19 Oe, H = 339.4 Oe and H = 471.2 Oe respectively. (a',b' and c'). The MOKE hysteresis curves of different thickness of platinum 1.0, 3.0 and 5.0 nm respectively

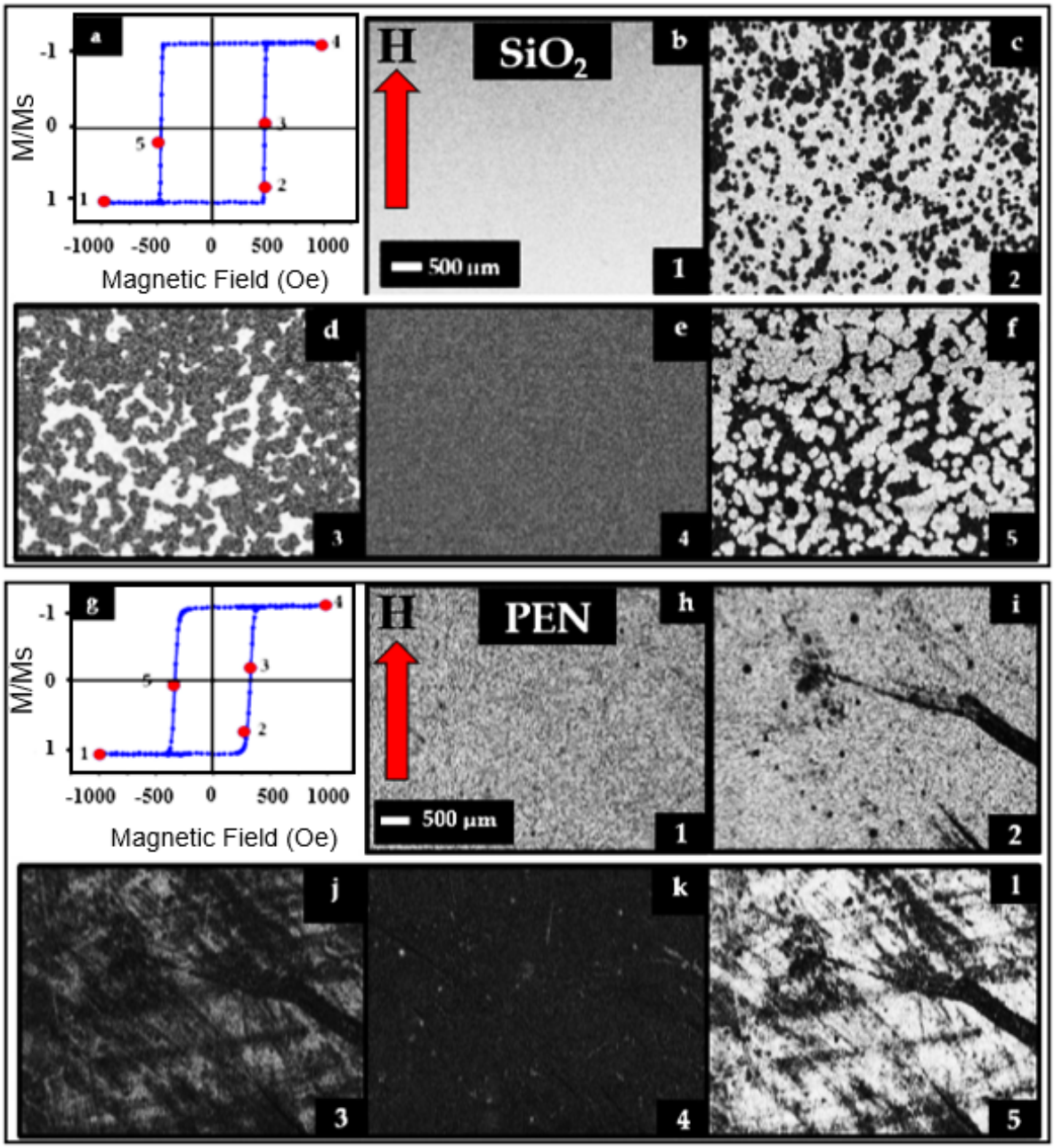

Fig. 8.11 Comparison of magnetisation reversal behaviours of Pt/Co/Pt multilayers on rigid SiO_2 and flexible PEN substrates. Hysteresis loop of t_{Pt}/t_{Co} (0.6)/t_{Pt} (nm) for SiO_2. Figs. (b) to (f) are domain images taken at fields marked by point 1 to 5 in (a) at H = 485 Oe, +456.6 Oe, + 471.2 Oe, + 502.9 Oe and -470 Oe, respectively. The white arrow in image (b) represents the direction of applied magnetic field (H). While (g). Hysteresis loop of t_{Pt}/t_{Co} (0.6)/t_{Pt} (nm) for PEN. Figs. (h) to (l) are domain images taken at fields marked by point 1 to 5 in (a) at H = -198.1 Oe, +377.9 Oe, + 327.9 Oe, + 209.3 Oe and -347.9 Oe, respectively. The red arrow in image (h) represents the direction of applied magnetic field (H).

film and not linked to any clear substrate features, but probably reflect some localized energy variations. In contrast, for trilayers on PEN, particularly for 5 nm Pt, the reversal proceeds via extended nucleation of irregular domains and growth of domains in many locations; which appears to follow some non-random lines and features associated with the flexible substrate.

8.9 Result and discussion

A detailed microscopy study has been undertaken on the nucleation and growth of domain in $t_{Pt}/t_{Co}/t_{Pt}$ ultra-thin multi-layered structures on both rigid SiO_2 and flexible PEN substrates. Many researchers have focused on the topic of perpendicular magnetic anisotropy [215, 252, 253, 222]. However, here the focus is on the development of magnetic anisotropy and magnetisation reversal behaviour of on rigid substrates. Magnetic thin films with perpendicular magnetic anisotropy were deposited directly onto flexible substrates, this process is receiving attention for the creation of flexible magnetic devices for sensors and other applications in flexible electronics [254, 8] therefore, a common flexible substrates PEN was used in this study and compared with the behaviour of similar films on traditional SiO_2 substrates. PEN is characterized by high flexibility is in expensive and widely used in flexible electronics [255]. A detailed explanation of the results and analysis of imaging magnetisation reversal is presented here. The sample of Co thickness from (0.3-0.6) nm and from (0.4-0.6) nm exhibit square out-of-plane hysteresis with 100 % remanence, clearly indicating PMA. This is due to the fact at low Co thicknesses the interfacial anisotropy causes the magnetisation to be out-of-plane direction while dipolar energy dominates [256] at higher thickness of cobalt, making the easy axis of magnetisation in-plane, thus showing the spin re-orientation. Interestingly, the hysteresis loop appears to a decrease of the sharpness for a Co thickness of 0.7 nm. This observation could be related to the stronger DW pinning effect (switching becomes somewhat broader at large Co thicknesses) [156, 257]. Through the analysis of Kerr microscopy images of the domains in trilayer thin films with t_{Co} larger than

0.3 nm and 0.4 nm, the number of domains nucleation increased in number and they grew less. The role of magnetic anisotropy may also be important because of its role in defining the DW width, where lower magnetic anisotropy give wider domain walls and higher magnetic anisotropy give narrower domain walls. However, the thickness of the cobalt magnetic layer was changing, thus there is an additional influence from the magnetostatic energy that can affect the DW width, see Fig. 8.12. The effect was associated with the low wall area energy in relative to the magnetic variation caused by d_{co} [258].

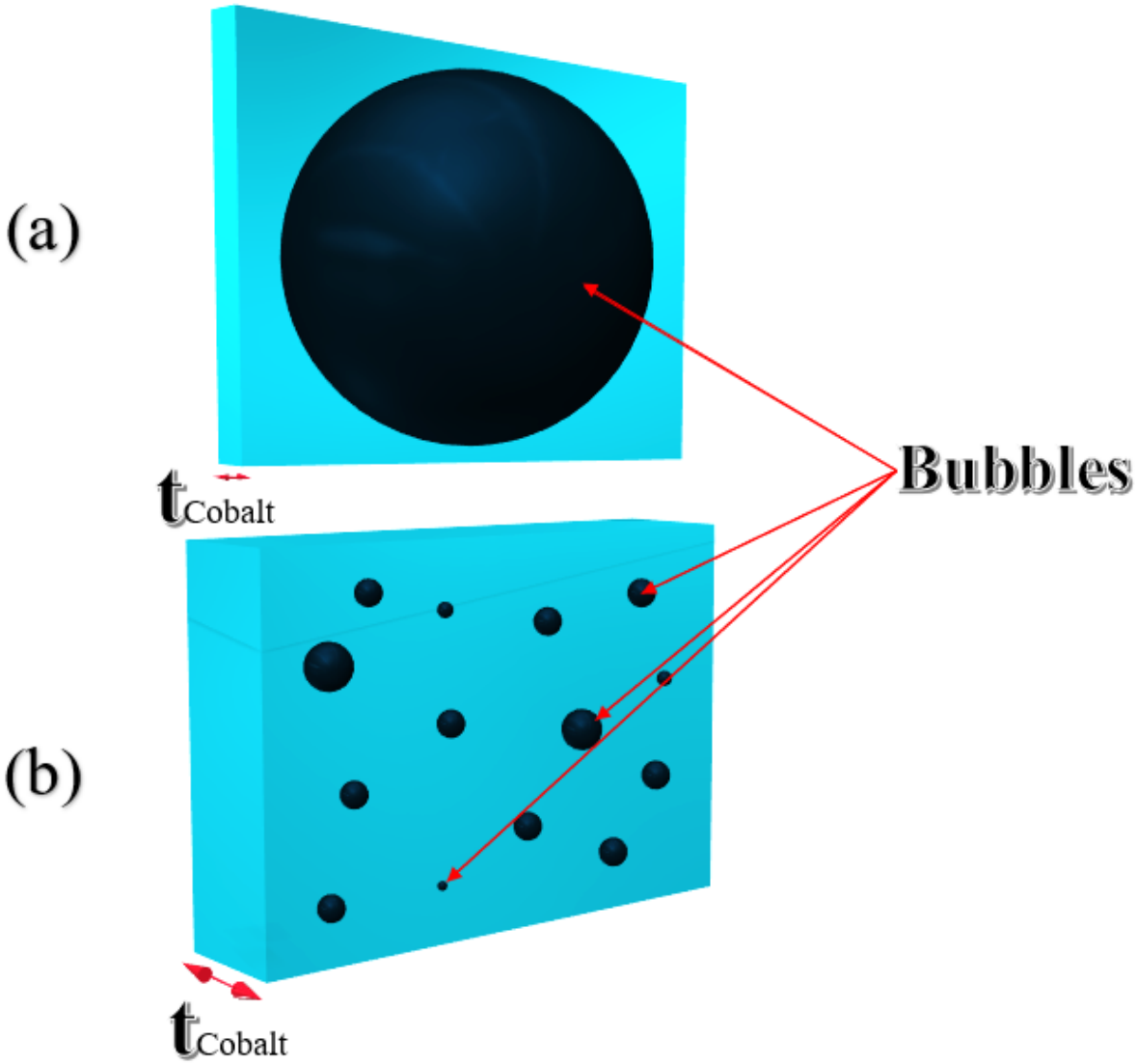

Fig. 8.12 Sketch of the width of magnetic bubble for different thickness : (a). thin cobalt thickness and (b). thick cobalt thickness respectively.

The Pt_s coverage at low thickness 1.0-3.0 nm may not 100 % [256] and hence the Co layer grown on top may have less Pt neighbours. As a result, some Co atoms may be contact in direct with substrate surface which did not create PMA. Pt being a fcc crystal grows predominantly in (111) orientation due to its lower surface energy compared to other planes [202] Pt (111) is reported to promote PMA in ultrathin Co films [259].

For the manufacture of magnetic films on flexible substrates, an appropriate non-magnetic layer is often needed to decrease the roughness of the flexible substrate, which can help to ensure the continuity of the magnetic films and multi-layered structures and functional performance [254, 8, 9]. The dependence on the buffer layer thickness can be understood; a 1.0 nm buffer Pt layer is not sufficiently thick to completely induce PMA at the Pt/Co interface and the crystalline structure in the buffer Pt layer becomes enhanced as its thickness increases from 1.0 nm to 3.0 nm [256]. The effectiveness of the buffer layer may be attributable to the inter diffusion at the upper Co/Pt interface [260, 261]. In case of using PEN substrate, when the Pt thickness increased from 1.0 nm to 3.0 nm, it was found that there was a significant influenced of the increasing of multi-nucleation sites on improving the shape anisotropy to be very squareness as it shown in Fig. 8.10 (b,b'). The reason of this may be coming due to the decreasing of RMS at 3.0 nm Pt thickness. In PEN case, the disappearing of multi-domain structure at 1.0 nm Pt thickness and at 5.0 nm it seems like inhomogeneous lines. This disappearing of multi-nucleation sites was associated with increasing of the RMS roughness when the platinum thickness was 1.0 nm and 5.0 nm as well [see chapter 6]. Therefore, at t_{Pt} = 5.0 nm, the shape anisotropy was shown to have decreased where the hysteresis loop was not square, as shown in Fig. 8.10 (c,c').

The results were done here offer two different methods. Firstly; by increasing the Co thickness (0.3-0.7) nm and fixed Pt thickness at 3.0 nm and 5.0 nm respectively; it was found that it tends to minimize the DWs velocity, and DW mobility that was associated with enhancing anisotropy. Secondly; by increasing the Pt thickness 2.0 nm, 3.0 nm and 5.0 nm

as well and fixed the Co thickness thickness to 0.5 nm, it was observed that the DW velocity is sensitive to the thickness of the non-magnetic Pt layers in $t_{Pt}/t_{Co}/t_{Pt}$ films. Hence, the anisotropy was increased with increasing Pt thickness.

A magnetic bubble represents in Fig. 8.13 shows a domain of reversed magnetisation that happens in a thin film with a uniaxial anisotropy, K_u, oriented perpendicular to the film. The magnetisation reversal through the domain wall will not be sudden because the exchange energy, E_x, leads to maintain the angles between neighboring spins small. Therefore, there is a region of transition, termed the bubble domain wall, which has a width [262].

Hence, based on this explanation and according to the results of this study, it was found that with increasing of the Co thickness, the anisotropy energy will be lowest when the magnetic moments are aligned with the lattice of crystal axes therefore decreasing the domain wall width. This was shown when the size of the magnetic bubble was decreased. Thus, it leads to increase the perpendicular magnetic anisotropy. Hence, the reduction of the velocity and the mobility of domain wall were confirm that there is an association with reduced anisotropy energy and enhanced anisotropy. On the contrary, at lower Co thickness, the size of magnetic bubble was larger when the magnetic moments are aligned parallel to each other so the exchange energy will be decreased [263] and therefore this tends to make the wall thicker, due to the repulsion between them [263]. Thus, the anisotropy will be reduced.

Fig. 8.12 (a) refers to that at lower thickness of cobalt for example at t_{Cobalt} = 0.3 nm, the width of bubble increased, meaning that the anisotropy will be low. While, Fig. (b) refers to that at higher thickness of cobalt for example at t_{Cobalt} = 0.6 nm, the width of bubble decreased, so the anisotropy will be high. Fig. 8.13, describes this further; when the wall energy (h) is smaller than the wall width (δw), energy of wall, a bubble, if created, would breakdown. While, when the wall energy (h) is larger than the wall width (δw) energy, it

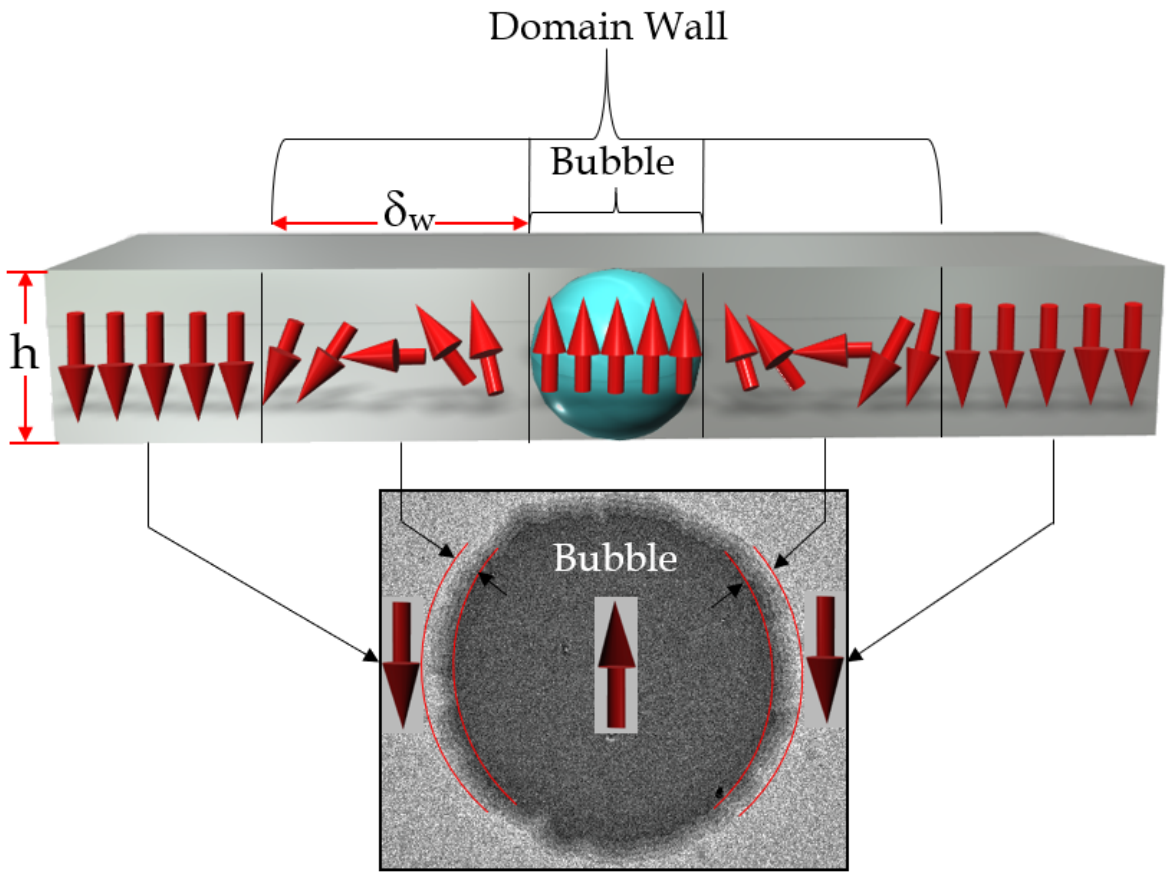

Fig. 8.13 Schematic figure to illustrate the spin up and spin down that is happen in domain wall, black and white contrast.

takes only a little energy of wall to expand the wall compared to amount of magnetostatic energy that the bubble provides [262].

The sample of 0.3 nm Co-layers exhibits a low velocity, low mobility and wider hysteresis loop, implying the formation of a multi-domain structure during magnetic reversal [264, 151]. Hence, it is probably related to the non-uniform coverage of these very thin Co films that is leading to decrease the DWs velocity. Moreover, the velocity and mobility of DWs were decreased relative to the thickness increase of Co-layer. While, in the case of changing Pt thicknesses, from the DWs velocity and mobility calculations, it was found at t_{Pt} = 2.0 nm, a higher velocity and mobility of DWs were obtained. Hence, it was shown that a Pt buffer layer equal to 2.0 nm basically changes the bubbles domain structures of magnetisation,

decreasing the threshold of magnetisation reversal due to symmetrical bubbles for both up/down and down/up direction of magnetisation. From t_{Pt} = 3.0 nm, to 5.0 nm an decrease in DW velocity and mobility were observed. This decrease of DWs velocity and mobility implies that the wall energy was decreased, and this is associated with increased anisotropy. Also, this change can be attributed to an improvement in the fcc (111) texturing of the layer of cobalt with thicker Pt buffer layers [86, 265, 123]. In addition, it is known that with increasing of Pt thickness, a reduction in Co/Pt interface roughness can enhance interfacial anisotropy; which should also contribute to an increase in coercivity [266].

8.10 Summary and Conclusion

It was found in this chapter there is a large correlation between the magnetic properties of thin film and the morphology; in particular upon the role of magnetic anisotropy that is represented by the ability of controlling PMA (Perpendicular Magnetic Anisotropy) in two cases: [(lower magnetic anisotropy/widely domain walls structure during reversal (DW_s)] at lower thickness of cobalt or [(higher magnetic anisotropy/tight domain walls structure during reversal (DW_s)] at higher thickness of cobalt. Also, the results showed that the magnetic reversal and anisotropy of Co/Pt multilayers depend strongly on the thickness of the magnetic Co layer, as well as the thickness of the non-magnetic Pt buffer. Hence, the interface transmission coefficient between Co and Pt layers plays an important role in this study. The magnetization reversal measurements showed that increasing the thickness of platinum leads to an increased coercivity; which is associated with a strong increase in the effective magnetic anisotropy. Films grown on PEN showed an increased film roughness, which in general, leads to a lower PMA than smoother films. This was shown to relate to the pinning of the magnetic domains at the asperities. It was found that in low-coercivity ultrathin Co films, the asymmetry in domain wall velocity and domain wall mobility increased with the applied field. To examine the effect of Pt spacer layers on domain wall velocity, Pt thickness

was increased from 2.0, 3.0 and 5.0 nm while keeping Co layer thickness fixed at 0.5 nm. It was found that the velocity and mobility of domain walls were approximately stable. The anisotropy in this case was increased due to decrease of the wall energy. Increasing the nucleation site density was related to enhance perpendicular magnetic anisotropy as it shown in both cases firstly; increasing Co thickness and fixed Pt thickness and secondly; increasing Pt layer thickness and fixed Co layer thickness.

Chapter 9

Conclusion and future work

9.1 Conclusion

The aim of this thesis is to highlight and understand the effect of perpendicular magnetic anisotropy using different kinds of substrate such as silicon dioxide, polyethylene naphthalate and polyimide substrates that is also influenced by the Hall resistivity due to Lorentz effect. Moreover, the usage of non-magnetic materials (like: Pt and Ru) that grown on those substrates consider as a beneficial for technological applications in data storage devices.

Giving a deeper understanding of the mechanisms of magnetic domain walls in trilayer thin films through sputtering deposition is done in this study. The focusing is on out-of-plane anisotropy magnetic materials, in particular the comparison between a Pt/Co/Pt and Ru/Co/Ru trilayer system. A detailed structural analysis is presented, reducing the roughness through using different buffer layer thickness. The study also includes an investigation into the relationship between domain wall structure and enhancing magnetization behaviour. This aimed to build a new knowledge about the relationship between domain wall and enhancing PMA using rigid/flexible substrates. Further knowledge about the behaviour and mechanisms for the control of domain walls in thin films will be highly relevant for the design of future

spintronic devices.

This thesis starts with an overview of several significant topics in theoretical and experimental physics, their history and how this project fits into the general scientific narrative. Key theory was provided, necessary for the understanding of results and measurement techniques and those techniques were described. The growth and characterisation of Pt/Co/Pt samples was explained, showing how several structural and magnetic properties of the films changed with deposition at room temperature. It was seen that the samples were crystalline and strongly textured, with the degree of their total interfacial disorder depending on the deposition at room temperature of the top ferromagnetic/non-magnetic bilayer and type of substrates. Improving the anisotropy that is associated with the role of strong spin-orbit coupling in different magnetic structure is currently a popular research topic in nanomagnetism. This thesis reports different experiments on this significant topic, by studying different types of substrates: silicon dioxide SiO_2 polyimide and polyethylene naphthalate as a substrate, where Pt/Co/Pt trilayer thin-film grown on them.

The magnetization measurements illustrate that increasing the thickness of Pt leads to an increase in coercivity which is associated with a strong increase in effective magnetic anisotropy. In general, films with a rough surface exhibit a lower PMA than smooth films. This is attributed to pinning of the magnetic domains. But, since applications such as hard disks need a smooth surface (danger of head crashes or a too large read/write distance), an increased roughness is not suitable. Decreasing the root mean square roughness of the Pt buffer layers plays an important role to improve the shape of hysteresis loop and this will be correlated to improve perpendicular magnetic anisotropy with decrease in Hall resistivity.

The full-width-half-maximum of the XRD patterns using 15 nm for Pt and Ru buffer lay-

ers allowed determmination of the perpendicular grain size. This was found to vary most significantly between different substrate materials. Improvement in the crystalline structure leads to enhance magnetocrystalline interface anisotropy. K_{eff} increases linearly with t_{Pt}. The grain size of the magnetic material is an important structural factor that effects the magnetic properties. When the shape of peaks [higher high with lesser width] suggest high crystal quality, this means the anisotropy is higher than for less intense, broader peaks, which indicate lower crystal quality. The reduction in full-width-half-maximum peak width refers to the increase in grain size of the thin-film. The shift in peak mode is suggested to be the strain as the for different substrate roughnesses. By using 15 nm Pt buffer layer, in both cases SiO_2 and polyimide substrates, the intense Pt (111) peak shows high crystal quality. When the shape of peaks [higher high with lesser width] indicates high crystal quality, this means the anisotropy is higher than when the shape of peak [lower high with larger width] indicates a poorer crystal quality.

The domain wall (DW) was detected using MOKE microscopy magnetic imaging technique. Where, it has been performed a detailed quantitative study of the symmetric/asymmetric bubble domain expansion in Pt/Co/Pt system in presence of H_z magnetic field. Previous studies have reported that the DW motion asymmetry due to the presence of the DMI. In this study, the detailed analysis of the symmetric and anti-symmetric components of the DW velocities showed Neel wall behaviour. The velocity of the domain wall and domain growth rate was calculated from the time resolved domain wall structure imaging. It has been studied the variation of the DW asymmetry. A main conclusion can be observed here, in the case of the Pt/Co/Pt, for small DW velocity region, the DW motion is a mixture of the pinning events. As a result, we can propose that symmetric DW bubbles studies can be used as a standard tool to understand the DW whether it is a steady state or oscillatory. The sample of cobalt thickness from 0.3-0.7 nm exhibit perfect squareness with 100 % remenance

clearly indicating PMA. This is due to the fact that at low cobalt thickness the interfacial anisotropy causes the magetization to be out-of-plane where as dipolar energy dominates at higher thickness of cobalt at 0.7 nm, making the easy axis of magnetization in-plane, thus exhibiting the spin re-orientation transition.

9.2 Future Work

This study has presented methods for knowing the effectiveness of Hall resistivity and the domain walls behaviour in trilayer. This has led to some finding, however, further scientific realization is still required before this knowledge can be utilized in technological applications. This section highlights some possible areas of research that could be persisted and may lead to additional advances in the fundamental grasping in magnetization process.

Several of the results presented here suggest that the pinning of domain walls shows a dependence on their structural properties where stronger pinning of thin films using plastic substrate that modifies the magnetic properties as well. This difference is likely to be of great importance in the development of domain wall devices and deserves a great deal of further attention through focusing on reduce roughnes to some extent to get a better foramation of thin films.

Finally, the velocity of bubbles study investigated here has been driven by applied magnetic field. The change in magnetic behaviour of these trilayer thin-film samples has been attributed to changes in the magnetic moment and the spin-orbit interaction for the atoms at the near interface region. These provide an explanation for the observed variation in the saturation magnetization which shows the most dramatic changes. For complete understanding of the magnetic properties,. the study of domain wall in case of in-plane magnetic anisotropy for smaller thickness of ruthenium will be need to do in the future using silicon dioxide and PEN substrates. In fact, the samples have been already prepared but there is a needing to use magneto optical kerr effect microscopy with higher magnetic field. Also,

the Ru buffer layers from 1.0 - 5.0 nm grown on both rigid/flexible substrates were already prepared. Then, atomic force microscope has been used for all those samples. Where, this could lead to the discovery of other layered structures that may give a greater level of control over the magnetization and my also add to the understanding of the physical properties taking place.

Also, Mgo/Co/Pt multilayer thin films were prepared but still some measurements need in order to have a full understanding about the effect of buffer layers like MgO on magnetisation in comparison with Pt and Ru buffer layers as well. Moreover, this plan can be completed in the future with using different kind of substrates like: silicon dioxide, polyethylene naphthalate and polyimide.

References

[1] D.-H. Kim and J. A. Rogers, "Stretchable electronics: materials strategies and devices," *Advanced Materials*, vol. 20, no. 24, pp. 4887–4892, 2008.

[2] S. Wang, J. Pu, D. S. Chan, B. J. Cho, and K. P. Loh, "Wide memory window in graphene oxide charge storage nodes," *Applied Physics Letters*, vol. 96, no. 14, p. 143109, 2010.

[3] B. Govoreanu, G. Kar, Y. Chen, V. Paraschiv, S. Kubicek, A. Fantini, I. Radu, L. Goux, S. Clima, R. Degraeve, *et al.*, "10× 10nm 2 hf/hfo x crossbar resistive ram with excellent performance, reliability and low-energy operation," in *Electron Devices Meeting (IEDM), 2011 IEEE International*, pp. 31–6, IEEE, 2011.

[4] K. Hatano, A. Chida, T. Okano, N. Sugisawa, T. Inoue, S. Seo, K. Suzuki, Y. Oikawa, H. Miyake, J. Koyama, *et al.*, "3.4-inch quarter high definition flexible active matrix organic light emitting display with oxide thin film transistor," *Japanese Journal of Applied Physics*, vol. 50, no. 3S, p. 03CC06, 2011.

[5] S. Mittal and J. S. Vetter, "A survey of software techniques for using non-volatile memories for storage and main memory systems," *IEEE Transactions on Parallel and Distributed Systems*, vol. 27, no. 5, pp. 1537–1550, 2016.

[6] A. J. van Breemen, J.-L. van der Steen, G. van Heck, R. Wang, V. Khikhlovskyi, M. Kemerink, and G. H. Gelinck, "Crossbar arrays of nonvolatile, rewritable polymer ferroelectric diode memories on plastic substrates," *Applied Physics Express*, vol. 7, no. 3, p. 031602, 2014.

[7] K. Bouziane, A. Al Rawas, M. Maaza, and M. Mamor, "Buffer effect on gmr in thin co/cu multilayers," *Journal of alloys and compounds*, vol. 414, no. 1-2, pp. 42–47, 2006.

[8] M. Breidbach, D. Bürgler, and P. Grünberg, "Current-in-plane giant magnetoresistance: The effect of interface roughness and spin-depolarization due to the proximity of a buffer layer," *Journal of magnetism and magnetic materials*, vol. 307, no. 2, pp. L1–L6, 2006.

[9] Z.-C. Tian, K. Sakaue, H. Terauchi, and H. Ito, "Epitaxial growth and giant magnetoresistance of co/cu (111) superlattices on cr buffer layers," *Journal of applied physics*, vol. 76, no. 6, pp. 3899–3901, 1994.

[10] B. Sun, X. Zhang, G. Zhou, T. Yu, S. Mao, S. Zhu, Y. Zhao, and Y. Xia, "A flexible nonvolatile resistive switching memory device based on zno film fabricated on a foldable pet substrate," *Journal of colloid and interface science*, vol. 520, pp. 19–24, 2018.

[11] W. D. Callister, D. G. Rethwisch, *et al.*, *"Materials science and engineering: an introduction"*, vol. 7. John wiley & sons New York, 2007.

[12] J.-g. Hu, G. Jin, A. Hu, and Y.-q. Ma, "Temperature dependence of exchange bias and coercivity in ferromagnetic/antiferromagnetic bilayers," *The European Physical Journal B-Condensed Matter and Complex Systems*, vol. 40, no. 3, pp. 265–271, 2004.

[13] M. Kläui and C. A. F. Vaz, "Magnetization configurations and reversal in small magnetic elements," *Handbook of Magnetism and Advanced Magnetic Materials*, 2007.

[14] S. EC, "The theory of electric and magnetic susceptibilities," *Nature*, vol. 130, pp. 490–491, 1932.

[15] P. Yu and M. Cardona, *"Fundamentals of Semiconductors"*. Springer-Verlag Berlin Heidelberg, 2003.

[16] S. Blundell, *"Magnetism in Condensed Matter (Oxford master series in condensed matter physics)"*. Oxford University Press, 2001.

[17] J. M. Coey, *"Magnetism and magnetic materials"*. Cambridge University Press, 2010.

[18] B. Cullity and C. Graham, "Introduction to magnetic materials. [sl]," 1972.

[19] H. Brune, "Microscopic view of epitaxial metal growth: nucleation and aggregation," *Surface Science Reports*, vol. 31, no. 4-6, pp. 125–229, 1998.

[20] J. Jung, S. Lim, and S. Lee, "Strong perpendicular magnetic anisotropy in thick cofeb films sandwiched by pd and mgo layers," *Applied Physics Letters*, vol. 96, no. 4, p. 042503, 2010.

[21] C.-H. Lambert, A. Rajanikanth, T. Hauet, S. Mangin, E. Fullerton, and S. Andrieu, "Quantifying perpendicular magnetic anisotropy at the fe-mgo (001) interface," *Applied Physics Letters*, vol. 102, no. 12, p. 122410, 2013.

[22] M. K. Kazimierczuk, *"High-frequency magnetic components"*. John Wiley & Sons, 2009.

[23] M. Johnson, P. Bloemen, F. Den Broeder, and J. De Vries, "Magnetic anisotropy in metallic multilayers," *Reports on Progress in Physics*, vol. 59, no. 11, p. 1409, 1996.

[24] K. J. Buschow, *"Concise encyclopedia of magnetic and superconducting materials"*. Elsevier, 2005.

[25] P. Bruno, "Magnetic surface anisotropy of cobalt and surface roughness effects within neel's model," *Journal of Physics F: Metal Physics*, vol. 18, no. 6, p. 1291, 1988.

[26] H. Draaisma, F. Den Broeder, and W. De Jonge, "Perpendicular anisotropy in pd/co multilayers," *Journal of applied physics*, vol. 63, no. 8, pp. 3479–3481, 1988.

[27] J. MacLaren and R. Victora, "Theoretical predictions of interface anisotropy in the presence of interdiffusion," *Journal of Applied Physics*, vol. 76, no. 10, pp. 6069–6074, 1994.

[28] D. Sander, A. Enders, and J. Kirschner, "Stress and magnetic properties of surfaces and ultrathin films," *Journal of magnetism and magnetic materials*, vol. 200, no. 1-3, pp. 439–455, 1999.

[29] D. Sander, "The correlation between mechanical stress and magnetic anisotropy in ultrathin films," *Reports on Progress in Physics*, vol. 62, no. 5, p. 809, 1999.

[30] D. Sander, "The magnetic anisotropy and spin reorientation of nanostructures and nanoscale films," *Journal of Physics: Condensed Matter*, vol. 16, no. 20, p. R603, 2004.

[31] C.-R. Chang, "Influence of roughness on magnetic surface anisotropy in ultrathin films," *Journal of applied physics*, vol. 72, no. 2, pp. 596–600, 1992.

[32] J.-S. Yang and C.-R. Chang, "The statistical roughness and magnetic surface anisotropy," *IEEE transactions on magnetics*, vol. 31, no. 3, pp. 1825–1828, 1995.

[33] N. Mehboob, *"Hysteresis properties of soft magnetic materials"*. PhD thesis, uniwien, 2012.

[34] R. O'Handley, C. Cockwill, T. McAllister, M. Jelinski, D. Morck, and M. Olson, "Duration of naturally acquired giardiosis and cryptosporidiosis in dairy calves and their association with diarrhea.," *Journal of the American Veterinary Medical Association*, vol. 214, no. 3, pp. 391–396, 1999.

[35] K. H. J. Buschow, F. R. Boer, *et al.*, *"Physics of magnetism and magnetic materials"*, vol. 92. Springer, 2003.

[36] É. Trémolet de Lacheisserie, M. Schlenker, and D. Gignoux, *"Magnetism: Materials and applications"*. Springer, 2005.

[37] I. Dzialoshinskii, "Thermodynamic theory of weak ferromagnetism in antiferromagnetic substances," *SOVIET PHYSICS JETP-USSR*, vol. 5, no. 6, pp. 1259–1272, 1957.

[38] T. Moriya, "Anisotropic superexchange interaction and weak ferromagnetism," *Physical Review*, vol. 120, no. 1, p. 91, 1960.

[39] A. Thiaville, S. Rohart, É. Jué, V. Cros, and A. Fert, "Dynamics of dzyaloshinskii domain walls in ultrathin magnetic films," *EPL (Europhysics Letters)*, vol. 100, no. 5, p. 57002, 2012.

[40] A. Rosch, "Skyrmions: moving with the current," *Nature nanotechnology*, vol. 8, no. 3, p. 160, 2013.

[41] Y. Lin, P. Grundy, and E. Giess, "Bubble domains in magnetostatically coupled garnet films," *Applied Physics Letters*, vol. 23, no. 8, pp. 485–487, 1973.

[42] N. Nagaosa and Y. Tokura, "Topological properties and dynamics of magnetic skyrmions," *Nature nanotechnology*, vol. 8, no. 12, p. 899, 2013.

[43] X. Yu, N. Kanazawa, Y. Onose, K. Kimoto, W. Zhang, S. Ishiwata, Y. Matsui, and Y. Tokura, "Near room-temperature formation of a skyrmion crystal in thin-films of the helimagnet fege," *Nature materials*, vol. 10, no. 2, p. 106, 2011.

[44] S. Heinze, K. Von Bergmann, M. Menzel, J. Brede, A. Kubetzka, R. Wiesendanger, G. Bihlmayer, and S. Blügel, "Spontaneous atomic-scale magnetic skyrmion lattice in two dimensions," *Nature Physics*, vol. 7, no. 9, p. 713, 2011.

[45] T. Okubo, S. Chung, and H. Kawamura, "Multiple-q states and the skyrmion lattice of the triangular-lattice heisenberg antiferromagnet under magnetic fields," *Physical review letters*, vol. 108, no. 1, p. 017206, 2012.

[46] S. Emori, U. Bauer, S.-M. Ahn, E. Martinez, and G. S. Beach, "Current-driven dynamics of chiral ferromagnetic domain walls," *Nature materials*, vol. 12, no. 7, p. 611, 2013.

[47] A. Hrabec, N. Porter, A. Wells, M. Benitez, G. Burnell, S. McVitie, D. McGrouther, T. Moore, and C. Marrows, ""measuring and tailoring the dzyaloshinskii-moriya

interaction in perpendicularly magnetized thin films"," *Physical Review B*, vol. 90, no. 2, p. 020402, 2014.

[48] G. Chen, A. T. N'Diaye, S. P. Kang, H. Y. Kwon, C. Won, Y. Wu, Z. Qiu, and A. K. Schmid, "Unlocking bloch-type chirality in ultrathin magnets through uniaxial strain," *Nature communications*, vol. 6, p. 6598, 2015.

[49] G. Chen, T. Ma, A. T. N'Diaye, H. Kwon, C. Won, Y. Wu, and A. K. Schmid, "Tailoring the chirality of magnetic domain walls by interface engineering," *Nature communications*, vol. 4, p. 2671, 2013.

[50] M. Bode, M. Heide, K. Von Bergmann, P. Ferriani, S. Heinze, G. Bihlmayer, A. Kubetzka, O. Pietzsch, S. Blügel, and R. Wiesendanger, "Chiral magnetic order at surfaces driven by inversion asymmetry," *Nature*, vol. 447, no. 7141, p. 190, 2007.

[51] K. R. Sopka, "The discovery of the hall effect: Edwin hall's hitherto unpublished account," in *The Hall Effect and Its Applications*, pp. 523–545, Springer, 1980.

[52] E. H. Hall, "On a new action of the magnet on electric currents," *American Journal of Mathematics*, vol. 2, no. 3, pp. 287–292, 1879.

[53] R. Griffiths, *"Anomalous Hall effect measurements of bilayer magnetic structures"*. PhD thesis, University of Manchester, 2017.

[54] E. H. Hall, "Xviii. on the "rotational coefficient" in nickel and cobalt," *The London, Edinburgh, and Dublin Philosophical Magazine and Journal of Science*, vol. 12, no. 74, pp. 157–172, 1881.

[55] A. Kundt, "Das hall'sche phänomen in eisen, kobalt und nickel," *Annalen der Physik*, vol. 285, no. 6, pp. 257–271, 1893.

[56] E. M. Pugh, "Hall effect and the magnetic properties of some ferromagnetic materials," *Physical Review*, vol. 36, no. 9, p. 1503, 1930.

[57] E. Pugh and T. Lippert, "Hall emf and intensity of magnetization," *Physical Review*, vol. 42, no. 5, p. 709, 1932.

[58] N. Nagaosa, J. Sinova, S. Onoda, A. MacDonald, and N. Ong, "Anomalous hall effect," *Reviews of modern physics*, vol. 82, no. 2, p. 1539, 2010.

[59] L. Berger, "Side-jump mechanism for the hall effect of ferromagnets," *Physical Review B*, vol. 2, no. 11, p. 4559, 1970.

[60] R. Karplus and J. Luttinger, "Hall effect in ferromagnetics," *Physical Review*, vol. 95, no. 5, p. 1154, 1954.

[61] J. Smit, "The spontaneous hall effect in ferromagnetics ii," *Physica*, vol. 24, no. 1-5, pp. 39–51, 1958.

[62] M. V. Berry, "Quantal phase factors accompanying adiabatic changes," *Proc. R. Soc. Lond. A*, vol. 392, no. 1802, pp. 45–57, 1984.

[63] G.-Y. Guo, S. Murakami, T.-W. Chen, and N. Nagaosa, "Intrinsic spin hall effect in platinum: First-principles calculations," *Physical review letters*, vol. 100, no. 9, p. 096401, 2008.

[64] G. Vignale, "Ten years of spin hall effect," *Journal of superconductivity and novel magnetism*, vol. 23, no. 1, p. 3, 2010.

[65] J. Smit, "The spontaneous hall effect in ferromagnetics i," *Physica*, vol. 21, no. 6-10, pp. 877–887, 1955.

[66] M. I. Dyakonov and A. Khaetskii, *"Spin physics in semiconductors"*, vol. 157. Springer, 2017.

[67] W. R. Grove *et al.*, "On the electro-chemical polarity of gases," in *Abstracts of the Papers Communicated to the Royal Society of London*, vol. 6, pp. 168–169, The Royal Society, 1854.

[68] S. Liou, Y. Liu, S. Malhotra, M. Yu, and D. J. Sellmyer, "Magnetic properties of nanometer-size copt particles," *Journal of applied physics*, vol. 79, no. 8, pp. 5060–5062, 1996.

[69] N. Sharma, G. Jones, S. Casey, and P. Grundy, "The microstructure and magnetic properties of cobalt-rich co-pt alloy thin films grown using ion-beam-assisted deposition," *Journal of Physics D: Applied Physics*, vol. 31, no. 21, p. 3020, 1998.

[70] S. Jeong, Y.-N. Hsu, D. E. Laughlin, and M. E. McHenry, "Atomic ordering and coercivity mechanism in fept and copt polycrystalline thin films," *IEEE transactions on magnetics*, vol. 37, no. 4, pp. 1299–1301, 2001.

[71] D. Oh and J. K. Park, "Effect of microstructure on the magnetic properties of l1 0 copt–20 at.% c magnetic thin film," *Journal of applied physics*, vol. 93, no. 10, pp. 7756–7758, 2003.

[72] S. Jeong, Y.-N. Hsu, D. E. Laughlin, and M. E. McHenry, "Magnetic properties of nanostructured copt and fept thin films," *IEEE transactions on magnetics*, vol. 36, no. 5, pp. 2336–2338, 2000.

[73] A. Zangwill, *"Physics at surfaces"*. Cambridge university press, 1988.

[74] M. Björck, *"A structural viewpoint of magnetism in Fe and Co based superlattices"*. PhD thesis, Acta Universitatis Upsaliensis, 2007.

[75] S. AZZAWI, R. ABDUL, *et al.*, *Understanding and Controlling Magnetic Damping Behaviour in Synthetic Ferromagnetic Thin-Film Multilayers*. PhD thesis, Durham University, 2018.

[76] B. Cullity, "Elements of x-ray diffraction, addison-wesely," *Reading, MA, USA*, 1978.

[77] W. Zeper, F. Greidanus, P. Carcia, and C. Fincher, "Perpendicular magnetic anisotropy and magneto-optical kerr effect of vapor-deposited co/pt-layered structures," *Journal of Applied Physics*, vol. 65, no. 12, pp. 4971–4975, 1989.

[78] D. Weller, W. Reim, K. Spörl, and H. Brändle, "Spectroscopy of multilayers for magneto-optic storage," *Journal of Magnetism and Magnetic Materials*, vol. 93, pp. 183–193, 1991.

[79] S. Zhang, J. Teng, J. Zhang, Y. Liu, J. Li, G. Yu, and S. Wang, "Large enhancement of the anomalous hall effect in co/pt multilayers sandwiched by mgo layers," *Applied Physics Letters*, vol. 97, no. 22, p. 222504, 2010.

[80] P. Zhang, W. Lin, D. Wu, Z. Jiang, and H. Sang, "Effective anomalous hall coefficient in an ultrathin co layer sandwiched by pt layers," *Journal of Applied Physics*, vol. 115, no. 6, p. 063908, 2014.

[81] C.-J. Lin, G. Gorman, C. Lee, R. Farrow, E. Marinero, H. Do, H. Notarys, and C. Chien, "Magnetic and structural properties of co/pt multilayers," *Journal of Magnetism and Magnetic Materials*, vol. 93, pp. 194–206, 1991.

[82] K. Sato, H. Ikekame, Y. Tosaka, K. Tsuzukiyama, Y. Togami, and M. Fujisawa, "Fundamental studies and application of short-wavelength magneto-optical effect in pt-based multilayers," *Journal of magnetism and magnetic materials*, vol. 126, no. 1-3, pp. 572–576, 1993.

[83] H. Braendle and D. Weller, ""j. c. scott, ss p. parkin and c"," *J. Lin, IEEE Trans. Magn*, vol. 28, p. 2964, 1992.

[84] K. Sato, H. Hongu, H. Ikekame, J. Watanabe, K. Tsuzukiyama, Y. Togami, M. Fujisawa, and T. Fukazawa, "Magnetooptical spectra in pt/co and pt/fe multilayers," *Japanese journal of applied physics*, vol. 31, no. 11R, p. 3603, 1992.

[85] S. Uba, L. Uba, A. Yaresko, A. Y. Perlov, V. Antonov, and R. Gontarz, "Optical and magneto-optical properties of co/pt multilayers," *Physical Review B*, vol. 53, no. 10, p. 6526, 1996.

[86] V. Mathet, T. Devolder, C. Chappert, J. Ferré, S. Lemerle, L. Belliard, and G. Guentherodt, "Morphology and magnetic properties of pt/co/pt sandwiches grown by argon

sputter deposition," *Journal of magnetism and magnetic materials*, vol. 260, no. 1-2, pp. 295–304, 2003.

[87] N. Ying, Y. Xin, P. Zhang, and S. Hai, "Magnetization and coercivity in co/pt multilayers with constant total co layer thickness," *Transactions of Nonferrous Metals Society of China*, vol. 20, no. 5, pp. 819–824, 2010.

[88] N. Nakajima, T. Koide, T. Shidara, H. Miyauchi, H. Fukutani, A. Fujimori, K. Iio, T. Katayama, M. Nỳvlt, and Y. Suzuki, "Perpendicular magnetic anisotropy caused by interfacial hybridization via enhanced orbital moment in co/pt multilayers: Magnetic circular x-ray dichroism study," *Physical Review Letters*, vol. 81, no. 23, p. 5229, 1998.

[89] M. Ota, M. Itou, Y. Sakurai, A. Koizumi, and H. Sakurai, "Perpendicular magnetic anisotropy in co/pt multilayers studied from a view point of anisotropy of magnetic compton profiles," *Applied Physics Letters*, vol. 96, no. 15, p. 152505, 2010.

[90] Y. An, L. Duan, T. Liu, Z. Wu, and J. Liu, "Structural and magnetic properties of pt in co/pt multilayers," *Applied Surface Science*, vol. 257, no. 17, pp. 7427–7431, 2011.

[91] T. Ueno, J. Sinha, N. Inami, Y. Takeichi, S. Mitani, K. Ono, and M. Hayashi, "Enhanced orbital magnetic moments in magnetic heterostructures with interface perpendicular magnetic anisotropy," *Scientific reports*, vol. 5, p. 14858, 2015.

[92] X. Z. , et.al, "Effect of buffer layer and external stress on magnetic properties of flexible fega films," *Journal of Applied Physics*, vol. 113, no. 17, p. 17A901, 2013.

[93] C. Christides and T. Speliotis, "Polarity of anomalous hall effect hysteresis loops in [pt/ co] 15/ af/[co/ pt] 15 (af= fe mn, nio) multilayers with perpendicular anisotropy," *Journal of applied physics*, vol. 97, no. 1, p. 013901, 2005.

[94] J. Caulet, C. Train, V. Mathet, R. Laval, B. Bartenlian, P. Veillet, K. Le Dang, and C. Chappert, "Influence of spin polarized pt on the extraordinary hall effect in sputtered

pt/au/co/pt sandwiches," *Journal of magnetism and magnetic materials*, vol. 198, pp. 318–320, 1999.

[95] J. Moritz, B. Rodmacq, S. Auffret, and B. Dieny, "Extraordinary hall effect in thin magnetic films and its potential for sensors, memories and magnetic logic applications," *Journal of Physics D: Applied Physics*, vol. 41, no. 13, p. 135001, 2008.

[96] T. C. Oakberg, "Magneto-optic kerr effect," *Hinds Instruments*, vol. 1, no. 1, 2005.

[97] M. Ali, "Growth and study of magnetostrictive fesibc thin films for device applications," 1999.

[98] R. Atkinson, "Magnetism in a new light," *Hinds Instruments Newsletter*, no. 10, 2001.

[99] R. Schäfer, "Investigation of domains and dynamics of domain walls by the magneto-optical k err-effect," *Handbook of magnetism and advanced magnetic materials*, 2007.

[100] O. Idigoras, P. Vavassori, J. Porro, and A. Berger, "Kerr microscopy study of magnetization reversal in uniaxial co-films," *Journal of Magnetism and Magnetic Materials*, vol. 322, no. 20, pp. L57–L60, 2010.

[101] N. ECNEDIF, F. OC, and O. ERUSAE, "Model 2100 6 1/2-digit resolution digital multimeter," 2007.

[102] C. Sequeira and D. Santos, "Theoretical considerations about solid-state diffusion of impurities into crystals," *Czechoslovak Journal of Physics*, vol. 56, no. 6, pp. 549–564, 2006.

[103] O. Philips'Gloeilampenfabrieken, "A method of measuring specific resistivity and hall effect of discs of arbitrary shape," *Philips Res. Rep*, vol. 13, no. 1, pp. 1–9, 1958.

[104] R. Chwang, B. Smith, and C. Crowell, "Contact size effects on the van der pauw method for resistivity and hall coefficient measurement," *Solid-State Electronics*, vol. 17, no. 12, pp. 1217–1227, 1974.

[105] D. W. Koon, "Effect of contact size and placement, and of resistive inhomogeneities on van der pauw measurements," *Review of Scientific Instruments*, vol. 60, no. 2, pp. 271–274, 1989.

[106] D. W. Koon and C. Knickerbocker, "What do you measure when you measure the hall effect?," *Review of scientific instruments*, vol. 64, no. 2, pp. 510–513, 1993.

[107] D. Koon and C. Knickerbocker, "Effects of macroscopic inhomogeneities on resistive and hall measurements on crosses, cloverleafs, and bars," *Review of scientific instruments*, vol. 67, no. 12, pp. 4282–4285, 1996.

[108] D. Koon, "Nonlinearity of resistive impurity effects on van der pauw measurements," *Review of scientific instruments*, vol. 77, no. 9, p. 094703, 2006.

[109] O. Bierwagen, T. Ive, C. G. Van de Walle, and J. S. Speck, "Causes of incorrect carrier-type identification in van der pauw–hall measurements," *Applied Physics Letters*, vol. 93, no. 24, p. 242108, 2008.

[110] N. Yom-Tov, C. Saguy, A. Bolker, R. Kalish, and Y. Yaish, "Accurate carrier-type determination of nonhomogenously doped diamond," *Journal of Applied Physics*, vol. 108, no. 4, p. 043711, 2010.

[111] D. K. Schroder, *"Semiconductor material and device characterization"*. John Wiley & Sons, 2006.

[112] A. W. J. Wells, *"Interface morphology and Dzyaloshinskii-Moriya interaction in Pt/Co thin films"*. PhD thesis, University of Leeds, 2017.

[113] L. G. Parratt, "Surface studies of solids by total reflection of x-rays," *Physical review*, vol. 95, no. 2, p. 359, 1954.

[114] P. Chowdhury, P. Kulkarni, M. Krishnan, H. C. Barshilia, A. Sagdeo, S. Rai, G. Lodha, and D. Sridhara Rao, "Effect of coherent to incoherent structural transition on magnetic anisotropy in co/pt multilayers," *Journal of Applied Physics*, vol. 112, no. 2, p. 023912, 2012.

[115] S. Emori and G. S. Beach, "Optimization of out-of-plane magnetized co/pt multilayers with resistive buffer layers," *Journal of applied physics*, vol. 110, no. 3, p. 033919, 2011.

[116] A. G. Kolesnikov, M. E. Stebliy, A. V. Ognev, A. S. Samardak, A. N. Fedorets, V. S. Plotnikov, X. Han, and L. A. Chebotkevich, "Enhancement of perpendicular magnetic anisotropy and coercivity in ultrathin ru/co/ru films through the buffer layer engineering," *Journal of Physics D: Applied Physics*, vol. 49, no. 42, p. 425302, 2016.

[117] V. Holy, J. Kubena, I. Ohli, K. Lischka, W. Plotz, *et al.*, "X-ray reflection from rough layered systems," *Physical review B*, vol. 47, no. 23, p. 15896, 1993.

[118] D. W. Breiby, O. Bunk, J. W. Andreasen, H. T. Lemke, and M. M. Nielsen, "Simulating x-ray diffraction of textured films," *Journal of Applied Crystallography*, vol. 41, no. 2, pp. 262–271, 2008.

[119] J. Daillant and A. Gibaud, *"X-ray and neutron reflectivity: principles and applications"*, vol. 770. Springer, 2008.

[120] M. Tolan, *"X-ray scattering from soft-matter thin films: materials science and basic research"*. Springer, 1999.

[121] S. Kobayashi and K. Inaba, "X-ray thin-film measurement techniques," *mass spectroscopy equipped with a skimmer-type interface*, p. 8, 2012.

[122] B. Yokhin, A. Dikopoltsev, T. Rafaeli, and A. Gvirtzman, "X-ray reflectometry with small-angle scattering measurement," May 17 2005. US Patent 6,895,075.

[123] T. Huang, R. Gilles, and G. Will, "Thin-film thickness and density determination from x-ray reflectivity data using a conventional power diffractometer," *Thin Solid Films*, vol. 230, no. 2, pp. 99–101, 1993.

[124] J. Als-Nielsen and D. McMorrow, *"Elements of modern X-ray physics"*. John Wiley & Sons, 2011.

[125] W. L. Bragg, "The structure of some crystals as indicated by their diffraction of x-rays," *Proc. R. Soc. Lond. A*, vol. 89, no. 610, pp. 248–277, 1913.

[126] C. Kittel, *"Elementary solid state physics: a short course"*. Wiley, 1962.

[127] Bahaaldin, *"Effect of copper ions on the Ni-Zn Ferrite Nanoparticles properties"*. LAP Lambert Academic Publishing, 2017.

[128] A. Patterson, "The scherrer formula for x-ray particle size determination," *Physical review*, vol. 56, no. 10, p. 978, 1939.

[129] P. Scherrer, "Bestimmung der inneren struktur und der größe von kolloidteilchen mittels röntgenstrahlen," in *Kolloidchemie Ein Lehrbuch*, pp. 387–409, Springer, 1912.

[130] B. E. Warren, *"X-ray Diffraction"*. Courier Corporation, 1990.

[131] G. K. Binnig, "Atomic force microscope and method for imaging surfaces with atomic resolution," Oct. 16 1990. US Patent App. 07/273,354.

[132] O. Iglesias-Freire, J. R. Bates, Y. Miyahara, A. Asenjo, and P. H. Grütter, "Tip-induced artifacts in magnetic force microscopy images," *Applied Physics Letters*, vol. 102, no. 2, p. 022417, 2013.

[133] L. Yi-Wei, Z. Qing-Feng, and L. Run-Wei, "Fabrication, properties, and applications of flexible magnetic films," *Chinese Physics B*, vol. 22, no. 12, p. 127502, 2013.

[134] D. M. , et.al, "Shapeable magnetic sensorics," in *Magnetics Conference (INTERMAG), 2015 IEEE*, pp. 1–1, IEEE, 2015.

[135] K. H. , et.al, "Engineering spin-orbit torque in co/pt multilayers with perpendicular magnetic anisotropy," *Applied Physics Letters*, vol. 107, no. 23, p. 232407, 2015.

[136] I. M. , et.al, "Current-driven spin torque induced by the rashba effect in a ferromagnetic metal layer," *Nature Mater*, vol. 9, no. 3, pp. 230–234, 2010.

[137] K. V. , et.al, "Effect of ta buffer layer and thickness on the structural and magnetic properties of co thin films," *Journal of Vacuum Science & Technology B: Microelectronics and Nanometer Structures Processing, Measurement, and Phenomena*, vol. 27, no. 5, pp. 2112–2116, 2009.

[138] R. Ö. , et.al, "Effect of ta buffer and nife seed layers on pulsed-dc magnetron sputtered ir 20 mn 80/co 90 fe 10 exchange bias," *Journal of Magnetism and Magnetic Materials*, vol. 323, no. 13, pp. 1827–1834, 2011.

[139] L. Z. , et.al, "Ordering promotion and intergrain decoupling in fept thin films by ta and ta/bi buffer layers," *Journal of applied physics*, vol. 102, no. 1, p. 013905, 2007.

[140] R. L. , et.al, "Effects of ta seed layer and annealing on magnetoresistance in co fe/ pd-based pseudo-spin-valves with perpendicular anisotropy," *Applied Physics Letters*, vol. 91, no. 24, p. 242504, 2007.

[141] M. M. , et.al, "Stretchable magnetoelectronics," *Nano letters*, vol. 11, no. 6, pp. 2522–2526, 2011.

[142] S. Azzawi, A. Ganguly, M. Tokaç, R. Rowan-Robinson, J. Sinha, A. Hindmarch, A. Barman, and D. Atkinson, "Evolution of damping in ferromagnetic/nonmagnetic thin film bilayers as a function of nonmagnetic layer thickness," *Physical Review B*, vol. 93, no. 5, p. 054402, 2016.

[143] K. L. , et.al, "Two-magnon scattering and viscous gilbert damping in ultrathin ferromagnets," *Physical Review B*, vol. 73, no. 14, p. 144424, 2006.

[144] W. MacDonald, K. Rollins, D. MacKerron, R. Eveson, R. Rustin, K. Rakos, and M. Handa, "P-46: Plastic displays—latest developments in polyester film for plastic electronics," in *SID Symposium Digest of Technical Papers*, vol. 35, pp. 420–423, Wiley Online Library, 2004.

[145] G. P. Martinsanz, *"Imaging: Sensors and Technologies"*. MDPI, 2018.

[146] e. a. Fisichella, Gabriele, "Micro-and nanoscale electrical characterization of large-area graphene transferred to functional substrates.," *Beilstein journal of nanotechnology 4*, vol. 234, 2013.

[147] M. Gijs and F. Petroff, *"Magnetic Ultra Thin Films, Multilayers and Surfaces"*, vol. 62. Elsevier, 1997.

[148] S. Tang, P. Carcia, D. Coulman, and A. McGhie, "Scanning tunneling microscopy of pt/co multilayers on pt buffer layers," *Applied physics letters*, vol. 59, no. 22, pp. 2898–2900, 1991.

[149] S. Landis, "Réseaux de plots magnétiques sub-microniques réalisés à partir de substrats prégravés," *Thesis*, 2001.

[150] G. Vinai, L. Frangou, C. Castán-Guerrero, V. Bonanni, B. Gobaut, S. Auffret, I. Prejbeanu, B. Dieny, V. Baltz, and P. Torelli, "Influence of mn diffusion on irmn thickness threshold for the onset of exchange bias in irmn/co bilayers," in *Journal of Physics: Conference Series*, vol. 903, p. 012061, IOP Publishing, 2017.

[151] K. Wang, M. Wu, S. Lepadatu, J. Claydon, C. Marrows, and S. J. Bending, "Optimization of co/pt multilayers for applications of current-driven domain wall propagation," *Journal of applied physics*, vol. 110, no. 8, p. 083913, 2011.

[152] M. D. Stiles, "Exchange coupling in magnetic heterostructures," *Physical Review B*, vol. 48, no. 10, p. 7238, 1993.

[153] S. S. Parkin, "Systematic variation of the strength and oscillation period of indirect magnetic exchange coupling through the 3d, 4d, and 5d transition metals," *Physical Review Letters*, vol. 67, no. 25, p. 3598, 1991.

[154] J. Moritz, F. Garcia, J. Toussaint, B. Dieny, and J. Nozières, "Orange peel coupling in multilayers with perpendicular magnetic anisotropy: Application to (co/pt)-based exchange-biased spin-valves," *EPL (Europhysics Letters)*, vol. 65, no. 1, p. 123, 2004.

[155] J. Knepper and F. Yang, "Oscillatory interlayer coupling in co/ pt multilayers with perpendicular anisotropy," *Physical Review B*, vol. 71, no. 22, p. 224403, 2005.

[156] M. Kisielewski, A. Maziewski, M. Tekielak, J. Ferré, S. Lemerle, V. Mathet, and C. Chappert, "Magnetic anisotropy and magnetization reversal processes in pt/co/pt films," *Journal of magnetism and magnetic materials*, vol. 260, no. 1-2, pp. 231–243, 2003.

[157] Y. Ding, J. H. Judy, and J.-P. Wang, "[co fe/ pt]× n multilayer films with a small perpendicular magnetic anisotropy," *Journal of applied physics*, vol. 97, no. 10, p. 10J117, 2005.

[158] M. Althammer, S. Meyer, H. Nakayama, M. Schreier, S. Altmannshofer, M. Weiler, H. Huebl, S. Geprägs, M. Opel, R. Gross, *et al.*, "Quantitative study of the spin hall magnetoresistance in ferromagnetic insulator/normal metal hybrids," *Physical Review B*, vol. 87, no. 22, p. 224401, 2013.

[159] A. Kobs and H. P. Oepen, "Disentangling interface and bulk contributions to the anisotropic magnetoresistance in pt/co/pt sandwiches," *Physical Review B*, vol. 93, no. 1, p. 014426, 2016.

[160] G. Fischer, H. Hoffmann, and J. Vancea, "Mean free path and density of conductance electrons in platinum determined by the size effect in extremely thin films," *Physical Review B*, vol. 22, no. 12, p. 6065, 1980.

[161] E. E. Fullerton, D. Stoeffler, K. Ounadjela, B. Heinrich, Z. Celinski, and J. Bland, "Structure and magnetism of epitaxially strained pd (001) films on fe (001): experiment and theory," *Physical Review B*, vol. 51, no. 10, p. 6364, 1995.

[162] J. Geissler, E. Goering, M. Justen, F. Weigand, G. Schütz, J. Langer, D. Schmitz, H. Maletta, and R. Mattheis, "Pt magnetization profile in a pt/co bilayer studied by resonant magnetic x-ray reflectometry," *Physical Review B*, vol. 65, no. 2, p. 020405, 2001.

[163] Z. Li, P. Carcia, and Y. Cheng, "Co thickness dependence of the microstructure of pt/co multilayers," *Journal of applied physics*, vol. 73, no. 5, pp. 2433–2437, 1993.

[164] S. Yuan, L. Sun, H. Sang, J. Du, and S. Zhou, "Interfacial effects on magnetic relaxation in co/pt multilayers," *Physical Review B*, vol. 68, no. 13, p. 134443, 2003.

[165] J. Shin, S. Hoon Kim, Y. Suwa, S. Hashi, and K. Ishiyama, "Control of in-plane uniaxial anisotropy of fe72si14b14 magnetostrictive thin film using a thermal expansion coefficient," *Journal of Applied Physics*, vol. 111, no. 7, p. 07E511, 2012.

[166] S. Otten, A. Kario, A. Kling, and W. Goldacker, "Bending properties of different rebco coated conductor tapes and roebel cables at t= 77 k," *Superconductor Science and Technology*, vol. 29, no. 12, p. 125003, 2016.

[167] S. Ota, Y. Hibino, D. Bang, H. Awano, T. Kozeki, H. Akamine, T. Fujii, T. Namazu, T. Takenobu, T. Koyama, *et al.*, "Strain-induced reversible modulation of the magnetic anisotropy in perpendicularly magnetized metals deposited on a flexible substrate," *Applied Physics Express*, vol. 9, no. 4, p. 043004, 2016.

[168] P. Shepley, A. Rushforth, M. Wang, G. Burnell, and T. Moore, "Modification of perpendicular magnetic anisotropy and domain wall velocity in pt/co/pt by voltage-induced strain," *Scientific reports*, vol. 5, p. 7921, 2015.

[169] J. A. Rogers, T. Someya, and Y. Huang, "Materials and mechanics for stretchable electronics," *science*, vol. 327, no. 5973, pp. 1603–1607, 2010.

[170] U. Gösele and Q.-Y. Tong, "Semiconductor wafer bonding," *Annual Review of Materials Science*, vol. 28, no. 1, pp. 215–241, 1998.

[171] N. Nishimura, T. Hirai, A. Koganei, T. Ikeda, K. Okano, Y. Sekiguchi, and Y. Osada, "Magnetic tunnel junction device with perpendicular magnetization films for high-density magnetic random access memory," *Journal of applied physics*, vol. 91, no. 8, pp. 5246–5249, 2002.

[172] S. Mangin, D. Ravelosona, J. Katine, M. Carey, B. Terris, and E. E. Fullerton, "Current-induced magnetization reversal in nanopillars with perpendicular anisotropy," *Nature materials*, vol. 5, no. 3, p. 210, 2006.

[173] J. Okabayashi, J. Koo, H. Sukegawa, S. Mitani, Y. Takagi, and T. Yokoyama, "Perpendicular magnetic anisotropy at the interface between ultrathin fe film and mgo studied by angular-dependent x-ray magnetic circular dichroism," *Applied Physics Letters*, vol. 105, no. 12, p. 122408, 2014.

[174] S. Hashimoto, Y. Ochiai, and K. Aso, "Perpendicular magnetic anisotropy and magnetostriction of sputtered co/pd and co/pt multilayered films," *Journal of applied physics*, vol. 66, no. 10, pp. 4909–4916, 1989.

[175] D. Odkhuu, S. Rhim, N. Park, and S. Hong, "Extremely large perpendicular magnetic anisotropy of an fe (001) surface capped by 5 d transition metal monolayers: A density functional study," *Physical Review B*, vol. 88, no. 18, p. 184405, 2013.

[176] S. Woo, M. Mann, A. J. Tan, L. Caretta, and G. S. Beach, "Enhanced spin-orbit torques in pt/co/ta heterostructures," *Applied Physics Letters*, vol. 105, no. 21, p. 212404, 2014.

[177] A. Van den Brink, M. van der Heijden, H. Swagten, and B. Koopmans, "Large time-dependent coercivity and resistivity modification under sustained voltage application in a pt/co/alox/pt junction," *Journal of Applied Physics*, vol. 117, no. 17, p. 17C717, 2015.

[178] M. Kitada and N. Shimizu, "Magnetic properties of sputtered co-pt thin films," *Journal of applied physics*, vol. 54, no. 12, pp. 7089–7094, 1983.

[179] T. McGuire, J. Aboaf, and E. Klokholm, "Magnetic and transport properties of co-pt thin films," *Journal of applied physics*, vol. 55, no. 6, pp. 1951–1953, 1984.

[180] P. Carcia, "Perpendicular magnetic anisotropy in pd/co and pt/co thin-film layered structures," *Journal of applied physics*, vol. 63, no. 10, pp. 5066–5073, 1988.

[181] L. Néel, "Anisotropie magnétique superficielle et surstructures d'orientation," *Journal de Physique et le Radium*, vol. 15, no. 4, pp. 225–239, 1954.

[182] F. Den Broeder, D. Kuiper, H. Donkersloot, and W. Hoving, "A comparison of the magnetic anisotropy of [001] and [111] oriented co/pd multilayers," *Applied Physics A*, vol. 49, no. 5, pp. 507–512, 1989.

[183] P. Bruno, "Tight-binding approach to the orbital magnetic moment and magnetocrystalline anisotropy of transition-metal monolayers," *Physical Review B*, vol. 39, no. 1, p. 865, 1989.

[184] F. El Gabaly, K. F. McCarty, A. K. Schmid, J. De La Figuera, M. C. Muñoz, L. Szunyogh, P. Weinberger, and S. Gallego, "Noble metal capping effects on the spin-reorientation transitions of co/ru (0001)," *New Journal of Physics*, vol. 10, no. 7, p. 073024, 2008.

[185] S. Peng, M. Wang, H. Yang, L. Zeng, J. Nan, J. Zhou, Y. Zhang, A. Hallal, M. Chshiev, K. L. Wang, *et al.*, "Origin of interfacial perpendicular magnetic anisotropy in mgo/cofe/metallic capping layer structures," *Scientific reports*, vol. 5, p. 18173, 2015.

[186] Y. Liu, J. Zhang, S. Wang, S. Jiang, Q. Liu, X. Li, Z. Wu, and G. Yu, "Ru catalyst-induced perpendicular magnetic anisotropy in mgo/cofeb/ta/mgo multilayered films," *ACS applied materials & interfaces*, vol. 7, no. 48, pp. 26643–26648, 2015.

[187] M. Sakurai, T. Takahata, and I. Moritani, "Magnetic and magneto-optical properties of co/ru multilayers," *IEEE translation journal on magnetics in Japan*, vol. 7, no. 2, pp. 176–182, 1992.

[188] J. Miyawaki, D. Matsumura, H. Abe, T. Ohtsuki, E. Sakai, K. Amemiya, and T. Ohta, "Perpendicular magnetic anisotropy associated with strain relaxation in ru/co/ru (0001): Anomalous relation of atomic and magnetic structures," *Physical Review B*, vol. 80, no. 2, p. 020408, 2009.

[189] F. El Gabaly, J. M. Puerta, C. Klein, A. Saa, A. K. Schmid, K. F. McCarty, J. I. Cerda, and J. de la Figuera, "Structure and morphology of ultrathinco/ru (0001) films," *New Journal of Physics*, vol. 9, no. 3, p. 80, 2007.

[190] H. Ding, A. Schmid, D. Keavney, D. Li, R. Cheng, J. Pearson, F. Fradin, and S. Bader, "Selective growth of co nanoislands on an oxygen-patterned ru (0001) surface," *Physical Review B*, vol. 72, no. 3, p. 035413, 2005.

[191] C. Vaz and J. Bland, "Dependence of the coercive field on the cu overlayer thickness in thin co/cu (001) and ni/cu (001) fcc epitaxial films," *Journal of Applied Physics*, vol. 89, no. 11, pp. 7374–7376, 2001.

[192] B.-Y. Wang, C.-C. Chiu, W.-C. Lin, and M.-T. Lin, "Enhanced perpendicular magnetic anisotropy in fe/mn bilayers by incorporating ultrathin ferromagnetic underlayer through magnetic proximity effect," *Applied Physics Letters*, vol. 103, no. 4, p. 042407, 2013.

[193] C. Chappert and P. Bruno, "Magnetic anisotropy in metallic ultrathin films and related experiments on cobalt films," *Journal of Applied Physics*, vol. 64, no. 10, pp. 5736–5741, 1988.

[194] N. Alekseevskii, K.-H. Bertel, A. Dubrovin, V. Nizhankovskii, and L. Urai, "Magnetoresistance of ruthenium in strong magnetic fields," *Soviet Journal of Experimental and Theoretical Physics Letters*, vol. 18, p. 163, 1973.

[195] J. Alstad, R. Colvin, and S. Legvold, "Single-crystal and polycrystal resistivity relationships for yttrium," *Physical Review*, vol. 123, no. 2, p. 418, 1961.

[196] L. L. Campbell, *"Galvanomagnetic and Thermomagnetic Effects: The Hall and Allied Phenomena"*, vol. 7. Longmans, Green and Company, 1923.

[197] J. Asmussen, R. Fritz, L. Mahoney, G. Fournier, and G. Demaggio, "Ecr ion and free radical sources for mbe applications," *Review of Scientific Instruments*, vol. 61, no. 1, pp. 282–284, 1990.

[198] J. Assmann, V. Narkhede, N. Breuer, M. Muhler, A. Seitsonen, M. Knapp, D. Crihan, A. Farkas, G. Mellau, and H. Over, "Heterogeneous oxidation catalysis on ruthenium: bridging the pressure and materials gaps and beyond," *Journal of Physics: Condensed Matter*, vol. 20, no. 18, p. 184017, 2008.

[199] P. Klapetek, D. Necas, and C. Anderson, "Gwyddion user guide," *Czech Metrology Institute*, vol. 2007, p. 2009, 2004.

[200] T. R. Hayase, M. and B. Wu., "Electronics packaging 3." the electrochemical society,"

[201] M. Je, H. Choi, Y. Hwang, K.-H. Yun, and Y.-C. Chung, "Surface structure effect on the magnetic anisotropy of co/pd (001) thin film: A first principles study," *Thin Solid Films*, vol. 589, pp. 252–257, 2015.

[202] S. Wei, B. Li, T. Fujimoto, and I. Kojima, "Surface morphological modification of pt thin films induced by growth temperature," *Physical Review B*, vol. 58, no. 7, p. 3605, 1998.

[203] S. Emori and G. S. Beach, "Roles of the magnetic field and electric current in thermally activated domain wall motion in a submicrometer magnetic strip with perpendicular magnetic anisotropy," *Journal of Physics: Condensed Matter*, vol. 24, no. 2, p. 024214, 2011.

[204] C. Liu and S. Bader, "Magnetism and growth of ultrathin co films grown epitaxially on ru (0001)," *Journal of magnetism and magnetic materials*, vol. 119, no. 1-2, pp. 81–86, 1993.

[205] C. Yu, D. Li, J. Pearson, and S. Bader, "Self-assembled metallic dots and antidots: Epitaxial co on ru (0001)," *Applied Physics Letters*, vol. 78, no. 9, pp. 1228–1230, 2001.

[206] H. Ding, A. Schmid, D. Li, K. Y. Guslienko, and S. Bader, "Magnetic bistability of co nanodots," *Physical review letters*, vol. 94, no. 15, p. 157202, 2005.

[207] Y.-P. Zhao, R. Gamache, G.-C. Wang, T.-M. Lu, G. Palasantzas, and J. T. M. De Hosson, "Effect of surface roughness on magnetic domain wall thickness, domain size, and coercivity," *Journal of Applied Physics*, vol. 89, no. 2, pp. 1325–1330, 2001.

[208] V. LaBella, D. Bullock, Z. Ding, C. Emery, A. Venkatesan, W. Oliver, G. Salamo, P. Thibado, and M. Mortazavi, "Spatially resolved spin-injection probability for gallium arsenide," *Science*, vol. 292, no. 5521, pp. 1518–1521, 2001.

[209] P. Kulkarni, M. Krishnan, H. C. Barshilia, and P. Chowdhury, "Effect of pt layer thickness on perpendicular magnetic anisotropy in ultrathin co/pt multilayers," in *AIP Conference Proceedings*, vol. 1512, pp. 1144–1145, AIP, 2013.

[210] e. A. Kayal Sumana, "Structural and resistive property of cobalt/silicon thin film as a function of thickness," *International Journal of Science and Research (IJSR) ISSN (Online)*, vol. 2319-7064, 2013.

[211] J. Prokop, D. Valdaitsev, A. Kukunin, M. Pratzer, G. Schönhense, and H. Elmers, "Strain-induced magnetic anisotropies in co films on mo (110)," *Physical Review B*, vol. 70, no. 18, p. 184423, 2004.

[212] H. Fritzsche, J. Kohlhepp, and U. Gradmann, "Epitaxial strain and magnetic anisotropy in ultrathin co films on w (110)," *Physical Review B*, vol. 51, no. 22, p. 15933, 1995.

[213] H. Tokano, H. Yanagihara, and E. Kita, "Perpendicular magnetic anisotropy of co/ rh (111) distorted superlattices," 2005.

[214] T. Kingetsu, "Phenomenological approach to the dependence of magnetic anisotropy on co layer thickness in epitaxial au/co and au/co/ag superlattices," *Japanese journal of applied physics*, vol. 36, no. 12B, p. L1658, 1997.

[215] D. Ravelosona, D. Lacour, J. Katine, B. Terris, and C. Chappert, "Nanometer scale observation of high efficiency thermally assisted current-driven domain wall depinning," *Physical review letters*, vol. 95, no. 11, p. 117203, 2005.

[216] O. Boulle, J. Kimling, P. Warnicke, M. Kläui, U. Rüdiger, G. Malinowski, H. J. Swagten, B. Koopmans, C. Ulysse, and G. Faini, "Nonadiabatic spin transfer torque in high anisotropy magnetic nanowires with narrow domain walls," *Physical review letters*, vol. 101, no. 21, p. 216601, 2008.

[217] T. A. Moore, I. Miron, G. Gaudin, G. Serret, S. Auffret, B. Rodmacq, A. Schuhl, S. Pizzini, J. Vogel, and M. Bonfim, "High domain wall velocities induced by current in ultrathin pt/co/alox wires with perpendicular magnetic anisotropy," *Applied Physics Letters*, vol. 93, no. 26, p. 262504, 2008.

[218] C. Burrowes, A. Mihai, D. Ravelosona, J.-V. Kim, C. Chappert, L. Vila, A. Marty, Y. Samson, F. Garcia-Sanchez, L. Buda-Prejbeanu, *et al.*, "Non-adiabatic spin-torques in narrow magnetic domain walls," *Nature Physics*, vol. 6, no. 1, p. 17, 2010.

[219] I. M. Miron, T. Moore, H. Szambolics, L. D. Buda-Prejbeanu, S. Auffret, B. Rodmacq, S. Pizzini, J. Vogel, M. Bonfim, A. Schuhl, *et al.*, "Fast current-induced domain-wall motion controlled by the rashba effect," *Nature materials*, vol. 10, no. 6, p. 419, 2011.

[220] K.-J. Kim, J.-C. Lee, S.-J. Yun, G.-H. Gim, K.-S. Lee, S.-B. Choe, and K.-H. Shin, "Electric control of multiple domain walls in pt/co/pt nanotracks with perpendicular magnetic anisotropy," *Applied physics express*, vol. 3, no. 8, p. 083001, 2010.

[221] T. Koyama, D. Chiba, K. Ueda, K. Kondou, H. Tanigawa, S. Fukami, T. Suzuki, N. Ohshima, N. Ishiwata, Y. Nakatani, *et al.*, "Observation of the intrinsic pinning of a magnetic domain wall in a ferromagnetic nanowire," *Nature materials*, vol. 10, no. 3, p. 194, 2011.

[222] J. Heinen, O. Boulle, K. Rousseau, G. Malinowski, M. Kläui, H. J. Swagten, B. Koopmans, C. Ulysse, and G. Faini, "Current-induced domain wall motion in co/pt nanowires: Separating spin torque and oersted-field effects," *Applied Physics Letters*, vol. 96, no. 20, p. 202510, 2010.

[223] A. Fert and P. M. Levy, "Role of anisotropic exchange interactions in determining the properties of spin-glasses," *Physical Review Letters*, vol. 44, no. 23, p. 1538, 1980.

[224] M. Heide, G. Bihlmayer, and S. Blügel, "Dzyaloshinskii-moriya interaction accounting for the orientation of magnetic domains in ultrathin films: Fe/w (110)," *Physical Review B*, vol. 78, no. 14, p. 140403, 2008.

[225] F. Freimuth, S. Blügel, and Y. Mokrousov, "Berry phase theory of dzyaloshinskii–moriya interaction and spin–orbit torques," *Journal of physics: Condensed matter*, vol. 26, no. 10, p. 104202, 2014.

[226] U. Rößler, A. Bogdanov, and C. Pfleiderer, "Spontaneous skyrmion ground states in magnetic metals," *Nature*, vol. 442, no. 7104, p. 797, 2006.

[227] S. Mühlbauer, B. Binz, F. Jonietz, C. Pfleiderer, A. Rosch, A. Neubauer, R. Georgii, and P. Böni, "Skyrmion lattice in a chiral magnet," *Science*, vol. 323, no. 5916, pp. 915–919, 2009.

[228] X. Yu, Y. Onose, N. Kanazawa, J. Park, J. Han, Y. Matsui, N. Nagaosa, and Y. Tokura, "Real-space observation of a two-dimensional skyrmion crystal," *Nature*, vol. 465, no. 7300, p. 901, 2010.

[229] Y. Yoshida, S. Schröder, P. Ferriani, D. Serrate, A. Kubetzka, K. von Bergmann, S. Heinze, and R. Wiesendanger, "Conical spin-spiral state in an ultrathin film driven by higher-order spin interactions," *Physical review letters*, vol. 108, no. 8, p. 087205, 2012.

[230] B. Dupé, M. Hoffmann, C. Paillard, and S. Heinze, "Tailoring magnetic skyrmions in ultra-thin transition metal films," *Nature communications*, vol. 5, p. 4030, 2014.

[231] E. Simon, K. Palotás, L. Rózsa, L. Udvardi, and L. Szunyogh, "Formation of magnetic skyrmions with tunable properties in pdfe bilayer deposited on ir (111)," *Physical Review B*, vol. 90, no. 9, p. 094410, 2014.

[232] J. Pommier, P. Meyer, G. Pénissard, J. Ferré, P. Bruno, and D. Renard, "Magnetization reversal in ultrathin ferromagnetic films with perpendicular anistropy: Domain observations," *Physical review letters*, vol. 65, no. 16, p. 2054, 1990.

[233] A. Kirilyuk, J. Ferré, V. Grolier, J. Jamet, and D. Renard, "Magnetization reversal in ultrathin ferromagnetic films with perpendicular anisotropy," *Journal of magnetism and magnetic materials*, vol. 171, no. 1-2, pp. 45–63, 1997.

[234] U. Nowak, J. Heimel, T. Kleinefeld, and D. Weller, "Domain dynamics of magnetic films with perpendicular anisotropy," *Physical Review B*, vol. 56, no. 13, p. 8143, 1997.

[235] S. Lemerle, J. Ferré, C. Chappert, V. Mathet, T. Giamarchi, and P. Le Doussal, "Domain wall creep in an ising ultrathin magnetic film," *Physical review letters*, vol. 80, no. 4, p. 849, 1998.

[236] L. Krusin-Elbaum, T. Shibauchi, B. Argyle, L. Gignac, and D. Weller, "Stable ultrahigh-density magneto-optical recordings using introduced linear defects," *Nature*, vol. 410, no. 6827, p. 444, 2001.

[237] D. Weller, L. Folks, M. Best, E. E. Fullerton, B. Terris, G. Kusinski, K. Krishnan, and G. Thomas, "Growth, structural, and magnetic properties of high coercivity co/pt multilayers," *Journal of Applied Physics*, vol. 89, no. 11, pp. 7525–7527, 2001.

[238] S.-B. Choe and S.-C. Shin, "Magnetization reversal in nanostructured co/pd multilayers," *Physical Review B*, vol. 57, no. 2, p. 1085, 1998.

[239] C. Canedy, X. Li, and G. Xiao, "Large magnetic moment enhancement and extraordinary hall effect in co/pt superlattices," *Physical Review B*, vol. 62, no. 1, p. 508, 2000.

[240] J.-C. A. Huang, L. Wu, M. Chen, T.-H. Wu, J.-C. Wu, Y. Huang, C.-H. Lee, and C. Fu, "Perpendicular magnetic anisotropy and magnetic domain structure of unpatterned and patterned co/pt multilayers," *Journal of magnetism and magnetic materials*, vol. 209, no. 1-3, pp. 90–94, 2000.

[241] R. Woodward, A. Lance, R. Street, and R. Stamps, "Variation of the magnetic domain structure with reversal field," *Journal of applied physics*, vol. 93, no. 10, pp. 6567–6571, 2003.

[242] J. E. Davies, O. Hellwig, E. E. Fullerton, G. Denbeaux, J. Kortright, and K. Liu, "Magnetization reversal of co/ pt multilayers: Microscopic origin of high-field magnetic irreversibility," *Physical Review B*, vol. 70, no. 22, p. 224434, 2004.

[243] A. Schwarz, M. Liebmann, U. Kaiser, R. Wiesendanger, T. W. Noh, and D. W. Kim, "Visualization of the barkhausen effect by magnetic force microscopy," *Physical review letters*, vol. 92, no. 7, p. 077206, 2004.

[244] R. A. Fry, L. H. Bennett, and E. Della Torre, "Kerr imaging of a co/pt bimodal magneto-optical medium," *Journal of applied physics*, vol. 85, no. 8, pp. 5169–5171, 1999.

[245] M. S. Pierce, C. Buechler, L. Sorensen, J. Turner, S. Kevan, E. Jagla, J. Deutsch, T. Mai, O. Narayan, J. Davies, *et al.*, "Disorder-induced microscopic magnetic memory," *Physical review letters*, vol. 94, no. 1, p. 017202, 2005.

[246] H. J. Richter, "Recent advances in the recording physics of thin-film media," *Journal of Physics D: Applied Physics*, vol. 32, no. 21, p. R147, 1999.

[247] R. Skomski, "Nanomagnetics," *Journal of physics: Condensed matter*, vol. 15, no. 20, p. R841, 2003.

[248] S. D. Bader, "Colloquium: Opportunities in nanomagnetism," *Reviews of modern physics*, vol. 78, no. 1, p. 1, 2006.

[249] O. Hellwig, A. Berger, J. B. Kortright, and E. E. Fullerton, "Domain structure and magnetization reversal of antiferromagnetically coupled perpendicular anisotropy films," *Journal of Magnetism and Magnetic Materials*, vol. 319, no. 1-2, pp. 13–55, 2007.

[250] C. Vaz, J. Bland, and G. Lauhoff, "Magnetism in ultrathin film structures," *Reports on Progress in Physics*, vol. 71, no. 5, p. 056501, 2008.

[251] G. Bertotti, *"Hysteresis in magnetism: for physicists, materials scientists, and engineers"*. Academic press, 1998.

[252] O. Boulle, "Nonadiabatic spin transfer torque in high anisotropy magnetic nanowires with narrow domain walls," *Phys. Rev. Lett.*, vol. 101, p. 216601, 2008.

[253] T. Moore, "Determination of perpendicular magnetic anisotropy in ultrathin ferromagnetic films by extraordinary hall voltage measurement," *Appl. Phys. Lett.*, vol. 93, p. 262504, 2008.

[254] M. M. Bouziane K, Al Rawas A D and M. M, "Buffer effect on gmr in thin co/cu multilayers," *J. Alloys Compounds*, vol. 414, p. 42, 2006.

[255] F. Eder, H. Klauk, M. Halik, U. Zschieschang, G. Schmid, and C. Dehm, "Organic electronics on paper," *Applied Physics Letters*, vol. 84, no. 14, pp. 2673–2675, 2004.

[256] V. M. Parakkat, K. Ganesh, and P. Anil Kumar, "Tailoring curie temperature and magnetic anisotropy in ultrathin pt/co/pt films," *AIP Advances*, vol. 6, no. 5, p. 056118, 2016.

[257] Kisielewski, "Magnetic anisotropy and magnetization reversal processes in pt/co/pt films," *J.magn.magn.mater*, vol. 260, 231, 2003.

[258] M. Kisielewski, A. Maziewski, T. Polyakova, and V. Zablotskii, "Wide-scale evolution of magnetization distribution in ultrathin films," *Physical Review B*, vol. 69, no. 18, p. 184419, 2004.

[259] C. Lee, R. Farrow, C. Lin, E. Marinero, and C. Chien, "Molecular-beam-epitaxial growth and magnetic properties of co-pt superlattices oriented along the [001],[110], and [111] axes of pt," *Physical Review B*, vol. 42, no. 17, p. 11384, 1990.

[260] S. Bandiera, R. Sousa, B. Rodmacq, and B. Dieny, "Asymmetric interfacial perpendicular magnetic anisotropy in pt/co/pt trilayers," *IEEE Magnetics Letters*, vol. 2, pp. 3000504–3000504, 2011.

[261] G. A. Bertero and R. Sinclair, "Kerr rotations and anisotropy in (pt/co/pt)/x multilayers," *IEEE transactions on magnetics*, vol. 31, no. 6, pp. 3337–3342, 1995.

[262] D. Jiles, *"Introduction to magnetism and magnetic materials"*. CRC press, 2015.

[263] M. MacCaig, *"Permanent magnets in theory and practice"*. Pentech press, 1987.

[264] S. Honda, H. Tanimoto, and T. Kusuda, "Magnetization process and coercivity of sputtered co/pt multilayered films," *IEEE Transactions on Magnetics*, vol. 26, no. 5, pp. 2730–2732, 1990.

[265] H. Stillrich, C. Menk, R. Frömter, and H. P. Oepen, "Magnetic anisotropy and spin reorientation in co/pt multilayers: Influence of preparation," *Journal of Magnetism and Magnetic Materials*, vol. 322, no. 9-12, pp. 1353–1356, 2010.

[266] T. Suzuki, "Coercivity mechanism in (copt) and (copd) multilayers," *Scripta metallurgica et materialia*, vol. 33, no. 10-11, pp. 1609–1623, 1995.